"CHEMICAL SYNTHESIS OF CADMIUM CHALCOGENIDE/rGO THIN FILMS FOR PHOTOELECTROCHEMICAL AND SENSOR APPLICATIONS"

A THESIS SUBMITTED TO

D. Y. PATIL EDUCATION SOCIETY (DEEMED TO BE UNIVERSITY), KOLHAPUR

FOR THE DEGREE OF

DOCTOR OF PHILOSOPHY

IN

PHYSICS

UNDER THE FACULTY OF INTERDISCIPLINARY STUDIES

BY

Mr. RANJIT PANDURANG NIKAM

M. Sc.

UNDER THE SUPERVISION OF

Prof. CHANDRAKANT D. LOKHANDE

M. Sc., Ph. D.

DEAN & RESEARCH DIRECTOR,
CENTRE FOR INTERDISCIPLINARY RESEARCH,
D. Y. PATIL EDUCATION SOCIETY (DEEMED TO BE UNIVERSITY), KOLHAPUR 416 006, MAHARASHTRA, (INDIA)

2024

DECLARATION

I am *Ranjit Pandurang Nikam*, hereby declare that the thesis entitled *"CHEMICAL SYNTHESIS OF CADMIUM CHALCOGENIDE/rGO THIN FILMS FOR PHOTOELECTROCHEMICAL AND SENSOR APPLICATIONS"* submitted for the degree of **Doctor of Philosophy (Ph.D.)** *in the* **Physics**, *Faculty of Interdisciplinary Studies*, under the guidance of *Prof. C. D. Lokhande*, **Centre for Interdisciplinary Research (CIR), D. Y. Patil Education Society (Deemed to be University), Kolhapur** is completed and written by me, has not before made the basis for the award of any other higher education institute in India or any other country. To the best of my knowledge and belief the thesis contains no material previously published or written by another person except where due reference is made. Further, I declare that I have not violated any of the provisions under the copyright and piracy/cyber/IPR Act amended from time to time.

Research Student

Place: Kolhapur

Date: /   /2024   **Mr. Ranjit Pandurang Nikam**

CERTIFICATE OF GUIDE

This is to certify that the thesis entitled *"CHEMICAL SYNTHESIS OF CADMIUM CHALCOGENIDE/rGO THIN FILMS FOR PHOTOELECTROCHEMICAL AND SENSOR APPLICATIONS"* which is being submitted herewith for the award of the Degree of *Doctor of Philosophy (Ph.D.) in Physics*, **Faculty of Interdisciplinary Studies**, *under the guidance of* *Prof. C. D. Lokhande*, **Centre for Interdisciplinary Research (CIR)**, *D. Y. Patil Education Society (Deemed to be University), Kolhapur*, is the result of the original research work completed by *Mr. Ranjit Pandurang Nikam* under my supervision and guidance and to the best of my knowledge and belief the work embodied in this thesis has not formed earlier the basis for the award of any degree or similar title of this or any other university or examining body.

Research Guide

Place: Kolhapur

Date: /   /2024

Prof. C. D. Lokhande
Dean and Research Director
Centre for Interdisciplinary Research,
D. Y. Patil Education Society,
(Deemed to be University),
Kolhapur – 416 006

ACKNOWLEDGEMENT

This was a beautiful journey, a journey of expanding the boundaries of knowledge, a journey of finding your strengths and weaknesses, a journey of becoming mentally and emotionally strong. It became more beautiful and interesting because of the people I met along the way. I would like to take this opportunity to acknowledge those fascinating people.

*I would like to express my first profound thanks and respect towards my cherished guide **Prof. Chandrakant D. Lokhande** (Dean and Research Director, Centre for Interdisciplinary Research, D. Y. Patil Education Society, Kolhapur) for his keen awareness, valuable guidance, encouragement, and support. I am always amazed by his enthusiasm for science and how effectively he has shaped the young minds of two generations. I am very thankful to him for choosing me as his PhD student and I feel very fortunate to be part of CDL group.*

*I would like to express my sincere thanks to President **Dr. Sanjay D. Patil Saheb**, Vice President **Mr. Satej D. Patil Saheb**, Vice-Chancellor **Prof. R. K. Mudgal**, Registrar **Dr. V. V. Bhosale,** and **Dr. Shimpa Sharma** for the inspiration and support. I thank **Dr. R. S. Patil, Dr. J. L. Gunjakar**, **Dr. U. M. Patil**, **Dr. Vishwajeet Khot, and Dr. Sharad Patil** who helped me to analyze the results with all their empathy and cooperative mind. I also thank **Dr. A. C. Lokhande**, and **Dr**. **V. C. Lokhande** for providing me important sample characterization data during entire research work.*

*I would like to express sincere thanks to my seniors **Dr. V. J. Mane**, **Dr. S. B. Ubale**, **Dr. D. B. Malvekar**, **Dr. P. P. Bagwade**, **Dr. P. K. Katkar**, **Dr. S. B. Pujari**, **Dr. S. A. Khalate**, **Dr. S. B. Sadavar**, **Dr. N. S. Padalkar**, **Dr. R. B. Shinde**, **Dr. S. B. Jadhav**, **Mr. V. V. Magdum**, **Mr. Y. M. Chitare**, and **Ms. S. P. Kulkarni** for insightful guidance, scientific discussions and valuable suggestions on the present work.*

*I would like to acknowledge my colleagues at Centre for Interdisciplinary Research, **Mr. S. D. Khot**, **Ms. J.P. Thorat**, **Ms. S. B. Patil**, **Mr. K. G. belekar** and, **Mr. D. J. Patil** for their wonderful collaboration.*

*I am thankful to labmates and juniors **Ajinkya**, **Divya**, **Prashant**, **Shweta**, **Shraddha**, **Mayura** and **Suraj**. I am also thankful to **Mrs. Namrata**, **Mr. Ramdas**,*

My heartfelt appreciation goes out to my father **Pandurang (Nana)**, my mother **Sangita (Aai)**, my lovely sister **Maya (Didoo)**, and my lovely brother in law **Annasaheb** for their continuous support and love.

~Ranjit

Place: Kolhapur

LIST OF PATENTS, PUBLICATIONS AND CONFERENCES ATTAINED

Patents: (Granted 05, Published 05, Filed 02)

1) Chemical synthesis of cadmium selenide/reduced graphene oxide composite thin film and photoelectronchemical cell application, Prof. C. D. Lokhande, **Mr. R. P. Nikam**, Mr. S. D. Khot, Ms. P. P. Bagwade, Mr. D. J. Patil (Grant number: 473475).

2) Electrodeposition of lanthanum selenide thin films and their application in oxygen evolution reaction, Prof. C. D. Lokhande, **Mr. R. P. Nikam**, Mr. S. B. Shaikh (Grant number: 434444)

3) Electrochemical supercapacitor device, Prof. C. D. Lokhande, Ms. P. P. Bagwade, Dr. D. B. Malavekar, Mr. S. D. Khot, **Mr. R. P. Nikam** (Grant number: 445967).

4) A method of synthesizing composite of reduced graphene oxide and nickel tungstate for energy storage, Prof. C. D. Lokhande, Mr. D. J. Patil, Dr. D. B. Malavekar, Mr. S. D. Khot, **Mr. R. P. Nikam** (Grant number: 479403).

5) Chemical synthesis of reduced graphene oxide-dysprosium selenide composite thin films for energy storage device, Prof. C. D. Lokhande, Mr. S. D. Khot, Dr. Dhanaji B. Malavekar, **Mr. R. P. Nikam,** Ms. P. P. Bagwade (Grant number: 433033).

6) A chemical synthesis process for cobalt tungstate/reduced graphene oxide composite thin film and use as electrocatalyst thereof, Prof. C. D. Lokhande, Ms. P. P. Bagwade, Mr. S. D. Khot, **Mr. R. P. Nikam** (Application No: 202221066956).

7) Method of synthesis of tungsten oxide/reduced graphene oxide composite thin coating for energy storage, Prof. C. D. Lokhande, Ms. S. B. Patil, **Mr. R. P. Nikam,** Mr. S. B. Shaikh, Prof. R. S. Patil (Application no. 202321054563)

8) Chemical synthesis of manganese phosphate thin coating for energy storage application, Prof. C. D. Lokhande, Dr. U. M. Patil, Mr. K. G. Belekar, **Mr. R. P. Nikam**, Ms. S. S. Patil (Application no. 202321053383)

9) Chemical synthesis of cobalt phosphate/polyaniline composite coating for energy storage application, Prof. C. D. Lokhande, Dr. U. M. Patil, Mr. K. G. Belekar, **Mr. R. P. Nikam**, Ms. S. S. Patil, Mr. G. D. Jadhav (Application no. 202321063189)

10) Chemical synthesis of layered double hydroxide coupled with carbon nanotube for electrochemical capacitor, Dr. Navnath S. Padalkar, Ms. Jayshri A. Shingade, Dr. Navajsharif Shamshuddin Shaikh, **Mr. Ranjit P. Nikam**, Ms. Apurva Patil, Dr. Abhinandan Patil (Application no. 202421002481)

11) Electrodeposition of reduced graphene oxide/cadmium selenide composite thin films and their photoelectrochemical cell application, Prof. Chandrakant D. Lokhande, **Mr. Ranjit P. Nikam**, Ms. Sujata B. Patil**,** Mr. Suraj R. Sankapal, Dr. Abhishek C. Lokhande (Application no. 202421079222).

12) Synthesis of reduced graphene oxide/cadmium sulfide composite thin films and their photoelectrochemical cell application, Prof. Chandrakant D. Lokhande, **Mr. Ranjit P. Nikam**, Ms. Sujata B. Patil, Mr. Suraj R. Sankapal, Dr. Vaibhav C. Lokhande (Application no. 202421081097).

Papers Published in International Journals: (10)

1) Chemical synthesis and (photo) electrochemical study of CdS/rGO nanocomposite films, **R. P. Nikam**, A. C. Lokhande, S. D. Khot, V. J. Mane, C. D. Lokhande, Journal of Korean Ceramic Society, 60, (2023), 238, **(I.F.-2.7)**.

2) Effect of post annealing on chemisynthesized cadmium selenide (CdSe) thin flms: physicochemical and photoelectrochemical properties, **R. P. Nikam**, V. C. Lokhande, S. D. Khot, P. P. Bagwade, J. L. Gunjakar, C. D. Lokhande, Journal of Materials Science: Materials in Electronics, 34, (2023), 1940, **(I.F.-2.8)**.

3) Performance of solid-state symmetric supercapacitors based on Dy_2S_3 electrodes, P. P. Bagwade, **R. P. Nikam**, R. P. Bhosale, S. D. Khot, C. D. Lokhande, Applied Surface Science Advances, 18, (2023), 100529, (**I.F.- 7.5**).

4) Porous $NiCo_2O_4$ electrodes for high-energy asymmetric supercapacitor: effect of annealing, J. P. Thorat, **R. P. Nikam**, V. C. Lokhande, C. D. Lokhande, Journal of Materials Science, 58, (2023) 9586, **(I.F. - 3.5)**.

5) Nanocrystalline cobalt tungstate thin films prepared by SILAR method for electrocatalytic oxygen evolution reaction, international journal of hydrogen energy, P. P. Bagwade D. B. Malavekar, V. V. Magdum, S. D. Khot, **R. P. Nikam**, D. J. Patil, U. M. Patil, C. D. Lokhande, International Journal of Hydrogen Energy, 48, (2023), 8465, **(I.F.-8.1)**.

6) MnS-La_2S_3/GO composite electrodes for high-performance flexible symmetric supercapacitor, V. J. Mane, A. C. Lokhande, **R. P. Nikam**, N. S. Padalkar, V. C. Lokhande, D. S. Dhawale, C. D. Lokhande. Applied Surface Science Advances 15, (2023), 100399 **(I.F.- 7.5)**.

7) Chemisynthesized tungsten oxide (Wo_3) electrodes for high-performance asymmetric supercapacitor application: effect of deposition time, S. B. Patil, **R. P. Nikam**, C. D. Lokhande, R. S. Patil, Journal of Materials Science: Materials in Electronics, 34, (2023) 1956, **(I.F. - 2.8)**

8) Chemically synthesized $ZnFe_2O_4$ electrodes for electrochemical oxygen evolution reaction and supercapacitor applications, S. D. Jituri, **R. P. Nikam**, V. J. Mane, S. B. Shaikh, C. D. Lokhande, S. H. Mujawar, Journal of Materials Science: Materials in Electronics, 34, (2023) 1842, **(I.F. - 2.8)**

9) SILAR synthesized dysprosium selenide (Dy_2Se_3) thin films for hybrid electrochemical capacitors, S. D. Khot, D. B. Malavekar, **R. P. Nikam,** S. B. Ubale, P. P. Bagwade, D. J. Patil, V. C. Lokhande, C. D. Lokhande, Synthetic Metals, 287, (2022), 117075 **(I.F.- 4.0)**.

10) Synthesis of reduced graphene oxide (rGO)/dysprosium selenide (Dy_2Se_3) composite electrode for energy storage; flexible asymmetric supercapacitor, S. D. Khot, D. B. Malavekar, P. P. Bagwade, **R. P. Nikam,** C. D. Lokhande, Journal of Physics and Chemistry of Solids, 179, (2023), 111419, **(I.F.- 4.3)**.

Papers Submitted at International Journals: (04)

1) Tungsten oxide/reduced graphene oxide composite electrodes for solid state asymmetric supercapacitor application, S. B. Patil, **R. P. Nikam**, V. C. Lokhande, C. D. Lokhande, R. S. Patil, Advanced Composites and Hybrid Materials, **(Under review, I.F.- 23.2)**.

2) Molybdenum oxide electrodes for asymmetric supercapacitor application: effect of precursor concentration, S. B. Patil, **R. P. Nikam**, P. K. Katkar, C. D. Lokhande, R. S. Patil, International Journal of Energy Research, **(Under review, I.F.- 4.3)**.

3) Binder free chemical bath deposition of rGO/WO_3 nanocomposites for supercapacitor application, S. B. Patil, **R. P. Nikam,** C. D. Lokhande, R. S. Patil, Journal of Physics and Chemistry of Solids, **(Submitted, I.F.- 4.3)**.

4) Electrochemically synthesized rGO/CdS composite photoelectrodes for photoelectrochemical (PEC) cell application, **Ranjit P. Nikam**, Sujata B. Patil, Dilip J. Patil, Chandrakant D. Lokhande, Solar Energy Materials and Solar Cells, (**Submitted, I.F.- 6.3)**.

Review Articles and Book Chapters Submitted at International Journals: (02)

1) Review on the design of innovative metal chalcogenide incorporating carbon-based nanostructured materials: emerging trends in energy storage devices, Vikas J. Mane, Rameshwar S. Tupke, Dinesh S. Bobade, **Ranjit P. Nikam**, Dattatray S. Dhawale, Zafar Said, Babasaheb R. Sankapal, Anuradha C. Pawar, Ji Man Kim, Ravindra N. Bulakhe, Nano Energy (**Submitted, I.F.- 16.8)**.

2) Book chapter: Basic principles in low dimension materials for energy storage: An introduction, smart and low dimensional materials for supercapacitor and solar cells, Sohel B. Shaikh, Sujata B. Patil, **Ranjit P. Nikam**, Chandrakant D. Lokhande, Padmaja N. Pawaskar, ACS Book Series (**Submitted)**.

Papers/Poster Presented at National/International Conferences: (08)

1) Presented research paper (oral) in "2 nd Asian e-Conference on Engineered science", on 5-6 December 2021, organised by Prof. C. D. Lokhande endowment charitable trust and engineered science publisher, USA.

2) Presented poster and **got best poster** price in international conference on "Advanced Materials Synthesis, Characterisation and Applications" 18th to 20th October 2022, organized by SPPU Pune.

3) Presented research paper in Three days International Conference on "Nano Composite for Aerospace Applications", 2nd to 4th February 2023, Department of Basic Science and Electronics and Communication Engineering, Cambridge Institute of Technology, Bengaluru.

4) Presented poster in international conference on "Nanotechnology Addresing the Convergence of Materials Science, Biotechnology and medical Science" 12th to 14th February 2024 organised by CIR, DYPES, Kolhapur.

5) Presented a paper (oral) in national conference on "Emerging Trends in Chemistry" 10th February 2022, organised by SMM college, Akluj.

6) Presented poster in national conference on "Emerging Trends in Chemical Sciences and Nanomaterials" 24th to 25th February 2023 held at Rajarshi Chatrapati Shahu College, Kolhapur.

7) Poster presented in ''Dnyanshodh-2022'' organized by CIR, D.Y. Patil Education Society, Kolhapur on 28th February 2022.

8) Poster presented in ''Dnyanshodh-2024'' organized by CIR, D.Y. Patil Education Society, Kolhapur on 28th February 2024.

Conference/Seminar/Workshop Participation: (04)

1) Attended workshop & hands-on training on XRD organised by SAIF-CFC under STRIDE programme in the Shivaji University, Kolhapur held from 11th to 12th November 2021.

2) Attended workshop on "Good Laboratory Practices"- 6th February 2021, DYP Education society, Kolhapur.

3) Attended an international conference on "Emerging Trends in Material Science" 9th to 10th November 2022, organised by D.P. Bhosale College, Koregaon, Satara.

4) Attended a national conference on "Recent Advances in Fabrication Technology of Nanomaterials- 2022" 20th November 2022, organised by department of physics Balwant college vita and MSBK kanya Mahavidyalaya, Kadegaon, Sangli.

CONTENTS

LIST OF FIGURES

Chapter IV : CdSe and rGO/CdSe thin films by successive ionic layer adsorption and reaction (SILAR) method: synthesis, characterization, and their photoelectrochemical (PEC) performance

LIST OF TABLES AND CHARTS

LIST OF ABBREVIATIONS

- ❖ **2D** - Two-dimensional
- ❖ **AACVD** - Aerosol-assisted chemical vapor deposition
- ❖ **ASTM** - American standard for testing of materials
- ❖ **BET** - Brunauer-Emmett-Teller
- ❖ **BHJ** - Bulk heterojunction
- ❖ **BJH** - Barrett-Joyner-Halenda
- ❖ **CBD** - Chemical bath deposition
- ❖ **C_{dl}** - Double layer capacitance
- ❖ **CE** - Counter electrode
- ❖ **CV** - Cyclic voltammetry
- ❖ **CVD** - Chemical vapour deposition
- ❖ **DDW** - Double distilled water
- ❖ **DSSC** - Dye sensitized solar cell
- ❖ **E** - Energy
- ❖ **E_c** - Conduction band energy
- ❖ **ECSA** - Electrochemical active surface area
- ❖ **ED** - Electrodeposition
- ❖ **EDAX** - Energy-dispersive x-ray spectroscopy
- ❖ **E_f** - Fermi energy level of semiconductor
- ❖ **$E_{f\ redox}$** - Fermi energy level of redox electrolyte
- ❖ **E_g** - Energy band gap
- ❖ **EGS** - Electrochemical gas sensors
- ❖ **EHP** - Electron-hole pair
- ❖ **EIS** - Electrochemical impedance spectroscopy
- ❖ **E_v** - Valence band energy
- ❖ **FE-SEM** - Field emission scanning electron microscopy
- ❖ **FF** - Fill factor
- ❖ **FTO** - Fluorine doped tin oxide
- ❖ **I_{max}** - Maximum current
- ❖ **IR** - Infra-red
- ❖ **I_{sc}** - Short circuit current
- ❖ **IUPAC** - International union of pure and applied chemistry
- ❖ **I-V characteristics** - Current-voltage characteristics

- ❖ **JCPDS** - Joint committee on powder diffraction standards
- ❖ **LASER** - Light amplification by stimulated emission of radiation
- ❖ **LED** - Light emitting diodes
- ❖ **LEL** - Lower explosive level
- ❖ **LSV** - Linear sweep voltammetry
- ❖ **MCs** - Metal chalcogenides
- ❖ **MOSs** - Metal oxides semiconductors
- ❖ **PCE** - Power conversion efficiency
- ❖ **PEC cell** - Photoelectrochemical cell
- ❖ **P_{in}** - Input power
- ❖ **PLD** - Pulsed laser deposition
- ❖ **P_{max}** - Maximum power
- ❖ **ppm** - Parts per million
- ❖ **PSC** - Polymer solar cells
- ❖ **PV cell** - Photovoltaic cell
- ❖ **QDSSC** - Quantum-dot sensitized solar cell
- ❖ **R_{ct}** - Charge transfer resistance
- ❖ **RE** - Reference electrode
- ❖ **RES** - Renewable energy sources
- ❖ **R_s** - Solution resistance
- ❖ **RT** - Room temperature
- ❖ **SCE** - Saturated calomel electrode
- ❖ **SILAR** - Successive ionic layer adsorption and reaction
- ❖ **SS** - Stainless steel
- ❖ **TFSC** - Thin-film solar cells
- ❖ **t_{rec}** - Recovery time
- ❖ **t_{res}** - Response time
- ❖ **UV-Vis** - Ultra violet-visible spectroscopy
- ❖ **V_{max}** - Maximum voltage
- ❖ **V_{oc}** - Open circuit voltage
- ❖ **VOCs** - Volatile organic compounds
- ❖ **W** - Warburg (diffusion) resistance
- ❖ **WE** - Working electrode
- ❖ **XRD** - X-ray diffraction
- ❖ **β** - Symmetry factor

Chapter-I

Introduction and literature survey

CHAPTER- I

Introduction and literature survey

Section A

1.1 General: Introduction

1.1.1 Solar cell

A solar cell or a photovoltaic (PV) cell is one type of semiconductor diode that converts light energy directly into electricity using the photovoltaic effect which was discovered by the French scientist Alexandre-Edmond Becquerel in 1839. The photo conversion efficiency (sunlight to electricity) is an important factor in the development of solar cells. A photovoltaic cell is composed of a semiconducting material that absorbs light and is coupled to an external circuit. When a photon of energy $E = h\nu$ falls on the PV cell (surface of the semiconducting material), it generates electron-hole pairs (EHPs) at the junction. The band gap energy (E_g), carrier concentration mobility of charge carriers, conductivity, and resistivity are all important factors in increasing photoconversion efficiency. When photon energy is greater than the forbidden energy gap electrons can excite from the valence band to the conduction band [1, 2].

An ideal solar cell is formed using two main types of materials, i.e., p-type material (semiconductor with excess positive charges-holes) and n-type material (semiconductor with excess negative charges- electrons) shown in **Fig. 1.1**. When both p and n materials are in contact, holes flow from the p region to n region and electrons from the n region to p region and forms a space charge region called depletion region.
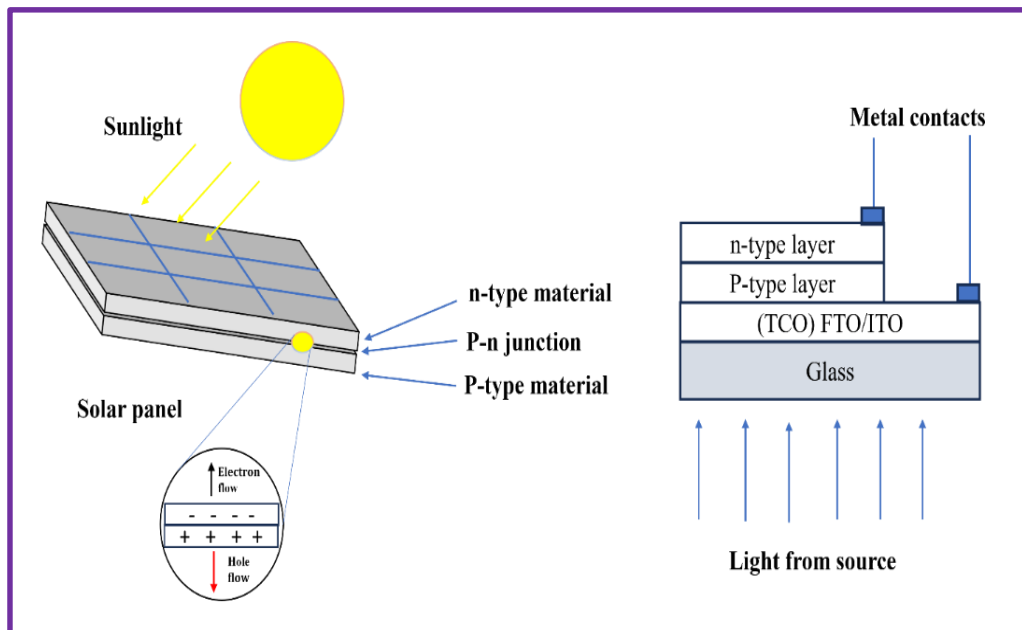
Fig. 1.1 Schematic representation of solar cell [3].

When light of energy $E = hv$, incidence on the surface of a solar cell, electron-hole pairs are generated as a result of light energy absorption from the incident photon. These charge carriers are pushed across the p-n junction by the electric field. If an external load is applied, an electric current and a potential difference between the cell terminals is established [4]. Solar cells are the building blocks of photovoltaic modules; solar cells are photovoltaic regardless of whether the source is natural or artificial light. They are employed as photodetectors, detecting light or other electromagnetic radiation in the visual spectrum, or measuring the intensity of light. Mainly for the operation of PV cells following conditions are required:

1) Most importantly the absorption of the light on the surface of the PV cell.

2) The generation of the electron-hole pairs after light absorption.

3) The separation of charge carriers of opposite types and,

4) The charge flow through the external load.

1.1.2 Types of solar cells

The atoms in silicon are ionized by light of finite wavelengths, and the internal field is created by the splitting of several negative charges (electrons) from positive charges (holes) in the photovoltaic device. The holes are thrown into the positive layer (p-layer) and the electrons are thrown into the negative layer (n-layer). These opposite charges attract each other. The majority of them recombine by traveling through an external circuit outside the material because of the internal potential energy barrier. Since the free electrons must travel through the entire load to recombine with the positive holes, current can be generated from the cells when they are illuminated [5]. The types of solar cells are given in **Chart 1.1**.

1.1.3 Development of solar cell technology
1.1.3.1 The solar cell generations
1) First generation

First generation solar cells that have a typical PV device are silicon-based p-n junctions, which account for more than 86% of the solar cell market and are the primary technology for profitable manufacturing. This cell is typically composed of a crystalline silicon wafer with a band gap of 1.1 eV. It is the most widely used PV technology with module efficiencies of up to 20%, while the best reported laboratory-

scale efficiency is 26.7%. However, the first-generation solar cells have high-cost, i.e., these cells may take years to pay back their purchasing costs.
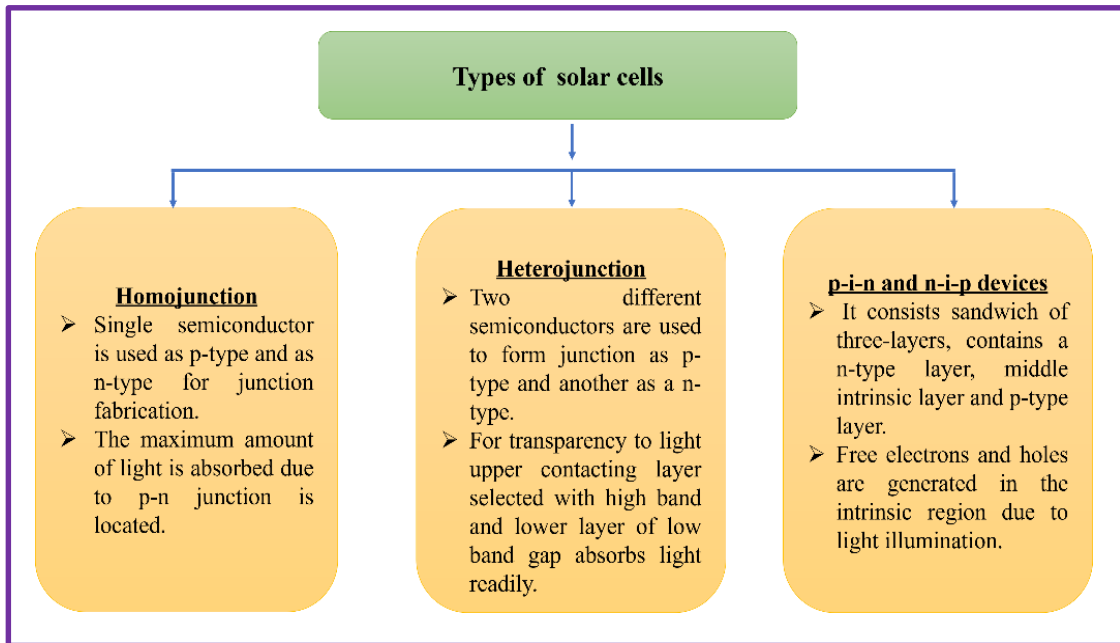
Chart 1.1 Types of solar cells.

Advantages

- ❖ Broad absorption spectrum.
- ❖ High performance.
- ❖ Heightened carrier mobilities.

Disadvantages

- ❖ Require high-cost production machinery.
- ❖ The raising and sawing of ingots is a process that uses a lot of energy.
- ❖ Preferred energy photons at the blue and violet extremities of the spectrum have a large heat capacity.

2) Second generation

Second generation solar cells were introduced to meet energy needs and avoid the high production costs of first generation solar cells. These thin film solar cells (TFSC) require low cost production technology and few materials. These solar cells are most commonly made from amorphous silicon, polycrystalline silicon, CdTe and CIGS. Solar cells made of amorphous silicon degrade when exposed to light, but still have a constant efficiency of 5-10%. The widely used thin film PV technologies include CIGS and CdTe. The efficiency of these solar cells is quite appealing at 23.4% and 21%, respectively.

Advantages

- ❖ Subordinate manufacturing expenditure.
- ❖ Minor charge per watt can be accomplished.
- ❖ Fewer supports are wanted when insertion panels lying on the roof.
- ❖ Allows fitting panels on light and flexible materials.

Disadvantages

- ❖ Amorphous silicon is not stable.
- ❖ Lower solar cells efficiency of thin film is compared with silicon (wafer-based) solar cells.
- ❖ High cost of In and Ga.

3) Third generation

Third generation solar cells are broadly divided into sensitized solar cell, i.e., dye sensitized solar cell (DSSCs), quantum-dot sensitized solar cell (QDSSCs), organic and polymer solar cells (PSCs). The goal of third generation solar cell development is the low-cost of manufacturing with significantly high power conversion efficiency (PCE). The third generation solar cells include multi-junction PV cells, tandem cells and nanostructured cells. The most popular devices used for third generation solar cells are photoelectrochemical (PEC) solar cells, DSSCs-Graetzel cell, QDSSCs, polymer solar cells.

Advantages

- ❖ Low energy and high processing technologies.
- ❖ Polymer cell - low material cost, solution processable, chemically synthesized.
- ❖ Graetzel cell - work even in low light condition.
- ❖ PEC cell - photons produced electron-hole pairs are used to generate electricity directly.
- ❖ DSSC - Potentially rechargeable.

Disadvantages

- ❖ Lower efficiency is evaluated with silicon (wafer-based) solar cells.
- ❖ Polymer cell - efficiency is decreased due to degradation effect, the high band gap.
- ❖ PEC cell - undergoes degradation of the electrodes from the electrolyte.
- ❖ DSSC - liquid electrolyte handling is difficult.

4) Fourth generation

Fourth generation solar cells contain polymer or organic solar cells. They have photo conducting polymers as n and p-type materials in solar cell. This generation solar cells are still in progress, which reporting minor efficiencies. These cells are not steady at higher temperatures due to unstable bonding in the polymers.

Advantages

- ❖ The first cheapest solar cell.
- ❖ Insertion in buildings, cloths and devices is possible.

Disadvantages

- ❖ Generally poor efficiency and less stability.

It is clear from the above information that photovoltaic field is conquered by inorganic semiconductor technologies like silicon or thin film solar cells. Solid wafers of around hundred micrometers thickness are used by conventional crystalline silicon cells **[6, 7]**.

1.1.4 Inorganic solar cells

Inorganic solar cells are made up of p-n junction of silicon and other inorganic semiconductors with a large surface area. Solid state p-n junction of two direct band gap/energy gap (E_g) semiconductors are used to fabricate inorganic solar cells. When light ($E > E_g$) is incident at this p-n junction, electron-hole pairs (EHP) are generated, which separated by the internal electric field and increases the photocurrent. This type of photovoltaic cell is the market leader in the manufacturing of commercial solar cells, accounting for more than 86% of the solar cell market. These cells typically have excellent efficiency, but the higher production cost is a main drawback.

1.1.5 Organic solar cells

These cells are frequently referred to as polymer solar cells or bulk heterojunction (BHJ) solar cells. These gadgets are solid state. They employ photoconducting organic polymer junctions to generate energy. The physical characteristics of these organic materials such as their solubility, charge transport, conduction and valance band energies, band gap, and morphology may be changed chemically. Some acceptor and donor polymers applied for organic solar cells are given below,

Acceptors: C60 (PCBM), 30-phenyl-30H-cyclopropa (1, 9) (5, 6) fullerene-C60-Ih-30-butanoic acid methyl ester; C70 (PCBM), 30-phenyl-30Hcyclopropa (8, 25) (5, 6) fullerene -C70-D5h (6)-30-butanoic acid methyl ester. Donors: MDMO - PPV, poly [2-methoxy-5-(30, 70-dimethyloctyloxy) p-phenylenevinylene]; Metal Pthalocyanines (CuPC, ZnPC, NiPC, etc.), P3HT, poly (3-hexylthiophene) **[8, 9]**.

1.2 Photoelectrochemical (PEC) solar cells

1.2.1 Introduction

Solid-state semiconductor solar cells are utilized to transform solar energy into electrical energy. These solar cells are fabricated employing high-tech processes based on p-n junctions made up of completely crystalline materials that are costly and rarely available. Because of this, solar cells are still costly, which prevents them from being wide use in the near future. The PEC solar cell offers a technically strong and financially viable alternative idea to the currently available p-n junction PV devices. In the past decades, significant progress has been made in the investigation of reliable solid-liquid junction PV solar cells for the PEC system. Because PEC solar cells don't employ a typical p-n junction to segregate photo-generated charge carriers, they vary significantly from inorganic and organic semiconductor devices. PEC cells and DSSC are a couple of modern gadgets. In the PEC cell, a solution i.e., electrolyte is introduced between two semiconductors (metal and an organic single semiconductor) to avoid physical contact. The PEC solar cell is consisting of a redox couple in the electrolyte, which can be solid or liquid. The PEC cell offers a superior electrical contact for solar energy significance, which is formed as soon as the semiconductor electrode is submerged in the electrolyte, and this is one of its advantages. Another benefit is that the barrier height is modified to the appropriate level by selecting the correct redox couple in the electrolyte and managing the fermi level in the electrolyte. In an electrochemical cell, an oxidation-reduction process between one or more electrolytes in the solution transfers electrical charges between two electrodes **[9]**.

The PEC solar cell design is significantly more cost effective than the classic solid-state cells. The PEC process is also advantageous in this regard because one of its versions, photoelectrolysis, allows direct translation of light energy into chemical energy of the PEC reaction products, and solves the storage problem along with suitable energy conversion. The initial benefit of the PEC cell is, it responds more

slowly than Schottky barrier solar cells in the vicinity of material grain boundaries **[10]**.

1.2.2 Structure of PEC solar cell

A PEC cell is made up of a semiconductor photoelectrode, a counter electrode, and an electrolyte as shown in **Fig. 1.2**.

1.2.2.1 Requirements of PEC solar cell (PEC cell)

1) Semiconductor photoelectrode

The nature of the semiconductor electrode surface in PEC solar cell plays a vital role in the conversion efficiency of impinging radiant energy into electrical energy. The semiconductor photoelectrode is a heart of the PEC cell. The PEC performance can be endorsed due to the chemical treatments and etching procedures which diminish the amount of recombination reactions on the surface of semiconductor electrodes. To use the semiconductor photoelectrode in the PEC cell, the following conditions are required:

1. Thickness of semiconductor material must be sufficient to absorb an entire incident beam.

2. It must be long-lasting and stable in the dark as well as under illumination.

3. It should be with high optical absorption coefficient.

4. For maximal solar spectrum absorption, the band gap (E_g) of photoelectrode materials should be a certain value.
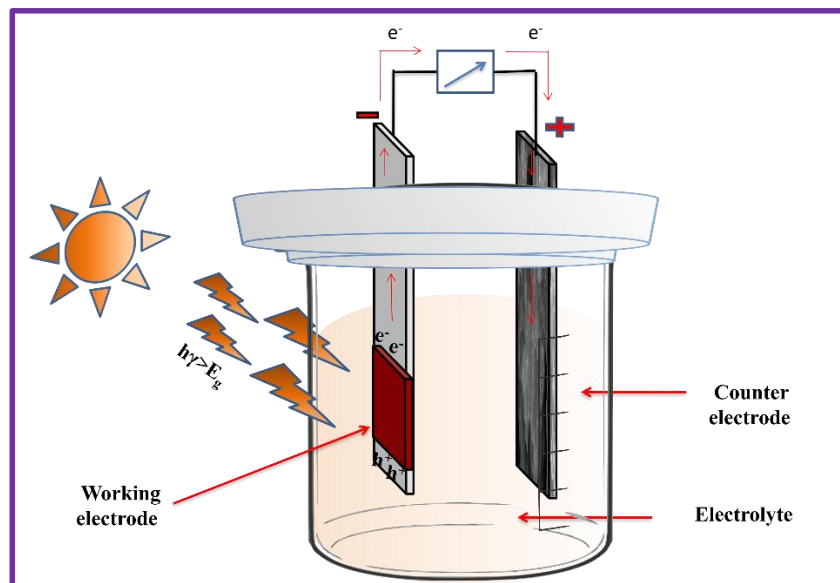
Fig. 1.2 Schematic of the PEC cell.

5. The values of shunt resistance R_{sh} should be large enough ($R_{sh} = \infty$) while series resistance R_S should as small ($R_S = 0$).

6. Minority charge carriers diffusion lengths must be as long as possible.

2) Counter electrode (CE)

The counter electrode (CE) is another main part of the PEC cell which is required to persuade regenerative procedure. The species present in the electrolyte are oxidized by the CE providing a refusal of net chemical change during the composition of the electrolyte. To obtain superior performance in PEC cells, the following conditions are necessities for the CE,

1.CE must be chemically inert i.e. it should not react with electrolyte.

2. To avoid concentration divergence, the electrode area should be large.

3. It has to subsist electronically active, i.e., the charge transfer among the redox species and CE within an electrolyte must be quick.

4. After immersing a counter electrode in the electrolyte, the half-cell potential of the semiconductor electrode must be comparable to that of an electrode.

5. Generally, graphite and platinum are employed as counter electrodes.

6. For the reduction process, the counter electrode must have a low potential.

3) Electrolyte

The other important component of the PEC cell is an electrolyte made up of both reduced and oxidized species. These species are ionic, which aids in the transfer of photoinduced holes from the photoelectrode to the counter electrode. The energy level in the electrolyte is related to the idea of energy levels in solids and E_f - redox corresponds to the fermi energy of a semiconductor electrode.

The prior unique redox potential ($E_{f\ redox}$) of an electrolyte solution and the fermi level (E_f) of the semiconductor equilibrate, when the semiconductor electrode comes into contact with the redox electrolyte and is connected to the exterior of the semiconductor. The fermi levels of an electrolyte and semiconductor are adjusted to each other. This creates a barrier height that is determined by the solution species and exacting semiconductors.

It is recognized that aqueous electrolytes are the basis of surface variation and contain the utilization of various semiconductors. Here are certain requirements for electrolyte characteristics during the development of PEC cells.

1. The electrolyte should have the lowest optical absorption.

2. The oxidation-reduction processes must take place at precise semiconductor band edges.

3. The electrolyte should not be corrosive to the electrodes.

4. Charge transfer rates of reduced and oxidized species by the counter electrode and semiconductor sides must be high or efficient.

5. The sustaining electrolyte and oxidized-reduced species concentrations should be sufficient to generate the required current densities inside the solvent.

6. Price, reactivity, and toxicity should be as low as possible.

After dipping both the semiconductor electrodes into the electrolyte, band bending in the semiconductor photoelectrode takes place (**Fig 1.3 a)** n-type semiconductor, and **b)** p-type semiconductor). The electrons shifting from or towards the electrolyte appear only in the energy region of the conduction band, though the holes shifting appear in the valance band region. This transfer process can take place between two states having equal energy or between the one unoccupied and other filled state.

After illumination at the interface of semiconductor photoelectrode-electrolyte, the EHPs are generated in the depletion region and divided in a separated manner via an electric field close to at the interface. The incident photon energy ought to be better than the band gap energy of semiconductor material. If n-type semiconductor photoelectrode is illumined and positive potential is applied to it, the formation of EHPs in the depletion region and the divided electrons increase near the top of the conduction band and holes within the valence band. As a result of this process a counter field is stimulated under open circuit conditions.
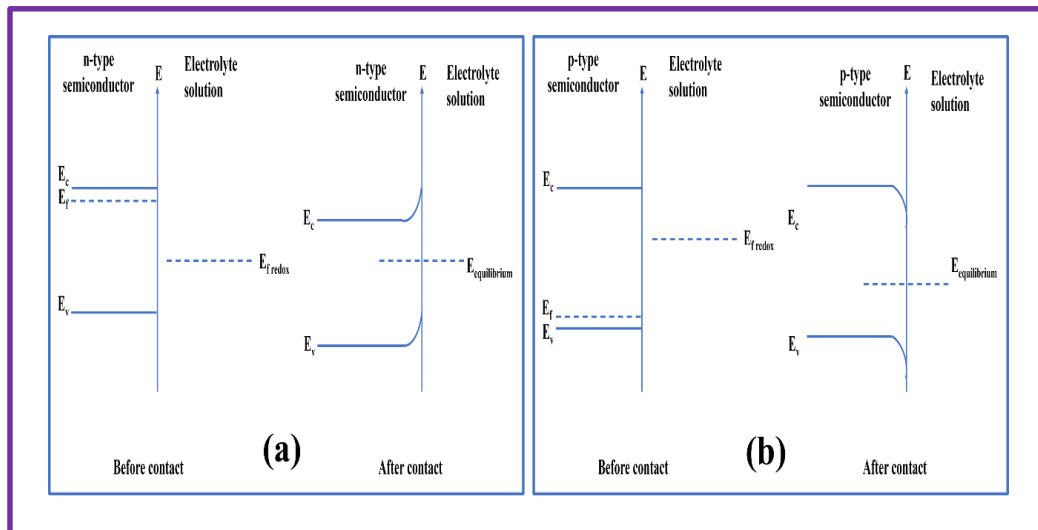
Fig. 1.3 Band bending observed in a) n-type semiconductor, and b) p-type semiconductor (Here, E_v = Valence band energy, E_c = Conduction band energy, E_f = Fermi energy level of semiconductor, $E_{f\ redox}$ = Fermi energy level of redox electrolyte).

Quite the opposite, if counter electrode exists within the equivalent electrolyte, the photo voltage operates like a driving force for the electrons to travel beneath the short-circuit state from semiconductor electrode toward counter electrode in conjunction with the constructive cell is created and is revealed in **Fig. 1.4**.

The majority charge carriers, i.e., electrons are stimulated to the conduction band which drift near the interior region, whereas minority carriers i.e., holes, move towards the semiconductor surface. In electrolyte solution, encounter of reduced species from redox couple is happening on semiconductor surface. At first, the element is oxidized due to holes which transported towards the counter electrode and hence again reduced. This reduction is coerced through the peripheral connection from the semiconductor **[9, 11].**
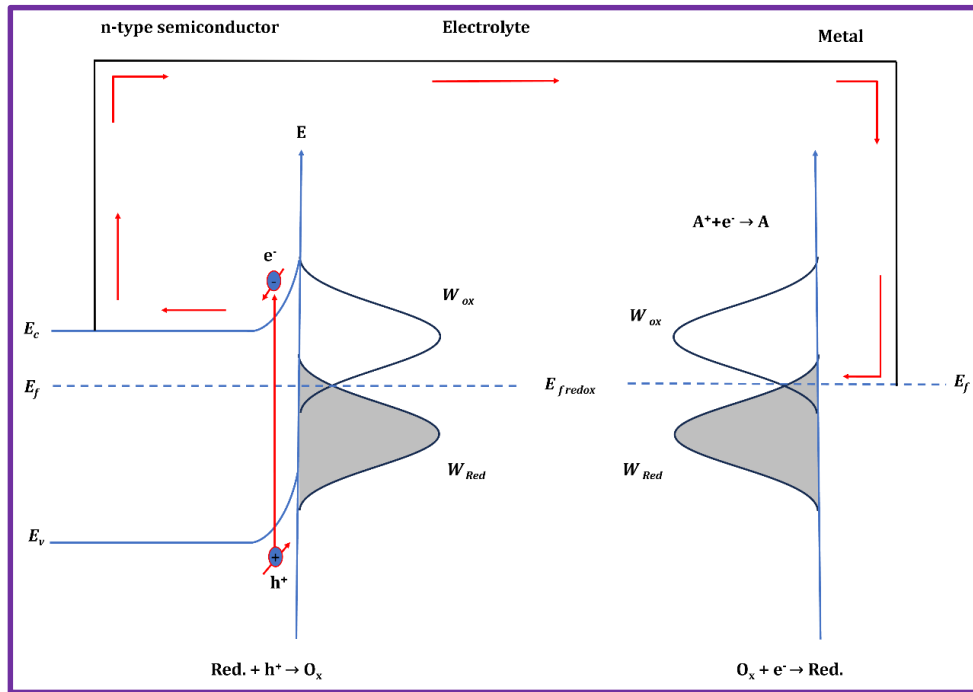
Fig. 1.4 Current flow and energy level diagram for n- type semiconductor PEC cell.

1.2.3 Characteristics of PEC solar cells

The current-voltage (I-V) characteristics of a PEC solar cell depicted in **Fig. 1.5**. For PEC cell junction symmetry factor (β) is an important, described in the Shockley diode equation. The 'β' is beneficial to study PEC cells, primarily in situations where the solid-liquid interface is where charge carriers' electrons and holes produced by light absorption in the semiconductor electrode are gathered. In PEC cell research, symmetry factor values are usually determined by computer simulations and experimental measurements. The below equations are commonly

used Butler-Volmer equations for I-V characteristics for electrochemical cells or electrode kinetics.

For solid liquid junction PEC cell **[12, 13]**,

$$I = I_0(e^{\frac{qV}{RT}}) \quad \text{(For small departure from equilibrium)} \tag{1.1}$$

$$I = I_0(e^{\frac{(1-\beta)qV}{RT}}) \text{ (For large departure from equilibrium)} \tag{1.2}$$

Here,

I = The net current flowing through junction

I_0 = Dark saturation current

V = Applied voltage across the terminals of junction

q = Absolute value of electron charge

β = Symmetry factor

R = Ideal gas constant

T = Absolute temperature

By simplifying equation (1.2) for 1-β, we got,

$$1 - \beta = (\log\frac{I}{I_0})RT/qV \tag{1.3}$$

But, $\dfrac{\log(\frac{I}{I_0})}{V}$ = Slope of the I-V curve (linear part)

$$\text{Therefore, } 1 - \beta = \frac{RT}{q} \times slope \tag{1.4}$$

$$\beta = 1 - (x), \text{ here } (x = \frac{RT}{q} \times slope) \tag{1.5}$$

Also, by using the equation of the Tafel slope **[14]**.

$$b = \frac{2.303\ RT}{\beta F} \tag{1.6}$$

$$\beta = \frac{2.303\ RT}{bF} \tag{1.7}$$

Here,

b = Tafel slope

R = Ideal gas constant

T = Absolute temperature

β = Symmetry factor

F = Faradaic constant

The 'β' have following physical significances:

1) Recombination processes: The 'β' states the relation of charge carrier recombination at the semiconductor-electrolyte interface against bulk recombination within the semiconductor material. Recombination at the interface predominates over bulk recombination when the symmetry factor is larger, which is usually preferred for effective charge transfer and collection.
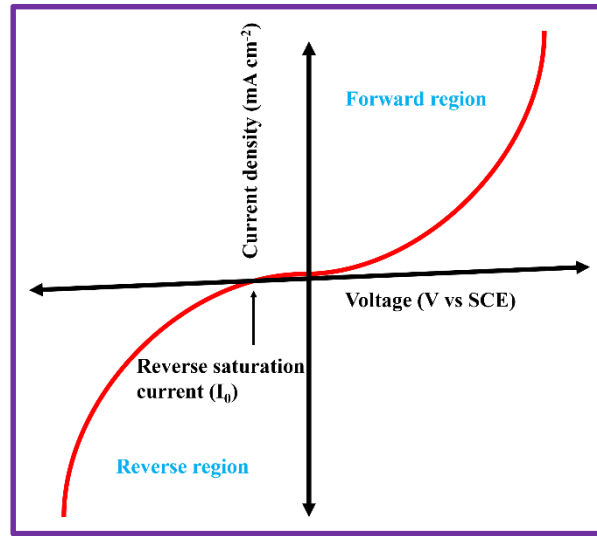
Fig. 1.5 I-V characteristics of PEC cell.

2) PEC cell performance optimization: 'β' helps to researchers to optimize PEC cell designs and operating settings to reduce recombination losses by balancing interface and bulk recombination processes. Approaches like changing interface between semiconductor-electrolyte, semiconductor properties, or optimizing composition of electrolytes are used.

3) Quality of interface: The 'β' can also reveal information about the semiconductor-electrolyte interface quality. When it close to 1 means better interface quality, which leads efficient transportation of charge carriers at the interface with lower recombination.

4) Comparison of cells: Comparing the 'β' of different PEC cell configurations, helps to decide proper materials and cell design ideas for future progress.

The 'β' value in PEC cells affects due to used materials, operating conditions and interface quality. In general, higher 'β' (close to 1) specifies lower recombination, while lower values close to 0 shows higher recombination losses. However, depending on the particular system being studied and the techniques employed to calculate the symmetry factor, the precise range may vary **[15, 16]**.

The effective conversion of the light energy by PEC cell is a most important factor. The parameters which are responsible for an efficiency (η) of solar cell are the maximum current (I_{max}), maximum voltage (V_{max}), maximum power (P_{max}), short circuit current (I_{sc}), open circuit voltage (V_{oc}), and the fill factor (*FF*).

The current-voltage (I-V) characteristic graph of a typical solar cell is illustrated in **Fig. 1.6**. The liberation of constant current during illumination is the main function of a photovoltaic cell. This process occurs at any illumination level, even as the photovoltage is basically determined by its resistance.

1) Maximum power point of solar cell (P_{max})

The maximum power is the product of the maximum cell current and voltage, wherever the output power of the cell is maximized. This point is positioned at the knee of the curve.

One solar cell can deliver the highest electrical power at its standard test condition. The maximum power (P_{max}) will obtain at bend position of the characteristic curvature of I-V curve. It is exposed within the I-V characteristics of solar cell through $P_{max.}$ In other words, the point at which the cell produces maximum electrical power and this is revealed at the crest right area of the green rectangle. This is the maximum power point (P_{max}).

a) Current at maximum power point (I_m)

It is the current at which maximum power takes place. This current at maximum power point is an exposed inside the I-V characteristics of solar cell by I_{max} or I_m.

b) Voltage at maximum power point (V_m)

It is the voltage at which maximum power takes place. The voltage at maximum power point is an exposed inside the I-V characteristics of solar cell by V_{max} or V_m.

2) Short circuit current (I_{sc})

A solar cell can produce the maximum current under illumination without damage its own restriction. It is measured by short-circuiting the cell terminals, i.e., when there is no applied potential that produces maximal output (V = 0). Hence it is estimated as Y-intercept of the I-V curve. The rate of generation of charge carriers into a solar cell besides depends upon the angle at which the light falls on the cell and

intensity of light. As the production of current also depends upon the illuminated surface area of the cell, it is superior to convey the maximum current density as an alternative maximum current. The I_{sc} depends on a number of aspects for example, optical properties of material (absorption, reflection and transmittance), spectrum of incident light, intensity of incident light and collection probabilities (area of the solar cell, the surface covering and the lifetime of minority charge carriers). For maximum I_{sc} density, it is implicit that there is a recombination deficiency within the material.
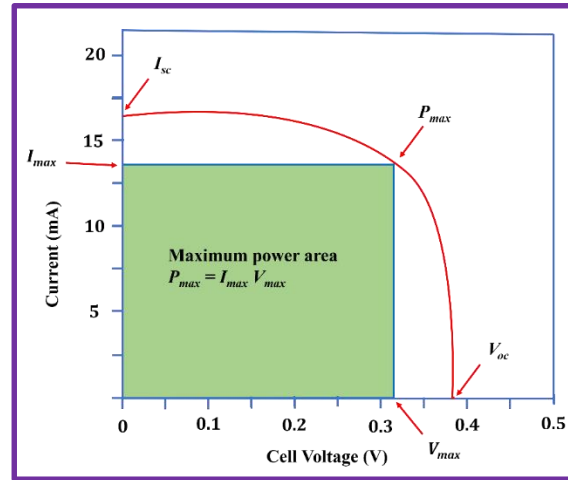
Fig. 1.6 The power output characteristic graph of a forward biased typical solar cell [9].

3) Open circuit voltage (V_{OC})

An open circuit voltage (V_{OC}) is estimated by measuring of voltage between the terminals of the cell while no load is connected to the cell. The potential difference illustrates a maximum value, when no external load is applied there, that correspondent to the V_{OC}. Hence, it is estimated by X-intercept of the I-V curve. The V_{OC} keep up a correspondence to the quantity of forward bias lying on the solar cell because of the bias of the solar cell junction through the light generated current. It is resolute through the dissimilarity within the work function of counter electrode and working electrode. This voltage relies upon the manufacturing techniques and temperature except the intensity of light and an area of bare surface. The measurement of V_{OC} is the total amount of recombination within the cell device. The V_{OC} can also be determined from the carrier concentration.

4) Fill factor of solar cell (*FF*)

The fill factor is nothing but the correlation between the maximum power (I_m V_m) to the array can really give an under normal working condition and the product of the open circuit voltage and the short-circuit current (V_{oc} I_{sc}). It is more commonly

identified by its abbreviation *FF*, is a parameter which, in conjunction with V_{OC} and I_{sc}, concludes the maximum power from a solar cell. This fill factor value provides an idea of the value of the array and the nearer the FF is to 1 (unity), the array can provide an additional power. The *FF* given by the following equation,

$$FF = \frac{I_m V_m}{I_{sc} V_{oc}} \qquad (1.8)$$

5) Efficiency (η) of solar cell

Efficiency is the universally employed parameter to evaluate the performance of one solar cell to another. An efficiency of solar cell is termed as the ratio of maximum electrical power output to the emission power input in the direction of the cell and it is presented in percentage (%). In accumulation to reflecting the performance of the solar cell itself, the efficiency of cell depends upon the intensity and spectrum of the incident sunlight and the heat of the solar cell. As a result, circumstances under which the efficiency is calculated have to be warily controlled sequences to evaluate the performance of a single device to another. The efficiency of the solar cell can be calculated by the following equation,

$$\eta \% = \frac{I_{sc} V_{oc} FF}{P_{in}} \times 100 \qquad (1.9)$$

Here, I_m = Maximum current, V_m = Maximum Voltage, I_{sc} = Short circuit current, V_{oc} = Open circuit voltage, P_{in} = Input power **[17, 18]**.

1.3 Sensor

1.3.1 Introduction

A sensor is a device that converts physical, chemical, or biological signals into electrical signals suitable for use in electronic circuits. The term "sensor" originates from the word "sense," reflecting its role in mimicking the functions of the human senses. The word "transducer" also has a similar meaning to that of "sensor." Transducer and sensor are sometimes interchangeable terms. The sensor is capable of detecting an input signal and converting it into the appropriate output signal. Sensors have a wide range of applications in industrial and domestic applications. Along that the sensors comprises huge use in the biomedical, photovoltaic, transport, and telecommunication fields **[19]**.

1.3.2 Classification of sensors

The purpose of usage, conversion principle, manufacturing technique, modes of application, output signal, and other factors are all taken into consideration while

classifying sensors. Sensors are categorized into two groups based on their principle of operation indicated in **chart 1.2**.

1) Physical sensors

Sensors that collect data on the physical features of system are known as physical sensors. They work by utilizing physical phenomena including photoelectric, piezoelectric, magnetostriction, ionization, thermoelectric, magnetoelectric, etc.

2) Chemical sensors

A chemical sensor is a device that changes chemical information into a useful signal, which can show the concentration of a specific part of a sample or give a complete analysis of the sample's composition. In these sensors, the chemical interaction between the analyte and the sensor surface may be the source of analyte (chemical) information. Gas, humidity, ionic, and biochemical sensors are examples of chemical sensors.

Detecting gasses like poisonous and igneous gases is major concern in household and industries parts. This chapter focuses on the development of effective gas sensors **[20, 21]**.
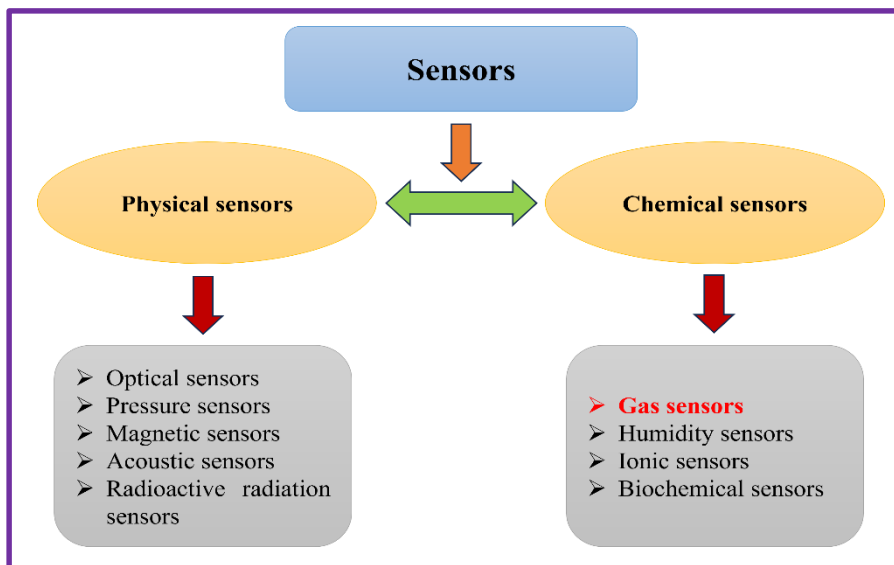
Chart 1.2 Sensor classification.

1.3.3 Gas sensor

1.3.3.1 Introduction

Due to revolutionary industrial and technical advancements, human living standards have drastically improved in the last several decades. Recent technological advancements have increased air pollution, posing risks to the environment and public health. For the protection of the environment and living organisms, it is crucial to

identify such harmful, dangerous, and flammable gases. Monitoring air quality is a crucial component of the ongoing study. Although the human olfactory system is a great tool for identifying and detecting numerous odors, but the majority of dangerous gases and vapors can only be recognized at extremely high concentrations or not at all.

Concerning atmospheric oxygen is the first category. For breathable atmosphere maintaining oxygen concentrations of roughly 20 % is necessary. Monitoring oxygen concentrations between 0 to 5 percent is necessary to regulate combustion processes (such as those in boilers and internal combustion engines). Toxic gases in the atmosphere, such as CO, H_2S, Cl_2, NO_2, etc., fall under the second group. To detect poisonous gas below the dangerous limit concentrations, which can range from 1 part per million (ppm) to several hundred ppm, the sensor used for this purpose must be able to detect such concentrations. Ignitable gases, such as C_2H_2, C_2H_4, C_3H_6, C_3H_8, LPG, etc., fall under the third category of gas monitoring. In this respect, concentrations of explosive (flammable) gases below the lower explosive level (LEL), which for the majority of gases is up to a few percent, must be monitored in order to safeguard against the unintentional occurrence of fire or explosion. In essence, a sensor needs to detect gases at low concentrations (in ppm) for monitoring harmful and flammable gases. **[20, 22-28]**.

Gas sensors are fabricated utilizing a variety of materials, technologies, and phenomena due to the rising need of them for environmental monitoring. Sensor technology has made enormous strides, and many more are on the horizon. For process control, environmental monitoring, and industrial health and safety, gas detection equipment is becoming more necessary. Consequently, significant research is being conducted in the area of gas sensors to enhance the performance of traditional devices using nanoengineering techniques.

1.3.3.2 Historical background of the gas sensor

After the discovery of the dangerous effects of hazardous gases on human health, work was done on techniques to detect gas leakages. Before the development of modern electronic sensors, early detection techniques relied on less accurate detectors. In the 19th and early 20th centuries, miners used canaries as an early warning system against life threatening gases such as CO_2, CO, and CH_4. The canary, which normally chirps, will stop chirping and eventually die if not freed from the fumes, which is a warning signal for workers to leave the mine.

Sir Humphry Davy invented the Davy lamp in 1815 to identify the presence of methane (firedamp) in underground coal mines. It was the first gas detector used in the industrial era. The oil flame in the flame safety lamp was raised to a predetermined height in the open air. With these lights, the flame was confined inside a glass sleeve with a mesh flame arrestor to avoid ignition. The presence of methane (higher) or the absence of oxygen (lower) affected the flame's height. Flame safety lamps are still in use today in several areas of the world.

The metal oxide (MO$_S$) sensors, fabricated in 1962 by Taguchi and Seiyama, enabled the detection of a variety of gases at a significantly lower cost. With the development of electrochemical sensors in around 1969, gas sensing was improved to a greater level. Various types of gas sensors, including single gas sensors and multi-gas sensor arrays, are currently in use at different locations. Advanced real-time gas sensing technologies include MOS, catalytic, electrochemical, and infrared (IR) sensors, which can function individually or together to detect a range of gases. A sensor array typically consists of a large number of gas sensors **[29]**. Because a single sensor cannot detect multiple substances in a complex environment, a sensor array is required. To establish sensors array, the same type of sensor or a number of sensors can be utilized concurrently. This array represents a substantial development in the measurement of the concentration of various gases and can be compared to an electronic nose.

Metal oxide semiconductors (MOSs) like SnO_2 , WO_3 , Fe_2O_3 , NiO, CuO, and ZnO are commonly used due to their redox properties, cost-effectiveness, and natural oxygen vacancies. However, they face challenges like instability, low sensor specificity, and high operating temperatures **[28, 30]**. In contrast, metal chalcogenides (MCs), with lower bandgap energies, better surface-to-volume ratios, and adsorption sites, show strong potential for sensor applications. MCs can address issues like signal drift and oxygen vacancy diffusion seen in MOSs. While MC-based gas sensing research is limited, materials like MoS_2 , WS_2 , SnS_2 , and PbS_2 are already in use. Cadmium chalcogenides (CdX, X = S, Se) offer stability, good electro-optical properties, and easy fabrication, warranting further exploration in sensor development.

1.3.3.3 Types of gas sensor

Chemical gas sensors divided into,

1) Solid electrolyte sensors

2) Catalytic combustion sensors

3) Semiconducting oxide sensors.

1) Solid electrolyte sensor

Electrochemical gas sensors (EGS), which can use redox processes to transmit information about the different gases and their concentrations, are the main type of solid electrolyte gas sensors.

These sensors function based on the principle that the ionic conductivity of solid electrolyte materials varies in the presence of gas molecules. The output from these sensors is an electrical signal that gives information about the chemical substances (gases). Solid electrolyte gas sensors typically operate in one of two modes: potentiometric or aerometric. They can be categorized as potentiometric, aerometric, combination (aerometric-potentiometric), and impedance-based gas sensors. Only low (ppm) gas concentrations can be detected by these sensors, but sensors have a short life (two year).

2) Catalytic combustion sensor

Catalytic microcalorimeters are catalytically active solid-state sensors. This type of sensor consists of an inert compensator element and a detector made of catalytic material (a thin coil of platinum wire) that responds to combustible gases. When a combustible gas burns on the detector, its temperature increases. As a result of this change occur in resistance in the output signal of the detector and sensor signal is generated. It mainly detects highly explosive hydrocarbon mixtures like LPG and methane, as well as other flammable gases such as propane, hazardous gases like CO, and monitors air quality for volatile organic compounds (VOCs). These sensors have some drawbacks, including restricted range, oxygen need, detector sensitivity decrease, and calibration requirements.

3) Semiconductor gas sensor

This category of solid-state gas sensors is now the fastest expanding type of gas sensors. Metal oxides are the most widely utilized materials in these sensor applications. The sensing element is made of a semiconducting material with a high surface area, usually applied to a ceramic base. While in use, the sensor is maintained on a heated platform, with electrical connections made at either end. The sensing mechanism relies on the variation in electrical conductivity, which results from changes in charge carrier concentration. This change occurs due to a temperature-dependent redox reaction between the target gas and oxygen species that are adsorbed on the surface of the semiconductor or the sensor itself. As a result, the effectiveness

of semiconductor gas sensors is affected by various factors, including operating temperature, catalytic surface properties, surface area, electrical properties of the sensor element, and its microstructure **[27]**.

1.3.3.4 Heterojunction gas sensor

It is a gas sensor which uses heterojunction structure for detection and measurement of specific gases. **Fig. 1.7** depicts schematic of heterojunction gas sensor.

It made up from different metal chalcogenide materials in contact to form a heterojunction. Sensing action occurs at heterojunction part. The sensitivity and selectivity of the heterojunction depends on selection of materials and junction formation.

Sensing mechanism consists of the following steps:

1) **Gas adsorption**

Gas molecules adsorb on the metal chalcogenide surface of the sensor when it is exposed to the target gas, reaching the heterojunction. The heterojunction sensor's electrical characteristics may alter primarily as a result of this adsorption process.
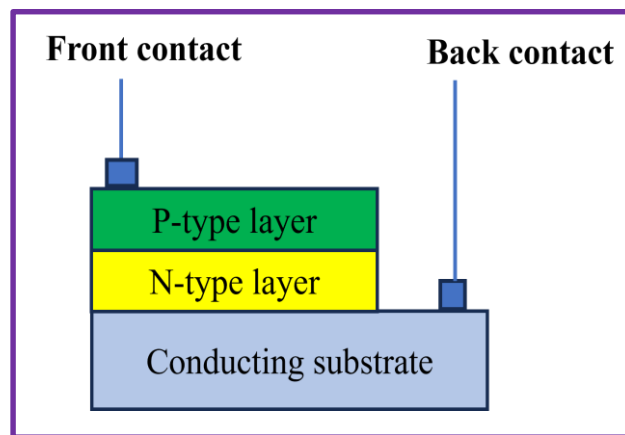
Fig. 1.7 Schematic of heterojunction gas sensor.

2) **Change in electrical conductivity**

The metal chalcogenides heterojunction's electrical conductivity may alter as a result of gas molecules reaches to the sensor heterojunction. The key to the sensing mechanism is this change in conductivity.

3) **Charge transfer and band bending**

The interaction between the gas molecules and the heterojunction can induce band bending, which can alter the electronic structure and conductivity, and gas

adsorption can lead to charge transfer between the gas molecules and the metal chalcogenide surface, which can alter the carrier concentration.

4) Sensing and signal output

The presence and concentration of the target gas are determined by measuring the change in electrical resistance of the metal chalcogenide heterojunction. An electrical signal that can be displayed or processed further is frequently created from the resistance change.

The sensor design, metal chalcogenide selection, and heterojunction combination are all designed to provide excellent sensitivity to low concentrations and selectivity for particular gases. These are useful due to tunable electronic properties and sensitivity for different gases. The interactions occur between heterojunction and target gases regulate the sensor performance. Researchers are continuing works on to discover and develop advanced materials for better efficiency and selectivity.

1.3.3.5 Gas sensor parameters

The **Fig. 1.8** depicts the block diagram of gas sensing assembly with parameter curve.

1) **Response and recovery time**

Response time (t_{res}): It is the time required for a signal to rise by 90% from its initial value to its maximum or saturated value. In applications requiring real-time monitoring, a shorter response time is desirable for timely detection of gas.

Recovery time (t_{rec}): It is the time required for the sensing element to return 90% of its initial value or beginning value after achieving its maximum or saturation value. A fast recovery time is important for continuous monitoring, allowing the sensor to quickly reset for the next measurement cycle

2) **Sensitivity (S)**

The sensitivity of a heterojunction gas sensor is defined as the extent to which a specific gas affects the sensor's resistance. Generally, it determined by the ratio of the junction current (I_a) in the air to the junction current (I_g) in presence of gas for a particular concentration of a gas. A sensor would have "high response or sensitivity" if exposure of low concentration of gas resulted in large change in electrical properties of the sensor device. For p-n junction heterojunction sensor, the electrical

properties changes (increase or decreases), so by measuring current change the gas response (S) is calculated using the formula,

$$S(\%) = \frac{I_a - I_g}{I_a} \times 100 \qquad (1.10)$$

High selectivity is crucial in applications where multiple gases may be present, and the sensor needs to reliably distinguish the target gas from interference.

3) Long term stability

Stable sensors ensure reliable and long-term operation, making them suitable for applications where consistent performance is critical. These parameters collectively contribute to the overall effectiveness of a gas sensor.
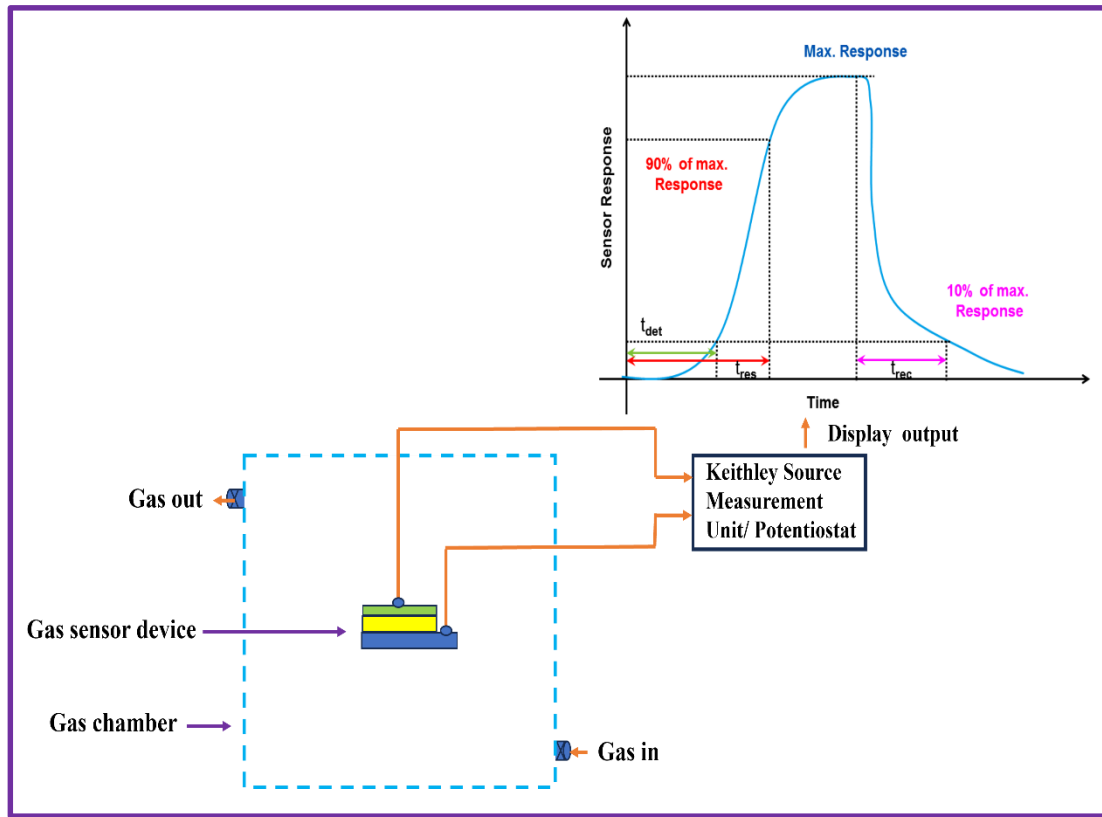
Fig. 1.8 Block diagram of gas sensing assembly with parameter curve.

The ideal sensor should exhibit high selectivity for the target gas, high sensitivity to low concentrations, rapid response and recovery times, and long-term stability. Achieving a balance among these parameters often involves careful material selection, sensor design optimization, and sometimes the incorporation of specific coatings or additional technologies to enhance performance. Researchers and engineers continually work on improving the parameters through advancements in sensor materials, design strategies, and signal processing techniques to meet the

diverse needs of various gas sensing applications, such as environmental monitoring, industrial safety, and medical diagnostics.

<div align="center">

Section: B

</div>
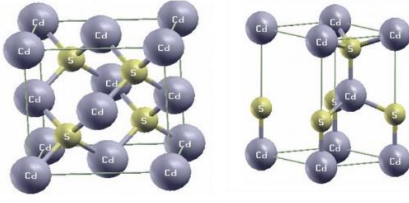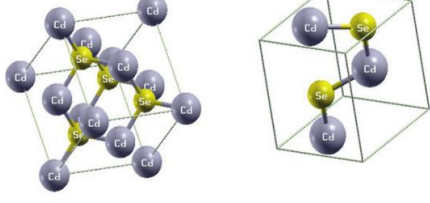
1.4 A review of literature of cadmium chalcogenides and their composites for PEC and gas sensor applications

1.4.1 Introduction

Transition metal sulfides and selenides have garnered significant interest due to their remarkable physical and electrical properties, making them highly suitable for use in electronic, optical, and optoelectronic devices. There has been much interest recently in the application of cadmium chalcogenide (CdX, where X = S, Se) electrodes to the construction of photoelectrochemical (PEC) cells for the conversion of solar energy into electrical energy. These materials have low band gap energies (1.4 - 2.4 eV) and reasonable overlap with the solar spectrum at the earth's surface. Also, for gas sensing application electrical, chemical and physical properties that are often highly sensitive to changes in their chemical environment. Some physical and chemical properties of cadmium chalcogenides shown in **Table 1.1**. The cadmium chalcogenide thin films were synthesized using different methods such as CBD, spin coating, solvothermal, hydrothermal, SILAR, electrodeposition, reflux condensation, precipitation, aerosol-assisted chemical vapor deposition (AACVD), one-step bacterial assisted, sputtering, spray pyrolysis, pulsed laser deposition, etc. **[31-46]** for various applications like photodetector, sensor device, light emitting diode, solar cell, optoelectronic devices applications **[47-53]**.

Table 1.1 Physical and chemical properties of cadmium chalcogenides [54, 55].

Parameter	Cadmium sulfide	Cadmium selenide
Chemical formula	CdS	CdSe
Molar mass	144.47 gmol^{-1}	191.385 gmol^{-1}
Appearance	Yellow-orange to brown solid	Black, translucent, adamantine crystals
Density	4.83 gcm^{-3}	5.81 gcm^{-3}
Melting point	1750 °C	1240 °C

Band gap	2.42 eV	1.74 eV
Crystal structure	Cubic structure Wurtzite structure	Cubic structure Wurtzite structure

Cadmium chalcogenides and its composite materials with their synthesis protocol and corresponding photoelectrochemical and gas sensing performance is summarized in **Table 1.2** and **Table 1.3**, respectively.

1.4.2 Literature survey of cadmium chalcogenides and their composites for PEC application

Swamy et al. **[56]** deposited the hexagonal cadmium sulfide (CdS) thin films by chemical bath deposition method on fluorine doped tin oxide (FTO) substrate. The deposited film was hydrophilic in nature with band gap of 2.32 eV. The two electrode PEC cell [CdS/1 M Polysulfide/Graphite] showed a fill factor (*FF*) and efficiency (*η*) of 0.35 and 0.067 %, respectively, which was attributed to the interconnected atomic flakes carrying the photogenerated charge carriers due to the low mutual contact. Rahane et al. **[57]** spin coated the CdS nanocrystals on a FTO substrate for different cycle numbers and investigated the effect of coating thickness on the photocurrent of the PEC cell. As the film thickness increased, the photocurrent also increased. For [CdS/0.5 M Na_2SO_4/Platinum(Pt)/SCE] cell highest observed value of the photocurrent was 0.021 mA cm^{-2}. Kumarage et al. **[58]** deposited CdS thin films on FTO substrate for various bath temperatures by CBD method (40 – 80 °C). The optoelectronic properties of CdS thin films were effectively altered by varying the deposition bath temperature which shows in tunable in flat band potential (electron affinity), energy band gap (*Eg*), open circuit voltage (*Voc*) and short circuit current (*I_sc*) values. The PEC cell [CdS/0.1 M $Na_2S_2O_3$/Platinum/(Ag/AgCl)] showed higher *Voc* (398 mV) and *I_sc* (0.019 mA cm^{-2}). Shinde et al. **[59]** electrodeposited the CdS thin films on FTO and stainless steel (SS) substrates. The deposited films were irradiated with an electron beam dose of 15-35 kGy. At a dose of 25 kGy, the photoelectrode showed a maximum efficiency of 1.8% in a 1 M Na_2SO_3 electrolyte in the presence of a graphite counter. The higher efficiency of the electrode is the result

of the highly porous nanosheets and the interconnection of these nanosheets provide a larger surface area compared to other nanostructures.

Veerathangam et al. **[60]** synthesized undoped and Ag-doped CdS quantum dots (QDs) on spin coated TiO_2 photoanode material by SILAR method. The [Ag-doped CdS/Iodide/triiodide (I^-/I_3^-)/Platinum] PEC cell showed enhanced photovoltaic parameters such as I_{sc}, V_{oc}, *FF*, and η are 2.35 mA cm^2, 704 mV, 0.72, and 1.25 % respectively. The replacement of Cd^{2+} ion by the Ag^+ ions enhance (increases) the optical properties results improved photovoltaic performance. The improvement of photocurrent density is due to the formation of additional energy levels. Bai et al. **[61]** successfully synthesized a three-tier system of Fe_2O_3/rGO/CdS on the FTO substrates by stepwise chemical (CBD and precipitation) and physical (spin coating) methods for various concentrations of the cadmium precursor $CdSO_4$ (2, 4 and 6 mM). The [Fe_2O_3/rGO/CdS/(0.5 M Na_2SO_4)/Platinum foil/ (Ag/AgCl)] PEC cell showed better PEC performance of 0.32 % (water splitting). It reveals that the insertion of rGO between Fe_2O_3 and CdS heterojunction effectively improves electronic transmission performance. The loading amount of CdS has an effect in photocurrent, and it is higher at the optimum concentration of 4.0 mM of $CdSO_4$.

Raut et al. **[62]** deposited the CdSe thin films by SILAR method on the SS and FTO coated glass substrates. The effect of pH on the structural, optical, wettability and morphological properties were studied. Structural studies reveal enhancement in crystallinity and particle size in company with and phase transformation with increase in pH from 11 to 12. Optical studies show maximum red shift in absorbance and decrease in band gap energy corresponding to pH = 12. The surface morphology of CdSe thin films found to be significantly modulated due to the pH. Bagade et al. **[63]** deposited CdSe thin films via arrested precipitation method on indium dopped tin oxide (ITO) substrates for various deposition time periods of 1, 2 and 3 h. The impact of deposition time on the optostructural, morphological and PEC properties of CdSe thin films were studied. The optical band gap energy changed from 1.87 to 1.71 eV with direct allowed type of transition. The [CdSe/Polysulfide/Graphite] PEC cell shows the conversion efficiency (η) of 0.27 to 0.62% with increasing deposition time. The improved efficiency is a result of surface morphology, improved crystallite size, and reduced grain boundaries. Raut et al. **[64]** electrosynthesized indium doped CdSe (volumetric doping from 0.025 to 0.50 vol%) thin films on stainless steel substrates and investigated the effect of doping on the

PEC properties. The photoelectrochemical (PEC) study of both films were carried out with [CdSe or In:CdSe/1 M Polysulfide/Graphite] cell. It is observed that indium doping in CdSe enhances the *FF* from 0.56 to 0.63 and η from 0.80% to 2.01%. The increased flat band potentials from -1.01 to -1.19 V/SCE, band bending factor found to be enhanced from 0.31 to 0.49 eV and lower charge transfer resistance due to indium doping leads to improved photo conversion efficiency. Jana et al. **[65]** prepared the polycrystalline n-type CdSe thin films from aqueous bath at room temperature by periodic voltammetry on FTO substrates for different number of the periodic cycles (50 - 500 by interval of 50). The [CdSe (250cycles)/ 0.5 M Polysulfide/Platinum] PEC cell exhibits significant photoresponse with ~0.37 - 0.40 *FF* and ~1% solar conversion efficiency. Mahato et al. **[66]** deposited nanocrystalline cadmium selenide (CdSe) thin films on ITO at room temperature (28 ^{o}C) by using simple two electrode electrodeposition process. The *FF* and η for [CdSe/1 M Polysulfide/Graphite] PEC cell configuration is found to be 0.19 and 1.16%, respectively for annealed CdSe thin film. The low electrical resistivity, good optical transmittance and tunable optical bandgap of CdSe thin films gives the better PEC properties.

Chauhan et al. **[67]** introduced the transition metal Cr (0.1 - 0.3 M) into the CdSe host lattice via periodic cyclic voltammetry method and investigated the PEC performance. The [Cr (0.2M) CdSe/(0.5 M Na$_2$S+2 M S)/Platinum/(Ag/AgCl)] PEC cell shows the better photocurrent of 1.32 mA cm^{-2}. Cr doping provides the low content of Cr dopants which act as trap centers for photogenerated charge carriers (electron or hole) increases the separation efficiency and hinder the recombination rate, thus improvs the current density leads better power conversion efficiency. Sabri et al. **[68]** prepared the CdSe thin films by chemical bath deposition method on FTO substrate. The films coated further by tetra(-4-pyridyl) porphyrinatomanganese III/II sulfate embedded inside polysiloxane. CdSe pre-annealing at 350 ^{o}C and followed coating with MnPyP/Polysil enhances the electrode PEC characteristics. The [CdSe-MnPyP-Polysil/ 0.1 M (Na$_2$S, S, KOH)/Platinum] cell exhibits PEC parameters of *FF* 0.35 and η of 0.28%. Hazra et al. **[69]** utilized the simple and cost effective galvanostatic technique to synthesize nanostructured mixed n-type chalcogenide semiconductor films (CdSeS) from a non-aqueous bath for 0.05 M to 0.20 M sulfur precursor concentration. The CdSeS (0.15 M S) film shows significant photo-response of *FF* 0.18 and η of 0.94 %.

Patil et al. **[70]** deposited CdS-GO composite films with different ratios of CdS to GO (10 - 50 weights %) by ultrasonic spray deposition approach. The cell [CdS-GO (50%)/1 M Na_2SO_4/Platinum/AgCl] shows the higher PEC parameters of *FF* 0.47 and η 3.95%. The significant improvement in efficiency is the result of well arrangement and uniform distribution of CdS nanoparticles on the GO film surface by the high frequency ultrasonic treatment. Nanoparticles of CdS anchored on GO inhibit the recombination of photogenerated electron hole pairs and reduce the band gap (2.40 eV for pure CdS, 2.05 eV for CdS-GO at 50% concentration), which improves the performance of the PEC solar cell.

1.4.3 Literature survey of cadmium chalcogenides and their composites for gas sensor application

Vanalakar et al. **[71]** fabricated 1-D bonded CdS nanowires by a simple and inexpensive chemical bath deposition method at low temperature for time spans of 10 to 40 minutes. The CdS sample deposited for 20 minutes (CdS:20) showed a fast response and recovery times with higher selectivity for NO_2 and sensitivity of about 1850% at a concentration of 100 ppm. Nanowire-like morphology and inter-wire space distance were observed to play a crucial role in the gas adsorption-desorption reaction, results in an improvement in the gas sensing properties. Sonkar et al. **[72]** prepared CdS thin films of different thicknesses by spin coating technique at different speeds (1000, 2000 and 3000 rpm). The CdS film shows gas response of 173 % for 20 ppm NO_2 gas concentration at 70 ^{o}C temperature. The observed response and recovery time periods were of 352 and 226 s. Mondal **[73]** deposited pure and Ni (3% and 5%.) doped CdS thin films by low-cost SILAR method. The LPG sensitivity of CdS thin film increases with nickel doping for all operating temperatures. Such increase in sensitivity from ~ 48 % for CdS to ~ 53% for 5% Ni doped CdS at operating temperature 120 °C for 300 ppm LPG might be due to enhanced surface roughness and porosity because of nickel doping.

Akbar et al. **[74]** used the co-dispersion technique to develop CdS decorated with polyaniline (PANI) as a nanocomposite. Structural and morphological studies show that CdS nanoparticles attach to polyaniline nanorods. The gas sensor properties of the PANI-CdS composite sensor are thoroughly investigated and compared with the bare PANI sensor. The gas response at room temperature to acetone, ammonia,

Table 1.2: Literature survey of cadmium chalcogenides and their composites for PEC application

Sr. no.	Deposited material	Deposition method	Substrate	Cell configuration	Input power (mWcm^{-2})	I_{sc} (mA cm^{-2})	V_{oc} (mV)	FF	η (%)	Ref.
1	CdS	CBD	FTO	[CdS/1 M Polysulfide/Graphite]	50	0.12	290	0.35	0.067	56
2	CdS	Spin coating	FTO	[CdS/0.5 M Na$_2$SO$_4$/Pt/SCE]	100	0.021	-	-	-	57
3	n-CdS	CBD	FTO	[CdS/0.1 M Na$_2$S$_2$O$_3$/Pt/Ag/AgCl]	-	0.019	398	-	-	58
4	CdS 25 kGy	ED	ITO/ SS	[CdS/1 M Na$_2$SO$_3$/Graphite]	30	0.640	865	0.48	1.85	59
5	TiO$_2$/Ag-doped CdS QDs	Spin coating, SILAR	FTO	[(TiO$_2$/Ag-DopedCdS)/(I$^-$/I$_3^-$)/Pt]	100	2.35	740	0.72	1.25	60
6	Fe$_2$O$_3$/rGO/ CdS	Spin coating and CBD	FTO	[(Fe$_2$O$_3$/rGO/CdS)/0.5 M Na$_2$SO$_4$/Pt foil/(Ag/AgCl)]	47	-	-	-	0.32	61
7	CdSe	CBD	SS and FTO	-	-	-	-	-	-	62
8	CdSe	Arrested precipitation technique (APT)	ITO	[CdSe/Polysulfide/Graphite]	-	1.1	583	0.28	0.62	63
9	In:CdSe	ED	SS	[In:CdSe/1 M Polysulfide/Graphite]	50	3.0	512	0.63	2.01	64

Sr. no.	Deposited material	Deposition method	Substrate	Cell configuration	Input power $(mWcm^{-2})$	I_{sc} $(mA\ cm^{-2})$	V_{oc} (mV)	*FF*	η (%)	Ref.
10	CdSe	Periodic voltammetry	FTO	[CdSe/0.5 M Polysulfide/Pt]	50	1.90	-	~38	~1	65
11	CdSe	ED	ITO	[CdSe/1 M Polysulfide/ Graphite]	-	-	-	0.19	1.16	66
12	Cr doped CdSe	Periodic cyclic voltammetry	ITO	[CrCdSe/0.5 M Na_2S +2M S) /Pt]	80	1.32	-	-	-	67
13	CdSe-MnPyP-Polysil	CBD	FTO	[(CdSe-MnPyP-Polysil)/0.1 M $(Na_2S$, S, KOH)/Pt]	20	0.28	-0.46	0.35	0.28	68
14	CdSeS	Galvanostatic method	FTO	[CdSeS/ Polysulfide/Graphite]	50	-	-	0.18	0.94	69
15	CdS-GO	Ultrasonic spray deposition	SS and Glass	[(CdS-GO(50%))/1 M Na_2SO_4/Pt /AgCl]	100	9.1	910	0.47	3.95	70

methanol, formaldehyde and ethanol was investigated and the sensor was found to be selective towards ammonia. The composite sensor showed a maximum gas response of 250% with 74% stability after being exposed to 100 ppm of NH_3 at ambient temperature. Response and recovery times decrease as NH_3 gas concentration increases. The PANI composition provides more porosity, which has a positive effect on the gas sensor properties. Zhang et al. **[75]** synthesized CdS nanorods on a polyaniline particles surface (CdS/PANI) using a hydrothermal synthesis method. The CdS/PANI based sensor showed an excellent response to low concentration formaldehyde gas in a wide temperature range of 80 - 140 ºC at working temperature. The CdS/PANI sensor had response and recovery times of around 25 and 30 s for 10 ppm formaldehyde gas, respectively. The CdS/PANI composites sea urchin-like nanorods morphology can be helpful for better gas sensing properties. Vishwakarma et al. **[76]** prepared CdS-doped TiO_2 nanocomposite (containing 1-2 wt% CdS) in the form of films as a gas sensor. The response of the fabricated sensor was measured with acetone, propanol, and LPG at different concentrations (0-5000 ppm) in ambient air at room temperature. The optimized doping of 2 wt% CdS gives the highest response, i.e., 71% for 5000 ppm acetone, which is more selective over propanol or LPG. The response and recovery times are improved from 85 to 190 s for undoped TiO_2 sensor to 55-115 s for acetone (5000 ppm). Madlul et al. **[77]** deposited the cadmium sulfide doped with copper by drop casting on glass and silicon substrates at 80 ºC temperature and annealed in air for 120 min at different temperatures (150 and 200 ºC). The CdS:Cu 5%/Si heterostructures annealed at 150 ºC exhibited a noticeable 26% gas response towards 1 ml ethanol diffuse at room temperature with rapid response-recovery times of around 160 and 183 s.

Feng et al. **[78]** fabricated CdS nanospheres doped with graphene for ethanol detection via a simple hydrothermal process. The ethanol sensing performance of the CdS/G sensor was studied in detail. The CdS/G sensor demonstrated high response of 30 % for 100 ppm ethanol at operating temperature 375 ºC with ultra-fast responding and recovering ability. The excellent ethanol sensing properties of the CdS/G sensor were result from the enhanced surface reaction assisted by graphene. Lokhande et al. **[79]** fabricated Cu_2SnS_3 (CTS)/CdS heterojunction for room temperature (27 ℃) liquefied petroleum gas (LPG) sensor. The heterojunction is fabricated between by sputter deposited CTS thin films and chemically bath deposited CdS thin films. The CTS/CdS heterojunction exhibited maximum LPG response of 56% at room

temperature under exposure of 780 ppm LPG concentration with 31 and 56 s response and recovery time, respectively. The enhanced sensing is due to structural, morphological and compositional properties due to the sulfurization.

Shao et al. **[80]** used simple solvothermal technique to grow CdS nanocones on the 2D layered RGO-MoS$_2$ substrate to form a new heterostructure. The RGO-MoS$_2$-CdS films used in the construction of the gas sensor resulted in a significantly improved sensor response of 27.4% when exposed to 0.2 ppm of NO$_2$ due to a higher specific surface area, more adsorption sites, and lots of heterojunctions. Moreover, the gas sensor displayed an outstanding selectivity toward NO$_2$ gas over the other gases. Dun et al. [81] used in situ growth strategy to prepare CdS quantum dots supported by ultrathin porous nanosheets assembled into hollowed-out Co$_3$O$_4$ microspheres (CdS QD/Co$_3$O$_4$HMSs). The fabricated sensor exhibited high response (12.7%) and ultra-fast response/recovery times (0.6/1.0 s) to 100 ppm H$_2$S at 25 °C with good reversibility and exceptional long-term stability. The superior gas sensing properties were ascribed to not only the large specific surface area and high activity of the interconnected CdS quantum dots at room temperature but also the scaffold of ultrathin porous nanosheets assembled into hollowed-out Co$_3$O$_4$ microspheres. Saxena et al. **[82]** deposited nanocomposite thin films of CdS: SiO$_2$ (1:1 ratio) using pulsed laser deposition method. The CdS: SiO$_2$ sensor tested for various reducing gases like LPG, H$_2$, H$_2$S, NO$_2$, and CO$_2$. The sensor showed highest response for LPG with observed value about ~ 71 % for 1000 ppm concentration at room temperature with response time and recovery time as 91 and 140 s respectively. Al-Hilli **[83]** deposited cadmium selenide (CdSe) thin films on a glass substrate via the plasma DC-sputtering method at room temperature by varying deposition time (30, 60, 90, and 120 min) CdSe showed sensitivity to carbon monoxide (CO) gas at room temperature with high response 65 % with response time 35 s and recovery time 65 s. Khudiar et al. **[84]** deposited pure and Cu doped CdSe thin films on glass substrates at room temperature by using thermal evaporation technique. The Cu:CdSe showed Co$_2$ sensing response of ≈ 25 %.

Sensitivity equation/Formula:

$$\textbf{1. } S = \frac{R_g - R_a}{R_a} \times 100 \qquad (1.11)$$

$$\textbf{2. } S = \frac{R_a - R_g}{R_a} \times 100 \qquad (1.12)$$

$$\textbf{3. } S = \frac{R_a}{R_g} \qquad (1.13)$$

$$\textbf{4. } S = \frac{R_g}{R_a} \qquad (1.14)$$

Table 1.3: Literature survey of cadmium chalcogenides and their composites for gas sensor application.

Sr. no.	Deposited material	Deposition method	Operating temperature (^oC)	Concentration of the target gas (ppm)	t_{res} (s)	t_{rec} (s)	Gas response/ sensitivity S (%)	Sensitivity Equation\Formula	Ref.
1	CdS	CBD	200	NO$_2$ (100 ppm)	-	-	1850	$S = \dfrac{R_g - R_a}{R_a} \times 100$	71
2	CdS	Sol gel, spin coating	70	NO$_2$ (20 ppm)	331	207	173	$S = \dfrac{R_g - R_a}{R_a} \times 100$	72
3	Ni in CdS	SILAR	120	LPG (300 ppm)	~ 25	150	~55	$S = \dfrac{R_a - R_g}{R_a} \times 100$	73
4	PANI-CdS	Co-dispersion technique	27	NH$_3$ (100 ppm)	-	-	250	$S = \dfrac{R_g - R_a}{R_a} \times 100$	74
5	CdS/PANI	Hydrothermal synthesis	120	Formaldehyde gas (10 ppm)	25	30	-	-	75
6	CdS-doped TiO$_2$	Printing	27	Acetone (5000 ppm)	55	115	71	$S = \dfrac{R_a - R_g}{R_a} \times 100$	76
7	CdS:Cu 5%/Si	Drop casting	150	Ethanol	160	183	26	$S = \dfrac{R_g - R_a}{R_a} \times 100$	77

Sr. no.	Deposited material	Deposition method	Operating temperature (°C)	Concentration of the target gas (ppm)	t_{res} (s)	t_{rec} (s)	Gas response/ sensitivity S (%)	Sensitivity Equation\Formula	Ref.
8	CdS/G	Hydrothermal	375	Ethanol (100 ppm)	-	-	30	$S = \dfrac{R_a - R_g}{R_a} \times 100$	78
9	Cu_2SnS_3/CdS	Sputtering, CBD	27	LPG (780 ppm)	31	56	56	$S = \dfrac{R_g}{R_a}$	79
10	RGO-MoS_2-CdS	Hydrothermal, solvothermal	75	NO_2 (0.2 ppm)	25	34	27.4	$S = \dfrac{R_g - R_a}{R_a} \times 100$	80
11	CdS QD/Co_3O_4 HMSs	Precipitation	25	H_2S (100 ppm)	0.6	1.0	12.7	$S = \dfrac{R_a}{R_g}$	81
12	CdS: SiO_2 NCTFs)	Pulsed laser deposition (PLD)	27	LPG (1000 ppm)	91	140	71	$S = \dfrac{R_a - R_g}{R_a} \times 100$	82
13	CdSe	DC- sputtering	27	CO (6 ppm)	35	65	60-65	$S = \dfrac{R_g - R_a}{R_a} \times 100$	83
15	CdSe: Cu	Thermal evaporation	-	CO_2	-	-	-	-	84

1.5 Orientation and purpose of the thesis

The non-renewable sources of energy are the diminishing day by day, leads current era facing the energy crisis situation due to the overpopulation. The extreme need of the economical, sustainable, secure and non-polluting energy supply become an integral part of human life. The solar energy is a most prominent source of energy. Recently, the low-cost cadmium chalcogenides PEC solar cells are attracted more attention to convert light energy to direct electricity due to its simple fabrication. But the lower electrical conductivity, photocorrosion, less electrode stability are some hurdles in its wide uses. To overcome the hurdles the different deposition methods, use of complexing agents, doping of some materials, post deposition techniques are utilized by researchers. In this topic composite material is chosen a cadmium chalcogenides and reduced graphene oxide (rGO). The rGO is used to control pore structure in electrode, enhances effective surface area and lowers equivalent series resistance (ESR). Hence, the problem of poor conductivity in cadmium chalcogenides can be solved by employing rGO as a backbone material. The pure cadmium chalcogenide (CdS, CdSe) and cadmium chalcogenide/rGO (rGO/CdS, rGO/CdSe) composite thin films are prepared by using low temperature chemical synthesis methods like SILAR and electrodeposition (ED).

The physical and chemical properties of the synthesized thin films are analyzed using various characterization techniques. XRD is employed for phase identification of the material, while the surface morphology is examined using FE-SEM. The elemental composition of the thin films is determined through EDAX. The wettability property of the material is evaluated by the contact angle method. The optical properties of prepared thin films are studied by UV- visible spectroscopy. The material surface area and pore size distribution of pure and rGO composited cadmium chalcogenides is evaluated by BET and BJH techniques.

The PEC properties of prepared thin films are investigated by current-voltage (I-V) characteristics in light, Dark and chopping conditions. Two electrode system is used for an electrochemical study in 1 M polysulfide electrolyte, consists of (CdS, CdSe) or (rGO/CdS, rGO/CdSe) thin film used as working electrode and graphite used as a counter electrode. Furthermore, the PEC parameters like short circuit current (Isc), open circuit voltage (Voc), fill factor (FF) and efficiency (η) of prepared thin films evaluated using respective formulae. The electrolyte electrode and its interface

resistances are evaluated by electrochemical impedance spectroscopy (EIS) in light and under dark conditions.

The gas sensing properties of prepared thin films are investigated by fabricating heterojunction type gas sensor device is measured using Keithley 6514 electrometer or potentiostat and homemade gas sensor regarding various parameters of sensitivity (S), selectivity, response time (t_{res}), recovery time (t_{rec}), and long-term stability. The gas response, the electrical current of the sensor is measured in air (I_a) and in the presence of gas (I_g) and sensitivity is evaluated by respective formula. The effect of rGO composition studied on its structural, chemical composition, the efficiency of PEC cell and sensitivity of the material for gas sensing.

1.6 References

1] K. Rath, R. Bulakhe, A. Bhalerao, Future challenges and applications in green technology, Green engineering and technology, (CRC Press., 2021) pp. 327-341.

2] M. Dambhare, B. Butey, S. Moharil, J. Phys. Conf. Ser., 1913 (2021) 012053-012068.

3] https://energyeducation.ca/encyclopedia/Photovoltaic_cell

4] N. Asthana, K. Pal, Polymerized hybrid nanocomposite implementations of energy conversion cells device, In nanofabrication for smart nanosensor applications, (Elsevier, 2020) pp. 349-397.

5] F. Wang, X. Liu, F. Gao, Fundamentals of solar cells and light-emitting diodes. In advanced nanomaterials for solar cells and light emitting diodes, (Elsevier, 2019) pp. 1-35.

6] A. Khatibi, F. Razi Astaraei, M. Ahmadi, Energy Sci. Eng., 7 (2019) 305-322.

7] Photovoltaics report, Prepared by Fraunhofer institute for solar energy systems, ISE with support of PSE projects (GmbH Freiburg, 2023) www.ise.fraunhofer.de.

8] J. Ajayan, D. Nirmal, P. Mohankumar, M. Saravanan, M. Jagadesh, L. Arivazhagan, Superlattices Microstruct., 143 (2020) 106549 (1-53).

9] Ph.D. thesis, H. D. Shelke, Chemical synthesis and characterization of copper tin sulfide (CTS) thin films for solar cell application, (Shivaji university, Kolhapur 2017) PP. 1-168

10] A. Bhalerao, B. Wagh, R. Bulakhe, P. Deshmukh, J. Shim, C. Lokhande, J. Photochem. Photobiol. A, 336 (2017) 69-76.

11] Ph.D. thesis, V. S. Raut, Studies on chemical synthesis and characterization if indium doped CdSe thin films for use in solar cells, (Shivaji university, Kolhapur 2018) pp. 1-178.

12] C. Lokhande, and S. Pawar, Mater. Chem. Phys., 11 (1984) 201-277.

13] D. Sathe, P. Chate, P. Hankare, A. Manikshete, U. Sankpal, V. Bhuse, Appl. Nanosci., 6 (2016) 191-196.

14] S. Gonuguntla, C. Vennapoosa, U. Pal, Sulfide and selenide electrode for photoelectrochemical water splitting. In sulfide and selenide based materials for emerging applications, (Elsevier, 2022) pp- 525-553.

15] M. Uplane, and S. Pawar, Bull. Mater. Sci., 7 (1985) 101-104.

16] J. Bockris, A. Reddy, M. Gamboa-Aldeco, Modern electrochemistry, fundamentals of electrodics, (Kluwer academic publishers, NEW YORK, 2002) pp- 771-1033.

17] A. Bhalerao, C. Lokhande, B. Wagh, Chalcogenides for photovoltaic applications, (Lambert academic publishing, 2020) pp. 1-201.

18] A. Jordehi, Renew. Sust. Energ. Rev., 61 (2016) 354-371.

19] L. Ge, X. Mu, G. Tian, Q. Huang, J. Ahmed, Z. Hu, Front. Chem., 7 (2019) 839 (1-7).

20] R. Shinde and J. Gunjakar, 2D nanomaterials: Chemiresisitive gas sensor (Lambert academic publishing, 2022) pp. 1-168.

21] D. Aswal and S. Gupta, Science and technology of chemiresistor gas sensors, (Nova publishers, New York, 2007) pp. 1-392.

22] A. Singh, S. Sikarwar, A. Verma, B. Yadav, Sens. Actuator A Phys., 332 (2021) 113127 (1-22).

23] https://en.wikipedia.org/wiki/Air_pollution.

24] L. Liu, Y. Wang, Y. Liu, S. Wang, T. Li, S. Feng, S. Feng, S. Qin, T. Zhang, Microsyst. Nanoeng., 8 (2022) 85 (1-22).

25] Ph.D. thesis, V. S. Jamadade, NiFe$_2$O$_4$-polyaniline based heterojunction for LPG sensor: fabrication and performance evaluation, (Shivaji university, Kolhapur, 2011) pp. 1-192.

26]   Ph. D. thesis, V. R. Shinde, Chemical preparation of zinc oxide thin films and their applications in gas sensors, (Shivaji university, Kolhapur, 2005) pp. 1-162.

27]   R. Shinde, N. Padalkar, S. Sadavar, S. Kale, V. Magdum, Y. Chitare, S. Kulkarni, U. Patil, V. Parale, H. Park, J. Gunjakar, J. Hazard. Mater., 432 (2022) 128734 (1-10).

28]   M. Javaid, A. Haleem, S. Rab, R. Singh, R. Suman, Sens Int., 2 (2021) 100121 (1-10).

29]   https://en.wikipedia.org/wiki/Gas_detector#:~:text=The%20first%20gas%20detector%20in,   specific%20height%20in%20fresh%20air.

30]   A. Dey, Mater. Sci. Eng. B, 229 (2018) 206-217.

31]   L. Ma, X. Ai, X. Yang, X. Song, X. Wu, J. Phys. Chem. C, 45 (2020) 25133-25141.

32]   N. Vanasundaram, M. Ahmad, A. Chaudhary, P. Sharma, Mater. Res. Express, 7 (2020) 025015 (1-10).

33]   L. Wang, J. Feng, Y. Tong, J. Liang, Int. J. Hydrog. Energy, 44 (2019) 128-135.

34]   K. Dai, T. Hu, J. Zhang, L. Lu, Appl. Surf. Sci., 512 (2020) 144783 (1-50).

35]   F. Chen, X. Zou, C. Chen, Q. Hu, Y. Wei, Y. Wang, B. Xiang, J. Zhang, Ceram., 45 (2019) 14376-14383.

36]   M. Indhumathy and A. Prakasam, J. Mater. Sci.: Mater. Electron., 30 (2019) 15444 - 15451.

37]   S. Deshmukh, V. Kheraj, A. Panchal, Mater. Today: Proc., 5 (2018) 21322-21327.

38]   K. Chaudhari, N. Gosavi, N. Deshpande, S. Gosavi, J. Sci-adv. Mater. Dev., 1 (2016) 476-481.

39]   V. Raut, C. Lokhande, V. Killedar, J. Electroanal. Chem., 788 (2017) 137-143.

40]   N. Meng, Y. Zhou, W. Nie, P. Chen, J. Nanopart Res., 18 (2016) 1-13.

41]   R. Ranjan, M. Kumar, A. Sinha, Int. J. Hydrog. Energy, 44 (2019) 10573-10584.

42]   C. Foo, H. Lim, A. Pandikumar, N. Huang, Y. Ng, J. Hazard. Mater., 304 (2016) 400-408.

43] K. Hareesh, S. Dhole, D. Phase, J. Williams, Mater. Res. Bull., 110 (2019) 82-89.

44] H. Rosly, K. Rahman, M. Harif, C. Doroody, M. Isah, H. Misran, N. Amin, Superlattices Microstruct., 148 (2020) 106716 (1-22).

45] T. Logu, K. Sankarasubramanian, P. Soundarrajan, K. Sethuraman, Electron. Mater. Lett., 11 (2015) 206-212.

46] Z. Bao, X. Yang, B. Li, R. Luo, B. Liu, P. Tang, J. Zhang, L. Wu, W. Li, L. Fengy, Mater. Sci. Semicond. Process., 48 (2016) 27-32.

47] N. Shelke, S. Karle, B. Karche, J. Mater. Sci.: Mater. Electron., 31 (2020) 15061-15069.

48] X. Wang, W. Tian, M. Liao, Y. Bando, D. Golberg, Chem. Soc. Rev., 43 (2014) 1400- 1422.

49] M. Wu, C. Kao, T. Lin, S. Chan, S. Chen, C. Lin, Y. Huang, Z. Zhou, K. Wang, C. Lai, Sens. Actuators B Chem., 309 (2020) 127760 (1-9).

50] N. Rathee and N. Jaggi, Vacuum, 169 (2019)108910 (1-6).

51] Y. Park, K. Lee, G. Lim, H. Seo, S. Kim, M. Kim, Y. Yi, H. Lee, D. Son, Org. Electron., 82 (2020) 105707 (1-6).

52] T. Santhosh, K. Bangera, G. Shivakumar, Mater. Sci. Semicond. Process., 68 (2017) 114-117.

53] A. Zyoud, N. Abdul-Rahman, G. Campet, D. Park, H. Kwon, T. Kim, H. Choi, M. Helal, H. Hilal, J. Electroanal. Chem., 774 (2016) 7-13.

54] https://www.apam.columbia.edu/files/seas/content/apam_ image/teshome_g_poster2_cds.pdf

55] https://www.researchgate.net/figure/CdSe-structures-cubic-and-wurtzite_fig2_282348361

56] T. Swamy, A. Shelke, A. Lokhande, H. Pushpalatha, C. Lokhande, R. Ganesha, Optik, 138 (2017) 192-199.

57) G. Rahane, S. Jathar, S. Rondiya, Y. Jadhav, S. Barma, A. Rokade, W. Russell, M. Nasane, V. Jadkar, N. Dzade, S. Jadkar, ES Mater. Manuf., 11 (2020) 57-64.

58) W. Kumarage, R. Wijesundera, V. Seneviratne, C. Jayalath, B. Dassanayake, J. Phys. D: Appl. Phys., 49 (2016) 095109 (1-7).

59] S. Shinde, G. Ghodake, N. Velhal, M. Takale, D. Kim, M. Rath, H. Dhaygude, V. Fulari, J. Solid State Electrochem., 21 (2017) 1517-1522.

60] K. Veerathangam, M. Pandian, P. Ramasamy, Mater. Res. Bull., 94 (2017) 371-377.

61] H. Bai, C. Chen, H. Wu, Z. Da, W. Fan, Cryst. Res. Technol., 51 (2016) 656-662.

62] V. Raut, C. Lokhande, V. Killedar, Int. J. Eng. Technol., 10 (2017) 568-572.

63] C. Bagade, V. Ghanwat, K. Khot, P. Bhosale, Mater. Lett., 164 (2016) 52-55.

64] V. Raut, C. Lokhande, V. Killedar, J. Electroanal. Chem., 788 (2017) 137-143.

65] A. Jana, M. Hazra, J. Datta, J. Solid State Electrochem., 21 (2017) 3083-3091.

66] S. Mahato, and A. Kar, J. Electroanal. Chem., 742 (2015) 23-29.

67] P. Chauhan, A. Patel, S. Narayan, J. Prasad, C. Sumesh, G. Solanki, K. Patel, S. Soni, P. Jha, V. Pathak, V. Patel, J. Alloys Compd., 862 (2021) 158016 (1-32).

68] H. Sabri, S. Saleh, A. Zyoud, N. Abdel-Rahman, I. Saadeddin, G. Campet, D. Park, M. Faroune, H. Hilal, Electrochim. Acta, 136 (2014) 138-145.

69] M. Hazra, A. Jana, J. Datta, Appl. Surf. Sci., 454 (2018) 334-342.

70] R. Patil, Y. Khollam, A. Kadam, B. Bond, R. Potdar, B. Nadekar, U. Nakate, S. Shiakh, P. More, Surf. Interfaces., 42 (2023) 103331 (1-12).

71] S. Vanalakar, V. Patil, P. Patil, J. Kim, New J. Chem., 42 (2018) 4232-4239.

72] R. Sonker, B. Yadav, V. Gupta, M. Tomar, Mater. Chem. Phys., 239 (2020) 121975 (1-7).

73] S. Mondal, Adv. Mater. Process., 8 (2022) 344-354.

74] A. Akbar, M. Das, D. Sarkar, Sens. Actuator A Phys., 310 (2020) 112071(1-11).

75] L. Zhang, X. Li, Z. Mu, J. Miao, K. Wang, R. Zhang, S. Chen, RSC Adv., 8 (2018) 30747-30754.

76] A. Vishwakarma, A. Sharma, N. Yadav, L. Yadav, Vacuum, 191 (2021) 110363 (1-9).

77] N. Madlul, N. Mahan, E. Ali, A. Abd, Mater. Today: Proc., 45 (2021) 5800-5803.

78] G. Feng, M. Zhang, S. Wang, C. Song, J. Xiao, Appl. Surf. Sci., 453 (2018) 513-519.

79] A. Lokhande, A. Yadav, J. Lee, M. He, S. Patil, V. Lokhande, C. Lokhande, J. Kim, J. Alloys Compd., 709 (2017) 92-103.

80]   S. Shao, L. Che, Y. Chen, M. Lai, S. Huang, R. Koehn, J. Alloys Compd., 774 (2019) 1-10.

81]   M. Dun, J. Tan, W. Tan, M. Tang, X. Huang, Sens. Actuators B: Chem., 298 (2019) 126839 (1-10).

82]   N. Saxena, P. Kumar, V. Gupta, Nanoscale Adv., 1 (2019) 2382-2391.

83]   Al-Hilli, Iraqi J. Sci., 59 (2018) 2234-2241.

84]   A. Khudiar, A. Jabor, Alkut university college journal, 7 (2023) 201-208.

Chapter-II

Theoretical background of synthesis methods and characterization techniques of thin films

CHAPTER- II

Theoretical background of synthesis methods and characterization techniques of thin films

Section A

2.1 Introduction

In the last few decades, thin film technology is continuously developing. Due to the scientific curiosity and tunable physicochemical characteristics, thin films have received massive interest in current research era. One method of depositing a fine (extremely less thick) of material on a substrate or on previously deposited layers is thin film deposition. The word "thin film" is relative because the technology available today can deposit a material in the range of a few nanometres to an angstrom. The main focus of the current research trend is to produce thin films of nanostructured materials with controlled physicochemical properties to achieve specific results. The ability to control these physicochemical properties has led to the practical use of thin films in applications such as photovoltaics, sensors, supercapacitors, photocatalysis, electrocatalysis, and many others [1, 2]. Due to low material consumption, ease of fabrication, and the potential use of flexible substrates, thin film devices are less expensive than bulk materials. It is crucial that the deposition process affects the properties of the thin film. The choice of the proper deposition method for thin films allows to achieve the flexibility and the required properties. Physical and chemical processes are the two basic categories used to classify thin film deposition methods. Sputtering and vacuum evaporation are two examples of physical processes where the deposited material is converted to a gaseous form during the evaporation process and then deposited on the substrate [3, 4].

CVD, photo CVD, metal-organic CVD (MOCVD), light amplification by stimulated emission of radiation (LASER) CVD, ED, CBD, SILAR, spray pyrolysis, sol-gel method, and other chemical processes are the chemical methods. The major disadvantages of physical processes include the need for sophisticated equipments, high working pressure, and the need to clean up the system after each deposition. On the other hand, chemical processes are fast, affordable, and well suited for the deposition of a range of materials that look like thin films, including metal hydroxides, metal oxides, metal chalcogenides, and composite materials [5, 6]. The comprehensive classification of thin film deposition methods is shown in **Chart 2.1**.

Among all of these thin film deposition methods, SILAR and ED methods are simple, low cost, less time consuming, and offer a wide advantage for selection of substrate materials and deposition parameters over more expensive methods.
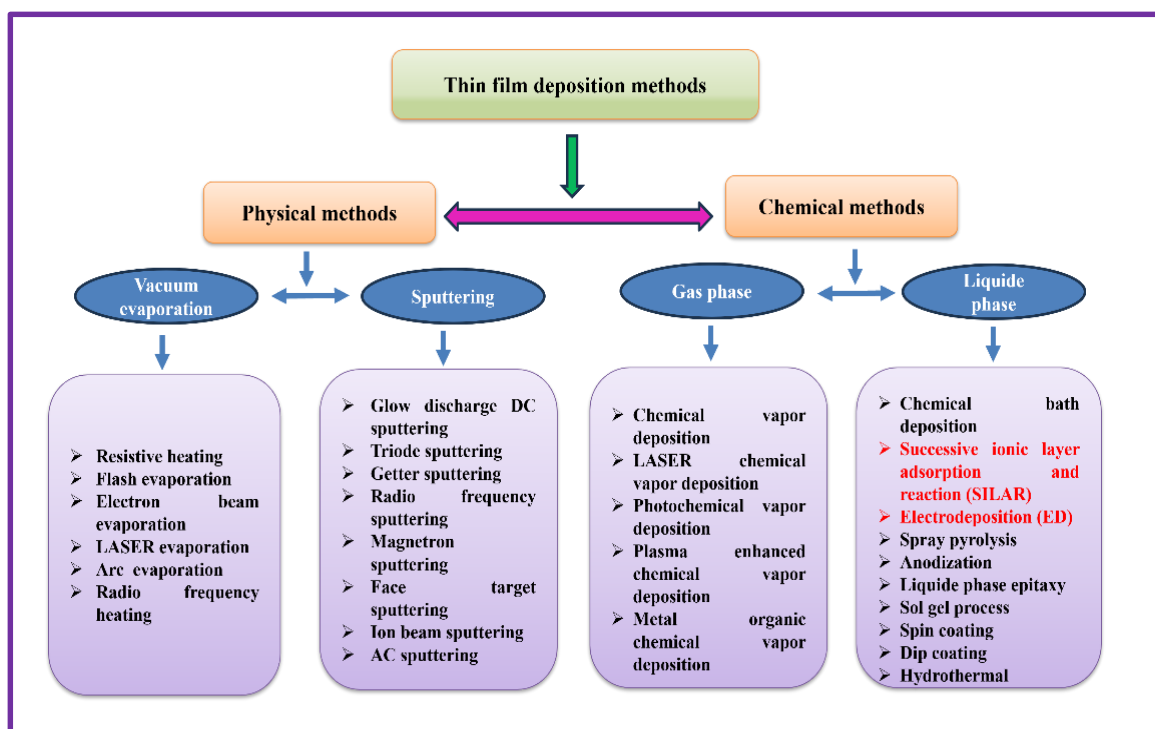
Chart 2.1 Classification of thin film deposition methods.

2.2 Thin film deposition methods

2.2.1 SILAR method

Introduction

The SILAR method is one of the favourable chemical methods for the deposition of variety of thin films. SILAR method is highly beneficial due to the excellent control over reaction parameters that helps one to tune the properties of the resultant material. Ristov et al. **[7]** first reported this method in 1985, and the name SILAR was first introduced by Nicolau et al. **[8]**. This method allows deposition of various chemical compounds as well as their composite films. Recently, various materials (metals, semiconductors, ceramics, superconductors, conducting polymers, etc.) have been deposited in the form of thin films by SILAR method.

2.2.1.1 Basic mechanism of SILAR method

The SILAR technique typically relies on the adsorption and reaction of the ions from the precursor solutions and the carrying of heterogeneous precipitation in the solution by double distilled water (DDW) washing in between each immersion. Adsorption, which is a key component of the SILAR process, can be defined as the deposition of a precursor substance on the surface of another material. When two heterogeneous phases come into contact with one another, adsorption may be predicted. The adsorption process can occur in contact between gas-liquid, liquid-solid

and gas-solid phases. The first phase of the SILAR method is mainly concerned with adsorption using the liquid-solid approach. The attraction between the ions in the solution and the surface of the substrate makes it feasible for adsorption, which is a surface event, to occur. These forces might be Vander Wall, chemically cohesive, or attractive. Atoms or molecules contain leftover or imbalanced forces on all sides to maintain the substrate particles in place. The adsorbed ion reacts with the anion in the second stage, forming a film.

2.2.1.2 Basic steps involved in SILAR method

1) Adsorption

The initial phase of SILAR involves dipping the substrate into a first beaker containing a cationic precursor solution, where some cations are adsorbed on the surface of the substrate and produce the Helmholtz electric double layer. The cations make up the positive layer, whereas the counter ions of the cations are found in the negative layer.

2) Rinsing-I

To remove loosely bound cations adsorbed on the substrate surface, which results in a saturated electrical double layer, the substrate is washed into a second beaker containing DDW in the second stage.

3) Reaction

The substrate (with adsorbed cations in step - I) is dip into an anionic precursor solution in a third beaker during this reaction phase. The solid phase material layer develops on the substrate when cation and anion interactions occur.

4) Rinsing- II

In the last step, a substrate is again rinsed into DDW of a fourth beaker, to remove some loosely bounded particles from the surface of the substrate i.e., the unreacted species and the reaction byproduct are removed. The schematic representation of SILAR method is shown in **Fig. 2.1**. The **Fig. 2.2** depicts the photograph of microcontroller-based SILAR instrument (Holmarc Optomechatronics. LTD) used for thin film deposition.

2.2.1.3 Deposition parameters

The deposition of thin films using the SILAR method depends on a variety of experimental variables that have a significant impact on the thin film quality. These factors include the cationic and anionic bath pH, the concentration of the cationic and

anionic solutions, the adsorption, reaction, and rinse periods, the complexing agent, and the kind of substrate used. These parameters are discussed in detail below:

1) Precursor concentration

The precursor concentration has an important role in the film thickness in all chemical reactions. At the higher concentration of cationic precursor, the adsorption rate increases, which leads to an increase in the film thickness. If the application to be tested is thickness dependent, then, the concentration of the precursors can be employed to control the film thickness.
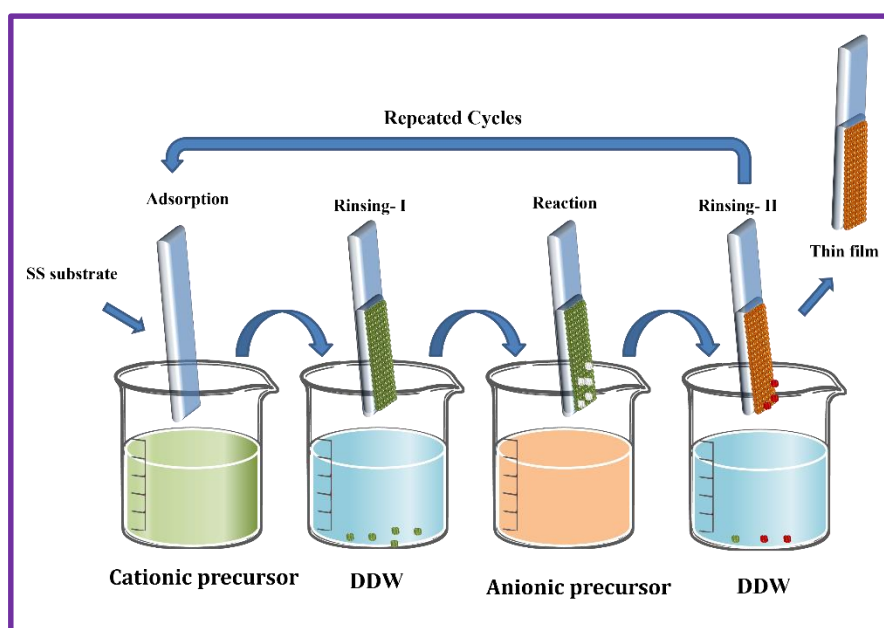
Fig. 2.1 The schematic representation of thin film deposition by SILAR method.

2) pH of precursor solutions

The pH of the precursor solution is also called the rate determining factor in the chemical reaction. The hydrolysis of cations in the cationic solution eventually decides the final phase formation of the material. Also, by controlling the pH of anionic solution the rate of reaction and film formation can be controlled. By adjusting the pH of the cationic and anionic solutions, it is also possible to tune the microstructure or morphology of the material. An extremely acidic pH might cause metallic substrates to corrode, therefore one should bear that in mind.

3) Temperature

The cationic and or anionic precursor solution temperature results in the crystallization of the material during film formation. The cationic and or anionic precursor solution temperature plays an important role in crystallinity which depends on thermodynamical energy received during the reaction. Typically, a heat treatment

that produces the development of an amorphous phase is not used in SILAR processes. However, by giving the solutions a necessary heat treatment, crystallinity can be enhanced. Most crucially, when utilizing a complexing agent, the complex is broken by heating the right solution.

Fig. 2.2 The photograph of SILAR instrument used for thin film deposition [9].

4) Complexing agent

The kinetics and development of the material are determined by the concentration of metal ions in the solution and their release into the solution. In many cases, it is necessary to continuously release metal ions in order to regulate their fast hydrolysis. Complexing agents with donors that form coordination bonds with the cations to slow down their fast adsorption can be utilized to accomplish this situation. The inclusion of a complexing agent adds an extra kinetics step to the reaction, allowing time for surface relaxing and promoting regular development. The complex that the complexing agents create with the cations can be further broken down by heating the solution. As a result, both the quick precipitation and greater thickness are avoided. Different chemicals like ethylenediamine tetraacetic acid (EDTA), ammonia, triethanolamine (TEA) etc. are used as a complexing agent.

5) Number of cycles

As the number of cycles in a SILAR reaction rises, the thickness of the film also rises. In order to deposit optimum thick film, the cycle number must be optimized. Less cycles lead to irregular and uneven material deposition, and more cycles might lead to cluster formation and the thin film peeling off.

6) Rinsing time

Rinsing can remove loosely bound counter ions from the material that can lead to impurities and prevent the unwanted formation of clusters. To achieve a homogeneous film thickness, it is crucial to empirically optimise the reaction rinsing durations.

2.2.1.4 Advantages of SILAR method

❖ SILAR method does not need any costly instruments and it is possible to deposit manually.

❖ SILAR method works at low operating temperatures. High temperature effects such as dopant redistribution, contamination, and interdiffusion are avoided. Also, corrosion of metallic substrates can be avoided.

❖ In this method, the deposition rate and film thickness can be effectively regulated by adjusting the number of cycles.

❖ The films of uniform thickness can be deposited on any kind of substrates of any shape.

❖ It is simple to modify the preparative parameters to obtain the appropriate thickness, which eventually impacts the materials physicochemical qualities.

❖ It also known as modified CBD method due to lower wastage of material.

❖ The doping of any foreign atom into the material in any required proportion is possible.

❖ For the deposition of binary, ternary chalcogenides and composite films, the SILAR method is effective **[8, 10]**.

2.2.2 Electrodeposition (ED) method

Electrochemical deposition or ED is a method of depositing conducting/semiconducting materials onto a substrate (typically conducting) using an electric field and redox reaction. It is an easy, cost-effective and famous method for the deposition of metallic coatings for various applications such as energy conversion and energy storage devices, anticorrosive coatings, etc. It is also known as electroplating/galvanization.

2.2.2.1 Fundamentals of ED method

In the ED process, generally, a direct current is passed through a solution containing metal ions, causing metal atoms to be deposited onto a conductive surface. The current is supplied from an external power source. **Fig. 2.3** illustrates the

schematic of the electrodeposition cell. The typical electrodeposition setup consists of the following key components;

1) Working electrode (WE) (Cathode) = SS substrate (1x5 cm^2)

2) Auxiliary electrode (Counter electrode (CE)) (Anode) = platinum (Pt) sheet or graphite sheet (1x5 cm^2)

3) Reference electrode (RE) = Saturated calomel electrode (SCE)

4) Electrolyte (Precursor salt solution)

5) Electrochemical workstation
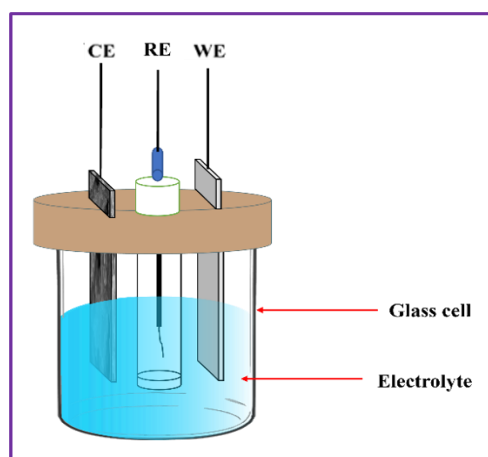
Fig. 2.3 The schematic of the electrodeposition cell.

When a direct current flows between the anode and cathode, positively charged metal ions are drawn to the cathode, where they deposit and neutralize the cathode electrically. The metal deposition on the cathode from the electrolyte with metal ions occurs through to the given reaction,

$$M^{n+} + ne^- \rightarrow M \tag{2.1}$$

Here,

M^{n+} = metal ions, e^- = electron, and n = number of charges.

Conversely, when the electrolyte contains multiple cationic species, the cations are deposited on the cathode simultaneously. For two distinct cationic species, the reactions in the electrodeposition process can be expressed as follows,

$$P^+ + e^- \rightarrow P \tag{2.2}$$

$$Q^+ + e^- \rightarrow Q \tag{2.3}$$

Or $\qquad P^+ + Q^+ + 2\,e^- \rightarrow PQ \tag{2.4}$
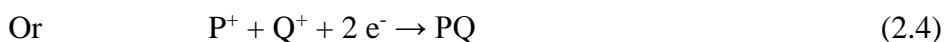
Here,

Q^+ is another metal ion.

2.2.2.2 Various modes of electrodeposition

Following are the various modes of electrodepositioin used for the thin film deposition,

1) Potentiostatic (constant potential)

2) Galvanostatic (constant current)

3) Potentiodynamic (Potential and current varies with time)

1) Potentiostatic (constant potential)

In this mode, constant direct current (DC) voltage is used for the deposition. Various charge transfer reactions were carried out in this manner at constant overpotential under steady state conditions and exchange current density. The different deposition factors like substrate nature, bath composition, and reversible potential of deposited species effects on the selection of deposition overpotential. Also, an appropriate value of deposition overpotential can be determined by taking into account standard electrode potential (reference electrode). The factors like substrate depositant interactions, hydrogen evolution overpotential, bath polarization, and interactions between compounds in compound electrodeposition were affects on the deposition potential. Significant features of potentiostatic electrodeposition are:

i) In this method working electrode potential is controlled with respect to reference electrode.

ii) To develop required potential across the working electrode, the potential is driven through counter electrode.

iii) The cell current changes over time in line with the output waveform.

2) Galvanostatic (constant current)

In this mode, the current between the working and counter electrodes is maintained at a constant level during the deposition process to ensure uniform deposition. The deposition rate is directly proportional to the respective current densities. Some important points are as follows;

i) At a specific current density, the current flowing between the CE and WE must be sufficient to move the electrolyte ions.

ii) The necessary cell current is produced by the applied potential delivered via the counter electrode.

iii) The reference electrode does not control the current; it is solely used to monitor the potential within the electrochemical cell.

iv) The cell potential changes over time in line with the output waveform.

3) Potentiodynamic (Potential and current varies with time)

In this mode, electrolysis current is recorded based on the applied potential. This can be done using cyclic voltammetry (CV) or linear sweep voltammetry (LSV). CV is commonly employed to investigate electrochemical processes during electrolysis, such as charge transfer and electrode kinetics, while also providing qualitative insights into electrochemical reactions. Cyclic voltammetry can be used to determine the redox potential values of electroactive species in a solution, illustrating electrochemical hysteresis. This method allows for the preparation of new materials on a substrate through the redox reactions of these species. Metal oxides can be deposited in a single step using this technique. The process involves first reducing metal ions at the reduction potential, then oxidizing them at the oxidation potential, resulting in a film on the metal substrate. The desired thickness can be achieved by repeating the deposition cycles. Some key features are listed below,

i) It records the current during a triangular potential sweep, enabling the observation of both anodic and cathodic responses.

ii) The output waveform, featuring forward and reverse peaks (redox peaks), provides information about the electroactivity of the solution and electrode **[11]**.

2.2.2.3 Deposition parameters

The properties of the material structural, optical, and morphological are directly affected by the preparation parameters of the electrodeposits. By managing factors such as substrate type, applied electric field, bath temperature, complexing agents, and bath pH, a smooth, uniform, and stoichiometric film can be produced. Some parameters are explored in the following discussion;

1) Substrate

In electrodeposition, the substrate is essential as it provides support for the electrodeposit and affects the material's morphology during its growth. Additionally, it alters the materials optical and electronic properties.

The following substrate criteria are essential for ensuring uniform electrodeposition.

i) The substrate should possess high conductivity.

ii) Its thermal expansion coefficient needs to align with that of the electrodeposit.

iii) It should exhibit strong mechanical strength.

iv) It must remain stable in the precursor solution.

Metal substrates are commonly used for electrodeposition because they offer high conductivity, low cost, and are readily available and easy to handle.

2) Bath temperature

Increasing the temperature of the electrodeposition bath enhances ionic mobility and diffusion rates. A higher bath temperature raises the current density and nucleation rate, leading to the formation of smooth and fine grained particles in the thin film. Additionally, elevated temperatures can reduce the precipitation of salts and gas evolution potential. Therefore, determining the optimal bath temperature is challenging and must be optimized through experimental testing.

3) Current density/Overpotential

Deposition rate is affected by current density or overpotential. Low values lead to slow ion discharge, a lower growth rate, and a dense structure. High values increase nucleation, resulting in finer grains and perpendicular deposition. Extremely high values can cause rapid hydrogen evolution, making the material porous and spongy, and may lead to salt precipitation. Therefore, current density or overpotential is crucial in determining the thickness and structure of the deposited material.

4) Complexing agent

Positively charged complex ions form when unstable metal ions combine with neutral molecules. These complex compounds ensure a steady ion supply and maintain high metal complex concentrations with low metal ion levels. This promotes smaller grain growth and minimizes precipitate formation.

5) pH of solution

Maintaining the pH of the electrodeposition bath is crucial for optimal efficiency and desired material properties. High pH can cause hydroxide ion formation and salt precipitation, altering the deposit. Low pH, on the other hand, necessitates higher current density for effective deposition.

2.2.2.4 Advantages of ED method

❖ A range of structures, alloys, and compounds with tailored compositions can be deposited, which is difficult to achieve with other deposition techniques.

❖ The morphology and thickness of thin films can be accurately regulated by modifying electrochemical parameters like potential and current.

❖ Uniform deposition is achievable on substrates with complex shapes.

❖ Unlike gas phase methods, there is no need for toxic gas precursors.

❖ The deposition reactions occur closer to equilibrium compared to gas phase methods, allowing for more precise control.

❖ The low temperature deposition process minimizes issues like contamination, dopant redistribution, and interdiffusion, leading to energy savings **[12-15]**.

Section B

The electrochemical characteristics of materials are closely linked to physicochemical properties such as chemical composition, crystal structure, surface morphology, specific surface area, and conductivity. So, the characterization and analysis of thin film materials by various characterisation techniques used to explain the relationship between different properties. These assistances to choose proper thin film material for its various applications. These techniques facilitate the detection of changes in thin film materials. Consequently, the thin films in this study were analysed using a range of characterization methods. The brief elaboration of the basics, instrumentation, and working of these techniques is described in this chapter.

2.3 Thin film characterization techniques

2.3.1 Thickness measurement

The optimized thickness of the thin film is more essential in the research field. The film thickness significantly affects the band gap, electrical conductivity, conversion efficiency in solar cell applications, as well as the physical and optical properties of the material.

The gravimetric, direct, and optical methods are some of the techniques used to measure film thickness. Out of these techniques, gravimetric method is a straightforward and simple method for film thickness calculation by use of the following formula **[16]**,

$$T = \frac{M-m}{A.\rho} \qquad (2.5)$$

Here,

T = Thickness of the film, M = Weight of the substrate after deposition, m = Weight of the substrate before deposition, A = Area of the film in cm^2, ρ = Density of the bulk material. The bulk materials value is often used as a reference since the bulk density of thin films is usually lower.

Advantages:

❖ It is very simple and cost-effective technique.

❖ It is a non-destructive characterisation technique.

❖ It is a less time-consuming technique.

Disadvantages:

❖ The estimated value of the thickness can be found.

2.3.2 X-ray diffraction (XRD)

In the material science field, the analysis of crystal structure and phase confirmation of prepared materials is a prime requirement which is carried out by X-ray diffraction (XRD) technique.

XRD relies on the constructive interference of monochromatic X-rays as they interact with the sample. Since interatomic distances in materials are on the order of a few angstroms (Å), which match the wavelength of X-rays (3-8 keV), this interaction reveals the crystalline structure. Both constructive and destructive interference patterns can be seen, and by measuring the intensity of diffracted X-rays at different scattering angles, a diffraction pattern is generated.

Working of X-ray

The three main components of X- ray diffractometer are X-ray source, sample holder, and X-ray detector. X-rays are produced using cathode ray tube, which includes a cathode, monochromator, and target material, all housed in a glass or ceramic vacuum-sealed container. Electrons are generated after heating a cathode (tungsten filament) by the application of high voltage generated electrons are highly accelerated towards target material (Cu, Fe, Mo, Cr). When electrons possess sufficient energy to remove inner shell electrons from the target element, outer electrons shift to the inner shells to fill the resulting vacancies. This process releases radiation to balance the energy difference, which is characteristic of the target material. For copper targets, Kα and Kβ radiation lines are emitted and filtered to produce monochromatic X-rays with a wavelength of CuKα = 1.5406 Å. These X-rays are collimated and aimed at the specimen. As the specimen and detector rotate, intensity peaks are recorded when Braggs condition is satisfied. The detector converts these signals into a count rate and transmits the data to a computer for analysis.

There are three methods to identify the crystal structure of a sample: 1) the Laue method, 2) the rotating crystal method, and 3) the powder method. The Laue method is the oldest technique for determining crystal structures, using a continuous X-ray spectrum with a fixed angle of incidence (θ). This method provides faster diffraction compared to those using monochromatic X-rays and it is useful for

observing dynamic processes in crystal structures. If the angle of incidence (θ) remains constant while the wavelength (d) varies, the technique is referred to as the rotating crystal method.

Fig. 2.4 Photograph of Rigaku Mini Flex 600 diffractometer [17].

In the rotating crystal method, a monochromatic hard X-ray beam is pointed at a sample that rotates at a constant angular speed. The powder method is often used for a more straightforward analysis of crystal structures.

In this method, the wavelength (λ) is kept constant while the angle of incidence (θ) is varied.

The crystallite size of materials was determined by using the Scherrer formula:

$$D = \frac{0.9\lambda}{\beta \cos\theta} \qquad (2.6)$$

Here,

β = diffraction peak FWHM, and θ = Peak position (radian).

Fig. 2.4 shows the photograph of Rigaku Mini Flex 600 X-ray diffractometer **[17]**. XRD technique is very important for the identification of unknown substances. The diffraction data from the material is compared with reference data from the JCPDS or ASTM. This analysis yields insights into the structure, phase, preferred crystal orientation, and various structural parameters, including lattice parameters, crystallite size, strain, and crystal defects.

Advantages

❖ Most convenient and least expensive technique for determination of the crystal structure.

❖ It is best technique for phase analysis and not need of an evacuated sample chamber because negligible absorbance of X-rays by air.

Disadvantages

❖ X-rays have minimal interaction with lighter elements.

❖ This approach is ineffective for analysing chemical composition.

❖ The XRD technique does not offer insights into the nature of chemical bonding **[18, 19]**.

The current study uses the powder XRD technique to examine the crystal structure, lattice dimensions, and crystallite size of nanoparticles.

2.3.3 Field emission-scanning electron microscopy (FE-SEM)

To study the surface structure (morphology) of material high resolution FE-SEM is used. For the imaging process, electrons are used rather than photons which released by a field emission source. The FE-SEM offers topographical and elemental information with magnifications of up to 3,00,000 times. By using a high energy electron beam, raster scanning of a sample surface is performed to capture its image.

The concentrated primary beam of electrons strikes to the sample surface and after interaction releases its energy inside the sample results in ejection of various types of electrons as illustrated in **Fig. 2.5**. This emission of the secondary electrons from the sample contains surface topography and composition of the sample. Further detector generates an electrical signal from secondary electrons and transforms it into an image after amplification **[20, 21]**.
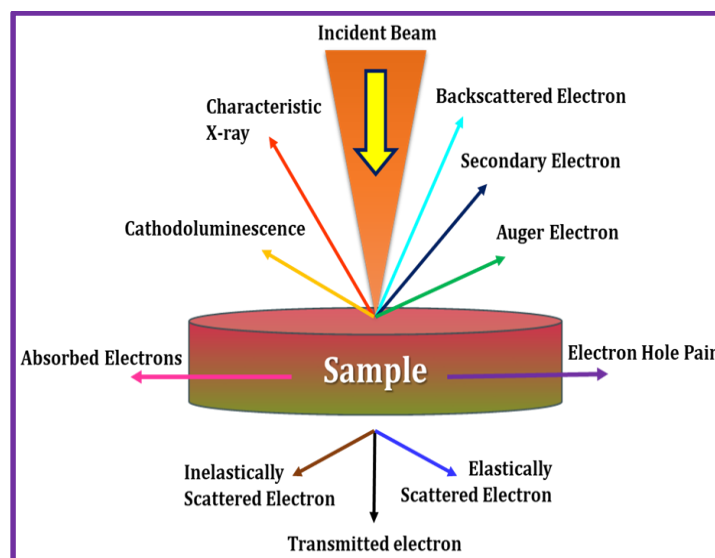
Fig. 2.5 Ray diagram depicting the emission of various types of electrons during the scanning process [22].

Working of the instrument

The main parts of FE-SEM instrument like electron source, magnetic lenses, accelerator (anode), sample holder and detector are mounted on a same desk shown in **Fig. 2.6**. High-energy electrons, known as primary electrons, are produced by heating a thin cathode (made of tungsten) and are then accelerated toward the sample by applying a high voltage difference between the anode and cathode. Electromagnetic lenses concentrate the electron beam into a small, precise spot. The sample is coated with a thin layer of a conductive metal (e.g. gold, platinum, or silver) and placed on a holder, then inserted into the microscopes vacuum chamber via a sample exchange system.
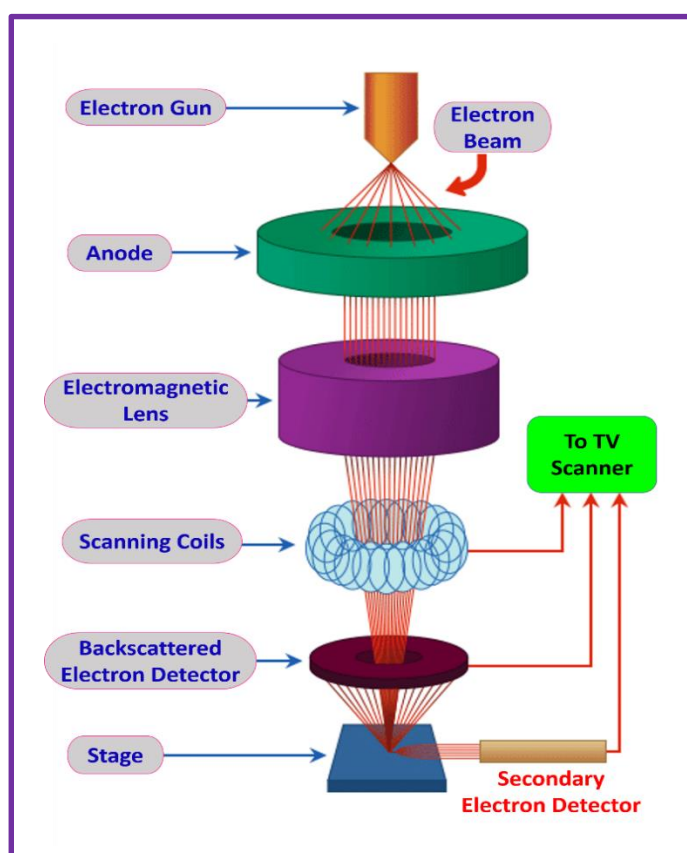
Fig. 2.6 The schematic representation of the FE-SEM instrument [23].

When the focused electron beam strikes the sample, it penetrates a few microns and interacts in several ways, resulting in the emission of electrons. The sample image is then produced by transforming and amplifying signals from secondary and backscattered electrons. When primary electrons eject inner shell electrons, higher energy electrons fall to lower levels, emitting X-rays. These characteristic X-rays from each element utilized to analyze the samples elemental composition with EDAX on an FE-SEM instrument **[24, 25].**

Advantages

- ❖ Larger depths of field can be studied.
- ❖ Samples just require a few simple preparatory procedures.
- ❖ Data is produced in digital form.

Disadvantages

- ❖ It works with only solid samples.
- ❖ It is sensitive to magnetic fields.

In the current work, the surface morphology, thickness, and porosity of the nanocomposite are examined using the FE-SEM method. This method is also employed to determine the chemical make up of nanocomposite materials.

2.3.4 Brunauer-Emmette-Teller (BET)

This approach is mostly used to find available surface area and pore volume for a given material. This is accomplished by applying relative pressure of N_2 gas to the material's surface. After some time, the gas is extracted and the difference between the amounts of gas supplied within and returned is calculated **[26]**. The surface area of the sample of interest is given by the result in $m^2 g^{-1}$.

For surface area measurements, there are two different working principles: volumetric and gravimetric. In both techniques, the sample is first placed within the chamber, heated to the necessary temperature, and then N_2 gas is injected into it at varied relative pressures. For volumetric approach, change in relative pressure is measured in relation to the reading obtained without the addition of material to the chamber. The quantity of N_2 adsorbed onto the surface and the difference between the amount of N_2 supplied inside and recovered are measured in the gravimetric technique, and the surface area and pore volume are calculated based on the results **[27]**. An isotherm is a graph showing the relationship between the amount of adsorbed material and the adsorptive pressure. Pressure is expressed as the ratio of adsorptive pressure (P) to the saturated vapor pressure (P_0). Volumetric measurement is commonly used since it is less expensive and has a simple process. However, the volumetric analysis dubious conclusions limit its widespread application. Gravimetric analysis is far more exact and accurate in this setting. There are five distinct isotherms based on the interaction of adsorbent with adsorbate. The many isotherms and their importance are listed below. (**Fig. 2.7 (a)**) depicts five types of adsorption isotherms in BET analysis.

1. Type I isotherm - chemisorption or physisorption on a substance with very tiny pores microporous materials having pore diameter less than 2 nm.

2. Type II isotherm- if adsorption energy is large in nonporous or microporous materials.

3. Type III isotherm- if adsorption energy is low in nonporous or microporous materials.

4. Type IV isotherm- if the energy of adsorption in mesoporous materials is large.

5. Type V isotherm- if the energy of adsorption in mesoporous materials is low.

The concept of desorption is bit different from adsorption and is called as hysteresis. As per International Union of Pure and Applied Chemistry (IUPAC) system, 4 distinct hysteresis curves are present (**Fig. 2.7 b**). The 4 hysteresis loops are termed as H1, H2, H3, and H4 analysis [28, 29].

To evaluate specific surface area (A_s) from cross sectional area of adsorbate molecule (a) and number of moles of adsorbate in a monolayer (n_m),

$$A_s = n_m N_A a \tag{2.7}$$

Here, $a = \left(\frac{M}{\rho}\right)^{\frac{2}{3}} N_A^{1/3}$, M = molar mass (g mol^{-1}), ρ = liquid density (gm^{-3}), and N_A = Avogadro's number (6.022×10^{-23} mol^{-1}).

Working of instrument

The volumetric and gravimetric approaches are the two ways to determine a material surface area. The assumption that N_2 adsorbs on the substance surface underlies the instruments normal operation. After being converted into the material specific surface area and pore size distribution, the amount of gas that has been adsorbed is computed as a function of temperature and pressure. The volumetric technique design is shown in **Fig. 2.8**. The system has non-scaled components. Sample chamber construction usually involves the use of Pyrex [28].
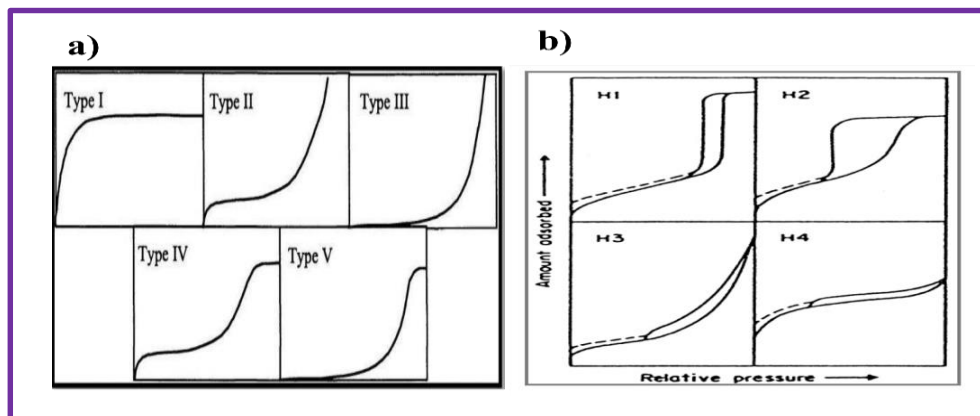
Fig. 2.7 a) Five types of adsorption isotherms, and b) The four hysteresis loops in BET [28].

The BJH method is employed to assess pore size and volume using the same technique.
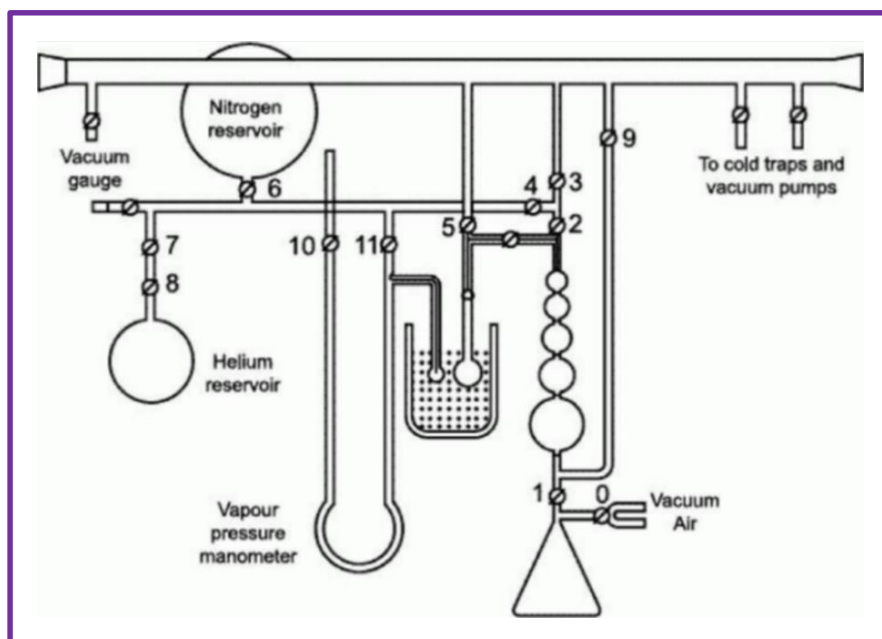
Fig. 2.8 Schematic illustration of the dynamic flow method apparatus [28].

Advantages

This method enables the identification of the type, size, and shape of porosity in the material, allowing for porosity measurements ranging from 0.4 to 50 nm.

Disadvantages

❖ This methodology is not appropriate for powder samples with micrometric particle sizes, has large measurement errors, takes a long time, and is insufficient to assess low level surfaces.

In this study, the BET technique is utilized to evaluate the specific surface areas and pore structure of nanocomposites **[30]**.

2.3.5 Wettability study

The wettability plays an important role in electrochemical applications. The wettability of the materials and the thin film samples are measured by using the oil or electrolyte or the water contact angle measurements. The contact angle is the angle created between the liquid-solid interface and the tangent line to the liquid droplet at the point where the liquid, solid, and air converge **[31]**. **Fig. 2.9 (a)** depicts the photograph of the Rame Hart contact angle measurement instrument, and **Fig. 2.9 (b)** the contact angle measurement of an unknown sample.
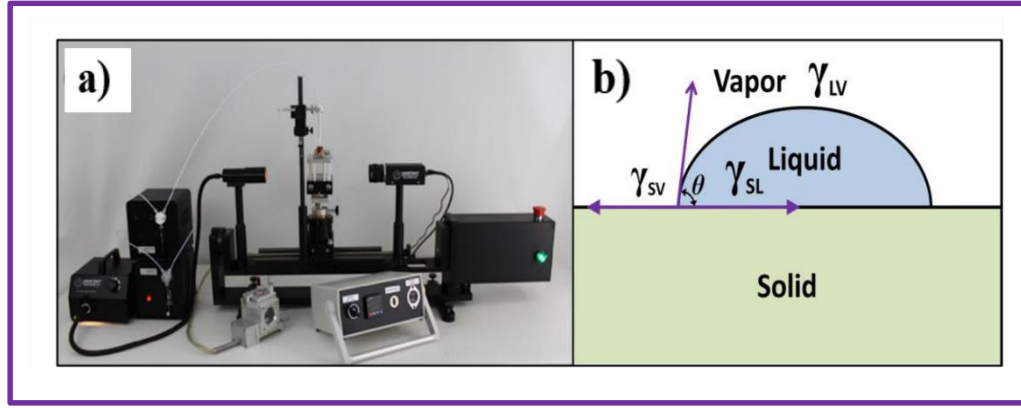
Fig. 2.9 a) The Rame Hart contact angle measurement instrument [32], b) the contact angle measurement of an unknown sample [33].

The contact angle of the unknown samples is measured by adopting the following steps;

i) Droplet placement: A droplet of the liquid under study is placed on a solid substrate. The droplet is carefully placed using a syringe, micropipette, or automated dispensing system.

ii) Image capturing: A high resolution camera captures an image of the droplet substrate interface. This image serves as the basis for contact angle measurement.

iii) Data analysis: The captured image is processed and analyzed by specialized software. The software detects the boundaries of the droplet and the solid substrate, along with the contact line where they meet.

iv) Contact angle calculations: Using image analysis algorithms, the software determines the shape of the droplet and calculates the contact angle formed at the contact line.

v) Contact angle measurements: The calculated contact angle values are provided as output, indicating the w etting behavior of the liquid on the solid surface. This is useful for various applications such as understanding surface properties, evaluating surface treatments, or studying surface interactions.

The contact angle (θ) is calculated by Youngs relation **[33]**.

$$\gamma_{s,v} = \gamma_{s,l} + \gamma_{l,v} \cos \theta \qquad (2.8)$$

Where, $\gamma_{s,v}$ = solid-vapour, $\gamma_{s,l}$ = solid-liquid and $\gamma_{l,v}$ = liquid-vapour interfacial energies.

The smaller contact angle (θ < 90 º) value denotes a hydrophilic surface whereas a higher contact angle (θ > 90 º) demonstrates hydrophobic nature.

Superhydrophilic implies an extreme wetting properties of surfaces. Low contact angle (≥ 0 º) refers the superhydrophilic surfaces. superhydrophobic implies extreme water repellent properties of high contact angle (≤ 150 °) **[34]**. The nature of the surface is decided from the value of the contact angle shown in **Fig. 2.10**.
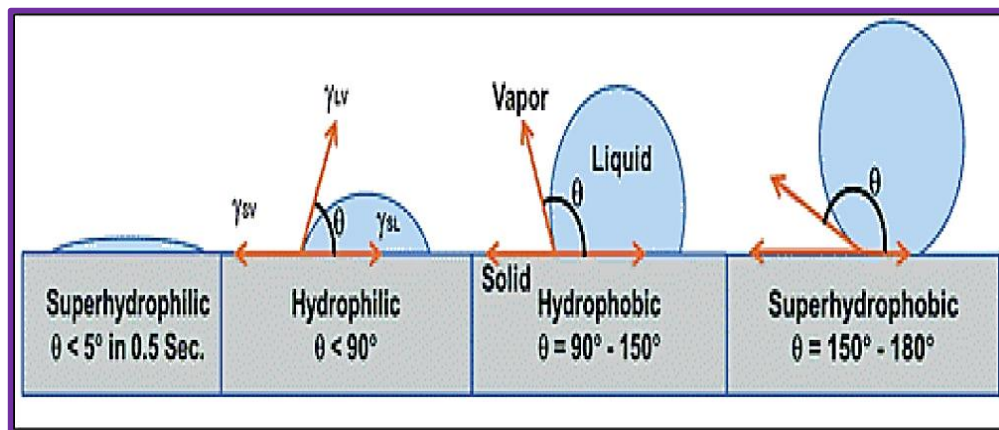
Fig. 2.10 Contact angle and nature of sample surface [34].

Advantages

❖ It is an inexpensive technique.

❖ The testing is easy and less time consuming.

❖ It provides information related to surface energies.

Disadvantages

❖ This technique is an environmental sensitive (factors such as humidity, temperature, and atmospheric pressure can influence measurement accuracy.

❖ Measurement accuracy may vary based on the operator skill and experience.

2.3.6 Ultra violet-visible spectroscopy

Ultraviolet-visible spectrophotometry refers to absorption spectroscopy in the ultraviolet-visible spectral region. This means it uses light in the visible and adjacent (near-UV and near-infrared (NIR)) ranges. The absorption in the visible range directly affects the perceived color of the chemicals involved.

In this part of the electromagnetic spectrum, molecules experience electronic transitions. This technique complements fluorescence spectroscopy, where fluorescence involves transitions from the excited state to the ground state, while absorption focuses on transitions from the ground state to the excited state **[35, 36]**.

Working of instrument

The design of the UV-Vis spectrophotometer includes both the parts of the spectrometer and photometer.

The schematic diagram depicted in the **Fig. 2.11** shows the major constituents of spectrophotometer instrument.

The valence band of an ideal semiconductor would be fully occupied with electrons at absolute zero temperature, preventing any electrons from being stimulated to a higher energy state from the valence band. A quanta absorption of adequate energy tends to move electrons from the valence band into the conduction band. The excitation of electrons from the valence band to the conduction band (which may also involve acceptor or donor impurity levels, traps, excitons, etc.) is responsible for the sharp rise in the optical absorption spectra of semiconductors that is typically observed at a specific value of the incident photon energy. Throughout the optical absorption process, the conservation of momentum and energy must be met.

At the fundamental edge of a crystalline semiconductor, two types of optical transitions can occur: direct and indirect. Both involve an electromagnetic wave interacting with an electron in the valence band, moving it across the energy gap to the conduction band. In the case of an indirect transition, this process also involves interaction with lattice vibrations. In an optical transition, the electron's wave vector can change, with the momentum being absorbed or released by a phonon. **Fig. 2.12 (a and b)** shows a diagram of direct and indirect transitions.
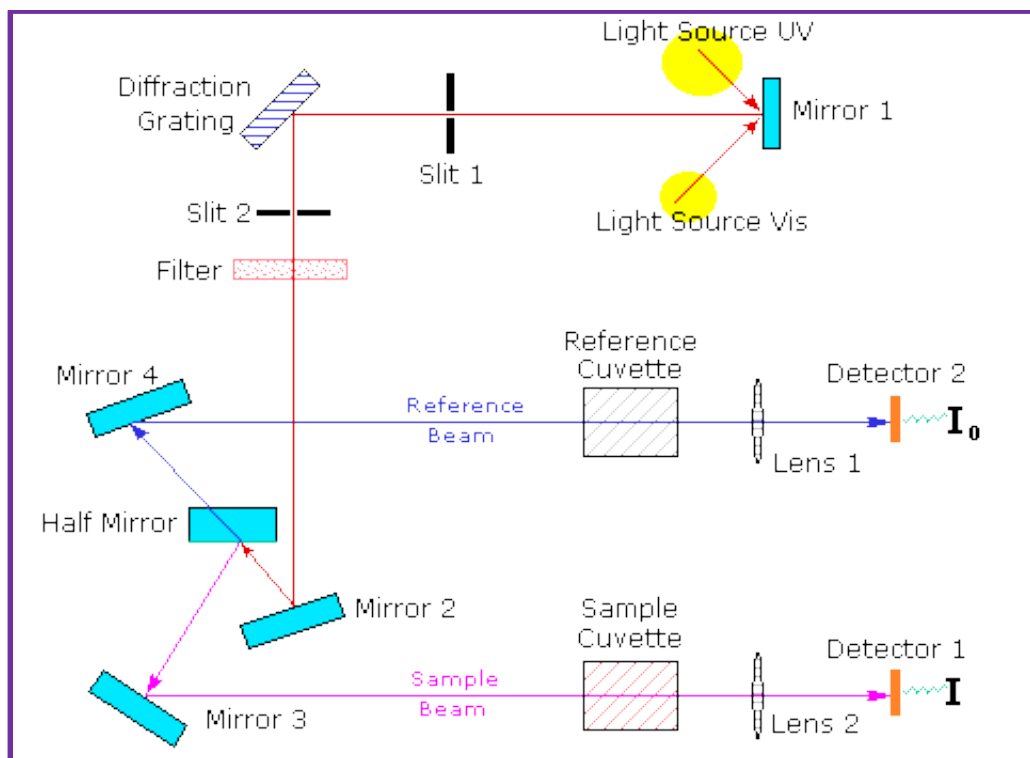
Fig. 2.11 Schematic diagram of an UV-visible spectrophotometer [37].

A direct interband optical transition involves electrons moving vertically from the valence band to the conduction band without any change in momentum, while conserving energy. The optical transition is represented by a vertical upward arrow. The shape of the absorption coefficient 'α' as a function of photon energy (hυ) depends on the energy of the initial and final state bands. For direct transitions and simple parabolic bands, this relationship applies.

$$\alpha = \frac{A(h\gamma - E_g)^n}{h\gamma} \qquad (2.9)$$

where, *A* is a constant depending upon the transition probability for direct transition, *n* = 1/2 or 3/2 depending on whether the transition is allowed or forbidden in the quantum mechanical sense, *Eg* is the optical gap.

Let's see a condition given in **Fig. 2.12 (b)** where interband transition takes place between different k-states. Since these must satisfy the momentum conservation laws, the only way such transition can take place is through the emission or absorption of a phonon with wave vector q i.e.

$$k' \pm q = k + K \qquad (2.10)$$

For indirect transitions,

$$\alpha = \frac{A(h\gamma - E_g)^n}{h\gamma} \qquad (2.11)$$

For allowed transitions, n = 2, and for forbidden transitions, n = 3. The band gap energy *Eg* is estimated by extending the linear portion of the plot of $(\alpha h\gamma)^n$ versus hγ to where it meets the energy axis at α = 0. When discussing the optical absorption edges in amorphous semiconductors, the following assumptions are made: (a) the matrix elements for electronic transitions remain constant across the relevant photon energy range, and (b) the K-conservation selection rule is relaxed. This is because, near the band edges, $\Delta k \sim k$, k is not a well-defined quantum number in amorphous semiconductors. In an E-k diagram, these transitions are non-vertical, but no phonon absorption or emission is needed to conserve momentum. All the required energy comes from the incident photons, making these transitions non-direct, unlike indirect ones. For many amorphous materials, with parabolic band assumptions, the absorption is often observed with n = 2. As a result, the absorption edge in many amorphous semiconductors follows a simple power law over a certain range of absorption coefficients, allowing an optical gap '*Eg*' to be defined **[38, 39]**.
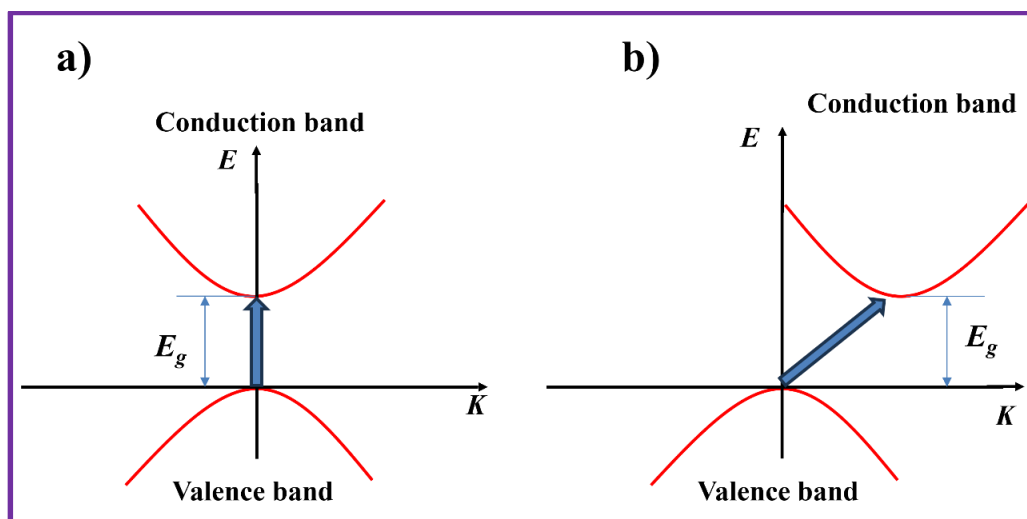
Fig. 2.12 a) Direct and b) indirect band gap transitions.

Advantages

- ❖ The technique is non-destructive.
- ❖ The technique is fairly simple and can be used easily.
- ❖ Measurement can be done in a short span of time, helping easy integration into experiments.
- ❖ Data analysis is simple and requires less processing.
- ❖ Instrumentation is relatively inexpensive and can be procured easily by laboratories.

Disadvantages

- ❖ A sample containing multiple absorbing species cannot be used to determine concentration using absorbance.
- ❖ Improper orientation of the sample holder or misalignment can imbibe errors in the measurement.

In the present study, UV-Vis spectroscopy measurements of the powder samples at room temperature were carried out on a JASCO (Model V-670) UV-Vis spectrophotometer.

2.3.7 Linear sweep voltammetry (LSV)

Linear sweep voltammetry is a technique where current at the working electrode is measured while the potential between the working electrode and a reference electrode is swept linearly in time. The LSV potential is ramped from one potential (V1) to another potential (V2) in a linear way (V1→V2) as shown in **Fig. 2.13 (a).** Hence, LSV is the forward scan of CV (**Fig. 2.13 (b)**) **[40]**.
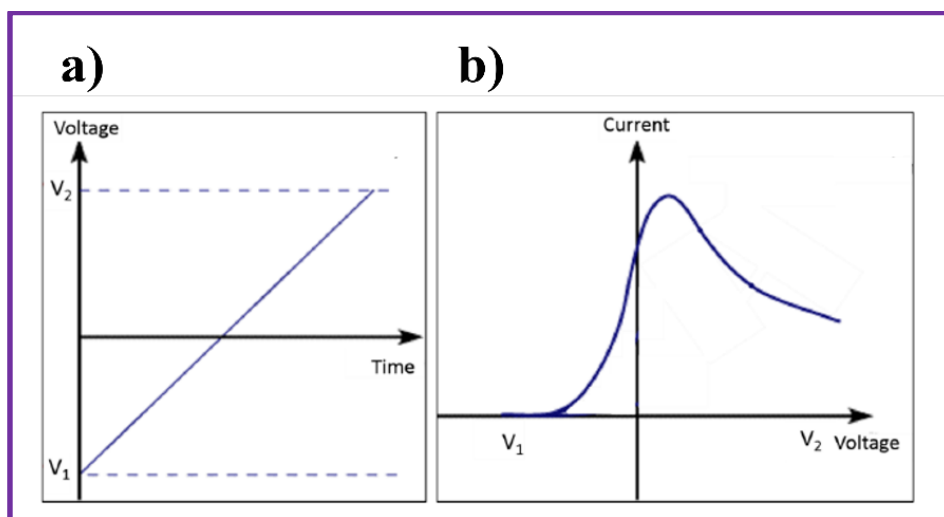
Fig. 2.13 a) Potential sweep between V_1 and V_2 with time in LSV and b) corresponding current response as a function of voltage [41].

In this work PEC and sensing properties are studied using LSV to carry out the I-V characteristics in a fixed potential window.

2.3.8 Electrochemical impedance spectroscopy (EIS)

The EIS is an effective and well-known technique for evaluating electrochemical system parameters. An extensive diversity of physical and chemical approaches was determined to investigate the electrical features of semiconductor electrodes in contact with a liquid electrolyte. Amongst, the EIS is a valued experimental technique since it delivers information about charge transfer occurrences, double layer features, carrier generation and recombination issues. The explanation of the EIS results needs the usage of appropriate models. The usage of equivalent electrical circuits to fit the EIS data is consequently foreseen as an efficient instrument to detect and infer the charge transfer phenomena happening in the PEC cell under characteristic operating circumstances.

A typical curve used to analyze electrochemical impedance is the 'Nyquist' curve shown in **Fig. 2.14**. It is also called the Cole-Cole plot or the complex impedance plane plot. It has several advantages. The biggest advantage is the structure of the plot, which makes it easy to understand the consequences of ohmic resistance. One can simply extend the semicircle toward the lower left corner of the x-axis to read the ohmic resistance if data with sufficiently high frequencies are used. Even though the ohmic resistance varies, the curves form, which is frequently a semicircle, remains unchanged **[42]**.
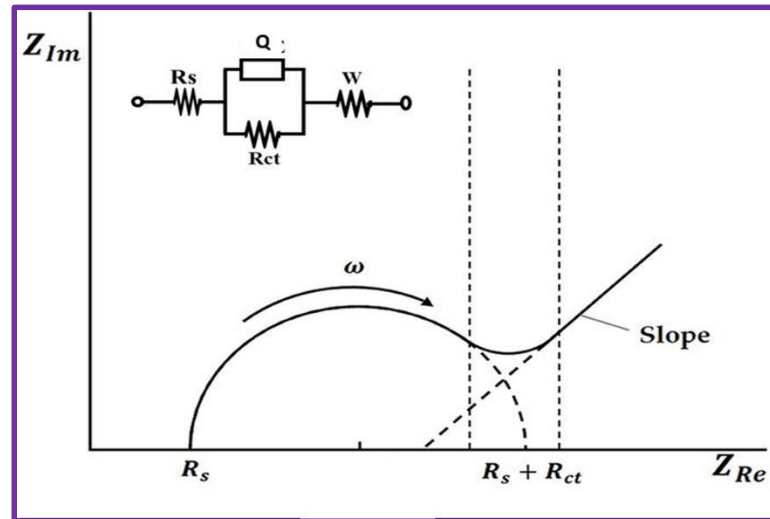
Fig. 2.14 Typical Nyquist plot with inset showing equivalent circuit [43].

The simulation of electrochemical processes at the electrode-electrolyte interface are given by equivalent electrical circuits consisting components like resistors and capacitors **[44]**. **Table 2.1** shows the components of equivalent circuits with the equations describing their I-V relations.

EIS Parameters

1) Solution resistance (R_s)

The impedance of an electrochemical cell depends primarily on the solution resistance. In fabrication of a typical three electrode electrochemical cell, the solution resistance between the counter electrode and the reference electrode and between the working electrode and the reference electrode must be considered. The temperature, the spatial geometry in which the current flows, the type of ions present, and the ion concentration all affect the resistance of an ionic solution. The contact resistance also contributes to the solution resistance.

Table: 2.1: Common electrical circuit elements used in EIS.

Component	Current Vs. Voltage	Impedance
Resistor	$E = IR$	$Z = R$
Inductor	$E = L\dfrac{di}{dt}$	$Z = j\omega L$
Capacitor	$I = C\dfrac{dE}{dt}$	$Z = \dfrac{1}{j\omega C}$

Unfortunately, the current distribution in most electrochemical devices is not constant over the specific electrolyte range. This means that calculating solution resistance from solution conductivity is less accurate. From the EIS spectrum, the solution resistance can be estimated.

2) Charge transfer resistance (R_{ct})

R_{ct} originates from electrochemical reactions of a single, kinetically controlled. It depends on reaction type, temperature, concentration, and applied potential. It measures the resistance during the charge transfer process.

3) Electrochemical active surface area (ECSA)

ECSA has the ability to affect an electrode's impedance properties. The impedance may be impacted by the active surface area, which also influences the electrodes' capacity to support electrochemical reactions. Because there are more active sites accessible for reaction, an increase in ECSA may result in a decrease in charge transfer resistance in systems where catalytic processes take place on the electrode surface. The kinetics of charge transport at the electrode-electrolyte interface can be investigated using EIS, and variations in ECSA can be seen in the impedance spectra.

4) Contribution from capacitive and electrostatic contribution

Within the framework of EIS, the capacitive contribution is frequently separated into two primary parts: a) the Warburg impedance (associated with diffusion processes) and b) the double layer capacitance (capacitive contribution resulting from charge buildup at the electrode electrolyte interface).

a) Double layer capacitance/leakage capacitance (Cdl/Q)

Electrode and the electrolyte interface, it forms an electrical double layer. A double layer is created at the interface as ions from the solution mix with the electrode surface. There is an insulating area an order of Angstrom broad between the charged electrode and the charged ions. Since a capacitor is formed by the separation of charges through an insulator, bare metal immersed in an electrolyte behaves in the similar manner. The value of the double layer capacitance depends on many factors such as electrode potential, temperature, ionic concentration, ion type, oxide layers, electrode roughness, impurity adsorption, etc. In the Nyquist plot of EIS, the

capacitive behavior is often observed as a semicircle at high frequencies, and the diameter of this semicircle is related to the double layer capacitance.

b) Warburg (diffusion) resistance (W)

The Warburg impedance is associated with mass transport limitations, particularly the diffusion of ions in the electrolyte to and from the electrode interface. In EIS, the Warburg impedance is typically observed as a sloping line at lower frequencies in the Nyquist plot. The slope of this line is related to the diffusion characteristics of the electroactive species. The Warburg impedance is minimal at higher frequencies because diffusing electrolyte ions in solution don't have to go very far. The Warburg impedance rises at lower frequencies because the ions diffuse more widely **[45].**

In the current study, EIS was carried out in the dark and the under light conditions for electrochemical resistance understanding of PEC cell. The electrical equivalent circuit was fitted by using the Zview and or Zman software. The generation and recombination of the charge carriers can be understood by comparing the EIS parameters in both conditions.

2.4 Photoelectrochemical (PEC) solar cell

Generally, the PEC effect occurs when a photoelectrode is exposed to light, and it creates voltage between the photoelectrode and counter electrode in the PEC cell. It is used to transform light energy into electrical energy. One may determine the PEC cell fill factor (FF), power conversion efficiency (η), and semiconductor type by the polarity of the voltage that is generated in the cell when it is illuminated. The PEC cell and its components are discussed in the **section 1.2 of chapter I**.

The band bending of the semiconductor photoelectrode takes place when both electrodes are submerged in the electrolyte. The brief description of the band bending for p and n type semiconductors given in **chapter I section 1.2.2.1.** Only the energy zone of the conduction band may be used for the transfer of electrons to or from the electrolyte, whereas the valance band region can be used for the transmission of holes. Such a transfer may take place between two identical energy levels, one empty and the other full. When the semiconductor photoelectrode electrolyte interface is illuminated, electron-hole pairs are formed in the depletion layer and separated by the electric field at the interface **[46].**

The separated electrons transfer to the top of the conduction band, while the separated holes go into the valence band. A counter field was created by this approach for open circuit conductions. Open circuit voltage (V_{oc}) is checked with a voltmeter across the output terminals of the solar panel module, without connecting any load. This parameter is used to check/test the module during installation and later for system design. The short- circuit current (I_{sc}) is the highest current that the solar panel cell can deliver without any damage. I_{sc} is used to determine how many amps a panel can handle when connected to a device like a solar charge controller or an inverter circuit.

The electrons promoted to the conduction band drift towards the interior, while the holes, the minority carriers, come to the surface of the semiconductor. Here they encounter the reduced form of the redox couple in the solution. The component is oxidized by the holes, transported to the counter electrode and therefore gets reduced. This reduction is driven by the external connection from the semiconductor **[47]**. The fill factor (FF) and conversion efficiency (η) were calculated using following formulae:

$$FF = \frac{I_m V_m}{I_{sc} V_{oc}} \text{ , and} \tag{2.12}$$

$$\eta \% = \frac{I_{sc} V_{oc} \, FF}{P_{in}} \times 100 \tag{2.13}$$

Here, I_m = Maximum current, V_m = Maximum Voltage, I_{sc} = Short circuit current, V_{oc} = Open-circuit voltage, P_{in} = Input power.

The laboratory made setup was used to study the current voltage (I-V)/power output characteristics of the photoelectrodes in 1 M polysulfide electrolyte with three electrode cell with SCE as a reference and graphite as a counter electrode. 35 W xenon lamp was used as light source of illumination intensity 25 mW cm^{-1}. The distance between lamp and PEC cell was maintained at 100 cm.

2.5 Gas sensor

The gas sensor and its types are discussed in **section 1.3 in chapter I.** For the gas response measurement, there are primarily two methods:

1) Flow through method

Gas flow meters are used to continuously measure the response curve as a known volume of analyte gas flows. By combining analyte gas with a carrier gas, most frequently nitrogen, concentration may be adjusted. This method has the advantage of it generate a repeating gas reaction in response to variations in gas concentration.

2) Static environment method

The sensor element is contained within a chamber of known volume. To ascertain the sensor resistance at the specified analyte gas concentration, a syringe is utilized to inject a known amount of gas with a known concentration into the test chamber. The sensor resistance is measured over time until a steady state is reached. The sensor is exposed to air after the gas has been taken out of the chamber to assess its ability to recover **[48]**.

In this work, the static environment technique was used to study gas sensor properties. As seen in **Fig. 2.15**, the following components make up the measurement setup for gas sensors.

i) Temperature controller

Semiconductor sensors are highly responsive at elevated temperatures. Therefore, a digital temperature controller (DTC) is employed to set the temperature at which the sensor's response to the analyte gas will be measured.

ii) Gas inlet

The analyte gas, at a specified concentration, is introduced into the test chamber through a small opening sealed with a rubber gasket to prevent any gas leakage.

iii) Heating plate

The sensor stage is a hot plate that has been heated to the DTC set functioning temperature. A sensor element with a 1 cm x 1 cm size is placed on the hot plate before the measurements are taken, and it is heated to warm the sensor element.

iv) Electrical contacts and probes

For electrical connections, a silver paste coating/copper foil/aluminium foil strip is applied to the sensor element, and two probes are used to attach it to an electrometer.

v) Probes to electrometer

The probes are extended to connect with a potentiostat to measure the change in resistance before and after introducing the analyte gas into the test chamber.

vi) Insulation

The test chamber is 315 cm^3 in size and is composed of stainless steel. The test chamber is protected by a stainless steel housing from corrosion brought on by certain gases **[49]**.
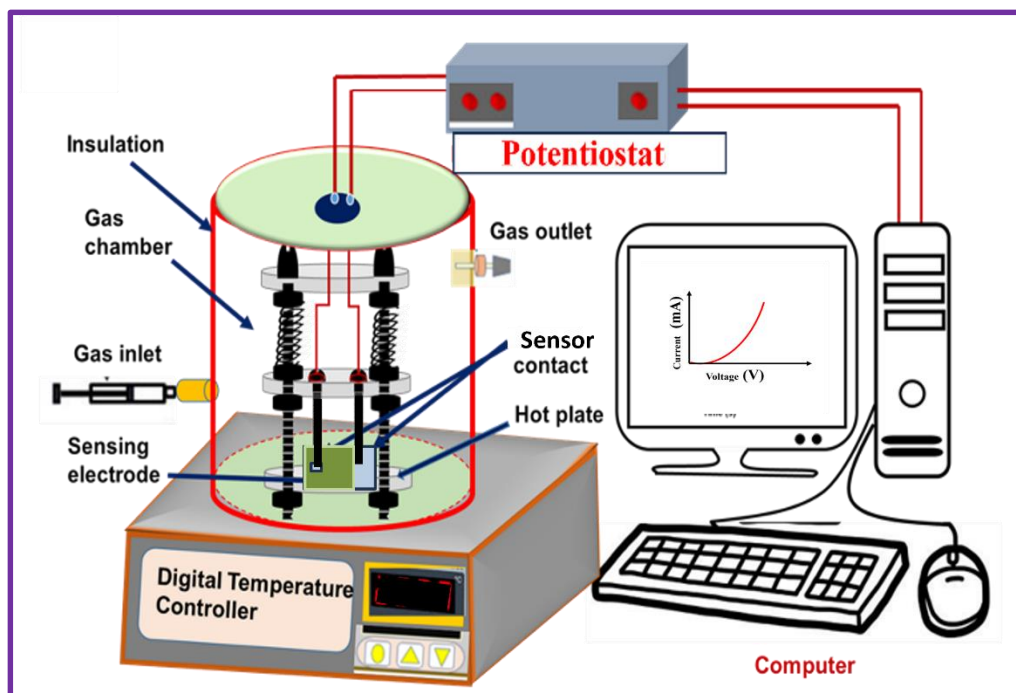
Fig. 2.15 Schematic of gas sensor measurement assembly [49].

Gas sensor techniques

Approaches for measuring gas sensors consider variables such as sensitivity, selectivity, response time, recovery time, and long term stability are discussed in **chapter I section 1.3.3.5** by using lab made sensor unit coupled with potentiostat (Zive MP1 electrochemical workstation).

2.6 References

1] V. Elanjeitsenni, K. Vadivu, B. Prasanth, Mater. Res. Express, 9 (2022) 022001 (1-30).

2] S. Ratnayake, J. Ren, E. Colusso, M. Guglielmi, A. Martucci, E. Gaspera, Small, 17 (2021) 2101666 (1-32).

3] O. Abegunde, E. Akinlabi, O. Oladijo, S. Akinlabi, A. Ude, AIMS Mater. Sci., 6 (2019) 174-199.

4] J. Budida, and K. Srinivasan, Mater. Today: Proc., 92 (2023) 1030-1033.

5] J. Arthur, Physical and chemical methods for thin film deposition and epitaxial growth. In Specimen handling, preparation, and treatments in surface characterization, (Springer, Boston, 1998) pp. 239-293.

6] A. Agarwal, B. Sankapal, Introduction, Simple chemical methods for thin film deposition. (Springer, Singapore, 2023) pp. 1-26.

7] M. Ristov, G. Sinadinovski, I. Grozdanov, Thin solid films, 123 (1985) 63-67.

8] Y. Nicolau and J. Menard, J. Cryst. Growth, 92 (1988) 128-142.

9] https://www.holmarc.com/silar_controller_with_stirrer.php.

10] B. Pandit, P. Nikam, M. Ubaidullah, Well-controlled nanostructured growth: successive ionic layer adsorption and reaction, simple chemical methods for thin film deposition: synthesis and applications, (Springer Nature, Singapore, 2023) pp. 97-158.

11] S. Saha, M. Johnson, F. Altayaran, Y. Wang, D. Wang, Q. Zhang, Electrochem., 1 (2020) 286-321.

12] E. Kalinina, and E. Pikalova, Mater., 14 (2021) 5584 (1-37).

13] F. Nasirpouri, K. Alipour, F. Daneshvar, M. Sanaeian, Electrodeposition of anticorrosion nanocoatings. In corrosion protection at the nanoscale, (Elsevier, 2020) pp. 473-497.

14] B. Pandit, E. Goda, S. Shaikh, Electrochemical deposition toward thin films. In Simple chemical methods for thin film deposition: Synthesis and applications (Springer Nature, Singapore, 2023) pp. 245-304.

15] X. Zheng, T. Ahmad, W. Chen, Energy Storage Mater., 39 (2021) 365-394.

16] S. Thanikaikarasan, T. Mahalingam, T. Ahamad, S. Alshehri, J. Saudi Chem. Soc., 24 (2020) 955-962.

17] https://www.rigaku.com/products/xrd/miniflex.

18] A. Bunaciu, E. UdriŞTioiu, H. Aboul-Enein, Crit. Rev. Anal. Chem., 45 (2015) 289-299.

19] E. Ameh, Int. J. Adv. Manuf. Technol., 105 (2019) 3289-3302.

20] B. Inkson, Scanning electron microscopy (SEM) and transmission electron microscopy (TEM) for materials characterization, In Materials characterization using nondestructive evaluation (NDE) methods, (Woodhead publishing, 2016) pp. 17-43.

21] A. Mayeen, L. Shaji, A. Nair, N. Kalarikkal, Morphological characterization of nanomaterials, advances and key technologies, micro and nano technologies, (Woodhead publishing, 2018) pp. 335-364.

22] https://ncmn.unl.edu/enif/microscopy/interact.shtml.

23] https://www.researchgate.net/figure/Shows-the-basic-block-diagram-of-a-Scanning-Electron-Microscope_fig3_254707658.

24]   M. Kannan, Scanning electron microscopy: Principle, components and applications. A textbook on fundamentals and applications of nanotechnology, (Daya Publishing House, 2018) pp. 81-92.

25]   https://www.scimed.co.uk/education/sem-scanning-electron-microscopy/.

26]   http://en.wikipedia.org/wiki/BET_theory.

27]   P. Sinha, A. Datar, C. Jeong, X. Deng, Y. Chung, L. Lin, J. Phys. Chem. C, 123 (2019) 20195- 20209.

28]   J. Condon, Surface area and porosity determinations by physisorption: measurements and theory, (Elsevier, Amsterdam, 2006) pp. 1-274.

29]   R. Bardestani, G. Patience, S. Kaliaguine, Can. J. Chem. Eng., 97 (2019) 2781-2791.

30]   F. Ambroz, T. Macdonald, V. Martis, I. Parkin, Small methods, 2 (2018) 1800173 (1-17).

31]   S. Krainer, U. Hirn, Colloids Surf. A Physicochem. Eng. Asp., 619 (2021) 126503-126512.

32]   http://www.ramehart.com/790.htm.

33]   https://naturesraincoats.com/liquid-version-of-youngs-law/

34]   K. Manoharan, and S. Bhattacharya, J. Micro Nano-Manuf., 2 (2019) 59-78.

35]   M. Akash, K. Rehman, Ultraviolet-visible (UV-VIS) spectroscopy. In: Essentials of pharmaceutical analysis, (Springer, Singapore, 2020) pp. 29-56.

36]   H. Perkampus, UV-VIS spectroscopy and its applications, (Springer Science and Business Media, 2013) pp. 1-237.

37]   https://www2.chemistry.msu.edu/faculty/reusch/virttxtjml/spectrpy/uv-vis/uvspec.htm.

38]   https://www.bragitoff.com/2018/03/uv-vis-spectroscopy/.

39]   J. Aldabib, and M. Edbeib, Int. Sci. Lett. J, 2 (2020) 1-11.

40]   https://resources.pcb.cadence.com/blog/2020-linear-sweep-voltammetry-for-batteries-and-regulator design.

41]   https://www.ceb.cam.ac.uk/research/groups/rg-eme/Edu/linear-sweep-and-cyclic-voltametry-the principles.

42]   H. Magar, R. Hassan, A. Mulchandani, Sens., 21 (2021) 6578 (1-21).

43]   B. Mei, O. Munteshari, J. Lau, B. Dunn, L. Pilon, J. Phys. Chem. C, 122 (2018) 194-206.

44]   S. Wang, J. Zhang, O. Gharbi, V. Vivier, M. Gao, M. Orazem, Nat. Rev. Methods Primers, 1 (2021) 41 (1-21).

45]   F. Ciucci, Curr. Opin. Electrochem., 13 (2019) 132-139.

46]   S. Tilley, Adv. Energy Mater., 9 (2019) 1802877 (1-13).

47]   G. Hodes, J. Phys. Chem. Lett., 3 (2012) 1208-1213.

48]   Ł. Fuśnik, B. Szafraniak, A. Paleczek, D. Grochala, A. Rydosz, Sens., 22 (2022) 2557 (1-30).

49]   R. Shinde and J. Gunjakar, 2D nanomaterials: Chemiresisitive gas sensor (Lambert academic publishing, 2022) pp. 1-168.

Chapter-III

CdS and rGO/CdS thin films by successive ionic layer adsorption and reaction (SILAR) method: synthesis, characterization, and their photoelectrochemical (PEC) performance

CHAPTER- III

CdS and rGO/CdS thin films by successive ionic layer adsorption and reaction (SILAR) method: synthesis, characterization, and their photoelectrochemical (PEC) performance

Section A

3.1 Introduction

The rising energy need, towering gasoline prices, gradual decrease of non-renewable power resources and their impact on environment are important problems. To fulfill the ever-increasing energy need and reduce environmental degradation mankind has been paying attention towards promising renewable energy sources like nuclear, solar, tidal, wind energy etc. **[1, 2]**. Between these different renewable sources, solar energy is one of the most excellent substitutions with outstanding rewards such as environmentally friendly, plentifully existing, infinite and permanent source of energy **[3, 4]**. So, the continuous conversion of solar energy into electrical energy is an important aspect to fulfill the energy demand of the current globe. It is familiar that photovoltaic devices are valuable for solar energy alteration. These devices use p-n junction for straight alteration of solar energy into electrical energy. Semiconductor-liquid junction solar cells attracted big interest above p-n junction solar cell due to natural storage capacity and ease in junction fabrication. The main part of effective and beneficial solar cell is photoelectrode (photocathode/photoanode) material, so suitable selection of it is a vital thing. The major constituents used in photovoltaics, photocatalysis and photoelectrochemical cell (PEC) processes are chalcogenide based nanocrystals due to their higher light harvesting properties. The sharp absorption edge, direct band gap and higher absorption coefficient of group II-IV semiconductors attract an attention of many researchers **[2, 5]**.

Nowadays, the chalcogenides of materials like Zn, Pb, Cu, and Cd, etc. are utilized for solar cells **[6-8]**. Among these, CdS owing to its comparatively tunable bandwidth which is beneficial to absorb the sunlight, especially visible light. It absorbs sunlight nearly of 50 % along with photogeneration of electron-hole pairs; however, the recombination of electron and hole pairs and less stability are major drawbacks. To overcome these drawbacks researchers utilized variety of ways to modify the properties of films like doping, synthesis method, film thickness, thermal treatment, support materials like carbon nanotubes, graphene, etc. for CdS **[9-12]**.

Recently, rGO/CdS nanocomposite has been investigated because of its improved chemical stability and absorption range in visible light. Those outstanding ability for the generation of electron hole pairs under excitation of solar energy and the reduced graphene oxide (rGO) facilitates the transfer of electrons and suppresses the recombination of photogenerated electron-hole pairs. The layered structure, reduced

number of oxygen functional groups, high electrical conductivity, and surface area are beneficial properties of rGO for nanocomposites **[13-15]**.

Different chemical methods like CBD **[16]**, spin coating **[17]**, solvothermal **[18, 19]**, hydrothermal **[20, 21]**, SILAR **[22]**, reflux condensation **[23]**, precipitation **[24]**, aerosol-assisted chemical vapor deposition (AACVD) **[25]** and one-step bacterial assisted **[26]** have been used to synthesize of rGO/CdS composite thin films. SILAR is an efficient technique for layer-by-layer assembly, allowing precise control over film thickness and enabling large-area deposition on various substrates without the need for a binder. Various types of substrates can be coated at near to room temperature by avoiding oxidation of substrates. The smooth and uniform deposits with enhanced grain structure are obtained due to easily controllable preparative parameters.

In the present chapter, CdS and rGO/CdS composite thin films were deposited using simple SILAR method and characterized for physicochemical and electrochemical properties which are discussed in upcoming sections.

3.2 Experimental details

3.2.1 Substrate cleaning

The cleanliness of the substrate is essential for the growth of thin films and the uniformity of the deposited layers. In current work, 304 grade stainless steel (SS) sheets are used as a substrate for the thin film deposition.

The substrate is cleaned by following procedure,

1: The dirt on SS substrate wiped firstly with acetone,

2: Using zero grade polish paper, the substrate is mirror polished,

3: Double distilled water (DDW) is used to clean the substrate after polishing,

4: Lastly, the substrate is cleaned by ultrasonically in DDW for 15 minutes, and dried naturally.

3.2.2 Material synthesis

3.2.2.1 Synthesis of reduced graphene oxide (rGO)

The preparation of graphene oxide (GO) suspension and the subsequent chemical reduction of GO to obtain reduced graphene oxide (rGO) described in the following steps:

1) **Preparation of GO suspension**

Firstly, 2 g graphite powder were combined with 100 mL of concentrated H_2SO_4 in a 500 mL glass conical flask. The mixture was placed in an ice bath container with

continuous stirring. Then, 1 g of $NaNO_3$ was added to the mixture. After that, 8 g of $KMnO_4$ were added slowly to the mixture while maintaining the reaction temperature below 293 K. Once the addition was finished, the reaction mixture was maintained at room temperature with continuous stirring for 12 hours. Then, 100 mL of double distilled water (DDW) was added, followed by another 300 mL of DDW and 8 mL of 30% H_2O_2. The yellowish color solution was obtained. The resulting solution was rinsed multiple times with 5% HCl, followed by several washes with DDW until the pH reached 6.5 ± 0.1. The concentration of the resulting GO slurry was measured using the gravimetric weight difference method.

2) Chemical reduction of GO to rGO

Fig. 3.1 illustrates the synthesis process of rGO. A 1000 mL suspension of GO at a concentration of 0.1 mg/mL was prepared and sonicated for 4 hours. 5 mL of hydrazine hydrate (HH) was added to the prepared GO solution.
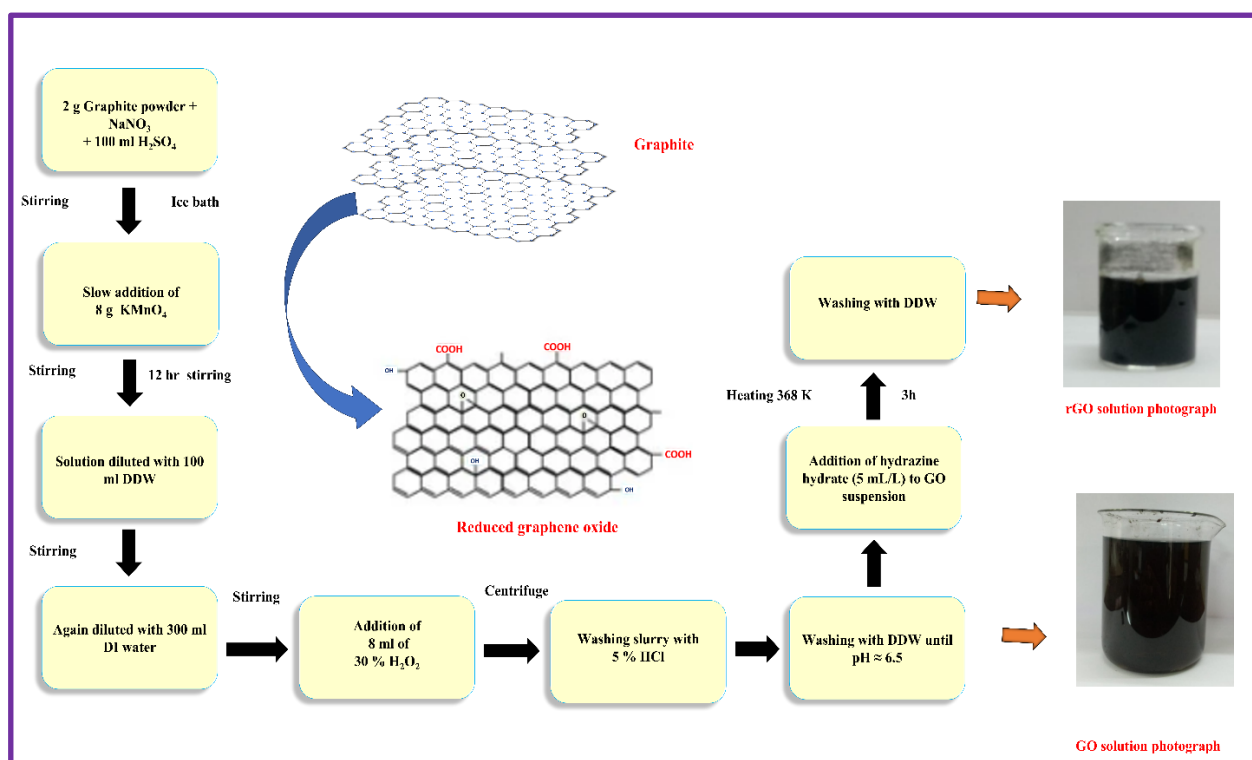
Fig. 3.1 The synthesis process schematic of rGO.

The prepared solution was heated to 368 K (about 95 °C) for 3 hours to reduce the GO sheets, producing rGO. The rGO dispersion was washed several times with DDW to eliminate any residual impurities **[27]**. The resulting rGO slurry was then used for thin film deposition and various characterization techniques. The chemical reaction of chemical reduction of GO using HH is given as follows,

$$GO + N_2H_4 \rightarrow rGO + N_2 + H_2O \qquad (3.1)$$
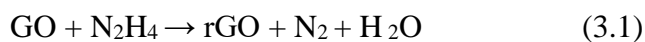
3.2.2.2 Deposition of rGO thin films

50 ml rGO solution of 1 mg mL^{-1} concentration was sonicated for 1 h. Then, SS substrate was immersed vertically in rGO solution for 10 s and dried for 20 s. Such 40 repeated cycles were performed to achieve uniform black colored rGO thin film on SS substrate using dip and dry strategy shown in **Fig. 3.2** and deposition parameters summarized in **Table 3.1**.
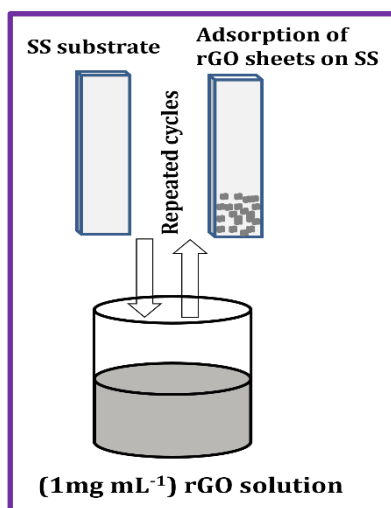
Fig. 3.2 Schematic of rGO thin film deposition.

Table 3.1: Deposition parameters of rGO thin film.

Parameter for rGO	Precursor solution (rGO)
Concentration (M)	1mg mL^{-1}
Immersion time (s)	10
Drying time (s)	20
Cycles	40

3.2.2.3 Deposition of CdS and rGO/CdS thin films by SILAR method

1) Chemicals

An analytical grade (AR) chemicals like cadmium chloride (CdCl$_2$), sodium sulfide (Na$_2$S), sulfur powder (S), and sodium hydroxide (NaOH) are used as received form for thin film deposition. DDW was utilized as a solvent for all solutions.

2) Deposition of CdS thin films

Thin films of CdS were deposited using SILAR method at room temperature (300 K). Typically, separately prepared 0.025 M CdCl$_2$ and 0.025 M Na$_2$S solutions

were used as cationic and anionic precursors, respectively. Firstly, the SS substrate was immersed in $CdCl_2$ solution for 15 s to adsorb Cd^{2+} ions, followed by rinsing in DDW for 10 s to eliminate weakly bound Cd^{2+} cations. After that, the substrate was dipped in Na_2S solution for 15 s for reaction of S^{2-} ions with Cd^{2+} cations. The substrate is again rinsed in DDW for 10 s to eliminate unreacted and unbounded species. This was regarded as a single SILAR cycle, such 40, 60, 80, and 100 cycles were performed and the films are denoted as CdS-40, CdS-60, CdS-80, and CdS-100, respectively. The optimized preparative parameters are summarized in **Table 3.2**.

Table 3.2: preparative parameters for deposition of CdS thin film by SILAR method.

Parameter for (CdS)	Precursor solution	
	Cationic ($CdCl_2$)	Anionic (Na_2S)
Concentration (M)	0.025	0.025
Solution pH	6 ± 0.1	10 ± 0.1
Immersion time (s)	15	15
Cycles	40, 60, 80, and 100	

3) Deposition of rGO/CdS composite thin films
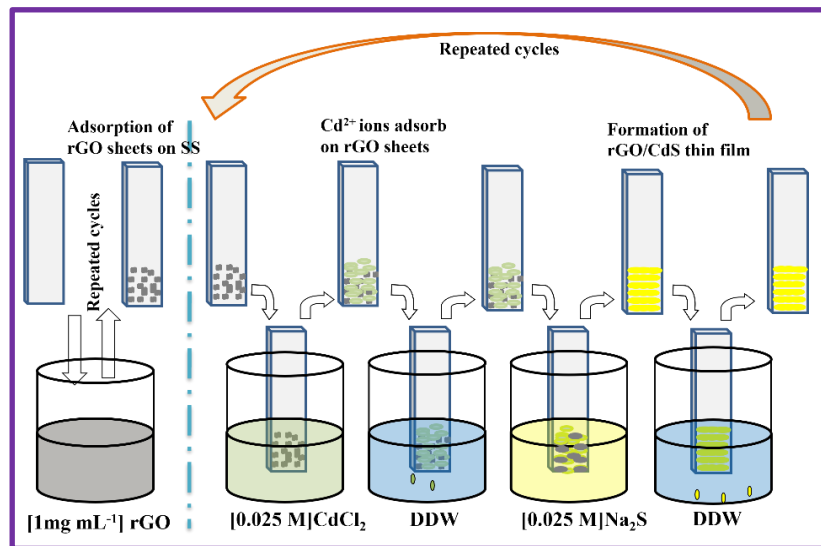
Fig. 3.3 Schematic of rGO/CdS thin film deposition by SILAR method.

The rGO thin films were deposited on SS substrate, as explained in above section **3.2.2.2.** and dipped in cationic and anionic precursors for CdS deposition as mentioned in section **3.2.2.3** for 40, 60, and 80 cycles. The schematic of rGO/CdS thin film fabrication by SILAR method is shown in **Fig. 3.3**. The deposited films were

named as rGO/CdS-40, rGO/CdS-60, and rGO/CdS-80 for 40, 60, and 80 SILAR cycles, respectively.

3.2.2.4 rGO/CdS film formation mechanism

As shown in schematic **Fig. 3.3**, firstly, rGO thin film deposited on SS substrate by use of dip and dry strategy (dip- 10 s, dry- 20 s). During this process, rGO sheets adhered to the SS substrate due to attractive forces between the ions in the solution and the substrate surface. These interactions could include cohesive forces, Van der Waals forces, or chemical attraction. Then, Cd^{2+} ions were adsorbed on rGO sheets due to reaction with extra-planer hydroxyl or carboxyl groups of rGO sheets when dipped into cationic precursor for 15 s. To detach loosely adsorbed cations (Cd^{2+}), the substrate was rinsed in DDW for 10 s. After that, SS substrate was dipped in anionic solution for 15 s, to react with S^{2-} ions and form CdS single layer on rGO thin film.

This is demonstrated by the reaction as;

$$Cd^{2+}_{(aqueous)} + S^{2-}_{(aqueous)} \rightarrow CdS_{(solid)} \qquad (3.2)$$
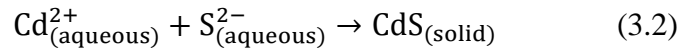
The unreacted ions (S^{2-}) were removed out by rinsing the substrate in DDW again for 10 s. This single cycle of SILAR method forms CdS layer and such cycles were repeated to obtain desired film thickness **[5].**

3.2.2.5 Thickness measurement

The gravimetric weight difference method was used to determine the thickness of rGO, CdS, and rGO/CdS thin films. The formula used for the measurement is given below,

$$t = \frac{M2 - M1}{A.\rho} \qquad (3.3)$$

Here,

t = thickness of the deposited film, M2 = weight of the SS substrate after deposition, M1 = weight of the SS substrate before deposition, A = area of the film in cm^2, ρ = density of the bulk material (for CdS, ρ = 8.15 gcm^{-3}, and for rGO, ρ = 2.1 gcm^{-3}) **[5, 28, 29]**.

The thickness of CdS films with various number of deposition cycles is shown in **Fig. 3.4 a)**. Thicknesses for CdS-40, CdS-60, CdS-80, and CdS-100 films were found to be 167, 459, 876, and 600 nm, respectively. It is observed that the thickness of CdS film increases with deposition cycles. The nonlinearity of thickness is because of nucleation and coalescence process. Furthermore, after 80 cycles, a decrease in CdS

film thickness is observed. The decrease in CdS film thickness may be due to the development of stress as well as the relatively poor adhesion in chemically deposited films, resulting in peeling off of the film after reaching beyond optimum thickness. Thus, the terminal thickness of CdS thin film was 876 nm for 80 cycles and such film was used for forming composite with rGO [30].
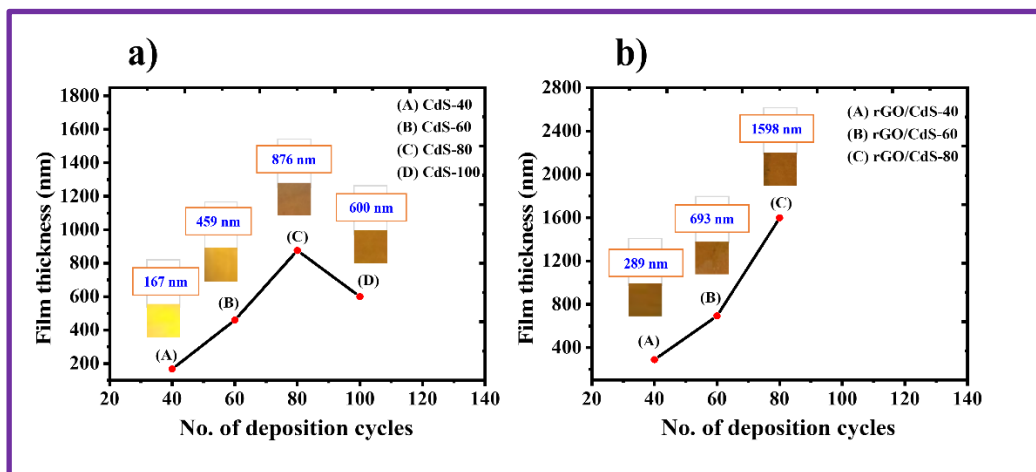
Fig. 3.4 The plot of thickness variation of a) CdS and b) rGO/CdS films with the number of SILAR deposition cycles.

The thickness of rGO/CdS films with various number of deposition cycles is shown in **Fig. 3.4 b)**. In case of rGO/CdS film, the thickness of rGO film was calculated first (90 nm) and this film was used as a substrate for CdS deposition. By gravimetric weight difference method, the thickness of CdS over rGO film calculated by mathematical addition of rGO and CdS layer thickness. Thicknesses for rGO/CdS-40, rGO/CdS-60, and rGO/CdS-80, films were found to be 289, 693, and 1598 nm, respectively. The increased thickness of rGO/CdS-80 may be due to availability of previous nucleation sites of rGO surface.

3.3 Physicochemical and electrochemical characterizations of thin films

The X-ray diffraction (XRD) technique (Rigaku miniflex-600) was used to probe the structural analyses of rGO, CdS, and rGO/CdS composite thin films. The surface morphology and elemental analyses were studied by Field-emission scanning electron microscopy (FE-SEM; JEOl-6360 Japan) equipped with energy dispersive X-ray spectroscopy (EDS; Oxford X-max). The Rame Hart-500 advanced goniometer was used to measure surface wettability. The surface area and pore size distribution of film materials were measured using the Brunner-Emmett-Teller (BET; Belsorp-II mini) technique.

The current-voltage (I-V) characteristics/power output of the [rGO or CdS or rGO/CdS//1 M (NaOH+Na$_2$S+S) //graphite//SCE] cell was studied under 25 mW cm^{-2} illuminations in the dark, under light and under chopped conditions on Zive MP1 electrochemical workstation. The 35 W xenon lamp was used as a light source. The 1 cm^2 area of photoelectrode was exposed for illumination. The remaining area of the photoelectrode was masked with epoxy resin. The electrochemical impedance spectroscopy (EIS) study of rGO, CdS and rGO/CdS thin film electrodes were studied in dark and under light conditions, in 1 M polysulfide (NaOH+Na$_2$S+S) electrolyte using two electrode cell.

3.4 Results and discussion

3.4.1 Physicochemical properties of rGO thin films

3.4.1.1 XRD study

The XRD pattern of rGO thin film is shown in **Fig. 3.5**. The broad peak observed at 2θ = 24° corresponds to rGO (002) plane **[26]**. The broad peak of rGO due to the lower amount and low diffraction intensity. The peaks indicated by the '*' are due to the SS substrate.
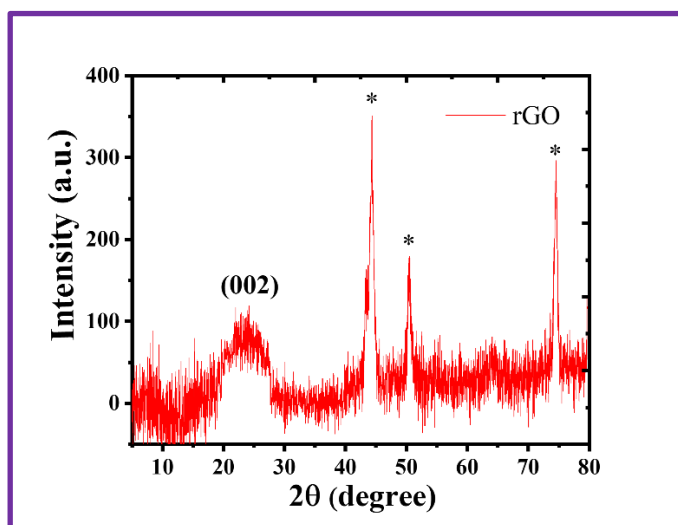
Fig. 3.5 The XRD pattern rGO thin film.

3.4.1.2 FE-SEM study

To examine the surface morphology of the rGO thin films, FE-SEM was employed. The FE-SEM images of rGO are presented in **Fig. 3.6 (a-b)** at magnifications of 10 and 25 kX.

Fig. 3.6 a) demonstrates the interconnected randomly aggregated rGO nanosheets on SS substrate. **Fig. 3.6 b)** shows the wrinkled rGO nanosheet with higher

surface area at the magnification of 25 kX. The rGO sheets acts the sitting mat for CdS nanoparticles for deposition.
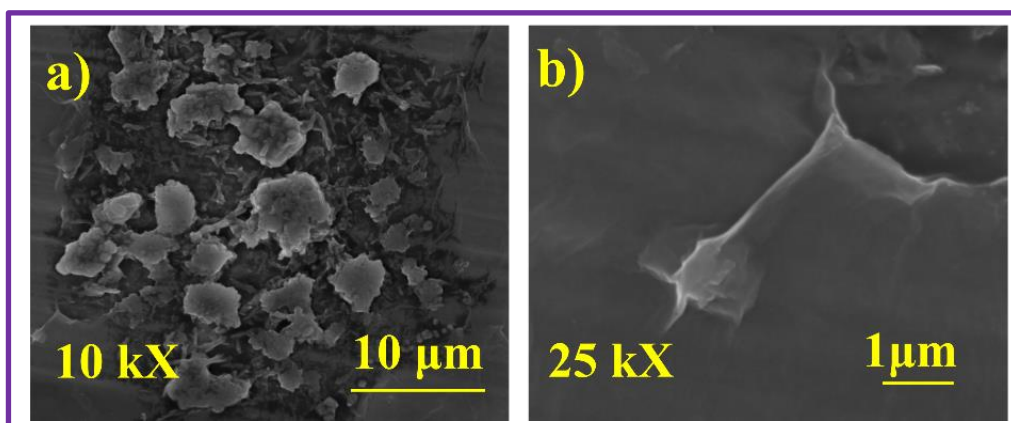
Fig. 3.6 The FE-SEM images of (a-b) rGO thin film at magnifications of 10 kX and 25 kX.

3.4.1.3 Energy dispersive X-ray analysis (EDAX) study

EDAX was utilized for elemental study of rGO thin film as shown in **Fig. 3.7**. From **Fig. 3.7** it is confirmed that, the presence of C and O species, the atomic percentage ratio of carbon to oxygen is 2.1:1 (atomic percentage C to O is 68.19:31.81).
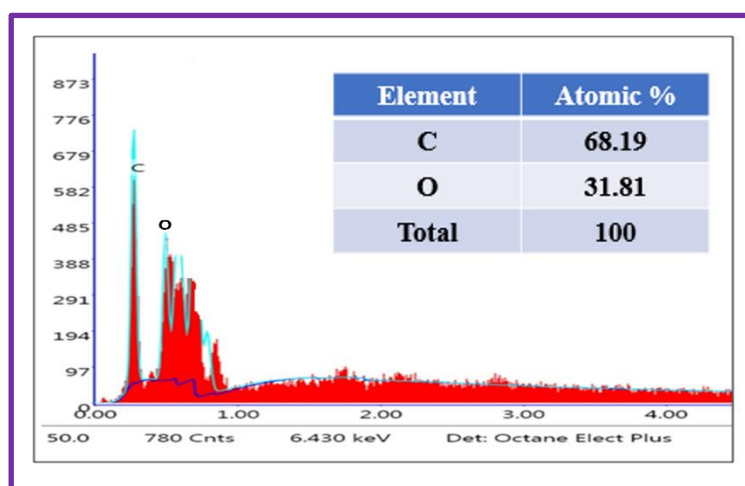
Fig 3.7 EDAX pattern of rGO thin film

3.4.1.4 Contact angle measurement

Contact angle measurement technique was used to study the interaction between electrolyte and photoelectrode surface. If the liquid is strongly attracted to the solid surface the droplet will completely spread over solid surface and the surface is hydrophilic and contact angle will be close to 0 º. On the other hand, if the solid surface is hydrophobic, the contact angle will be larger than 90 º.

In the present study, rGO film have the contact angle of 95 ° (**Fig. 3.8**). rGO film shows hydrophobic nature. The rGO exhibits higher value of contact angle due to an elimination of oxygen containing functional groups (carbonyl, carboxyl, and hydroxyl) and lead weak hydrogen bond interactions at the interface **[31]**.
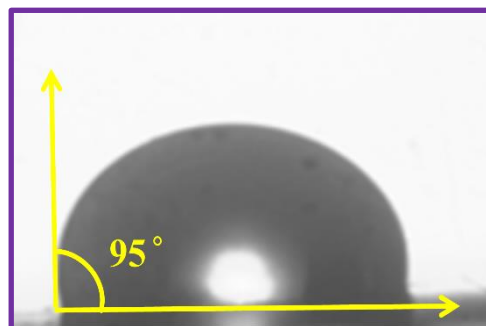
Fig. 3.8 Photograph of rGO thin film contact angle.

3.4.1.5 BET study

Fig. 3.9 (a) displays the N2 adsorption-desorption isotherm for the rGO thin film.
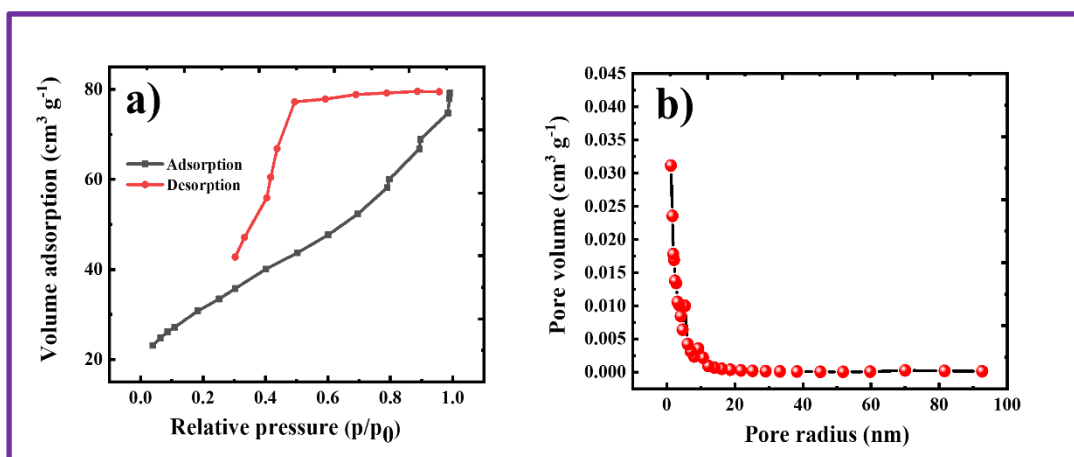
Fig. 3.9 a) The N₂ adsorption-desorption isotherm and b) the BJH size distribution curves for rGO sample.

The BET curve of rGO exhibits type IV isotherm with H2 type hysteresis loop which is a characteristics of high adsorption energy with mesoporous morphology and specific surface area of 73.50 m^2 g^{-1}. Its corresponding BJH plot confirm the mesoporous nature as shown in **Fig. 3.9 b)**.

3.4.2 Physicochemical properties of CdS and rGO/CdS thin films

3.4.2.1 XRD study

The XRD patterns of CdS-40, CdS-60, and CdS-80, thin films are shown in **Fig. 3.10 a)** and rGO/CdS-40, rGO/CdS-60, and rGO/CdS-80 in **Fig. 3.10 b)**. The broad peak observed in CdS, and rGO/CdS composite samples at $2\theta = 26.28°$ corresponds to

(111) plane of cubic phase CdS and it is in good agreement with literature (JCPDS: 00-010-0454) **[32]**.
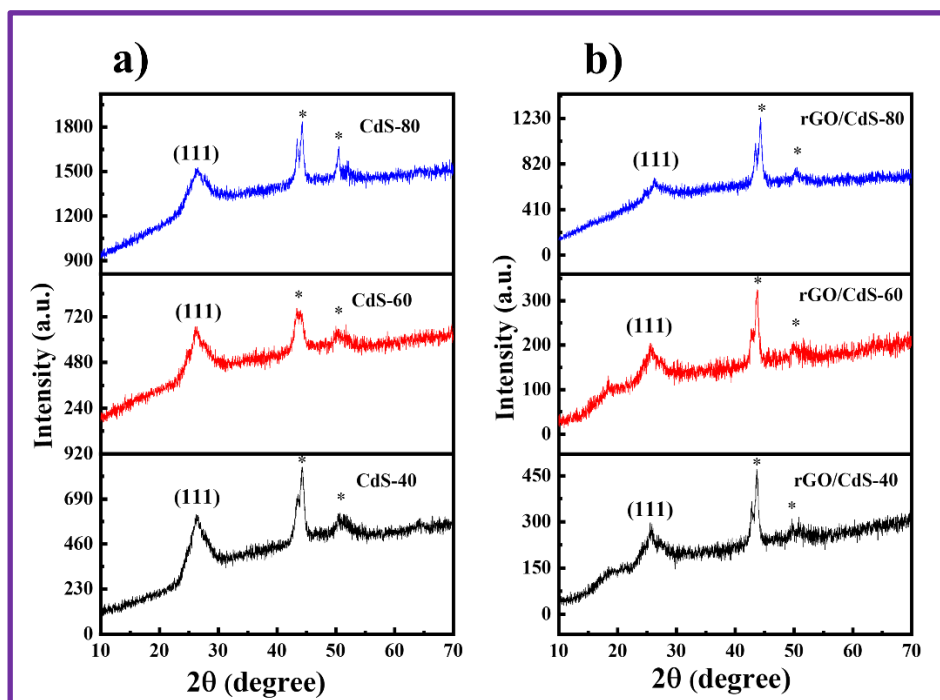
Fig 3.10 The XRD patterns of a) CdS-40, CdS-60, CdS-80, and b) rGO/CdS-40, rGO/CdS-60, and rGO/CdS-80 thin films.

The broad peak of XRD confirms the nanocrystalline structure of CdS thin film. The peaks indicated by '*' are due to SS substrate. The relative peak intensity of (111) plane enhances with increase in film thickness for CdS-40, CdS-60, and CdS-80 thin films.

Table 3.3: The XRD parameters of CdS and rGO/CdS thin films.

Sample Code	Crystallite size 'D' (nm)
CdS-40	15
CdS-60	19
CdS-80	21
rGO/CdS-40	19
rGO/CdS-60	17
rGO/CdS-80	18

This enhanced crystallinity of the films is attributed to the rearrangement of the molecules and elimination of defects due to the layer-by-layer deposition in SILAR

method. Ashith and Rao [32] reported enhancement in film crystallinity with growing film thickness for SILAR synthesized CdS thin films. No typical diffraction peak of rGO is observed in XRD pattern of rGO/CdS composite thin films, which may be due to the small amount and relatively low diffraction intensity of rGO material [33]. The crystallite size was determined using Scherrer equation. All structural parameters are summarized in **Table 3.3**.

From **Table 3.3**, it is observed that, the films of CdS-80, and rGO/CdS-80 have the crystallite sizes of 21, and 18 nm, respectively. The reduction in the crystallite size of rGO/CdS-80 film nanoparticles is due to the more nucleation sites for growth CdS on rGO layer. The peak broadening in the XRD signals for rGO/CdS-80 composite demonstrates the reduction in the crystallite size of CdS nanoparticles. Similar reduction in crystallite size over growth on rGO is reported by the Mondal et al. [10] and Nosheen et al. [34] for rGO/CdS composites.

3.4.2.2 FE-SEM study

To study surface morphology of CdS and rGO/CdS thin films, FE-SEM was used. The FE-SEM images of CdS-40, rGO/CdS-40, CdS-60, rGO/CdS-60, CdS-80, and rGO/CdS-80 are shown in **Fig. 3.11 (a-f)** at magnification of 25 kX.

Fig. 3.11 (a-b) shows the compact type of the morphology changes to some traces of the growth of the CdS nanoparticles on the rGO surface for CdS-40 and rGO/CdS-40 thin films. The equal pattern and intermediate growth of CdS nanoparticles over rGO sheets observed for CdS-60 and rGO/CdS-60 thin films **Fig. 3.11 (c-d)**. The agglomeration of spherical shaped CdS nanoparticles of average size 24 nm with overgrowth of clusters is observed in CdS-80 thin film [**Fig. 3.11 (e)**] [33, 35].

Fig. 3.11 (f) depicts that CdS nanoparticles are uniformly distributed over rGO sheets. The rGO provides the mat for sitting the CdS nanoparticles leads in highly porous spongy nanoparticles (size 20 nm) morphology with reduced agglomeration on rGO sheets. The nanoparticle growth and conductive backbone of the rGO may provide the electrode higher conduction of the electron hole pairs and result in less photocorrosion. This will improve the PEC performance. Chen et al. [20] reported similar type of morphology for CdS@rGO by hydrothermal method.
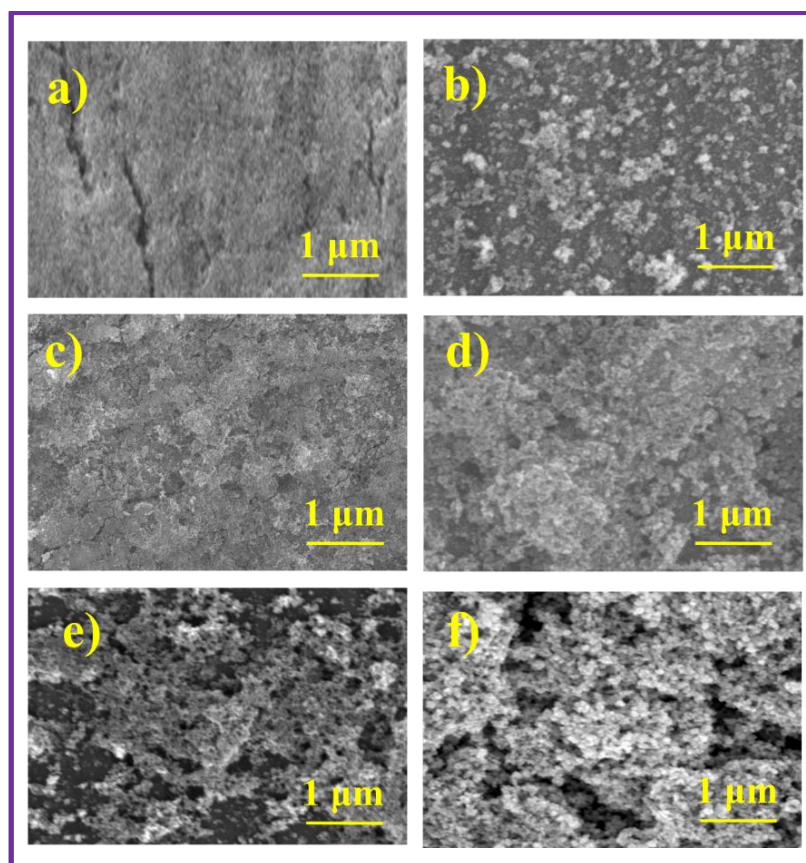
Fig. 3.11 The FE-SEM images of (a-b) CdS-40 and rGO/CdS-40, (c-d) CdS-60 and rGO/CdS-60, and (e-f) CdS-80 and rGO/CdS-80 thin films at magnification of 25 kX.

3.4.2.3 EDAX study

Energy dispersive X-ray analysis (EDAX) was utilized for elemental study of CdS-80 and rGO/CdS-80 thin films as shown in **Fig. 3.12 (a and b)**. **Fig. 3.12 a)** confirms the presence of Cd and S species, the atomic percentage of cadmium (Cd), sulfur (S), and oxygen (O) was 29.37: 38.33:32.30 shows sulfur rich material.
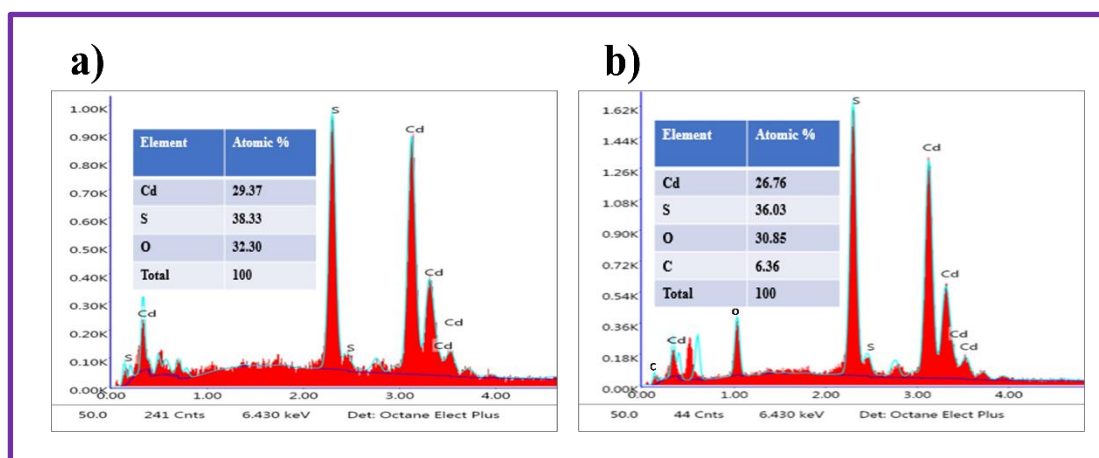
Fig. 3.12 EDAX patterns of a) CdS-80, and b) rGO/CdS-80 thin films

Fig. 3.12 b) confirms the presence of Cd, S, O, and C species with atomic percent 26.76:36.03:30.85:6.36 in sample rGO/CdS-80. The observed elemental composition well supports to XRD study and is in good agreement with the deposition composition.

3.4.2.4 Contact angle measurement

There is a strong association between surface roughness and pore size among the contact angle value of every material. Certainly, being a non-porous or porous surface strongly affects the value of contact angle because, due to the capillary forces water drop can penetrate into the big pores of the surface and spreads on the surface, resulting into reduction of contact angle value.

The contact angle values of CdS-40, rGO/CdS-40, CdS-60, rGO/CdS-60, CdS-80, and rGO/CdS-80 thin films are 73 º, 70 º, 65 º, 40 º, 36 º, and 33 º respectively, shown in **Fig. 3.13 (a-f).** All deposited films are hydrophilic in nature.
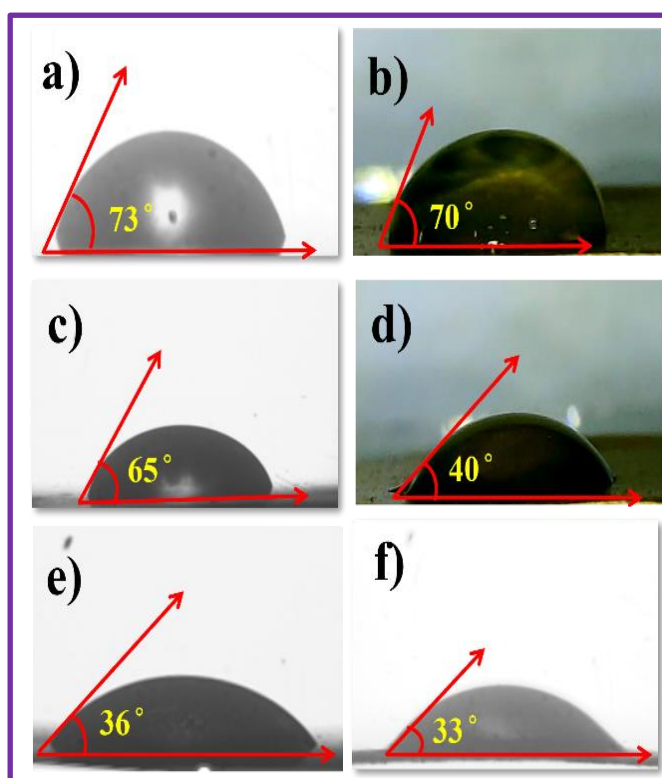
Fig. 3.13 Photographs of contact angles of a-b) CdS-40 and rGO/CdS-40, c-d) CdS-60 and rGO/CdS-60, e-f) CdS-80, and rGO/CdS-80 thin films.

The reduction in contact angle for CdS and rGO/CdS films is attributed to the surface roughness, and porosity of the film surface. Shelke et al. **[30]** reported the similar result decrease in film contact angle with increasing film thickness for SILAR

deposited Cu_2SnS_3 thin films. **Fig. 3.13 (f)** shows contact angle value of 33 $^\circ$ for rGO/CdS-80 film.

From the observation of **Fig. 3.13 (a-f)** CdS composited with rGO samples shows the reduction in value of the contact angle with respective CdS sample of same number of SILAR cycles.

After composition with rGO, the surface morphology alteration, surface area, and porosity of rGO/CdS films changes which lead to increased hydrophilicity of the composite film. The porous morphology which support to the lower value of contact angle of rGO/CdS film seen in FE-SEM study. The photoelectrode hydrophilic surface leads to intimate contact between photoelectrode and redox electrolyte in solar cell which results in improvement of the PEC performance of the electrode. The lower value of contact angle facilitates superior electrolyte penetration and reduces charge transfer resistance, enhancing electron transfer efficiency and PEC performance **[34]**.

3.4.2.5 BET study

The surface area plays most important role during light absorption at different incident angles in the solar cell. So, it is significant to study BET analysis for CdS-80, and rGO/CdS-80 composite materials. N_2 adsorption-desorption isotherms measured for CdS-80, and rGO/CdS-80 samples are shown in **Fig. 3.14 (a, b)**.
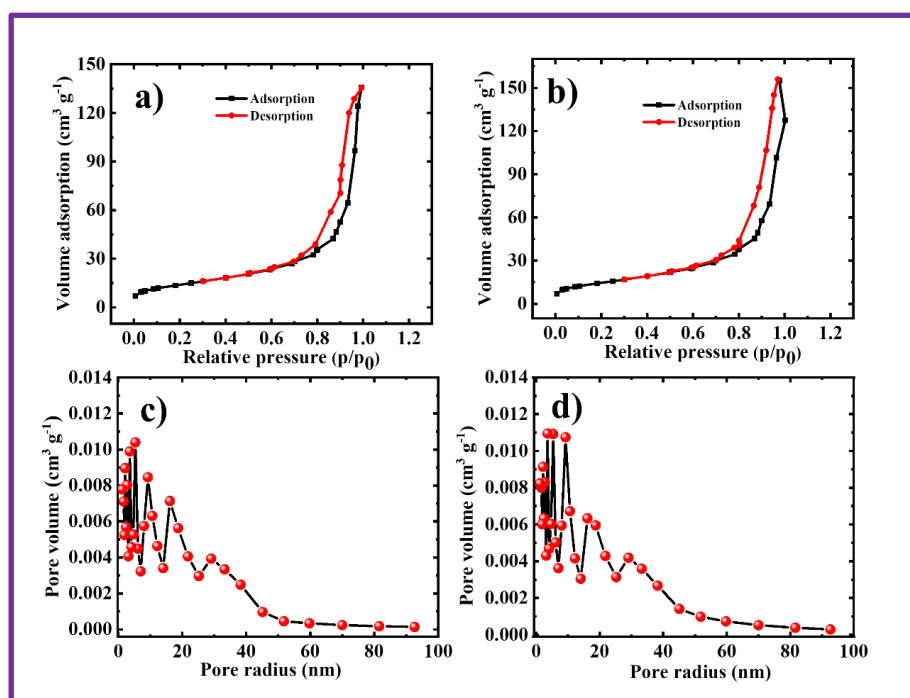
Fig. 3.14 The N_2 adsorption-desorption isotherms for a) CdS-80, and b) rGO/CdS-80 samples and the BJH size distribution curves of c) CdS-80 and d) rGO/CdS-80 samples.

The curves of relative pressure vs volume adsorption for CdS-80 and rGO/CdS-80 composite show type V isotherms amended by H1 type hysteresis loop **[36]**. The CdS-80 and rGO/CdS-80 show the presence of mesopores with specific surface area of 49.92 and 52.52 $m^2 g^{-1}$, respectively. After composition with rGO the surface area of the sample increased which helps in better electrochemical contact and improvement in the power conversion efficiency.

The average pore size distribution of the fine crystallites nature is built-in during Barrett-Joyner-Halenda (BJH) graph. The plots of pore volume vs pore radius of CdS-80 and rGO/CdS-80 shown in **Fig. 3.14 (c, d)** reveal the mesoporous nature **[21]**.

The observed results of the BET analysis strongly support to contact angle change trend for CdS-80, and rGO/CdS-80 films.

3.4.2.6 Optical absorption study

Fig. 3.15 a-b with insets shows the absorption spectra of CdS and rGO/CdS composite thin films. The absorption band edges for CdS-40, CdS-60, CdS-80, rGO/CdS-40, rGO/CdS-60, and rGO/CdS-80 are at 531, 545, 583, 530, 555, and 590 nm, respectively. The CdS and rGO/CdS thin films show the absorbance in the visible range from 500 to 800 nm. A significant red shift was observed for rGO/CdS-80 composite thin film due to enhancement of the surface electric charge of CdS due to rGO. Hence, rGO/CdS-80 composite thin film is more efficient to utilize visible light **[33, 37, 38]**. **Fig. 3.15 a)** shows the DRS spectra of CdS-40, CdS-60, CdS-80, and **b)** rGO/CdS-40, rGO/CdS-60, and rGO/CdS-80 thin films. The band gaps of CdS and rGO/CdS samples were determined using the Kubelka-Munk standard equation as:

$$[F(r)hv]^{\frac{1}{n}} = A(E_g - hv) \tag{3.4}$$

Here, *F(r)* is Kubelka-Munk (K-M) function (i.e. $\frac{K}{S}$), hv is photon energy of light and *n* is different values for allowed transitions, for direct transition $n = \frac{1}{2}$ and for allowed indirect transition $n = 2$.

Equation (3.4) is almost similar to the Tauc plot. The band gap values are found to be 2.43, 2.40, 2.29, 2.33, 2.23, and 2.17 eV for CdS-40, CdS-60, CdS-80, rGO/CdS-40, rGO/CdS-60, and rGO/CdS-80 thin films, respectively.

In the present study for CdS and rGO/CdS composite thin films the particle size increases from 15 to 21 nm, as the number of SILAR cycle increases. Ashith and Rao **[32]** reported the similar result of an increase in film crystallinity with increasing film thickness for SILAR deposited CdS thin films. In case of rGO/CdS-80 composite thin

film, the calculated particle size was 18 nm, which is slightly reduced from pristine CdS-80 thin film; the reduction in the crystallite size of CdS nanoparticles is due to growth over the graphene sheet. The peak broadening observed in the XRD signals for rGO/CdS-80 (**Fig. 3.10**) shows the formation of the small nanoparticles in the composite.
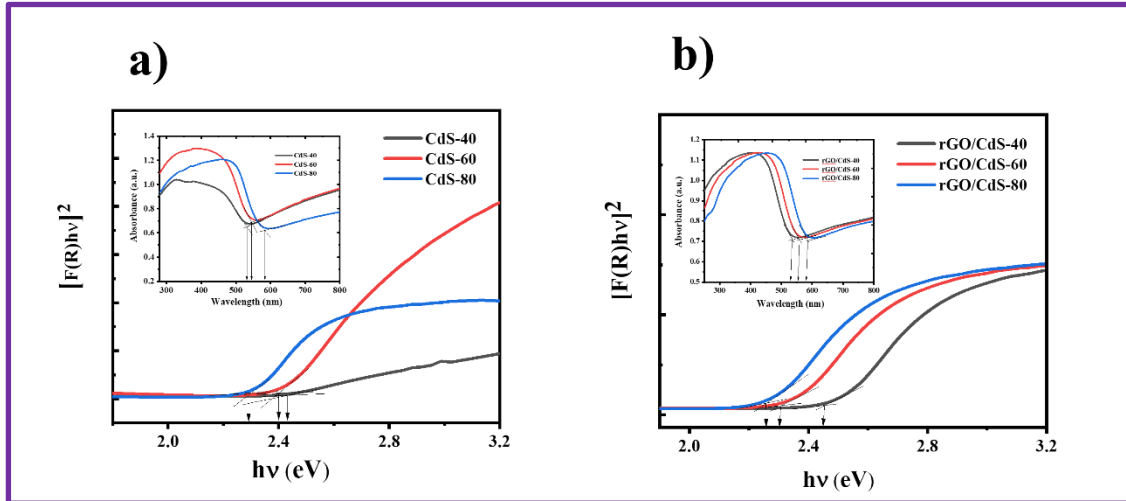
Fig. 3.15 Diffused reflectance spectra of a) CdS-40, CdS-60, CdS-80, and b) rGO/CdS-40, rGO/CdS-60, and rGO/CdS-80 thin films.

According to the size quantization, the value of band gap variation is related to nanosize of the particle. As mentioned earlier, the crystallite size of the films is in the nano domain where optical properties of the film are considerably different from that of the bulk material. The band gap values are reduced from 2.43 to 2.29 eV for CdS-40, CdS-60, and CdS-80 electrodes. The band gap value for rGO/CdS-80 (2.17 eV) is slightly narrower than CdS-80 (2.29 eV) which is attributed to the chemical bonding between semiconductor and graphene support. Nosheen et. al. **[34]** reported similar results for rGO/CdS composites.

Section B

3.5 Electrochemical Characterizations of rGO, CdS and rGO/CdS thin films

3.5.1 Polysulfide electrolyte preparation

An electrolyte plays a key role in the function of the PEC cell. For the preparation of polysulfide, the analytical grade sodium hydroxide (NaOH), sodium sulfide flakes (Na$_2$S), and sulfur powder (S) were used. The solvent used was double distilled water (DDW). The preparation of polysulfide electrolyte consists of following steps:

1. To prepare 1 M aqueous polysulfide solution, initially NaOH pellets, Na₂S flakes, and sulfur powder were weighted appropriately (as per requirement for 1 M).

2. Firstly, NaOH pellets were dissolved in DDW followed by Na₂S flaks.

3. After that, a sulfur powder was slowly added to this solution which then heated and maintained to temperature 45-50 ° C.

4. Then, after constant stirring 20-30 minutes, under constant stirring sulfur powder was found almost dissolved and pale-yellow solution was turned into the yellowish orange.

5. The solution was allowed to cool to room temperature which further filtered to remove scanty undissolved sulfur powder and stored in tight capped glass bottle. The pH of polysulfide solution was 11.8 ± 0.1.

3.5.2 I-V characteristics of rGO thin film

The three-electrode cell was made up of rGO as a working, SCE as a reference, graphite as a counter electrode, and 1 M polysulfide as an electrolyte. The I-V curves of rGO thin films in dark and under light conditions are given in **Fig. 3.16**.

The junction quality factor 'β' was calculated from the slope of the I-V curves by using the formulae given in **chapter I section 1.2.3**. The values of 'β' for rGO polysulfide junction are given in **Table 3.4**.
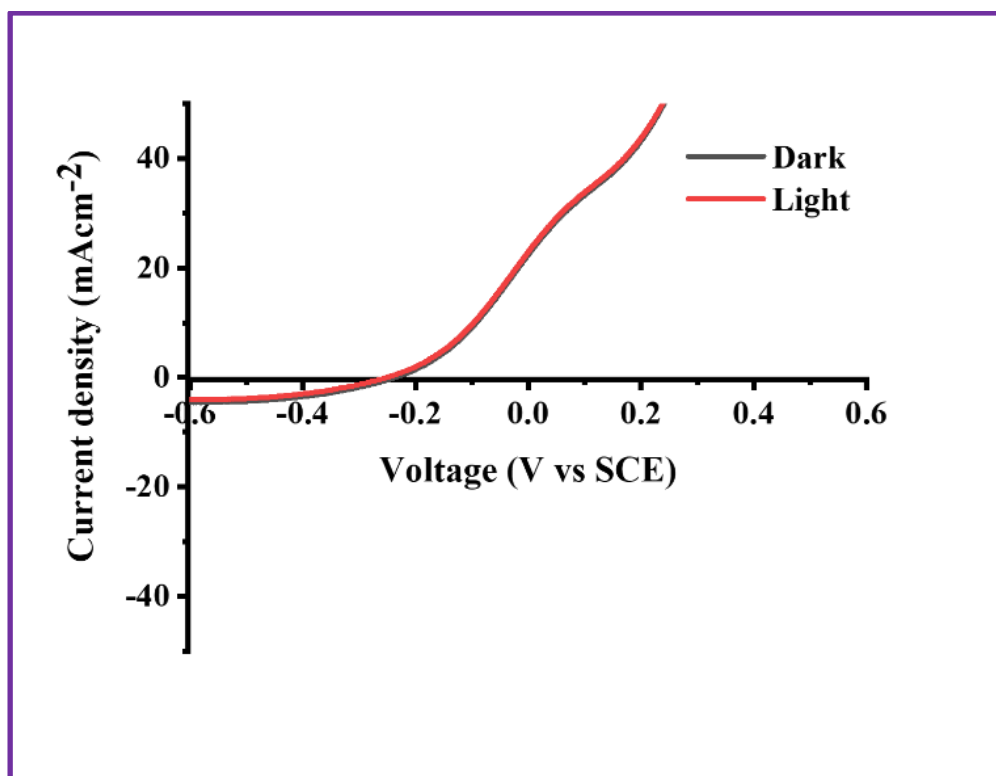
Fig. 3.16 I-V curve of rGO in dark and under light conditions.

Table 3.4: The 'β' values of rGO thin film electrode in dark and under light conditions.

Sr. No.	Electrode	Measurement condition	$\beta = \dfrac{2.303\,RT}{bF}$	$\beta = 1 - \dfrac{\left(\log \dfrac{I}{I_0}\right)RT}{qV}$
1	rGO	Dark	0.97	0.97
		Light	0.97	0.97

Table 3.4 shows that the 'β' values for rGO are close to 1 in both conditions, indicating good contact between the electrode and electrolyte. A higher 'β' value means a better quality interface, allowing charge carriers to move across efficiently with minimal losses.

3.5.3 I-V characteristics of CdS and rGO/CdS electrodes

The three-electrode cell set up consisting of CdS or rGO/CdS as a working, SCE as a reference, graphite as a counter electrode, and 1 M polysulfide as an electrolyte.
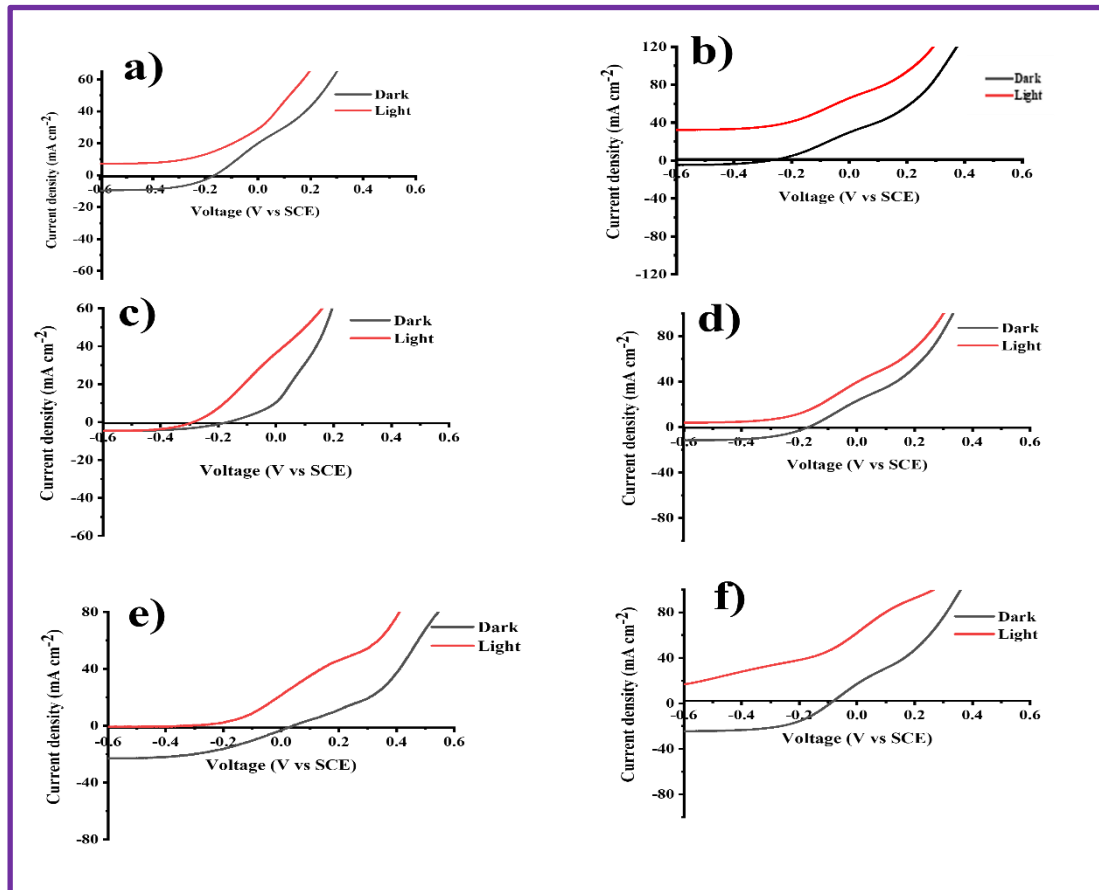
Fig. 3.17 The I-V characteristics of a) CdS-40, b) rGO/CdS-40 c) CdS-60, d) rGO/CdS-60, e) CdS-80, and f) rGO/CdS-80 thin films in dark and under light conditions.

Fig. 3.17 (a-f) depicts the I-V curves of CdS-40, rGO/CdS-40, CdS-60, rGO/CdS-60, CdS-80, and rGO/CdS-80 thin films in dark and under light conditions. The symmetry factor (β) was estimated from the I-V curves by using formulae as mentioned in **chapter I section 1.2.3**. The values of 'β' for CdS and rGO/CdS polysulfide junctions are given in **Table 3.6.**

Table 3.5 The 'β' values of CdS and rGO/CdS thin film electrodes in dark and under light conditions.

Sr. No.	Electrode	Measurement condition	$\beta = \dfrac{2.303\,RT}{bF}$	$\beta = 1 - \dfrac{\left(\log\dfrac{I}{I_0}\right)RT}{qV}$
1	CdS-40	Dark	0.96	0.97
		Light	0.93	0.96
2	rGO/CdS-40	Dark	0.92	0.96
		Light	0.96	0.97
3	CdS-60	Dark	0.97	0.95
		Light	0.98	0.92
4	rGO/CdS-60	Dark	0.97	0.95
		Light	0.96	0.96
5	CdS-80	Dark	0.97	0.94
		Light	0.97	0.95
6	rGO/CdS-80	Dark	0.94	0.95
		Light	0.96	0.97

3.5.4 Construction of PEC Cell

The PEC cell was made up of two-electrode cell set up consisting of rGO or CdS or rGO/CdS as a working (WE), and graphite as a counter (CE) in 1 M polysulfide electrolyte. For illumination of the PEC cell, a Xenon lamp (35 W) with AM 1.5 G filter was used as a light source.

An area of 1 cm^2 of photoelectrode was exposed to the illumination and remaining area was masked with the epoxy resin. Masking helps to minimize the dark current and dark potential. The photograph of two electrode PEC cell setup under light condition with enlarged view of two electrode cell is shown in **Fig. 3.18**.
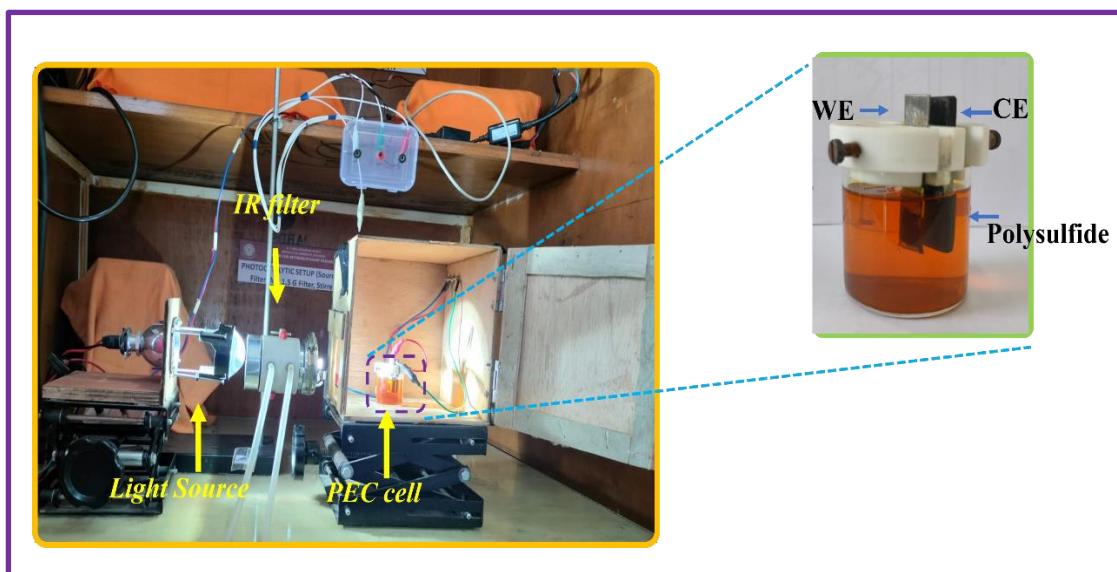
Fig. 3.18 Photograph of two electrode PEC cell under light condition with enlarged view of PEC cell

3.5.5 Power output characteristics of rGO thin film

Power output curves for rGO in dark, under light, and in chopping conditions are given in **Fig. 3.19**.

It is observed that, there is no noticeable difference in the power output curves of rGO under light, in dark, and in chopping conditions. That, implies the negligible generation of the charge carriers. So, rGO plays a role as a conductive backbone.
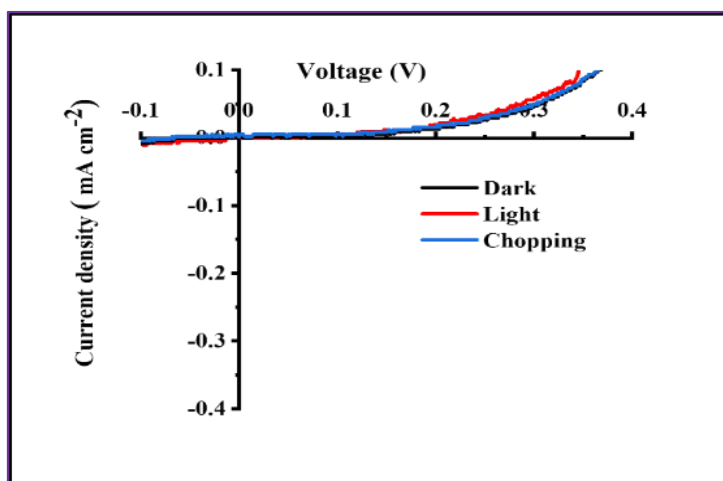
Fig. 3.19 Power output curves of rGO thin film electrode in dark, under light, and in chopping conditions.

3.5.6 Power output characteristics of CdS and rGO/CdS thin films

The power output characteristics of the CdS-40, rGO/CdS-40, CdS-60, rGO/CdS-60, CdS-80, and rGO/CdS-80 thin films in dark, under light, and in chopping conditions are showed in **Fig 3.20 (a-f)**.

The pure CdS and rGO/CdS composited thin films show cathodic behavior under illumination, confirming n-type electrical conductivity. The performance parameters of PEC cell such as fill factor (*FF)* and power conversion efficiency η (%) were calculated using equations (3.5) and (3.6), respectively

$$FF = \frac{(I_m \, V_m)}{(I_{sc} \, V_{oc})} \qquad (3.5)$$

Here,

I_m = the maximum current, and V_m = maximum voltage that can be extracted from PEC cell and I_{sc} and V_{oc} represent short circuit current and open circuit voltage, respectively. The relation for power conversion efficiency 'η' is,

$$\eta = \frac{I_{sc} \, V_{oc} \, FF}{P_{in}} \times 100 \qquad (3.6)$$
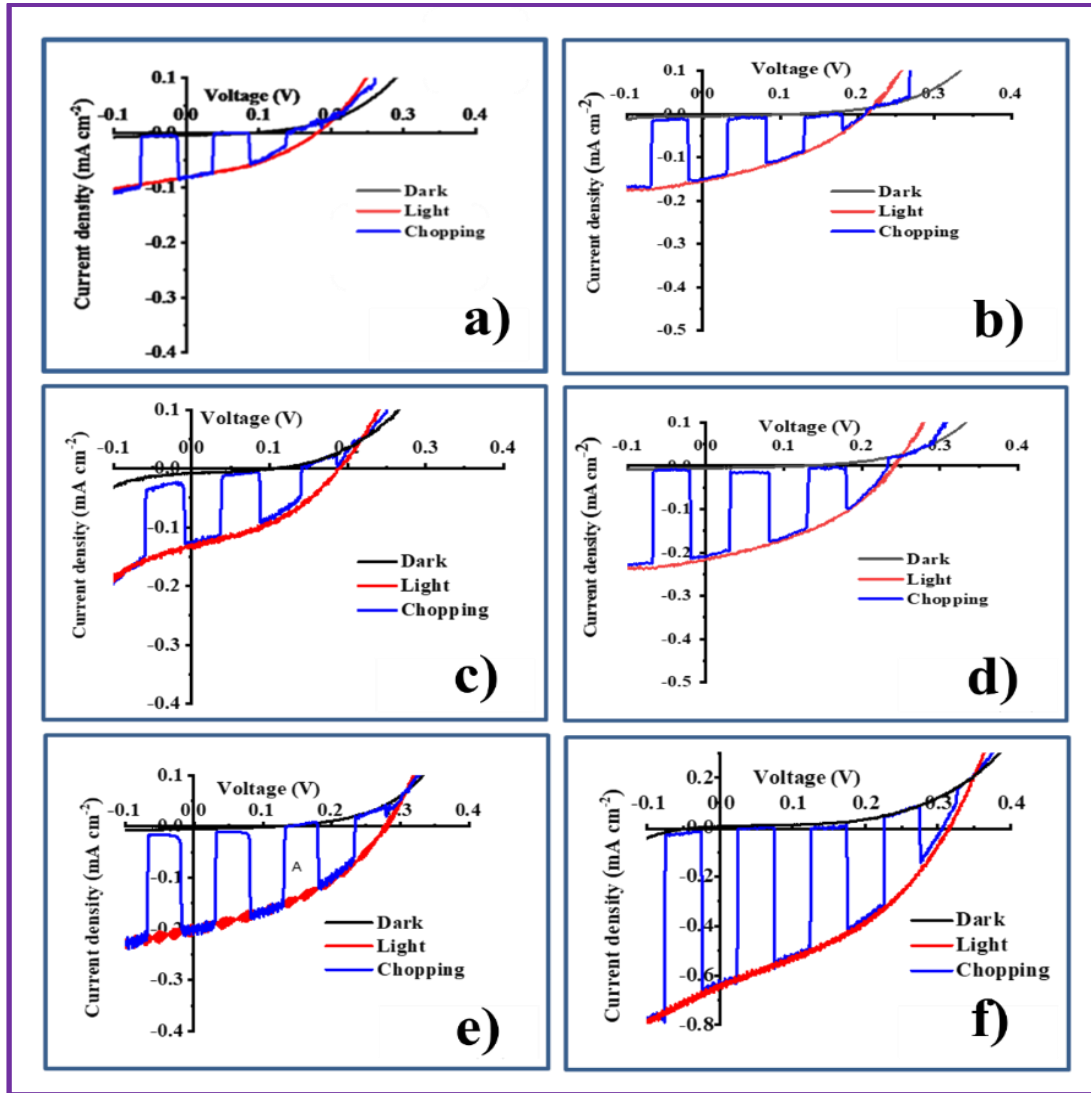
Fig. 3.20 Power output curves of a) CdS- 40, b) rGO/CdS-40, c) CdS- 60, d) rGO/CdS-60, e) CdS- 80, and f) rGO/CdS-80 thin film electrodes in dark, under light and in chopping conditions.

The PEC parameters are summarized in **Table 3.6**. The PEC performance gradually increases with thickness of CdS film. The rGO composited CdS electrodes showed higher performance than the bare CdS electrodes. The rGO/CdS-80 electrode showed $I_{SC} =$ 0.64 mA cm^{-2}, *Voc* = 0.31 mV, *FF* = 0.39 and η = 0.31 %.

Table 3.6: PEC parameters of CdS and rGO/CdS composite thin film electrodes.

Sample	*Isc* (mA cm^{-2})	*V_{OC}* (V)	*I_m* (mA cm^{-2})	*V_m* (V)	*FF*	Efficiency 'η' (%)
CdS-40	0.08	0.18	0.06	0.10	0.36	0.02
rGO/CdS-40	0.15	0.21	0.12	0.08	0.29	0.04
CdS-60	0.13	0.22	0.08	0.12	0.33	0.04
rGO/CdS-60	0.22	0.24	0.16	0.11	0.34	0.07
CdS-80	0.20	0.28	0.12	0.19	0.38	0.09
rGO/CdS-80	0.64	0.32	0.40	0.20	0.39	0.31

From **table 3.6**, it is observed that after CdS composited with rGO, the values of the *FF* and the η are enhanced. This enhancement may be due to the increased rate of the charge carries generation and the reduced self-recombination rate. Also, spherical shaped CdS nanoparticles are distributed on the rGO sheets having increased surface area and the porous morphology leads to the intimate contact between electrolyte and photoelectrode results in enhanced power conversion efficiency for rGO composited electrodes. In case of rGO/CdS-80 electrode, the higher value of 'η' is a reflection of more porous morphology, higher surface area, reduced contact angle value, and better optical absorbance properties.

3.6 Electrochemical impedance spectroscopy (EIS)

Electrochemical impedance spectroscopy (EIS) is a most significant tool used to investigate the charge transfer processes on the electrode, at the interface of electrode electrolyte and in electrolyte. The EIS studies were performed in the dark and under light conditions using Zive MP-1 electrochemical workstation within 1 kHz to 100 MHz frequency range. The Nyquist plot describes the relation between real impedance component (Z′) and imaginary impedance component (Z″). Each point on the Nyquist plot indicates impedance for the particular frequency. The Nyquist plot consists of left portion, middle portion and right portion corresponding to higher, middle and lower frequencies, respectively **[25]**.

3.6.1 EIS study of rGO thin films

The impedance spectra for rGO in dark and under light conditions are shown in **Fig. 3.21.** The impedance data are fitted to well suitable electrical circuit by Z-view software and the best suited equal electrical analog is fixed for all these spectra.

The fitted electrical analog circuit elements contain of R_S, R_{ct}, Q_1, and W. The R_S represents the ohmic series resistance and its value corresponds to intercept on the real axis (Z') in the high frequency region. The value of Rs depends on the sheet resistance of the substrate, electrical resistivity of redox solution and exterior contact resistance (wire connections) of the PEC cell. The R_{ct} indicates semicircle in high frequency range because of charge transfer resistance. The Q_1 leakage capacitance evolved due to mesoporous nature of the electrodes at the electrode electrolyte interface [38, 39].
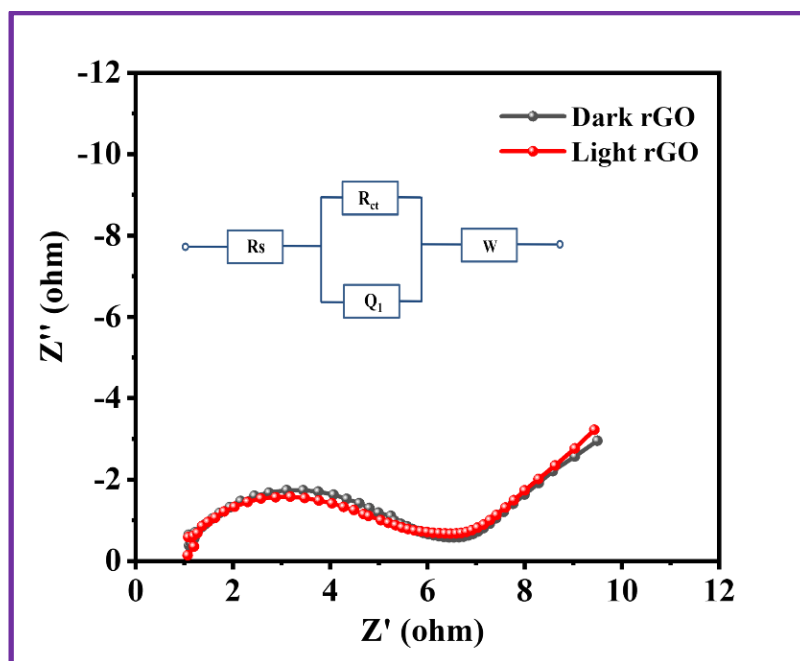
Fig. 3.21 Nyquist plot for rGO thin film in dark and under light environment with an equivalent circuit diagram.

The W represents the Warburg impedance (diffusion resistance). rGO shows the $Rs = 1.3 \ \Omega \ cm^{-2}$, $R_{ct} = 5 \ \Omega \ cm^{-2}$, $Q_1 = 43 \ \mu F$, and $W = 1.1 \ m \ \Omega$ in light conditions (**Table 3.7**). The lower value of R_{ct} indicates the higher charge transfer kinetics at the electrode electrolyte junction.

Table 3.7: EIS parameters of rGO thin film.

Sample	Condition	Rs (Ω cm^{-2})	R_{ct} (Ω cm^{-2})	Q_1 (μF)	W (mΩ)
rGO	Dark	1.4	5	44	1.1
	Light	1.3	5	43	1.1

3.6.2 EIS study of CdS and rGO/CdS thin films

The Nyquist plots of CdS-40, CdS-60, CdS-80, rGO/CdS-40, rGO/CdS-60, and rGO/CdS-80 thin film electrodes in dark and under light conditions are shown in **Fig. 3.22.** The obtained data are fitted to well suitable electrical circuit by Z-view software and the best suited equal electrical analog is fixed. The parameters after fitting data are summarized in **Table 3.8**.
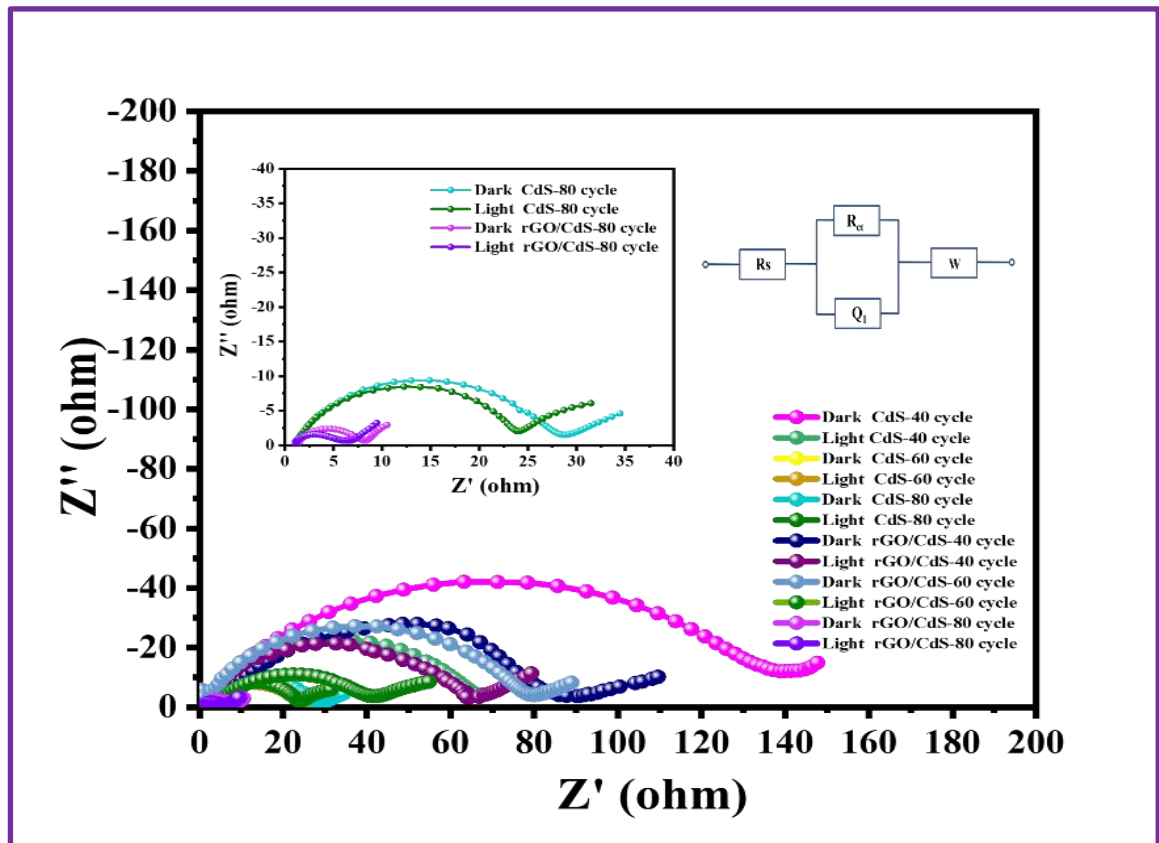
Fig. 3.22 Nyquist plots for CdS-40, CdS-60, CdS-80, rGO/CdS-40, rGO/CdS-60, and rGO/CdS-80 thin films in dark and under light environment with an equivalent circuit diagram (inset shows enlarged plots of CdS-80, and rGO/CdS-80).

The fitted electrical analog circuit elements contain of R_S, R_{ct}, Q_1 and W. It is seen from **Table 3.8**, under light condition, Rs values for CdS-80 and rGO/CdS-80 are 1.4 and 1.2 Ω cm^{-2}. For dark condition Rs values are 1.5 and 1.3 Ω cm^{-2}. In light condition R_{ct} values for CdS-80 and rGO/CdS-80 are 26 and 10 Ω cm^{-2}.

The Rs shows no significant change, specifying its independence on the same and minimum value of R_{ct} reveals the more dominant charge transfer kinetics in rGO/CdS composited thin films than pure CdS in visible light as compared to dark condition. rGO plays an important role as an electron shuttle between CdS and SS substrate leading to improve photocurrent **[18, 20]**. The EIS output agrees well with the photocurrent voltage characteristics.

Table 3.8: EIS parameters of rGO, CdS and rGO/CdS composite thin films.

Sample	Condition	Rs (Ω cm^{-2})	R_{ct} (Ω cm^{-2})	Q_1 (μF)	W (mΩ)
CdS-40	Dark	1.8	97	44	174
	Light	1.6	71	38	175
CdS-60	Dark	1.9	68	46	119
	Light	1.6	52	39	118
CdS-80	Dark	1.5	28	54	44
	Light	1.4	26	24	37
rGO/CdS-40	Dark	1.4	89	46	56
	Light	1.3	64	32	61
rGO/CdS-60	Dark	1.4	65	52	47
	Light	1.2	42	47	38
rGO/CdS-80	Dark	1.3	25	54	11
	Light	1.2	10	54	28

3.7 Conclusions

In present work, CdS and rGO/CdS films were successfully deposited by SILAR method on stainless steel substrates. The CdS and rGO/CdS films showed nanocrystalline structure with cubic phase. The EDAX studies revealed the presence of

Cd, S, C and O in stoichiometric amount with slightly sulfur rich content in rGO/CdS-80 film. The surface morphological study showed spherical shaped nanoparticles randomly sited on rGO sheets. Wettability study of rGO, CdS, and rGO/CdS revealed hydrophilic nature with lower contact angle of 33 ° for rGO/CdS-80. The composite made with rGO improves the values of fill factor (*FF*) and power conversion efficiency (*η*). The rGO composited film rGO/CdS- 80, showed the *FF* and (*η*) 0.39 and 0.31 %, respectively. The EIS studies showed that rGO composite lowers the charge transfer resistance which is valuable for superior charge transport process. Hence, it is concluded that composite of rGO with CdS boosts the power conversion efficiency nearly 3.5 times compared to CdS alone. So, rGO/CdS-80 is the best for the PEC cell application as compare to CdS-80 only.

3.8 References

1]   S. Bai, Q. Li, J. Han, X. Yang, X. Shu, J. Sun, L. Sun, R. Luo, D. Li, A. Chen, Int. J. Hydrog. Energy, 44 (2019) 24642-24652.

2]   V. Raut, C. Lokhande, V. Killedar, J. Electroanal. Chem., 788 (2017) 137-143.

3]   S. Cao, X. Yan, Z. Kang, Q. Liang, X. Liao, Y. Zhang, Nano Energy, 24 (2016) 25-31.

4]   C. Jiang, S. Moniz, A. Wang, T. Zhang, J. Tang, Chem. Soc. Rev., 46 (2017) 4645-4660.

5]   D. Dhawale, D. Dubal, M. Phadatare, J. Patil, C. Lokhande, J. Mater. Sci., 46 (2011) 5009-5015.

6]   S. Kumar and K. Rao, Energy Environ. Sci., 7, (2014) 45-102.

7]   A. Bhalerao, C. Lokhande, B. Wagh, IEEE Trans Nanotechnol., 12, (2013) 996-1001.

8]   A. Bhalerao, B. Wagh, R. Bulakhe, P. Deshmukh, J. Shim, C. Lokhande, J. Photochem. Photobiol. A, 336 (2017) 69-76.

9]   P. Deshmukh, U. Patil, K. Gurav, S. Kulkarrni, C. Lokhande, Bull. Mater. Sci., 35 (2012) 1181-1186.

10]   S. Mondal, S. Sudhu, S. Bhattacharya, S. Saha, J. Phys. Chem., 119 (2015) 27749-27758.

11]   H. Li, S. Xiao, J. Zhou, J. Zhao, F. Liu, G. Li, D. Zhang, Chem. Commun., 55 (2019) 2741-2744.

12]   M. Gopannagari, D. Kumar, H. Park, E. Kim, P. Bhavani, D. Reddy, T. Kim, Appl. Catal. B, 236 (2018) 294-303.

13]   H. An, X. Yan, H. Li, B. Yang, J. Wei, G. Yang, ACS Appl. Energy Mater., 2 (2019) 4195-4204.

14]   Q. Shen, X. Shi, M. Fan, L. Han, L. Wang, Q. Fan, J. Electroanal. Chem., 759 (2015) 61-66.

15]   A. Marlinda, N. Yusoff, S. Sagadevan, M. Johan, Int. J. Hydrog. Energy, 45 (2020) 11976-11994.

16]   L. Ma, X. Ai, X. Yang, X. Song, X. Wu, J. Phys. Chem. C, 45 (2020) 25133-25141.

17]   N. Vanasundaram, M. Ahmad, A. Chaudhary, P. Sharma, Mater. Res. Express., 7 (2020) 025015 (1-10).

18]   L. Wang, J. Feng, Y. Tong, J. Liang, Int. J. Hydrog. Energy, 44 (2019) 128-135.

19]   K. Dai, T. Hu, J. Zhang, L. Lu, Appl. Surf. Sci., 512 (2020) 144783 (1-50).

20]   F. Chen, X. Zou, C. Chen, Q. Hu, Y. Wei, Y. Wang, B. Xiang, J. Zhang, Ceram., 45 (2019) 14376-14383.

21]   M. Indhumathy and A. Prakasam, J. Mater. Sci.: Mater. Electron., 30 (2019) 15444-15451.

22]   S. Deshmukh, V. Kheraj, A. Panchal, Mater. Today: Proc., 5 (2018) 21322-21327.

23]   N. Meng, Y. Zhou, W. Nie, P. Chen, J. Nanopart Res., 18 (2016) 1-13.

24]   R. Ranjan, M. Kumar, A. Sinha, Int. J. Hydrog. Energy, 44 (2019) 10573-10584.

25]   C. Foo, H. Lim, A. Pandikumar, N. Huang, Y. Ng, J. Hazard. Mater., 304 (2016) 400-408.

26]   K. Hareesh, S. Dhole, D. Phase, J. Williams, Mater. Res. Bull., 110 (2019) 82-89.

27]   H. Chen, L. Ding, K. Zhang, Z. Chen, Y. Lei, Z. Zhou, R. Hou, Int. J. Electrochem. Sci., 15 (2020) 10231-10242.

28]   A. Mitkari and A. Ubale, Mater. Manuf. Process, 5 (2019) 49-56.

29]   H. Xia, X. Zhang, Z. Shi, C. Zhao, Y. Li, J. Wang, G. Qiao, Mater. Sci. Eng. A, 639 (2015) 29-36.

30]   H. Shelke, A. Lokhande, V. Raut, A. Patil, J. Kim, C. Lokhande, J. Mater. Sci. Mater. Electron., 28 (2017) 7912-7921.

31]   S. Sengupta and M. Kundu, Energy Technol., 11 (2023) 2300078 (1-10).

32] V. Ashith and G. Rao, Thin Solid Films, 616 (2016)197-203.

33] H. Liu, T. Lv, X. Wu, C. Zhu, Z. Zhu, Appl. Surf., 305 (2014) 242-246.

34] E. Nosheen, S. Shah, Z. Iqbal, J. Photochem. Photobiol. B, 167 (2017) 117-127.

35] C. Lee, S. Yu, T. Kim, Nanomater., 8 (2018) 17 (1-13).

36] J. Condon, Surface area and porosity determinations by physisorption: measurements and theory. 1 st ed^n. (Elsevier, Amsterdam; Boston, 2006), pp. 1-274.

37] R. Bera, S. Kundu, A. Patra, ACS Appl. Mater. Interfaces., 7 (2015) 13251-13259.

38] A. Bhalerao, B. Wagh, N. Shinde, S. Jambure, C. Lokhande, Energy Procedia, 54 (2014) 549-556.

39] N. Zainal, J. How, X. Choo, C. Soon, IEEE, SCOReD, (2020) 385-390.

Chapter-IV

CdSe and rGO/CdSe thin films by successive ionic layer adsorption and reaction (SILAR) method: synthesis, characterization, and their photoelectrochemical (PEC) performance

CHAPTER- IV

CdSe and rGO/CdSe thin films by successive ionic layer adsorption and reaction (SILAR) method: synthesis, characterization, and their photoelectrochemical (PEC) performance

Section A

4.1 Introduction

In recent days, the global energy need is rising day by day due to overpopulation and worldwide techno-economic growth. The progress of humans and nation is depending on the utilization of energy. In order to have rapid development, adequate energy is a key requisite. At present, mainly fossil fuels viz. petrol, diesel, coal, etc., are used to fulfill the energy requirement of the world. However, due to limited availability, environmental pollution, and overutilization of fossil fuels, mankind is going through a drastic energy crisis situation. In order to resolve this energy crisis, scientists are looking forward for pollution free, eco-friendly, affordable, secure, and sustainable sources of energy [1].

To reduce dependency on fossil fuels and quench energy requirement, researchers are gregariously paying interest in renewable energy sources (RES) including solar, nuclear, wind, tidal, geothermal, etc.. Among them, solar energy is one of the best options. It is a clean and green energy source, as it does not generate any pollutants or byproducts hazardous to the environment; also, it is an abundantly available, eternal, and infinite source of energy [2]. The continuous alteration of light into electrical energy is a main aspect to utilize solar energy efficiently. Photovoltaic devices are used for the conversion of light into electrical energy. But photoelectrochemical (PEC) solar cells have specifically attracted more attention due to easy junction fabrication and natural storage capacity [3]. The semiconductor photoelectrode (cathode or anode) is a heart of the PEC solar cell, so the proper selection and matching of it with electrolyte is a prime requisite to fabricate efficient long lasting solar cell.

Binary semiconductors group of II–VI (ZnSe, CdS, CdTe, CdSe, etc.) compounds provides wide applications in the sector of science and technology mainly in an optoelectronic and photovoltaic applications such as photodetector, sensor device, light emitting diode, solar cell, optoelectronic device, as well as PEC cell [4-10]. The band gap value of cadmium selenide (CdSe) is 1.74 eV (bulk), which covers the maximum wavelength of the visible part of the solar spectrum. Therefore, CdSe is a remarkable material to enhance the photocurrent of PEC cell. Many researchers are working on CdSe to improve its performance in an optoelectronic application by engineering its structural, optical, electrical, etc. properties. To improve PEC efficiency of CdSe, the strategies like various deposition methods, optimization of

layer thickness, etching, thermal annealing, bonding with carbonaceous materials and other materials, etc. are applied **[11, 12]**.

Graphene has two-dimensional (2D) honeycomb structure with sp^2 hybridization creating more interest in multidisciplinary applications due to unique electrical, thermal, optical, and mechanical characteristics, it also has high surface area and complex surface characteristics **[13, 14]**. But it is less used for optoelectronics and photonics applications due to theoretical zero band gap. The composite with graphene or nanoparticles deposited over graphene sheets have widened applications and maximizes the potential of graphene as well as supports the nanoparticles in optoelectronics.

Different chemical methods like hydrothermal, doctor blade, CVD, SILAR, electrodeposition (ED) **[15-20]** have been used to synthesize rGO/CdSe composite thin films. SILAR is a low cost, simple method for rGO/CdSe deposition with control of film thickness and large scale area deposition on any type of substrates.

Present chapter concerns the deposition of CdSe and rGO/CdSe composite thin films via SILAR method on stainless steel substrates. The physicochemical characterizations of films were studied. The photoelectrochemical (PEC) and electrochemical impedance spectroscopy (EIS) properties were investigated using three electrode system in 1 M polysulfide electrolyte.

4.2 Experimental details

4.2.1 Substrate cleaning

Stainless steel (SS) substrates were cleaned as per procedure explained in **chapter III section 3.2.1.**

4.3 Material synthesis

4.3.1 Chemicals

The cadmium sulfate ($CdSO_4$), selenium powder (Se), sodium sulfite (Na_2SO_3), and tartaric acid ($C_4H_6O_6$) purchased from Thomas Baker (TB) and utilized as received. DDW was used to prepare all solutions. SS (304 grade) plates of 5 cm x 1 cm dimensions were used as substrates for deposition.

4.3.2 Deposition of rGO thin films

The rGO preparation and deposition of thin films by using the dip and dry strategy is explained in **chapter III section 3.2.2.1** and **3.2.2.2**, respectively.

4.3.3 Deposition of CdSe thin films

CdSe thin films were deposited using SILAR method at room temperature. Typically, Aqueous solutions of 0.2 M $CdSO_4$ (pH = 2.4 ± 0.1) and freshly prepared 0.1 M sodium selenosulfate (Na_2SeSO_3) (pH = 9 ± 0.1) were utilized as cationic and anionic precursors, respectively. 0.1 M $C_4H_6O_6$ is used as a complexing agent. Primarily, the SS substrate was immersed in cationic solution for 40 s to adsorb [Cd $(C_2H_6O_6)]^{2+}$ complexed ions, followed by rinsing in DDW for 30 s to eliminate weakly bound [Cd $(C_2H_6O_6)]^{2+}$ cations. After that, the substrate was dipped in anionic solution for 40 s for reaction of Se^{2-} ions to form solid CdSe monolayer. The substrate is again rinsed in DDW for 30 s to eliminate unreacted species. This was regarded as a single SILAR cycle; such 400 optimized SILAR cycles were performed. The deposited films were named as CdSe and annealed at 400 K for 60 min in air atmosphere. The optimized preparative parameters are summarized in **Table 4.1**.

Table 4.1: Preparative parameters for deposition of CdSe thin film by SILAR method.

Parameters for (CdSe)	Precursor solution	
	Cationic ($CdSO_4$)	Anionic (Na_2SeSO_3)
Concentration (M)	0.2	0.1
Solution pH	2.4 ± 0.1	9 ± 0.1
Complexing agent (0.1 M)	$C_2H_6O_6$	
Immersion time (s)	40	40
Cycles	400	

4.3.4 Deposition of rGO/CdSe composite thin films

For the deposition of rGO/CdSe composite thin films, rGO deposited SS substrates of thickness 90 nm were dipped in cationic and anionic precursors for CdSe deposition as mentioned in previous **section 4.3.3** for optimized 400 SILAR cycles. The deposited films were named as rGO/CdSe and annealed at 400 K temperature for 60 min.

4.3.5 rGO/CdSe film formation mechanism

In SILAR, solvated cations and anions are deposited successively on rGO deposited SS substrate surface to form rGO/CdSe film. The rGO thin films were deposited on SS substrate as explained in **section 4.3.2**. **Fig. 4.1** is a schematic representation of rGO/CdSe thin film deposition via four beaker SILAR method on rGO deposited SS substrate at room temperature. 0.2 M $CdSO_4$ (pH = 2.4 ± 0.1) and freshly prepared 0.1 M Na_2SeSO_3 (pH = 9 ± 0.1) were utilized as cationic and anionic precursors, respectively.
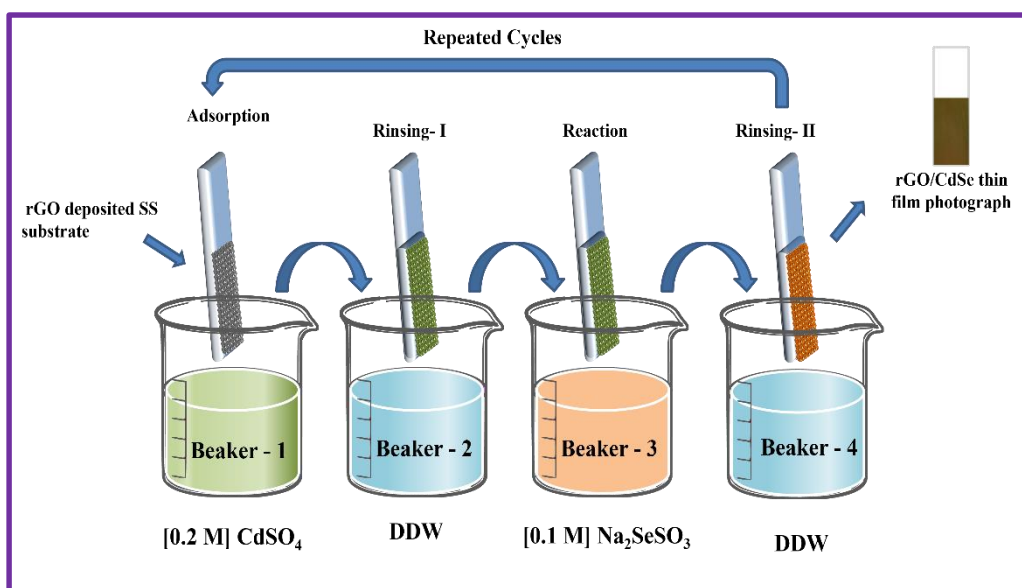
Fig. 4.1 Schematic of rGO/CdSe thin film deposition by SILAR method on SS substrate.

Deposition consists of the following subsequent steps:

Beaker - 1 (Adsorption): rGO deposited SS substrate was immersed for 40 s in a cationic precursor solution of $CdSO_4$ complexed with tartaric acid ($C_2H_6O_6$). The cadmium complex $[Cd (C_2H_6O_6)]^{2+}$ adsorbes on rGO deposited substrate surface. This adsorption may be due to reaction with extra-planer hydroxyl or carboxyl groups of rGO sheets.

Beaker - 2 (Rinsing – I): After that, it was rinsed in DDW for 30 s to eliminate unadsorbed $[Cd (C_2H_6O_6)]^{2+}$.

Beaker - 3 (Reaction): Further, the SS substrate was dipped in a hydrolyzed anionic precursor solution containing Se^{2-} ions for 40 s,

$$Na_2SeSO_3 + 2OH^- \rightarrow Se^{2-} + Na_2SO_4 + H_2O \qquad (4.1)$$

Se^{2-} ions react with Cd^{2+} complexed ions to form a CdSe layer on rGO surface. The net reaction can be shown as,

$$Cd\ (C_2H_6O_6)^{2+} + Se^{2-} + Na_2SO_4 + H_2O \rightarrow CdSe + C_2H_6O_6 + H_2O \qquad (4.2)$$
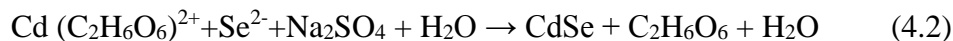
Beaker - 4 (Rinsing – II): The unreacted and overloaded CdSe particles were removed by dipping the substrate in DDW for 30 s to complete a single SILAR cycle and such 400 cycles were performed to obtain well adherent uniform CdSe thin films on rGO substrate. After deposition, film annealed at optimized temperature of 400 K for 60 min and named as rGO/CdSe.

4.4 Thickness measurement

The gravimetric weight difference method was used to determine thickness of CdSe and rGO/CdSe thin films as explained in **chapter III section 3.2.2.5**.

By gravimetric weight difference method, thickness for CdSe thin film was found to be 1421 nm for 400 SILAR cycles and such film was used for forming composite with rGO. In case of rGO/CdSe film, the thickness of rGO film was calculated first and this film was used as a substrate for CdSe deposition. For rGO/CdSe thin film, the thickness of CdSe over rGO film calculated by mathematical addition of rGO and CdSe layer by gravimetric weight difference method, calculated thicknesses for rGO and rGO/CdSe are 90 and 1558 nm, respectively. The increased thickness of rGO/CdSe composite thin film may be due to availability of previous nucleation sites of rGO surface and higher surface area (sheet like surface).

4.5 characterizations of films

The characterizations of CdSe and rGO/CdSe were carried out as mentioned in **chapter III section 3.3**.

4.6 Results and discussions

4.6.1 Physicochemical properties of CdSe and rGO/CdSe thin films

4.6.1.1 XRD study

Fig. 4.2 depicts the XRD patterns of CdSe and rGO/CdSe thin films. The predominant peak observed at $2\theta = 25.19\ °$ in XRD pattern of films, shows strong

orientation along (111) plane of the cubic CdSe which well matched with JCPDS card no: 019-0191 **[21-23]**.

The '*' peaks belong to the SS substrate. No specified diffraction peak of rGO was observed in XRD pattern of rGO/CdSe composite thin film, which may be due to the low diffraction intensity and relatively small amount of rGO **[24]**. Scherrer equation was used to calculate crystallite size **[25]**. The estimated values of crystallite sizes for CdSe and rGO/CdSe was found to be 4 and 2 nm for (111) plane.

The reduction in the crystallite size of nanoparticles of rGO/CdSe electrode is observed due to more nucleation cites and centres for growth of CdSe on rGO layer. The peak broadening in the XRD signals for rGO/CdSe composite demonstrates the formation of smaller crystallites of CdSe **[26]**. Similar reductions in crystallite size were reported by the Nosheen et al. **[27]** and Mondale et al. **[28]** for rGO/CdS composites by chemical deposition methods.
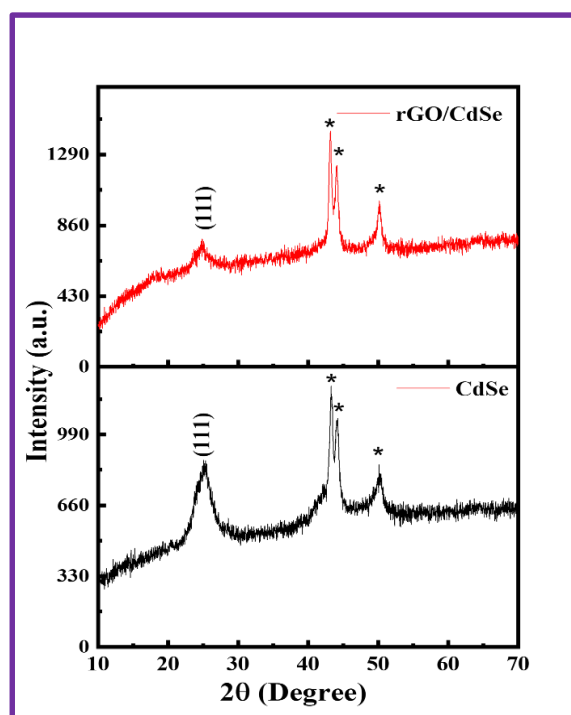
Fig 4.2 The XRD patterns of CdSe and rGO/CdSe thin films on SS substrate.

4.6.1.2 FE-SEM study

Surface morphology of CdSe, and rGO/CdSe thin films were studied with the help of FE-SEM analysis. The FE-SEM images of CdSe and rGO/CdSe are given in **Fig. 4.3 (a-d)** at two magnifications (5 kX and 10 kX). CdSe electrode shows uniform film surface with aggregation of the spherical nanoparticles with cauliflower-like structure (**Fig. 4.3 (a-b)**).
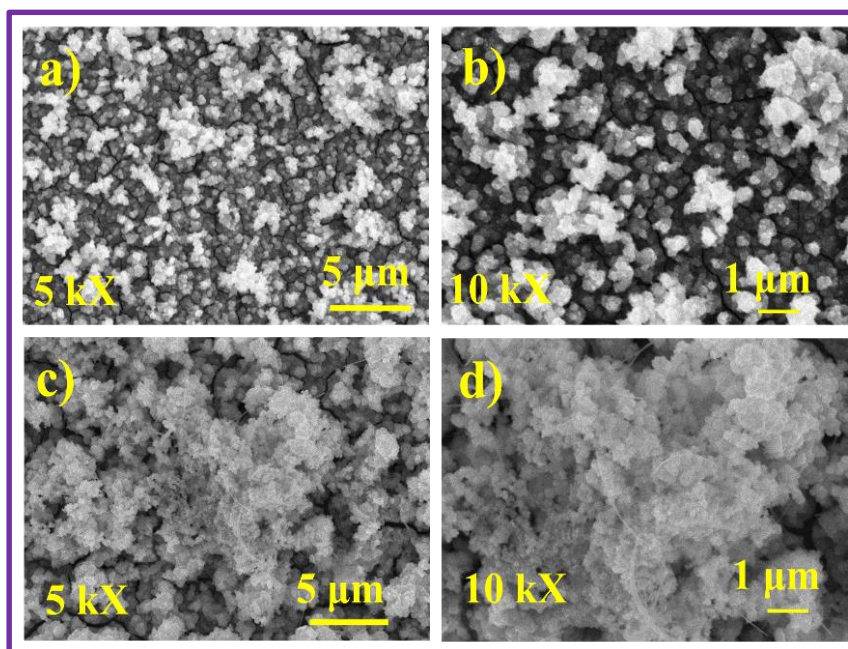
Fig. 4.3 The FE-SEM images of (a-b) CdSe, and (c-d) rGO/CdSe composite thin films at two magnifications of 5 kX and 10 kX.

The appearance of some cracks may because of different thermal expansion coefficients of SS and CdSe during annealing process. For rGO composited thin film, surface becomes more porous and spongier consisting the larger number of the spherical shaped nanoparticles distributed on rGO sheets with less agglomeration **Fig. 4.3 (c-d)**. The rGO sheets in FE-SEM of rGO/CdSe composite are not seen, which may be due to a less amount of rGO and hidden behind the upper layer of CdSe nanoparticles. But it played its role to reduce the agglomeration of CdSe nanoparticles **[17]**. Patidar et al. **[15]** have reported the similar morphology by hydrothermal method for rGO/CdSe composite. The more porous morphology leads hydrophilicity useful for the better electrochemical properties due to establishment of proper contact of electrode surface with an electrolyte.

4.6.1.3 EDAX study

Elemental composition of CdSe, and rGO/CdSe samples were carried out via EDAX study. **Fig. 4.4 a)** gives evidence of the existence of both cadmium (Cd) and selenium (Se) species; the average atomic percentage of Cd:Se are 52:48; with nearly 1:0.92 stoichiometry of CdSe sample. The **Fig. 4.4 b)**, evidences the presence of Cd, Se, and carbon (C) were nearly stoichiometric which implies that Se deficient electrode. The average atomic percentage of Cd:Se:C are 44:41:15 with stoichiometry of the sample nearly 1:0.93:0.34, for rGO/CdSe sample. The loss of Se is due to the

evaporation of free elemental Se from the film during annealing. The successful composition of CdSe with rGO evidenced by the appearance of rGO in the EDAX pattern of rGO/CdSe composite, it supports to XRD study.
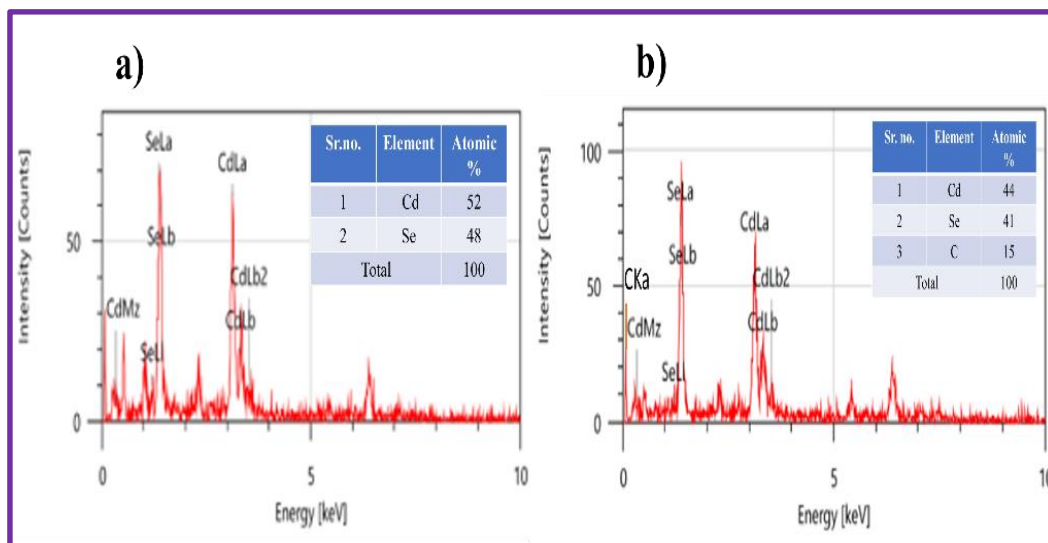
Fig. 4.4 The EDAX patterns of a) CdSe and b) rGO/CdSe samples.

4.6.1.4 Contact angle measurement

The surface wettability study of electrodes was investigated using water contact angle measurement. It is an angle between liquid/air and solid interfaces. It is fixed for any known system and its value determines interactions across the three interfaces. The smaller contact angle value denotes hydrophilic (less than 90 °) surface whereas higher contact angle demonstrates hydrophobic (greater than 90 °) nature.
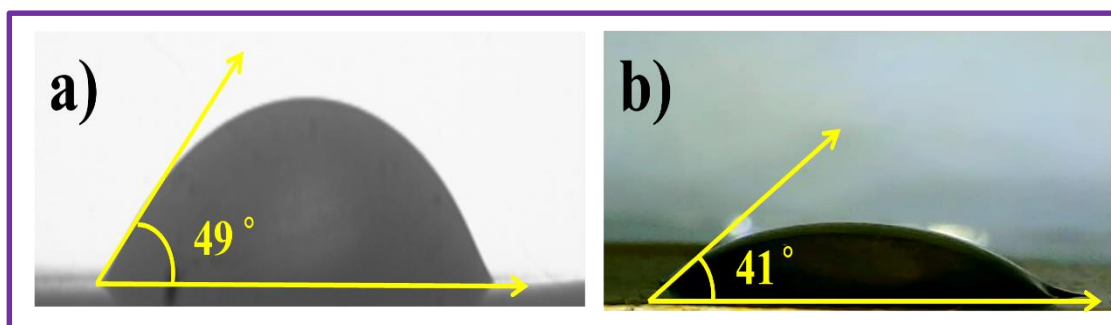
Fig. 4.5 Contact angle photographs of a) CdSe, and b) rGO/CdSe thin films.

From **Fig. 4.5 (a-b)**, it is observed that CdSe and rGO/CdSe electrodes have the water contact angle values of 49 and 41 °, respectively. Both films showed hydrophilic nature. There is a strong relationship between surface porosity and roughness with the contact angle value of each material whether it is a metal or polymeric film. Indeed, being a dense (non-porous) or porous surface highly affects the contact angle value because water drop can penetrate into the big pores of the

surface due to the capillary forces and accordingly spread on the surface leading to a contact angle reduction **[29, 30]**.

In present case, the reduction in contact angle for rGO/CdSe film is attributed to an irregular morphology, spongy and porous surface of the film. Logu et al. **[31]** reported a decrease in the contact angle with an increase in surface roughness. Similar results of reduction in contact angle value were reported by Raut et al. **[32]**, Gawali and Bhosale **[33]** for electrodeposited CdSe electrodes.

4.6.1.5 BET study

The surface area is very significant during light absorption at various incident angles in the solar cell. Thus, it is important to investigate BET analysis for CdSe and rGO/CdSe composite materials. **Fig. 4.6 (a-b)** displays the N_2 adsorption-desorption isotherms measured for powder samples of CdSe and rGO/CdSe.

The curves of relative pressure vs volume adsorption for CdSe and rGO/CdSe composite showed type IV isotherm amended by H1 type hysteresis loop **[34]**. The CdSe and rGO/CdSe showed the specific surface areas of 11.75 and 13.86 m^2 g^{-1}, respectively. The noticeable increment in surface area of rGO/CdSe sample is observed after composition with rGO, which may be due to higher surface area property of rGO, this allows for greater electrochemical contact and an improvement in power conversion efficiency.
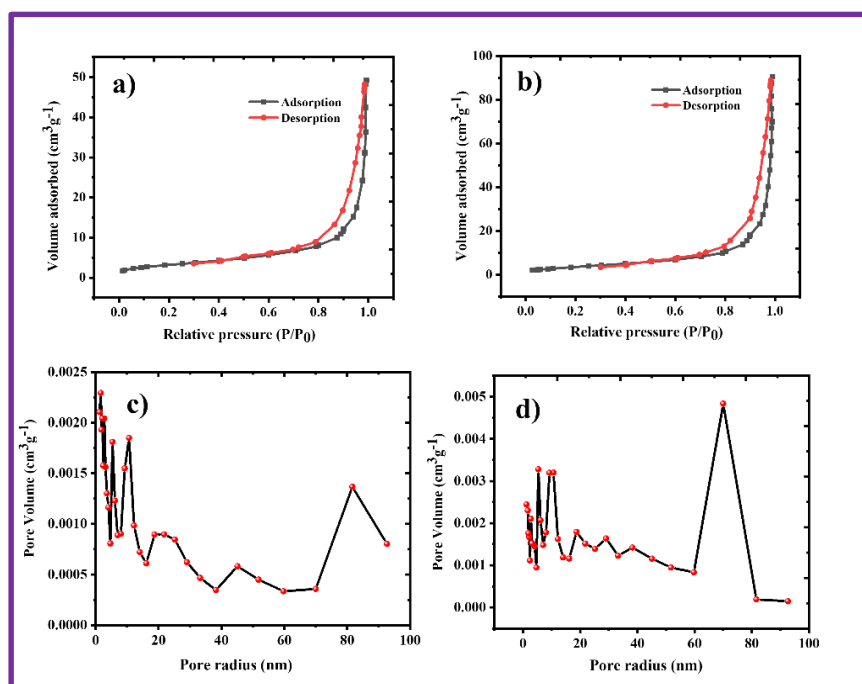
Fig. 4.6 (a-b) N_2 sorption plots, and (c-d) BJH plots of CdSe and rGO/CdSe samples.

In BJH graph, the average pore size distribution of the fine crystallite nature is integrated. The plots of pore volume vs pore radius of CdSe and rGO/CdSe shown in **Fig. 4.6 (c-d)** reveal the mesoporous to macroporous nature **[35].** The observed results of the BET analysis strongly support to contact angle reduction due to porous nature of CdSe, and rGO/CdSe films. Porous materials with interconnected pore structures have more surface area, enhancing their ability to capture light effectively. These pores also aid in efficient movement of charged particles within the material, allowing photoexcited carriers to quickly reach electrode surfaces, minimizing loss. Moreover, the intimate contact between electrode and electrolyte due to these pores promotes surface reactions, improving the utilization of photo generated charge carriers. The porosity and increased surface area of the sample helps in good electrochemical contact with electrolyte and electrode leads an improved electrochemical property.

4.6.1.6 Optical absorption study

Diffuse reflectance spectroscopy (DRS) was used to study optical properties of CdSe and rGO/CdSe electrodes. **Fig. 4.7** shows the Tauc plots of CdSe and rGO/CdSe electrodes. Both electrodes show the absorbance in the visible range from 500 to 800 nm. The absorption band edges are found at 703 and 723 nm for CdSe, and rGO/CdSe, respectively (**Fig. 4.7 Inset**).
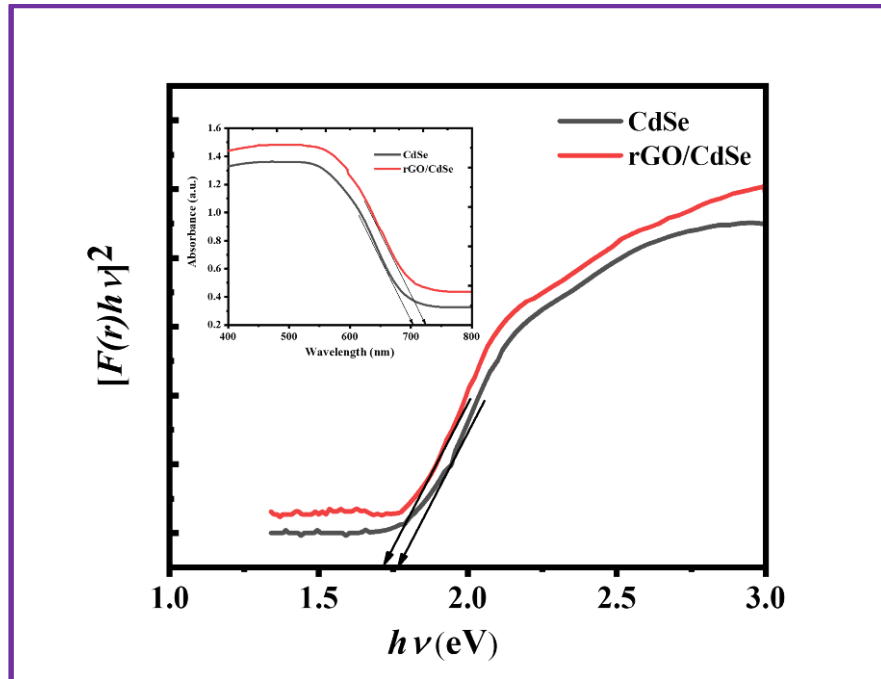
Fig. 4.7 Diffuse reflectance spectra of CdSe, and rGO/CdSe thin films (Inset shows absorbance spectra of CdSe, and rGO/CdSe).

The red shift in absorbance is due to the CdSe composite with rGO [36]. It has not only high electron mobility but also suppresses recombination of electron hole pairs. The rGO/CdSe thin film shows more proficiency in utilizing visible light than that of CdSe [17]. Kubelka-Munk standard equation is used to calculate band gap *(Eg)* of the electrodes.

The band gap values are found to be 1.77, and 1.72 eV for CdSe and rGO/CdSe electrodes, respectively. Hence, composite with rGO exhibits shift in optical spectrum because of charge localizations in each nanocrystal. This may be due to crystallite size-dependent modifications observed in semiconductor properties. The reduction in band gap energies for lower crystallite sizes has been reported for thin films deposited by chemical methods [24, 37].

Section B

4.7 Electrochemical characterizations of CdSe and rGO/CdSe thin films

For PEC solar cell technology electrochemical studies are most crucial. The proper formation of electrode electrolyte junction, semiconductor material type, and generation of electron hole pairs are studied using I-V characteristics of CdSe and rGO/CdSe materials. The PEC cell parameters of CdSe and rGO/CdSe are studied using power output characteristics. For both CdSe and rGO/CdSe electrodes, the charge transfer processes at the electrode electrolyte junction are understood through the use of electrochemical impedance spectroscopy (EIS).

4.7.1 I-V characteristics of CdSe and rGO/CdSe thin films

For I-V characteristics three electrode cell was fabricated consisting of CdSe or rGO/CdSe as a working, SCE as a reference, graphite as a counter electrode, and 1 M polysulfide as an electrolyte.

Fig. 4.8 (a-b) depicts the I-V curves of CdSe and rGO/CdSe thin films in dark and under light conditions. The symmetry factor (β) was estimated from the I-V curves by using formulae as mentioned in **chapter I section 1.2.3**. The values of 'β' for CdSe and rGO/CdSe polysulfide junctions are given in **Table 4.2.**
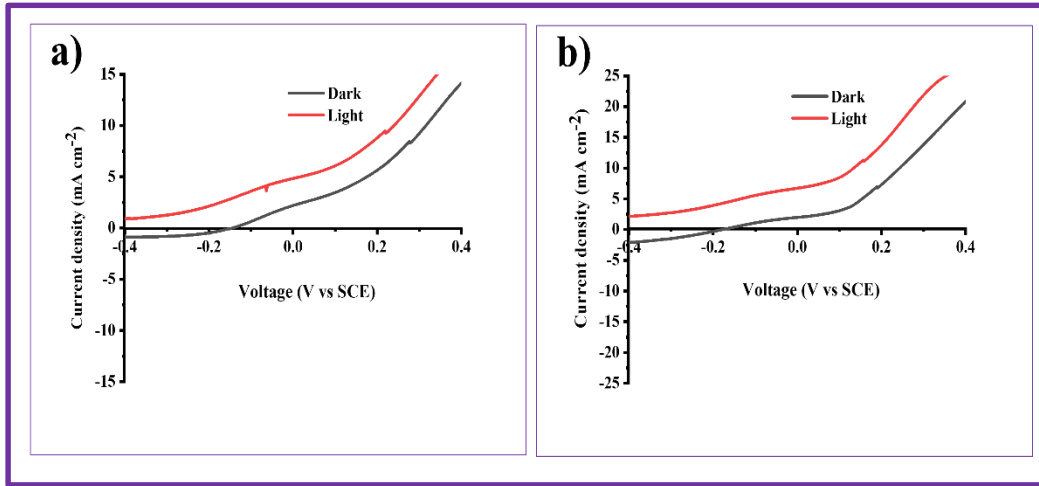
Fig. 4.8 The I-V characteristics of a) CdSe and b) rGO/CdSe thin films in dark and under light conditions.

Table 4.2: The 'β' values of CdSe and rGO/CdSe thin film electrodes in dark and under light conditions.

Sr. No.	Electrode	Measurement condition	$\beta = \dfrac{2.303\ RT}{bF}$	$\beta = 1 - \dfrac{\left(\log \dfrac{I}{I_0}\right) RT}{qV}$
1	CdSe	Dark	0.93	0.93
		Light	0.95	0.95
2	rGO/CdSe	Dark	0.94	0.93
		Light	0.96	0.96

From **Table 4.2**, the 'β' values for CdSe and rGO/CdSe in both measurement conditions are closer to 1, that implies the proper electrode electrolyte contact. In case of rGO composited CdSe electrode, the value of the 'β' factor under light condition is slightly greater than the dark condition which implies the reduction in the recombination process and the bulk charge transfer phenomenon. The higher value of 'β' implies the better interface quality, where charge carriers are efficiently transported across the interface without significant losses due to recombination. The higher value of 'β' support to the wettability study which shows intimate contact between electrode surface and the electrolyte. For 'β' and the ideality factor ('n') are related to each other in the sense, for lower recombination (greater 'β'), 'n' tends towards unity, indicating improved device performance and reduced non-ideal behavior.

4.7.2 Power output characteristics of CdSe and rGO/CdSe thin films

The two electrode PEC device was fabricated using CdSe or rGO/CdSe as a WE and graphite as a CE in 1 M polysulfide electrolyte.

Fig. 4.9 (a-b) depicts power output curves for CdSe, and rGO/CdSe electrodes. The experimental arrangement used for measurement of PEC parameters of device are explained in previous **chapter III section 3.5.4.** CdSe electrode showed cathodic nature under light condition, which confirms n-type electrical conductivity **[10]**. The fill factor (*FF*) and power conversion efficiency (*η*) were calculated by using equations given in **chapter III section 3.5**.
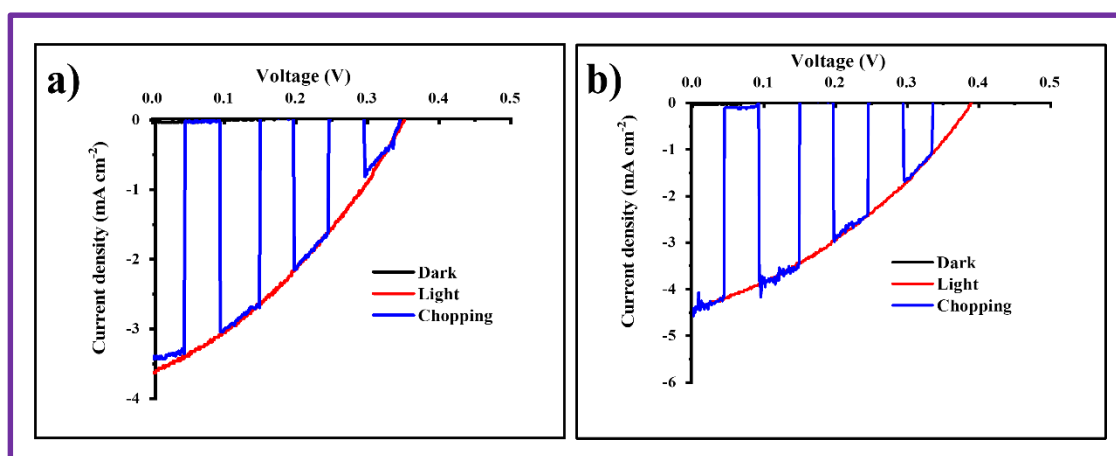
Fig. 4.9 Power output curves of a) CdSe, and b) rGO/CdSe thin films in dark, under light, and in chopping conditions.

The obtained PEC parameters of electrodes are tabulated in **Table 4.3**. It is observed from **Table 4.3**, rGO/CdSe electrode demonstrated higher PEC efficiency (η = 2.18 %) than pure CdSe electrode (η = 1.54 %). This enhancement can be attributed to the reduced recombination rate of charge carriers due to conductive backbone of rGO. This improvement can be explained by considering the changes in morphology, crystalline quality, reduced grain boundaries, hydrophilicity and optical properties caused by composite with rGO **[15, 38]**. The surface structure of CdSe electrode and the reduced recombination of electron-hole pairs allow easy charge flow through the composite with rGO, which result in an improved PEC performance. From PEC study it can be say that, the rGO composited CdSe electrode is more efficient than CdSe may due to good electrical, surface morphological and optical properties of rGO.

Table 4.3: The PEC parameters of CdSe and rGO/CdSe thin film electrodes.

Sr.no	Sample	I_{SC} (mA cm^{-2})	V_{OC} (V)	I_m (mAcm^{-2})	V_m (V)	*FF*	Efficiency 'η' (%)
1	CdSe	3.60	0.35	1.71	0.24	0.32	1.54
2	rGO/CdSe	5.41	0.28	2.60	0.22	0.37	2.18

4.7.3 Electrochemical impedance spectroscopy (EIS) study

In electrochemical applications, the interaction between the electrode material and its interface with electrolyte plays an eminent role. The EIS is a prominent tool used to investigate the charge transfer processes at the electrode and electrolyte interface. The Nyquist plot of real impedance (*Z'*) vs imaginary impedance (*Z''*). The three portions of Nyquist plot are right, middle, and left which are assigned to higher, middle and lower frequencies, respectively. The EIS study of the electrodes was conducted from 1 kHz to 1 MHz with an AC amplitude of 10 mV, both in the dark and under light conditions, as illustrated in **Fig. 4.10**.
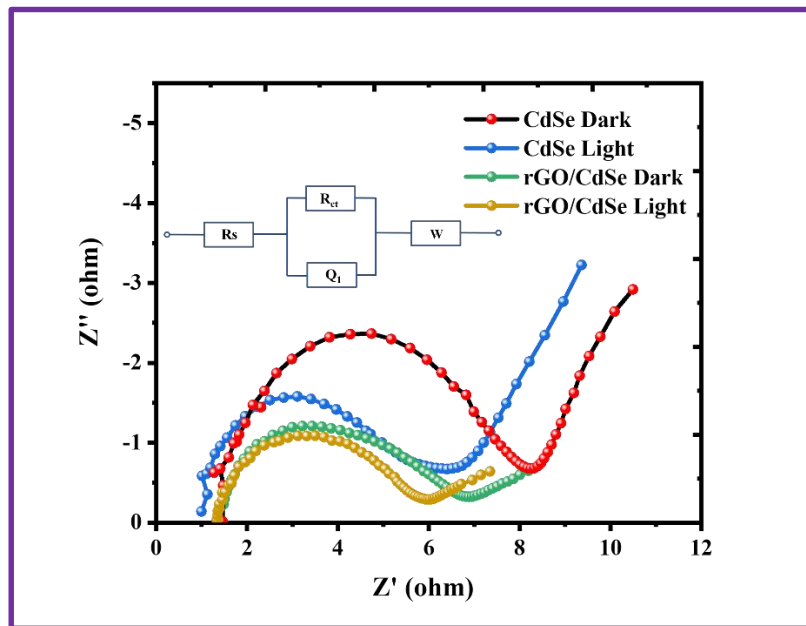
Fig. 4.10 Nyquist plots for CdSe, and rGO/CdSe thin films in dark and under light conditions with an equivalent circuit diagram.

The Nyquist plots of CdSe and rGO/CdSe composited electrodes were analyzed using equivalent circuit by 'Z view' software and findings are summarized in **Table 4.4**.

Fig. 4.10 inset shows equivalent electrical circuit comprising of an element series resistance (R_S), charge transfer resistance (R_{ct}), leakage capacitance (Q_1) and Warburg or diffusion resistance (W). It is seen that, as a semicircle diameter of Nyquist plot smaller, the charge transfer resistance (R_{ct}) be smaller. From **Table 4.3**, the R_s, and R_{ct} values of both samples are significantly lower under light than in dark environment, which evidences that both electrodes generate charge carriers under light.

Table 4.4: EIS parameters of CdSe and rGO/CdSe thin film electrodes.

Sr. No.	Sample	Testing condition	R_s (Ω cm^{-2})	R_{ct} (Ω cm^{-2})	Q_1 (μF)	W (mΩ)
1	CdSe	Light	1.1	6	85	34
		Dark	1.2	7	94	28
2	rGO/CdSe	Light	1.3	5	51	23
		Dark	1.5	7	63	11

For CdSe, the R_s, and R_{ct} values are 1.1 Ω cm^{-2} and 6 Ω cm^{-2}, respectively under light condition. Along that, rGO/CdSe have R_s, and R_{ct} values are 1.3 Ω cm^{-2} and 5 Ω cm^{-2}, respectively under light condition. The reduction in R_{ct} value for rGO/CdSe composited electrode may be due to the presence of rGO better electrical conductivity which improves the charge transfer rate at electrode electrolyte interface reflects in an enhanced electrochemical performance **[39]**. Also, surface morphology, hydrophilicity, and the binder free synthesis of CdSe eliminates the limitations of binders like addition of resistance and dead volume.

4.8 Conclusions

In the current work, CdSe and rGO/CdSe composite thin films were deposited on SS substrate by binder free SILAR method. CdSe, and rGO/CdSe electrodes showed nanocrystalline structure with cubic phase. The EDAX studies revealed a slight Se deficiency in stoichiometric amount of rGO/CdSe films. The study of surface morphology revealed that the spherical nanoparticles exhibited a cauliflower-like structure for CdSe and a more porous and spongy structure for rGO composited CdSe electrode with hydrophilic nature. The rGO/CdSe thin film showed a reduced optical band gap value (Eg = 1.72 eV) than CdSe (Eg = 1.77 eV) due to quantization

in nanocrystalline semiconductor which shows the improved absorption in visible region. The higher 'β' value (0.96) for rGO composited CdSe electrode an implies the better charge transfer with less recombination. The *FF* and *η* values are 0.37 and 2.18 %, respectively for rGO/CdSe thin film. The EIS studies showed that after composition of CdSe with rGO, charge transfer resistance lowers which results in superior charge transport process. Hence, it is concluded that rGO composited CdSe thin film enhances the power conversion efficiency. So, the composite of CdSe with rGO is more PEC efficient over CdSe.

4.9 References

1]   C. Solanki, Solar photovoltaics: Fundamentals technologies and applications, (PHI learning Pvt. Ltd., New Delhi, 2013), pp. 3-22.

2]   R. Dutta, and N. Neog, Mater. Today: Proc., 42 (2021) 893-896.

3]   J. Zheng, H. Zhou, Y. Zou, R. Wang, Y. Lyu, S. Jiang, S. Wang, Energy Environ. Sci., 12 (2019) 2345-2374.

4]   N. Shelke, S. Karle, B. Karche, J. Mater. Sci.: Mater. Electron., 31 (2020) 15061-15069.

5]   X. Wang, W. Tian, M. Liao, Y. Bando, D. Golberg, Chem. Soc. Rev., 43 (2014) 1400-1422.

6]   M. Wu, C. Kao, T. Lin, S. Chan, S. Chen, C. Lin, Y. Huang, Z. Zhou, K. Wang, C. Lai, Sens. Actuators B Chem., 309 (2020) 127760 (1-25).

7]   N. Rathee and N. Jaggi, Vacuum, 169 (2019) 108910 (1-6).

8]   Y. Park, K. Lee, G. Lim, H. Seo, S. Kim, M. Kim, Y. Yi, H. Lee, D. Son, Org. Electron., 82 (2020) 105707 (1-6).

9]   T. Santhosh, K. Bangera, G. Shivakumar, Mater. Sci. Semicond. Process., 68 (2017) 114-117.

10]   A. Zyoud, N. Abdul-Rahman, G. Campet, D. Park, H. Kwon, T. Kim, H. Choi, M. Helal, H. Hilal, J. Electroanal. Chem., 774 (2016) 7-13.

11]   R. Li, J. Lee, B. Yang, D. Horspool, M. Aindow, F. Papadimitrakopoulos, J. Am. Chem. Soc., 127 (2005) 2524-2532.

12]   R. Sahebi, M. Roknabadi, M. Behdani, Optik, 204 (2020) 164204 (1-13).

13]   H. Li, X. Wang, L. Zhang, B. Hou, Corros. Sci., 94 (2015) 342-349.

14]   Y. Lin, K. Zhang, W. Chen, Y. Liu, Z. Geng, J. Zeng, N. Pan, L. Yan, X. Wang, J. Hou, ACS nano., 4 (2010) 3033-3038.

15] D. Patidar, A. Yadav, D. Paul, A. Sharma, S. Nehra, Phys. E: Low-Dimens. Syst. Nanostructures., 114 (2019) 113560 (1-42).

16] F. Hosseini, and S. Mohebbi, J. Clust. Sci., 29 (2018) 289-300.

17] P. Li, B. Zhu, P. Li, Z. Zhang, L. Li, Y. Gu, Nanomater., 9 (2019) 957 (1-13).

18] I. Lightcap, and P. Kamat, J. Am. Chem. Soc., 134 (2012) 7109-7116.

19] K. Yu, G. Lu, S. Mao, K. Chen, H. Kim, Z. Wen, J. Chen, ACS Appl. Mater. Interfaces, 3 (2011) 2703-2709.

20] Ö. Uğuz, Ö. Budak, A. Koca, Int. J. Hydrogen Energy, 46 (2021) 35290-35301.

21] F. Hone, F. Ampong, I. Nkrumah, R. Nkum, F. Boakye, Elixir Thin Film Tech., 84, (2015) 33486-33489.

22] V. Raut, P. Jadhav, D. Dhongade, C. Bobade, J. Thorat, C. Lokhande, V. Killedar, Bull. Env. Pharmacol. Life Sci. Special Issue [1], (2022) 1545-1550.

23] V. Raut, C. Lokhande, V. Killedar, J. Mater. Sci.: Mater. Electron., 28 (2017) 3140-3150.

24] W. Ke, D. Zhao, A. Cimaroli, C. Grice, P. Qin, Q. Liu, L. Xiong, Y. Yan, G. Fang, Mater. Chem. A, 3 (2015) 24163-24168.

25] M. Hassen, R. Riahi, F. Laatar, H. Ezzaouia, Surf. Interfaces, 18 (2020) 100408 (1-10).

26] F. Kong, J. Wang, Z. Han, B. Qian, S. Tao, H. Luo, L. Gao, Chem. Comm., 55 (2019) 2996-2999.

27] E. Nosheen, S. Shah, Z. Iqbal, J. Photochem. Photobiol. B, 167 (2017) 117-127.

28] S. Mondal, S. Sudhu, S. Bhattacharya, S. Saha, J. Phys. Chem., 119 (2015) 27749-27758.

29] S. Krainer and U. Hirn, Colloids Surf. A Physicochem. Eng. Asp. 619 (2021) 12503 (1-10).

30] V. Mane, A. Lokhande, R. Nikam, N. Padalkar, V. Lokhande, D. Dhawale, C. Lokhande, Appl. Surf. Sci. Adv., 15 (2023) 100399 (1-12).

31] T. Logu, K. Sankarasubramanian, P. Soundarrajan, K. Sethuraman, Electron. Mater. Lett., 11 (2015) 206-212.

32] V. Raut, C. Lokhande, V. Killedar, J. Electroanal. Chem., 788 (2017) 137-143.

33] S. Gawali, and C. Bhosale, Mater. Chem. Phys., 129 (2011) 751-755.

34] J. Condon, Surface area and porosity determinations by physisorption: measurements and theory, (Elsevier, Amsterdam, 2006) pp. 1-274.

35] Z. Li, D. Jin, Z. Wang, Surf. Interfaces., 29 (2022) 101702 (1-8).

36] I. Mkhalid, and A. Shawky, Ceram. Int., 46 (2020) 20769-20776.

37] N. Ghobadi, P. Sohrabi, H. Hatami, Chem. Phys., 538 (2020) 110911 (1-17).

38] J. Sun, Z. Bai, Z. Huang, Z. Zhang, Lett. Mater., 10 (2020) 200-205.

39] Q. Shen, Y. Wang, J. Xue, G. Gao, X. Liu, H. Jia, Q. Li, B. Xu, Appl. Surf. Sci., 481 (2019) 1515-1523.

Chapter-V

CdS and rGO/CdS thin films by electrodeposition (ED) method: synthesis, characterization, and their photoelectrochemical (PEC) performance

CHAPTER- V

CdS and rGO/CdS thin films by electrodeposition (ED) method: synthesis, characterization, and their photoelectrochemical (PEC) performance

Section A

5.1 Introduction

Scientists from all over the world are interested in finding clean, sustainable energy sources. Non-renewable resources such as fossil fuels are running out and also pollution is increasing. Solar energy's green, readily available, and endless qualities have made it the best alternative over other renewable resources. However, researchers facing several hurdles in efficiently converting energy from renewable resources **[1, 2]**. Solar cells made up of semiconductor-liquid (S-L) junction are more advantageous for the direct conversion of light into electrical energy than solar cells with p-n junction, as they are easy to manufacture. The most important component of a solar cell of S-L junction is a photoelectrode (also known as a photocathode or photoanode). Therefore, photoelectrodes with direct band gaps, sharp absorption edges, and greater absorption coefficient qualities are needed for the efficient extraction of light from the solar spectrum **[3, 4]**.

Binary and ternary metal chalcogenides (group II and IV) are frequently used in solar cell technology. CdS thin films are of great interest due to their wide band gap, good optical transmittance, easy ohmic contact, and relatively high conductivity which reduces electrical losses in solar cell devices. CdS has been extensively explored as a photoanode in photoelectrochemical (PEC) solar cell applications due to its unique optical bandgap (2.4 eV) covering the visible region of the solar spectrum and its low production cost. In addition, CdS thin films are widely used in a variety of applications including visible-light mediated photocatalysis, window material for solar cells, water-splitting, PEC cells, and gas sensing **[5]**.

Various methods have been used for the deposition of rGO/CdS thin films, such as electrodeposition (ED), hydrothermal method, spin coating, one-step γ-irradiation, CBD, SILAR, microwave-assisted solvothermal method, and bacteria-assisted method **[6-15]**. ED deposition offers advantages such as easy control of growth conditions, easily controllable deposition parameters, simplicity and low cost. The ED also allows film preparation on any conducting substrate at low temperatures and under gentle operating circumstances, so it is used for deposition of CdS and rGO/CdS thin films **[16]**.

The basic monolayer of sp^2-hybridized carbon atoms, arranged in a hexagonal pattern, forms the two-dimensional (2D) lattice known as graphene. It serves as the basis for numerous other carbon-based materials, including 3D graphite, carbon nanotubes and

fullerene buckyballs. Due to its 2D hexagonal structure, it has both remarkable electrical and mechanical properties, which are due to π-bonds and strong planar bonds. Graphene is considered to be the thinnest stretchable crystal with high electron mobility and good thermal conductivity [17]. It has applications such as optoelectronic devices, sensors, biomaterials and bionics, energy storage and batteries, etc. [18-23]. However, due to the zero band gap, its usability is limited in some cases. To overcome photocorrosion in semiconductor photoelectrodes, increase the surface area and electrical conductivity while maintaining the stability of the material, such materials are assembled with rGO or deposited over rGO layers. The improved electrical and mechanical properties due to composite with rGO can contribute to an improvement in the electrochemical properties and increase the efficiency of the solar cell.

The current study consists of the potentiostatic electrodepositon approach to deposit CdS and rGO/CdS composite thin films on SS substrates. The electrodeposited CdS and rGO/CdS thin films were annealed at 400 K for 60 min. and characterized for various physicochemical properties. PEC and electrochemical impedance spectroscopy (EIS) were studied using a three electrode system in 1 M polysulfide electrolyte.

5.2 Experimental section

5.2.1 Substrate cleaning

The substrate cleaning process is explained in **chapter III section 3.2.1**.

5.2.2 Chemicals used

Graphite flakes, sodium nitrate ($NaNO_3$), sulfuric acid (H_2SO_4), potassium permanganate ($KMnO_4$), hydrogen peroxide (H_2O_2), hydrazine hydrate (H_6N_2O), sodium thiosulfate ($Na_2S_2O_3$), cadmium sulfate ($CdSO_4$), Ethylenediaminetetraacetic acid (EDTA) tetrasodium salt, sodium sulfide (Na_2S), sulfur powder (S), sodium hydroxide (NaOH) were purchased from Thomas Baker and utilized without any refinement. All solutions were prepared in double distilled water (DDW). The stainless steel (SS) strips of 1 cm x 5 cm dimensions were used as substrates for deposition.

5.2.3 Material synthesis

5.2.3.1 Deposition of rGO thin films

The synthesis process and rGO thin films deposition were explained in **chapter III section 3.2.2.1 and 3.2.2.2**.

5.2.3.2 Deposition of CdS thin films by ED method

5.2.3.2.1 Experimental setup

The experimental set up for thin film deposition by ED method consisting working electrode, counter electrode, reference electrode, glass container, substrate holder, precursor solution, and electrochemical workstation (potentiostat). The setup and its requirements are briefly discussed in **chapter II** in **section 2.2.2.1**.

Fig. 5.1 a) shows the schematic representation of the experimental set-up for the ED method. **Fig. 5.1 b)** shows a three-electrode cell with a SS substrate with an area of 1x1 cm^2 was made available for electrolyte contact and remaining covered with insulating tape acts as WE, SCE as the reference electrode and a graphite plate as the CE. By using a substrate holder, three electrodes setup was held on a glass container with a capacity of 50 mL. The graphite plate and WE were placed in a fixed location during deposition using a substrate holder. A substrate holder (**Fig. 5.1 c)** is a round, circular plate made of Teflon with a thickness of 8 mm and a diameter of 26 mm with four openings (two notches and two round openings) for holding WE, CE and RE with a movable screw arrangement to fix the electrodes properly. The SCE is mounted near the WE. An electrochemical workstation Zive MP1 serves as a constant voltage source (potentiostat) for the electrolysis.

5.2.3.2.2 Precursor solution preparation

For CdS thin films preparation, cadmium sulfate (0.05 M CdSO$_4$) and sodium thiosulfate (0.5 M Na$_2$S$_2$O$_3$) were used as a source for cadmium and sulfur ions, respectively. The pH of the solution bath maintained at 9.5 $\pm$ 0.1 using 0.1 M Ethylenediamine tetraacetic acid (EDTA) tetrasodium salt.

5.2.3.2.3 Estimation of the potentials

Potentiostatic mode of ED consists of deposition of thin film at a certain fixed potential. Hence, the deposition potential estimation is an important part in the deposition process. Linear sweep voltammetry (LSV) is the best technique for the same, which consists of scanning of the potentials in the given range with synchronized recording of deposition current. Once the polarization plot is recorded, reduction potential is estimated just by drawing a tangent to polarization curve. The potential corresponding to the point of intersection of the tangent, on potential axis stands for the reduction or deposition potential.
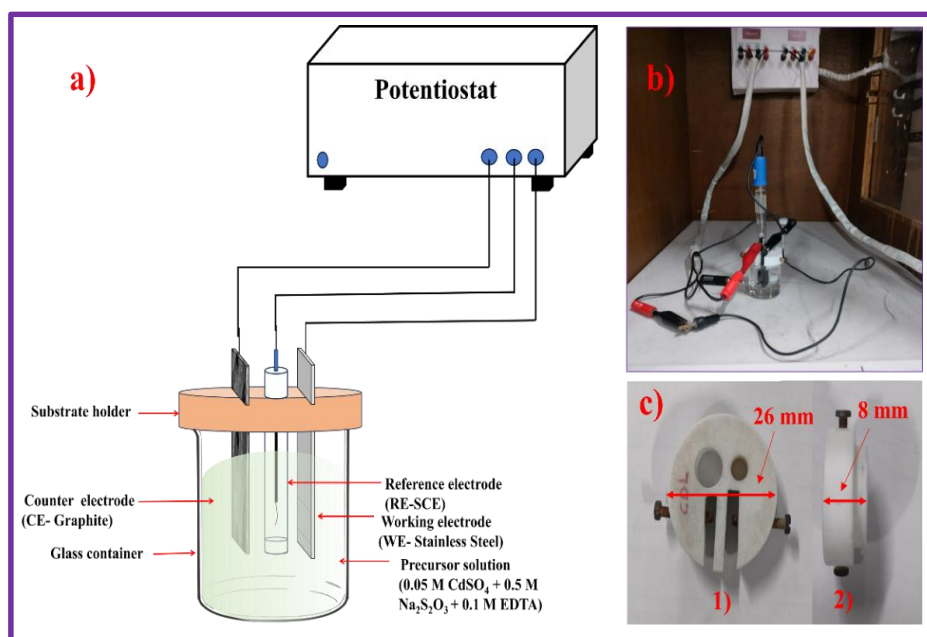
Fig. 5.1 a) Schematic of experimental set up used for ED method, b) Photograph of three electrode cell, and c) Teflon substrate holder

In order to estimate deposition potential for CdS, the polarization curves were recorded for Cd, S, and CdS (on fixed surface area of SS 1 cm^2) from their respective baths as 0.05 M CdSO$_4$ (pH = 5.2 ± 0.1), 0.5 M Na$_2$S$_2$O$_3$ (pH = 7.3 ± 0.1), and 0.05 M CdSO$_4$ + 0.5 M Na$_2$S$_2$O$_3$ + 0.1 M EDTA tetrasodium salt (pH = 9.5 ± 0.1). The potential was scanned from 0 to -1.5 V/SCE with scan rate 20 mV/s. All the potentials were recorded with respect to SCE.

Fig. 5.2 shows the polarization curves for Cd, S, and CdS thin films on SS substrate. The estimated reduction potentials are listed in **Table 5.1**.
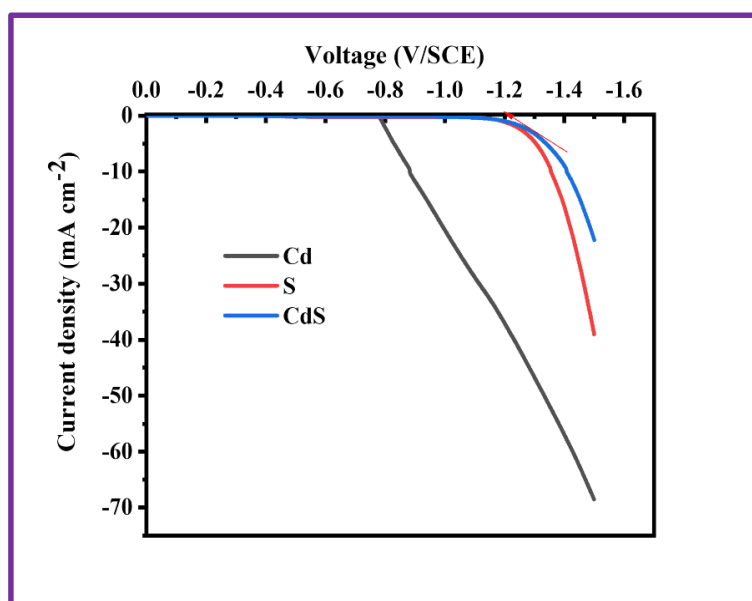
Fig. 5.2 Polarization curves of Cd, S, and CdS on SS substrate.

It is observed that the deposition potential of CdS lies among the reduction potentials of cadmium and sulfur. The yellowish orange color CdS thin film was deposited at potential -1.20 V/SCE.

Table 5.1: Estimated deposition potentials for Cd, S, and CdS films on SS substrate.

Sample	Cd	S	CdS
Deposition potential (V/SCE)	-0.78	-1.23	-1.20

5.2.3.2.4 Deposition of CdS thin films

For CdS deposition, aqueous solutions of 0.05 M $CdSO_4$ (pH = 5.2 ± 0.1) and 0.5 M $Na_2S_2O_3$ (pH = 7.3 ± 0.1) were utilized as cationic and anionic precursors, respectively. Both solutions were mixed in 1:9 volumetric ratio in glass container and the pH of electrolytic bath maintained at 9.5 ± 0.1 by using dropwise addition of 0.1 M EDTA tetrasodium salt. The potentiostatic deposition of CdS thin films were carried out at constant potential -1.20 V/SCE for 30 min using three electrode cell at room temperature. After film deposition, it was annealed at 400 K for 60 min in N_2 atmosphere and stored in airtight container.

5.2.3.3 Deposition of rGO/CdS composite thin film

5.2.3.3.1 Precursor solution preparation

For rGO/CdS composite thin film deposition, 0.05 M $CdSO_4$ and 0.5 M $Na_2S_2O_3$ were used as a source for cadmium and sulfur ions, respectively. EDTA (0.1 M) tetrasodium salt was used to adjust pH of aqueous deposition bath. rGO coated SS substate were used as a substrate for deposition of rGO/CdS composite thin films.

5.2.3.3.2 Estimation of the deposition potentials

In order to estimate deposition potential, the polarization curves were recorded for Cd, S, and CdS (on fixed surface area of rGO deposited SS 1 cm^2) from their respective baths as 0.05 M $CdSO_4$ (pH = 5.2 ± 0.1), 0.5 $Na_2S_2O_3$ (pH = 7.3 ± 0.1), and 0.05 M $CdSO_4$ + 0.5 M $Na_2S_2O_3$ + 0.1 M EDTA tetrasodium salt (pH = 9.5 ± 0.1). The potential was scanned from 0 to -1.5 V/SCE with scan rate 20 mV/s. **Fig. 5.3** shows the polarization curves for Cd, S, and CdS thin films on rGO deposited SS substrate and an estimated reduction potentials are listed in **Table 5.2**.
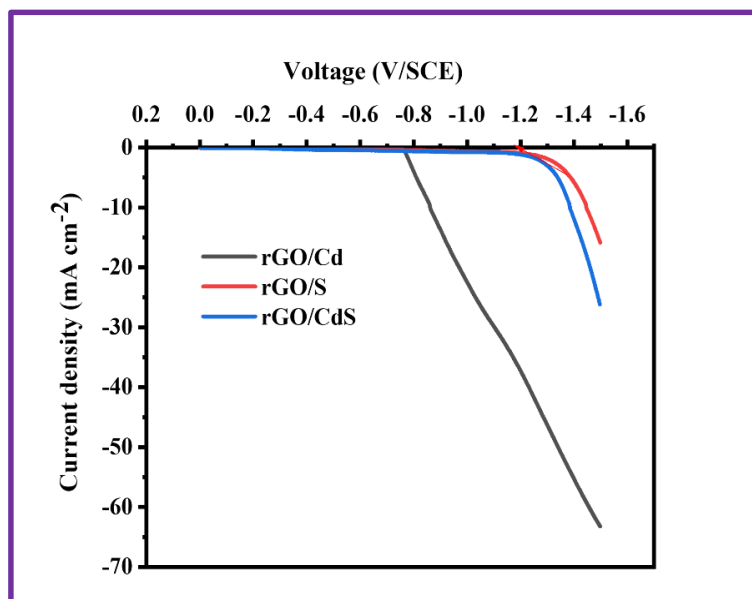
Fig. 5.3 Polarization curves of Cd, S, and CdS on rGO deposited SS substrate.

Table 5.2: Estimated deposition potentials for rGO/CdS films on SS substrate.

Sample	rGO/Cd	rGO/S	rGO/CdS
Deposition potential (V/SCE)	**-0.75**	**-1.20**	**-1.18**

It is observed that the deposition potential of CdS on rGO lies between the reduction potentials of Cd and S. The yellowish orange rGO/CdS thin film deposited at a deposition potential of -1.18 V/SCE. **Table 5.2** shows that, there is no significant difference between the deposition potentials of CdS on SS and CdS on rGO. Only the deposition potential shifts slightly towards a positive potential. This could be due to the better conductivity of rGO, the larger surface area and the presence of the previous nucleation sites on rGO surface.

5.2.3.3.3 Deposition of rGO/CdS composite thin films

The rGO thin films are deposited on a SS substrate, as explained in section **5.2.3.1**. The SS substrate deposited with rGO is used to deposit CdS thin film by a potentiostatic process, as explained in the previous section **5.2.3.2.4**. The potentiostatic deposition of CdS thin films were carried out at a constant potential of -1.18 V/SCE for 30 min using a three-electrode system. After 30 min, the yellow orange colored rGO/CdS thin films were removed from the electrolytic bath, annealed at 400 K for 60 min and stored in an airtight container.

5.2.3.3.4 Thin film formation and reaction mechanism

The ED of cadmium sulfide (CdS) on cathode (rGO deposited SS substrate) from cadmium sulfate ($CdSO_4$) and sodium thiosulfate ($Na_2S_2O_3$) involves following steps,

1) Dissociation of cadmium sulfate (eqⁿ 5.1), and sodium thiosulfate (eqⁿ 5.2),

$$CdSO_4 \rightarrow Cd^{2+} + SO_4^{2-} \qquad (5.1)$$

$$Na_2S_2O_3 \rightarrow 2Na^+ + S_2O_3^{2-} \qquad (5.2)$$
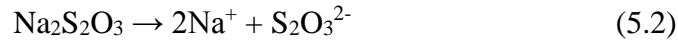
2) Ions migration

The cadmium ions (Cd^{2+}), sulfate ions (SO_4^{2-}), sodium ions (Na^+), and thiosulfate ions ($S_2O_3^{2-}$) move towards the respective electrodes under the influence of the applied electric field.

3) Reduction at cathode

At the cathode (negative electrode), cadmium ions undergo reduction

$$Cd^{2+} + 2e^- \rightarrow Cd \qquad (5.3)$$

4) Reaction with sulfur source

Simultaneously, at the cathode, the sulfur source (thiosulfate ions) may also undergo reduction:

$$S_2O_3^{2-} + 2e^- \rightarrow 2S + 3O^{2-} \qquad (5.4)$$
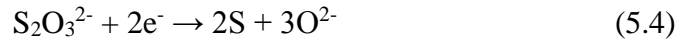
This reduction reaction results in the formation of elemental sulfur (S) and oxygen ions (O^{2-}).

5) Formation of CdS

The elemental cadmium formed at the cathode surface reacts with the sulfur generated from the thiosulfate reduction to form cadmium sulfide

$$Cd + S \rightarrow CdS \qquad (5.5)$$

The overall electrochemical deposition reaction can be represented as,

$$Cd^{2+} + S_2O_3^{2-} + 2e^- \rightarrow CdS + SO_4^{2-} \qquad (5.6)$$

5.3 Thin film characterizations

The characterizations of CdS and rGO/CdS were carried out as mentioned in **chapter III section 3.3**.

5.4 Thickness measurement

The thickness of CdS and rGO/CdS thin films were calculated using the weight difference method according to the following formula given in **chapter III section 3.2.2.5**.

The thickness of CdS film is found to be 310 nm. For rGO/CdS film, thickness of rGO film measured first and it was used as a substrate for further CdS deposition. The calculated thicknesses for rGO, and rGO/CdS were 90, and 450 nm, respectively. The increases in film thickness of rGO/CdS thin film may be due to the previous nucleation sites of rGO surface.

5.5 Results and discussions

5.5.1 XRD analysis

The XRD patterns of CdS, and rGO/CdS thin films are depicted in **Fig. 5.4**. The broad peak observed at $2\theta = 26.11°$ corresponds to (111) plane of cubic phase of CdS and it is good agreement with literature report (JCPDS: 01-080- 0006) **[24, 25]**.
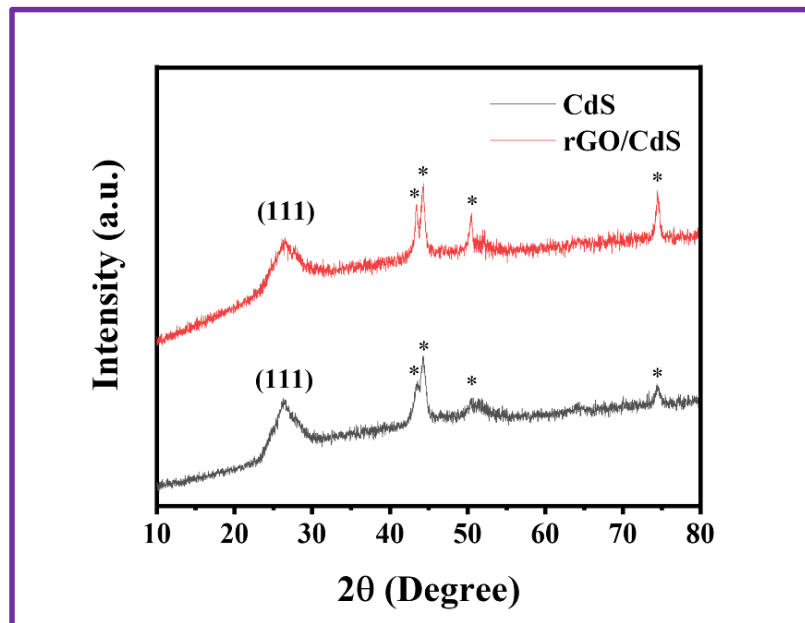
Fig. 5.4 The XRD patterns of CdS and rGO/CdS thin films.

The '*' peaks are present in XRD patterns of CdS, and rGO/CdS are due to the SS substrate. The broadening of the XRD peak evidences the formation of the nanosized particles. In rGO/CdS composite thin film XRD pattern, no any rGO peak is observed, this is may be due to its less amount, and low diffraction intensity. Along with that, the broad peak of CdS observed at $2\theta = 26.11°$ overlaps with rGO peak, so rGO peak is not observed in XRD pattern of rGO/CdS. The crystallite sizes for CdS, and rGO/CdS are estimated by Scherer formula. The crystallite sizes for CdS, and rGO/CdS are 13 and 17 nm, respectively. An improvement in crystallite size of CdS, after composite with rGO may be due to growth of CdS on the surface of rGO **[8]**.

5.5.2 FE-SEM study

The surface morphology of the electrode significantly influences the electrochemical properties of the material. FE-SEM was used to study the surface morphology of CdS, and rGO/CdS thin films. **Fig. 5.5 (a-d)** depicts the FE-SEM images of CdS, and rGO/CdS thin films at two magnifications of 20 kX and 40 kX. **Fig. 5.5 a)** shows the compact aggregation of CdS nanoparticles on the surface of SS substrate. At higher magnification, the aggregation of spherical nanoparticles is seen clearly (**Fig. 5.5 b**). For rGO composited CdS electrode, the morphology of electrode becomes more porous and uniform distribution of CdS particles on rGO sheets is observed (**Fig. 5.5 c**). The rGO plays a back stage role as a conductive backbone and provides more surface area to grow CdS. As seeking higher magnified images, some overgrown highly porous spongy nanoparticles uniform arrangement with reduced agglomeration on rGO sheets is observed (**Fig. 5.5 d**). The reduced aggregation of nanoparticles and more porosity of the electrodes make intimate contact between the electrolyte and the electrode surface results in good electrochemical properties of the materials. Chen et al. **[26]** reported similar type of morphology for CdS@rGO by hydrothermal method.
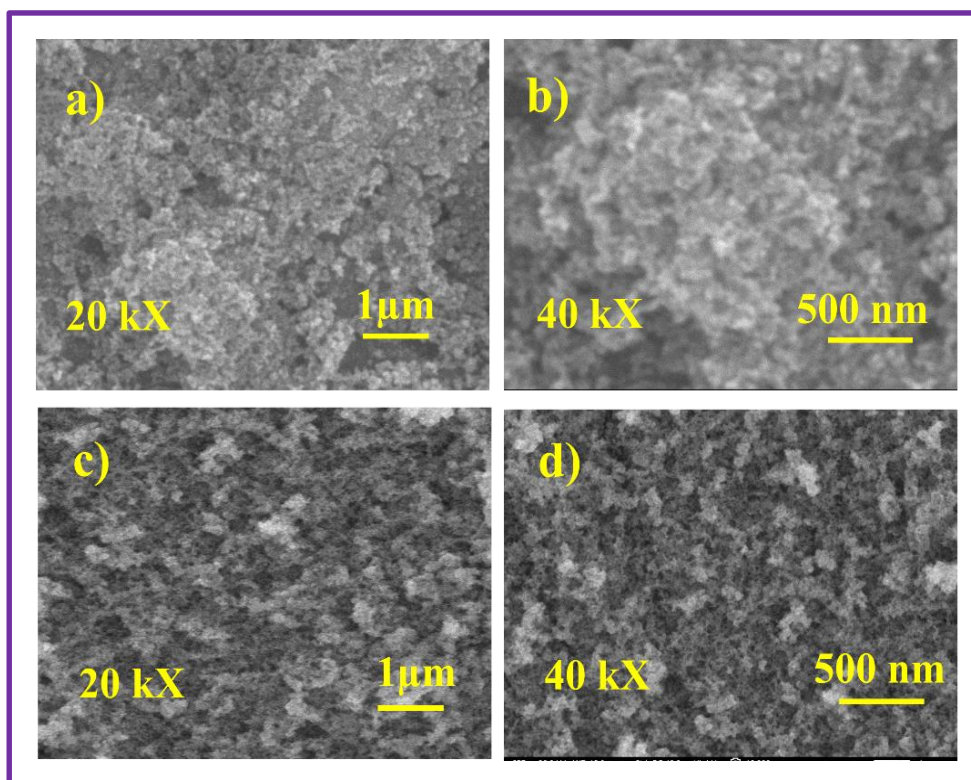
Fig. 5.5 The FE-SEM images of a-b) CdS, and c-d) rGO/CdS thin films at magnifications of 20 kX and 40 kX.

5.5.3 EDAX study

The elemental appearance in CdS, and rGO/CdS samples were studied using EDAX study, shown in **Fig. 5.6 (a-b)**.

From **Fig. 5.6 a)**, it is evidenced that, presence of Cd and S elements in the atomic percentage of 51.49:48.51. It confirms the stoichiometric deposition of Cd and S in CdS sample. For rGO composited CdS sample, the presence of Cd, S, and carbon (C) are confirmed from **Fig. 5.6 b)**. The Cd, S, and C elements are present in atomic percentage of 46.08:42.13:11.79. The observed C species in the EDAX of rGO/CdS sample confirms rGO present in rGO/CdS sample. The EDAX supports well to XRD results for formation of slightly sulfur deficient CdS and rGO/CdS samples and proves the successful composition between CdS and rGO.
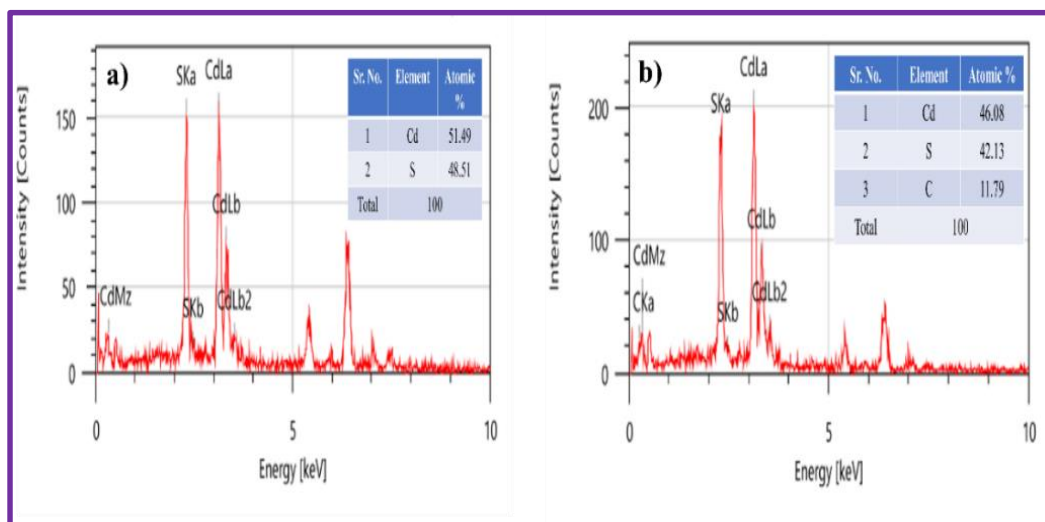
Fig. 5.6 The EDAX patterns of a) CdS, and b) rGO/CdS samples.

5.5.4 Surface wettability study

The material surface wetting characteristics have drawn a lot of interest from both an electrochemical application and a basic surface science perspective. A lower contact angle value indicates that the material is hydrophilic. The term 'hydrophilic' refers to materials that readily absorb water molecules because they contain active polar functional groups.

The higher value of contact angle indicates that the surface is hydrophobic. Hydrophobic materials make interaction with water in the opposite way as materials with hydrophilic properties. Water tends to bead on the surfaces of hydrophobic materials, which are "water hating" materials because they interact with water little or not at all **[27]**.

The photographs of contact angle of CdS and rGO/CdS are shown in **Fig. 5.7 (a-b)**. CdS and rGO/CdS thin films show the contact angle values of 58 and 41°, respectively. It is seen from **Fig. 5.7 (a-b)** the reduction in contact angle value is observed for rGO composited CdS electrode. The reduction in contact angle may be due to pore size and surface morphology of material surface. Undoubtedly, a porous or non-porous surface has a significant impact on the contact angle value because capillary forces allow water droplets to enter the large pores on the surface and disperse, which lowers the contact angle value **[28]**. The reduction could be because of rGO/CdS film surface roughness, and porosity increased due to composition with rGO, increasing the hydrophilicity. Due to large surface area of rGO, increased immobilization of CdS nanoparticles on rGO nanosheets is also responsible for the greater hydrophilicity of rGO/CdS **[29]**. The proper contact that the photoelectrode surface creates with the redox electrolyte in the solar cell enhances the electrode PEC performance. So, PEC performance of photoelectrode is improved due to hydrophilicity **[30]**.
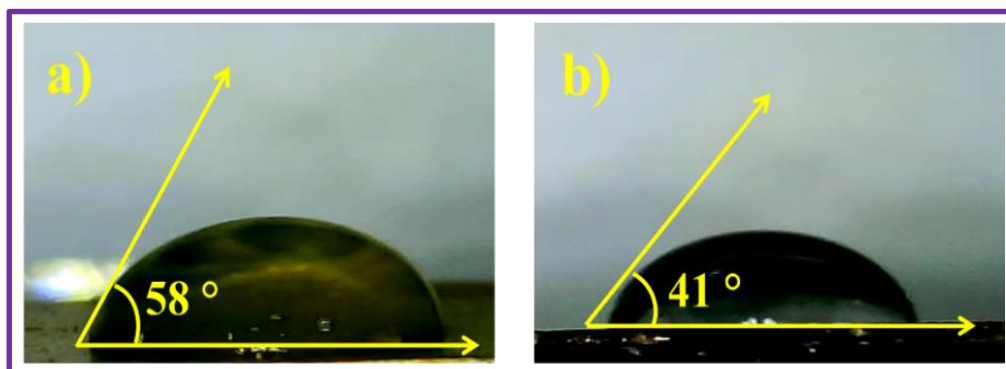
Fig. 5.7 The contact angle photographs of a) CdS, and b) rGO/CdS thin films.

5.5.5 BET study

The N_2 sorption curves for CdS and rGO/CdS composite exhibit type V isotherms, accompanied by H1 type hysteresis loops as shown in **Fig. 5.8 (a, b)**. Both CdS and rGO/CdS demonstrate the existence of mesopores, with specific surface areas measuring of 48 and 55 $m^2 g^{-1}$, respectively. After integrating rGO, the sample surface area is expanded, leading to improved electrochemical interaction and ultimately enhancing power conversion efficiency.

The BJH graph shows the average pore size distribution, revealing the underlying fine crystallite nature. The pore volume plotted against pore radius for CdS and rGO/CdS, as depicted in **Fig. 5.8 (c, d)**, indicate their mesoporous characteristics.

Mesoporosity of CdS and rGO/CdS plays a crucial role in enhancing the efficiency of PEC cell. The interconnected pore structures of porous materials lead to a higher surface area, which improves the materials ability to capture incident photons effectively. Furthermore, the interconnected pores facilitate efficient charge transport within the material. This allows photoexcited charge carriers to move rapidly to the electrode surface, minimizing recombination losses. Additionally, the intimate contact between the electrode surface and the electrolyte, developed due to mesoporosity, promotes surface reaction kinetics. This ensures efficient utilization of photo-generated charge carriers in electrochemical processes, ultimately enhancing the overall performance of PEC devices. The findings from the BET analysis strongly correlate with the observed reduction in contact angle change for both CdS and rGO/CdS films.
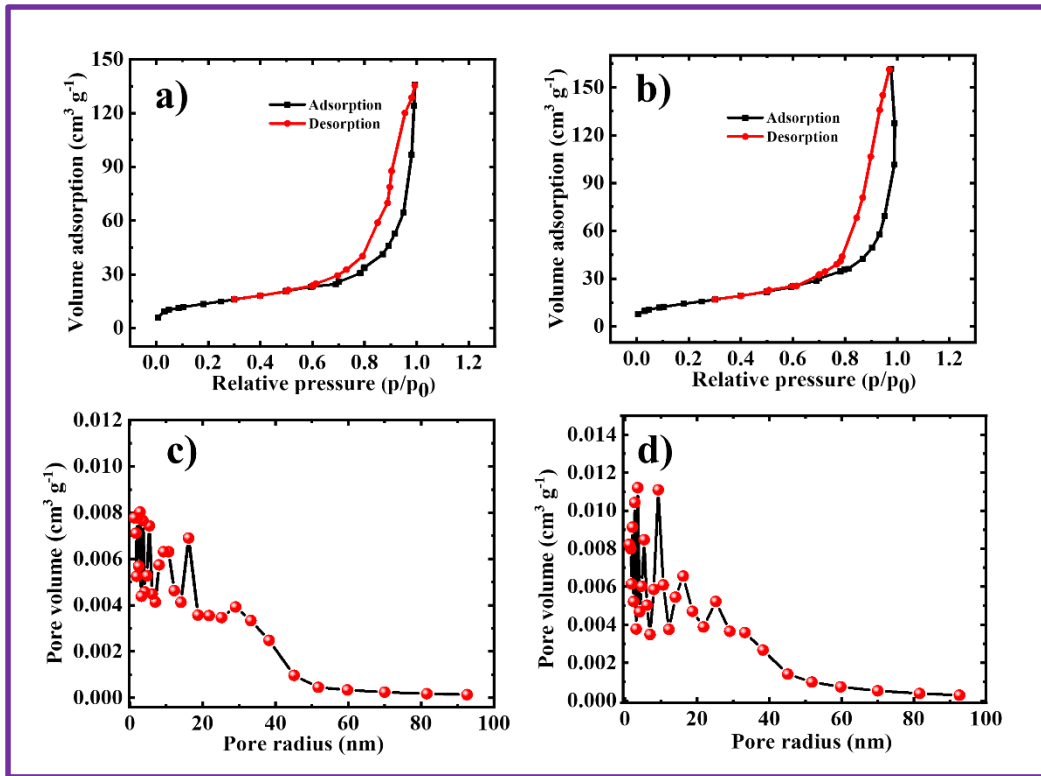
Fig. 5.8 The N_2 adsorption-desorption isotherms for a) CdS, and b) rGO/CdS samples and the BJH size distribution curves of c) CdS, and d) rGO/CdS samples.

5.5.6 Optical absorption study

The optical absorption properties of CdS, and rGO/CdS were studied by diffuse reflectance spectra (DRS). The Tauc plots of CdS, and rGO/CdS are shown in **Fig. 5.9.** The absorption band edges for CdS, and rGO/CdS are at 588, and 619 nm,

respectively in visible region (**Fig. 5.9 Inset**). A red shift in absorption edge for rGO/CdS composite thin film due to enhancement of the surface electric charge of CdS composite with rGO. So, rGO/CdS composite thin film is more efficient to utilize visible light **[30, 31]**. The band gaps of CdS and rGO/CdS samples were determined using the Kubelka-Munk standard equation as discussed in **chapter III section 3.4.2.6**.

The band gap values are found to be 2.43, and 2.15 eV for CdS and rGO/CdS, respectively. The red shift in optical band gap spectrum is attributed due to size quantization in nanocrystalline semiconductor **[8]**.

In the present study CdS and rGO/CdS composite thin films are synthesized using the ED method, the particle size increases from 13 nm to 17 nm. For rGO/CdS composite thin film the calculated particle size was 17 nm, which is slightly greater from CdS thin film, the increase in the crystallite size of CdS nanoparticles is due to growth over the graphene sheet. Nosheen et al. **[30]** reported similar reduction of the band gap value for rGO/CdS composites.
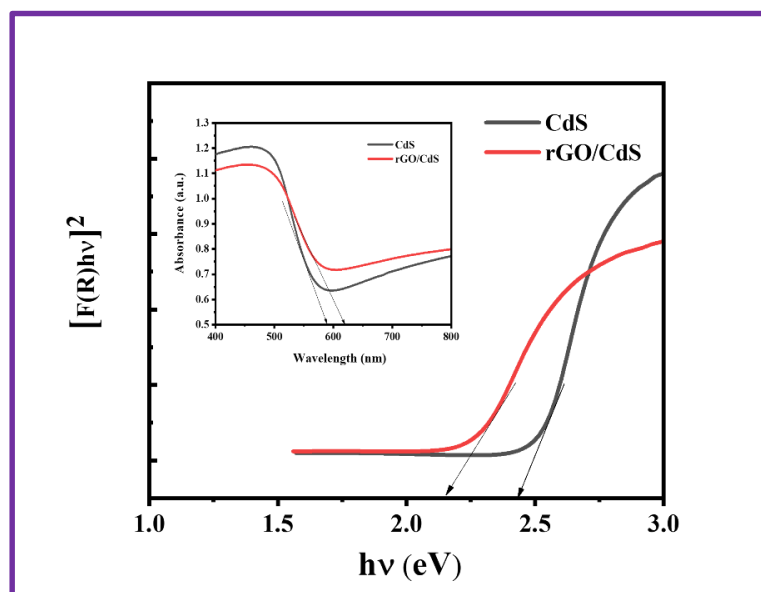
Fig. 5.9 The Tauc plots of CdS, and rGO/CdS thin films (Inset shows absorption spectra for CdS and rGO/CdS).

Section B

5.6 Electrochemical studies

Electrochemical studies are most important for PEC solar cell technology. To study the quality of electrode electrolyte junction, type of the semiconductor material, and generation of the charge carriers the I-V characteristics of CdS and rGO/CdS

materials are performed. The power output characteristics of CdS and rGO/CdS PEC cell device are used to study the PEC cell parameters of the semiconductor photoelectrodes. These studies also pinpoint limiting factors like charge recombination and electrode degradation, informing strategies for improvement. Overall, electrochemical analyses drive innovation, ensuring efficient and sustainable solar energy conversion. The charge transfer processes at the electrode electrolyte junction for CdS and rGO/CdS electrodes is understood by the electrochemical impedance spectroscopy (EIS).

5.6.1 I-V characteristics of CdS, and rGO/CdS thin films

The PEC cell was made up of three-electrode set up consisting CdS or rGO/CdS as a working, SCE as a reference, and graphite as a counter electrode in 1 M polysulfide electrolyte.
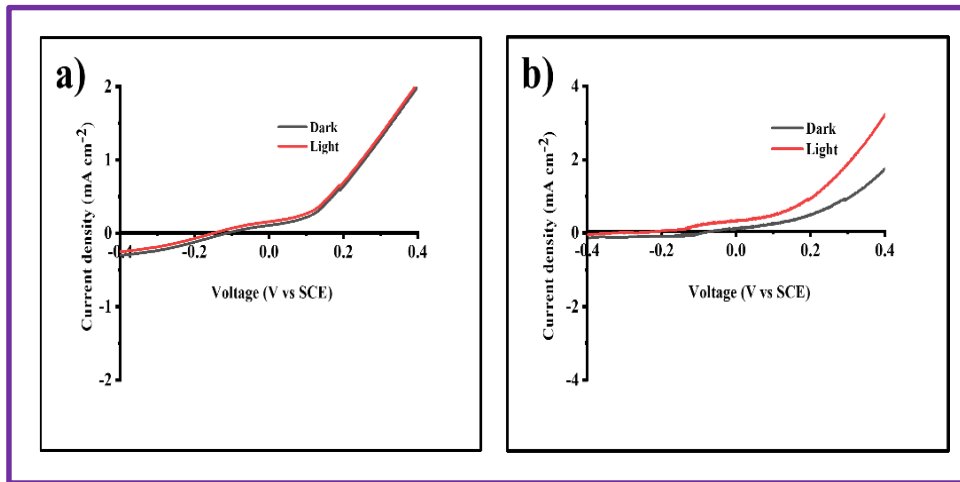
Fig. 5.10 The I-V characteristics of a) CdS and b) rGO/CdS thin films in dark and under light conditions.

Fig. 5.10 (a-b) depicts the I-V curves of CdS and rGO/CdS thin films in dark and under light conditions. The symmetry factor (β) was estimated from the I-V curves by using formulae as mentioned in **chapter I section 1.2.3**. The values of 'β' of CdS and rGO/CdS with polysulfide junction are given in **Table 5.3**

From **Table 5.3**, the higher value (near to 1) of the 'β' for rGO composited electrode implies the more useful for the optical applications. In light conditions, the 'β' factor for rGO composited CdS electrodes shows a slight increase compared to dark conditions, indicating a reduction in recombination processes and bulk charge transfer phenomena.

Table 5.3: **The 'β' values of CdS and rGO/CdS thin film electrodes in dark and under light conditions in contact with 1 M polysulfide.**

Sr. No.	Electrode	condition	$\beta = \dfrac{2.303\, RT}{bF}$	$\beta = 1 - \dfrac{\left(\log \dfrac{I}{I_0}\right) RT}{qV}$
1	CdS	Dark	0.96	0.95
		Light	0.97	0.96
2	rGO/CdS	Dark	0.97	0.96
		Light	0.98	0.97

A greater 'β' value signifies enhanced interface quality, facilitating efficient transport of charge carriers across the interface with minimal losses attributed to recombination. When, the recombination rate decreases (higher 'β'), the ideality factor (n) tends to decrease as well, indicating improved device performance and reduced non-ideal behavior. Conversely, an increase in recombination rates (lower 'β') may lead to higher ideality factors, signifying increased non-ideal behavior and reduced device performance.

5.6.2 Power output characteristics of CdS, and rGO/CdS thin films

The experimental setup explained in **chapter III section 3.5.4** is used for determination of the power output characteristics of CdS or rGO/CdS//polysulfide//graphite device in dark, under light, and in chopping conditions are showed in **Fig. 5.11 (a-b).**
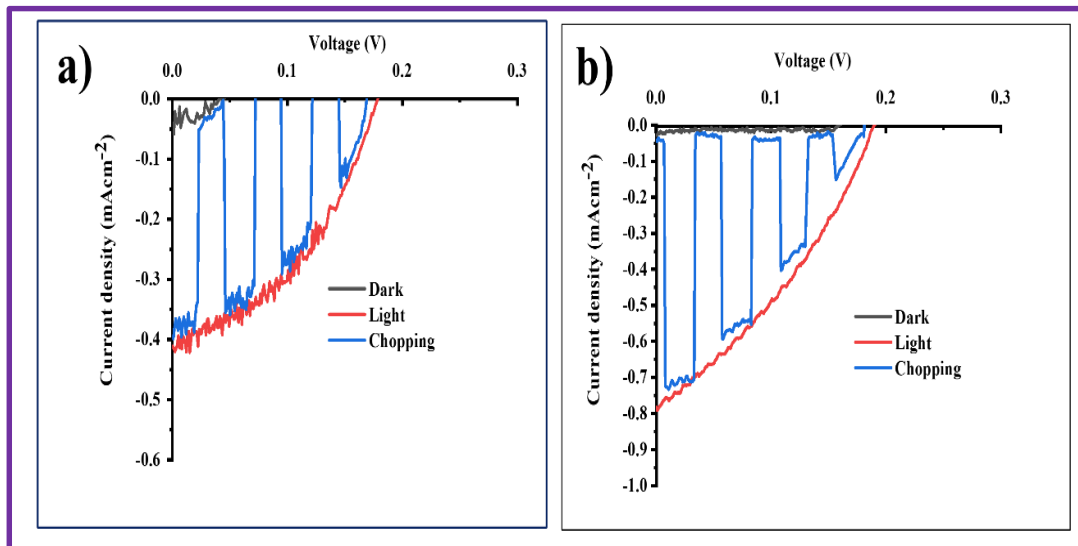
Fig. 5. 11 The power output curves of a) CdS, and b) rGO/CdS thin films in dark, under light, and in chopping conditions.

The PEC parameters are estimated by using formulae in **chapter III section 3.5.6** and tabulated in **Table 5.4**.

Table 5.4: The PEC parameters of CdS and rGO/CdS thin films in dark and under light conditions.

Sample	I_{sc} (mA cm^{-2})	V_{OC} (V)	I_m (mA cm^{-2})	V_m (V)	FF	Efficiency 'η' (%)
CdS	0.41	0.17	0.35	0.07	0.34	0.10
rGO/CdS	0.78	0.19	0.53	0.11	0.38	0.22

It is observed that, from **Table 5.4**, rGO composited CdS electrode showed an enhancement in power conversion efficiency 'η' (0.22 %) over bare CdS (0.10 %), nearly of 2.2 times. The good electrical, surface morphological properties of rGO are may responsible for enhanced charge carrier generation and its reduced recombination. The uniform distribution of CdS nanoparticles on rGO sheets provides higher surface area which results in hydrophilicity for intimate contact at electrode/electrolyte interface.

5.6.3 EIS Study

EIS represent a combination of electrical (resistance, capacitance or inductance) and electrochemical (faradaic) impedances. In particular, thin films on an electrode surface behave like dielectrics, as does the double layer that forms spontaneously on an electrified interface. Therefore, electrical circuits are often used to analyze experimental results, but such an approach masks the physical and chemical properties of the interface **[32-34]**. EIS measurements depend on both the mechanism under investigation and extrinsic parameters, such as the electrode geometry.

The charge transfer phenomena between polysulfide, CdS or rGO/CdS photoelectrode interfaces were investigated by EIS. The EIS studies were performed in dark and under light conditions in 1 KHz to 100 MHz frequency range. Nyquist plot is a plot of an imaginary part against the real part of impedance data. The **Fig. 5.12** depicts the Nyquist plots for CdS, and rGO/CdS thin film electrodes in dark and under light conditions. By use of 'Z' view software, impedance data was fitted to well suitable electrical circuit. The EIS parameters solution resistance (R_S), charge transfer resistance (R_{ct}), leakage capacitance (Q_1), and diffusion resistance (W) are summarized

in **Table. 5.5**. The brief description about *Rs*, R_{ct}, Q_1, and *W* is given in **chapter III section 3.6.1**.
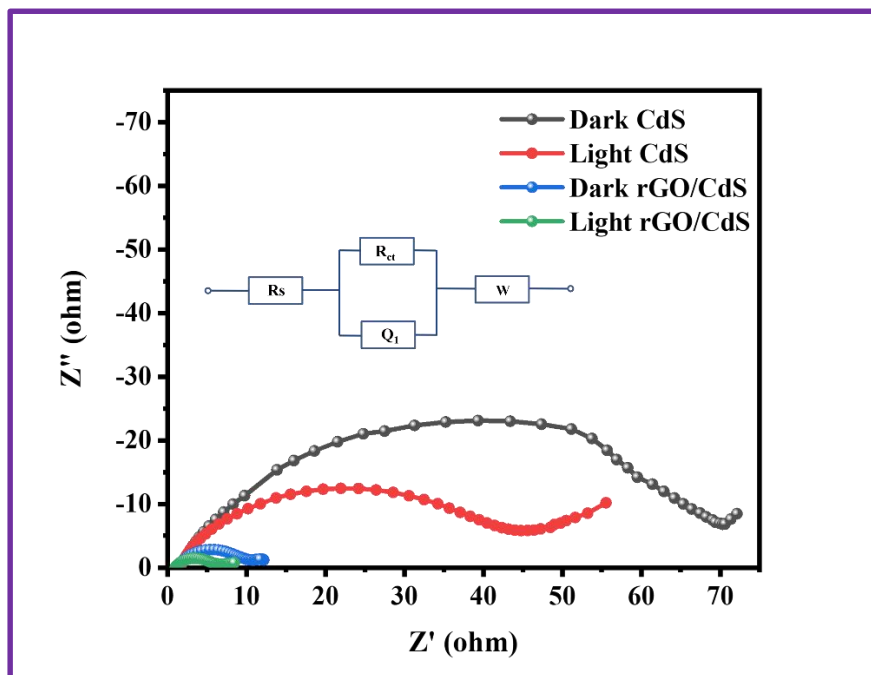
Fig. 5.12 Nyquist plots for CdS, and rGO/CdS thin films in dark, and under light conditions with an equivalent circuit diagram.

Table 5.5: The EIS parameters of CdS, and rGO/CdS electrodes in dark and under light conditions.

Sample	Condition	*Rs* (Ω cm^{-2})	R_{ct} (Ω cm^{-2})	Q_1 (μF)	*W* (mΩ)
CdS	Dark	1.9	68.1	46	76
	Light	1.5	44.7	57	63
rGO/CdS	Dark	1.2	11.9	69	55
	Light	1.0	7.4	83	36

It is seen from **Table 5.5** that under light illumination, *Rs* values for CdS and rGO/CdS are 1.5 and 1.0 Ω cm^{-2}. For dark condition *Rs* values are 1.9 and 1.2 Ω cm^{-2}. Under light illumination, R_{ct} values for CdS and rGO/CdS are 44.7 and 7.4 Ω cm^{-2}. For dark condition R_{ct} are 68.1 and 11.9 Ω cm^{-2}. The minimum value of R_{ct} reveals the more dominant charge transfer kinetics in rGO/CdS thin film in light as compared to

dark. This is may be due to the increased electron-hole pair generation density of CdS and the superior capability of capturing, storing, and transporting electrons of rGO. Hence, rGO plays an important role as an electron exchanger between CdS and SS substrate leading to improve photocurrent [35]. The EIS output agrees well with the photocurrent voltage characteristics.

5.7 Conclusions

Present work consists of successful deposition of CdS and rGO/CdS thin films by potentiostatic ED method on SS substrates. The XRD study implies the cubic crystal structure of CdS and rGO/CdS thin films. The EDAX study evidences the successful composition of CdS and rGO/CdS thin films. The FE-SEM study showed the deposition of CdS nanoparticles on rGO sheets. The less aggregation of the particles on rGO surface enhances the porosity of the electrode surface. The both CdS and rGO/CdS electrodes are hydrophilic in nature showing the contact angle values of 58, and 41 °, respectively. The band gap reduction is observed from 2.43 to 2.15 eV for CdS and rGO/CdS thin films due to size quantization properties in nanocrystalline semiconductors. The rGO/CdS electrode showed an improved *FF*, and η of 0.38, and 0.22 %, respectively than CdS of 0.34, and 0.10 %. The EIS studies showed that R_{ct} for both electrodes in light condition are lower than the dark one which implies the charge carrier generation in the electrodes. For rGO composited CdS electrode, the R_{ct} value significantly lower than CdS which is responsible for superior charge transport process. Hence, CdS composited with rGO mainly lifts up 2.2 times η compared over CdS and good option for PEC application.

5.8 References

1]   N. Kannan, and D. Vakeesan, Renew. Sust. Energ. Rev., 62 (2016) 1092-1105.

2]   E. Kabir, P. Kumar, S. Kumar, A. Adelodun, K. Kim, Renew. Sust. Energ. Rev., 82 (2018) 894-900.

3]   S. Tilley, Adv. Energy Mater., 9 (2019) 1802877 (1-13).

4]   K. Sivula, and R. Van De Krol, Nat. Rev. Mater., 1 (2016) 1-16.

5]   K. Khot, S. Mali, R. Kharade, R. Mane, P. Patil, C. Hong, j. Kim, J. Heo, P. Bhosale, J. Mater. Sci. Mater. Electron., 25 (2014) 5606-5617.

6]   B. Altiokka, and A. Yildirim, J. Korean Phys Soc., 72 (2018) 687-691.

7]   H. Salim, O. Olusola, A. Ojo, K. Urasov, M. Dergacheva, I. Dharmadasa, J. Mater. Sci. Mater. Electron., 27 (2016) 6786-6799.

8]   M. Indhumathy, and A. Prakasam, J. Mater. Sci. Mater. Electron., 30 (2019) 15444-15451.

9]   N. Quang, S. Majumder, C. Kim, D. Kim, J. Electrochem. Soc., 166 (2019) 3112-3118.

10]   W. Daniyal, Y. Fen, S. Saleviter, N. Chanlek, H. Nakajima, J. Abdullah, N. Yusof, Polym., 13 (2021) 478 (1-18).

11]   X. Liu, G. Zeng, S. Jiang, Radiat. Phys. Chem., 119 (2016) 24-28.

12]   L. Ma, X. Ai, Y. Lu, S. Yan, X. Wu, J. Alloys Compd., 828 (2020) 154406 (1-8).

13]   H. Li, Z. Xia, J. Chen, L. Lei, J. Xing, Appl. Catal. B, 168 (2015) 105-113.

14]   N. Jiang, Z. Xiu, Z. Xie, H. Li, G. Zhao, W. Wang, Y. Wu, X. Hao, New J. Chem., 38 (2014) 4312-4320.

15]   K. Hareesh, S. Dole, D. Phase, J. Williams, Mater. Res. Bull., 110 (2019) 82-89.

16]   A. Mukherjee, B. Satpati, S. Bhattacharyya, R. Ghosh, P. Mitra, Phys. E: Low-Dimens. Syst. Nanostructures, 65 (2015) 51-55.

17]   R. Tarcan, O. Todor-Boer, I. Petrovai, C. Leordean, S. Astilean, I. Botiz, J. Mater. Chem. C, 8 (2020) 1198-1224.

18]   R. Garg, S. Elmas, T. Nann, M. Andersson, Adv. Energy Mater., 7 (2017) 1601393 (1-22).

19]   M. Xu, J. Qi, F. Li, X. Liao, S. Liu, Y. Zhang, RSC Adv., 7 (2017) 30506-30512.

20]   B. Thompson, E. Murray, G. Wallace, Adv. Mater., 27 (2015) 7563-7582.

21]   X. Shuai, Z. Bo, J. Kong, J. Yan, K. Cen, RSC Adv., 7 (2017) 2667-2675.

22]   C. Tang, B. Li, Q. Zhang, L. Zhu, H. Wang, J. Shi, F. Wei, Adv. Funct. Mater., 26 (2016) 577-585.

23]   E. Kecsenovity, B. Endrodi, P. Toth, Y. Zou, R. Dryfe, K. Rajeshwar, C. Janaky, J. Am. Chem. Soc., 139 (2017) 6682-6692.

24]   W. Yang, Z. Wu, Z. Lu, X. Yang, L. Song, Microelectron. Eng., 83 (2006) 1971-1974.

25]   C. Wang, J. Fang, J. He, C. O'Connor, J. Mater. Sci., 22 (2003) 413-415.

26] F. Chen, X. Zou, C. Chen, Q. Hu, Y. Wei, Y. Wang, B. Xiang, J. Zhang, Ceram., 45 (2019) 14376-14383.

27] R. Hebbar, A. Isloor, A. Ismail, Contact angle measurements. In Membrane characterization, (Elsevier, 2017) pp. 219-255.

28] S. Krainer, U. Hirn, Colloids Surf. A Physicochem. Eng. Asp., 619 (2021) 126503 (1-10).

29] C. Lee, S. Yu, T. Kim, Nanomater., 8 (2018) 17 (1-13).

30] E. Nosheen, S. Shah, Z. Iqbal, J. Photochem. Photobiol. B: Biol., 167 (2017) 117-127.

31] H. Liu, T. Lv, X. Wu, C. Zhu, Z. Zhu, Appl. Surf., 305 (2014) 242-246.

32] S. Wang, J. Zhang, O. Gharbi, V. Vivier, M. Gao, M. Orazem, Nat. Rev. Methods Primers., 1 (2021) 41 (1-21).

33] A. Lazanas, and M. Prodromidis, ACS meas. sci. Au., 3 (2023) 162-193.

34] S. Sarker, A. Ahammad, H. Seo, D. Kim, Int. J. Photoenergy, 2014 (2014) 851705 (1-17).

35] G. Xie, K. Zhang, H. Fang, B. Guo, R. Wang, H. Yan, L. Fang, J. Gong, Chem. Asian J., 8 (2013) 2395-2400.

Chapter-VI

CdSe and rGO/CdSe thin films by electrodeposition (ED) method: synthesis, characterization, and their photoelectrochemical (PEC) performance

CHAPTER- VI

CdSe and rGO/CdSe thin films by electrodeposition (ED) method: synthesis, characterization, and their photoelectrochemical (PEC) performance

Section A

6.1 Introduction

Energy plays an essential role in the progress of mankind. The rapid increase in humanity's energy consumption due to overpopulation in recent decades has drawn attention to the problem of the energy crisis **[1]**. The energy demand has been met with the help of resources such as coal, petroleum, firewood, sunshine and natural gas. The burning of fossil fuels produces a variety of harmful gases. Scientists from all over the world are interested in finding clean and sustainable energy sources as non-renewable resources such as fossil fuels are depleting and pollution is increasing. The environmentally friendly, readily available and endless qualities of solar energy have made it a viable strategy in this regard **[2]**. Researchers facing a major hurdle in the efficient conversion of energy from renewable resources.

For direct transformation of light into electrical energy the semiconductor-liquid (S-L) junction solar cells are most useful due to simple junction structure over semiconductor-semiconductor (p-n) junction solar cells. A photoelectrode (photocathode/photoanode) is a more important part of PEC solar cell **[3]**. So, for an effective extraction of light from solar spectrum, the photoelectrodes with sharp absorption edges, direct band gap and higher absorption coefficient properties are required.

The binary and ternary metal chalcogenides of groups II and VI are widely used for solar cell applications. Cadmium selenide (CdSe) is used in various applications such as light amplification by stimulated emission of radiation (LASER), photovoltaics, light emitting diodes (LED), sensors and electroluminescence. CdSe with a band gap of 1.76 eV absorbs almost half of the visible light along with the generation of electron-hole pairs. So, it is an extremely important material for solar cells. But photocorrosion and lower stability, limit its use in solar cell applications **[4, 5]**. To overcome these challenges, various ways are used to modify the film properties through synthesis strategies, optimal film thicknesses, post-treatments, doping and support materials such as carbon nanotubes, graphene, etc. for CdSe **[6, 7]**.

Graphene have 2D honeycomb structure with sp^2 hybridization, creating more interest in multidisciplinary applications due to unique electrical, thermal, optical, and mechanical characteristics, it also has high surface area and complex surface characteristics. But, less used for optoelectronics and photonics applications due to theoretical zero band gap. The composite with or nanoparticles deposited over

graphene sheets widen the application range and maximizes the potential of graphene as well as supports the nanocrysts in optoelectronics [8-10].

Different chemical methods like chemical vapor deposition (CVD), hydrothermal, spin coating, chemical bath deposition (CBD), successive ionic layer adsorption and rection (SILAR), electrodeposition (ED) [11-18] etc. have been used to synthesize CdSe and rGO/CdSe composite thin films. Among them ED is a simple, cost-effective method for uniform and well adherent deposition of CdSe and rGO/CdSe films on any conducting substrate of any shape and size. Also, it is easy to control the deposition parameters, low temperature deposition, less time consuming, simplicity, and useful to deposit composites and compounds [19].

Present work concerns with deposition of CdSe and rGO/CdSe composite thin films via ED (potentiostatic) method on stainless steel (SS) substrates. The physicochemical properties of thin films were studied by different characterizations techniques. The photoelectrochemical (PEC) and electrochemical impedance spectroscopy (EIS) properties of CdSe and rGO/CdSe are investigated using three electrode system in 1 M polysulfide electrolyte.

6.2 Experimental section

6.2.1 Substrate cleaning

The 304 grade stainless steel (SS) substrates are cleaned as the procedure explained in **chapter III section 3.2.1.**

6.2.2 Chemicals used

Cadmium sulfate octahydrate ($CdSO_4.8H_2O$), sulfuric acid (H_2SO_4), sodium sulfide (Na_2S), sulfur powder (S), sodium hydroxide (NaOH), selenium dioxide (SeO_2) were purchased from Thomas Baker and utilized without any refinement. All solutions were prepared in double distilled water (DDW). Precleaned SS strips of 1 cm x 5 cm dimensions were used as substrates for deposition.

6.2.3 Material synthesis

6.2.3.1 Deposition of rGO thin films

The rGO preparation and its thin film deposition process were explained in **chapter III** section **3.2.2.1** and **3.2.2.2**.

6.2.3.2 Deposition of CdSe thin films by electrodeposition (ED) method

6.2.3.2.1 Experimental setup

The experimental set up for thin film deposition by ED method includes working electrode (WE), counter electrode (CE), reference electrode (RE), glass container, substrate holder, precursor solution, and electrochemical workstation (potentiostat). The brief description and requirements of setup parts is given in **chapter II** in **section 2.2.2.1**.

A three-electrode cell and experimental setup used for ED purpose is discussed in the **chapter V section 5.2.3.2.1**.

6.2.3.2.2 Precursor solution preparation

For CdSe thin films preparation, 100 ml solution of cadmium sulfate octahydrate (0.05 M $CdSO_4.8H_2O$) and 100 ml solution of selenium dioxide (0.01 M SeO_2) were used as sources for cadmium (Cd) and selenium (Se) ions, respectively.

6.2.3.2.3 Estimation of the deposition potentials

In order to estimate deposition potential, the polarization curves were recorded for Cd, Se, and CdSe, (on fixed surface area of SS 1 X 1 cm^2) from their respective baths as 0.05 M $CdSO_4.8H_2O$ (pH = 5.2 ± 0.1), 0.01 M SeO_2 (pH = 3.1 ± 0.1), and 0.05 M $CdSO_4.8H_2O$ + 0.01 M SeO_2 (pH = 2.9 ± 0.1). The potential was scanned from 0 to -1 V/SCE with scan rate 20 mV/s. **Fig. 6.1** shows the polarization curves of Cd, Se, and CdSe thin films on SS substrate. The estimated deposition potentials are listed in **Table 6.1**.
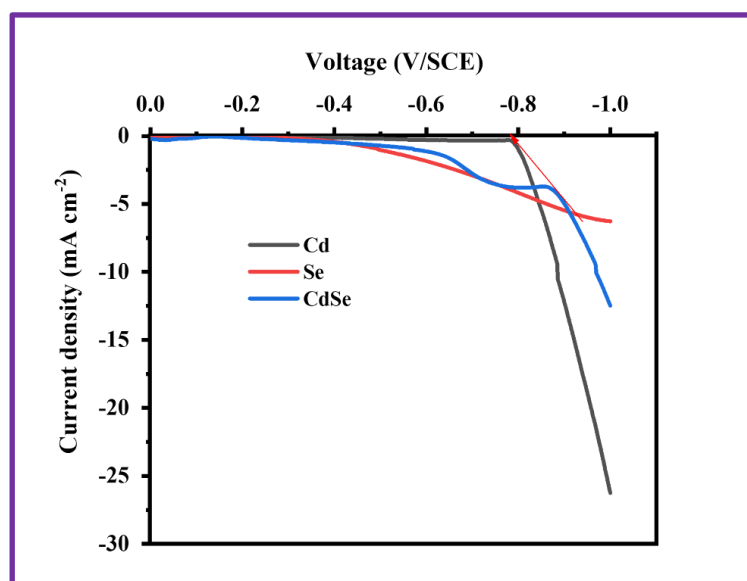
Fig. 6.1 Polarization curves of Cd, Se, and CdSe on SS substrate.

Table 6.1: Estimated deposition potentials for Cd, Se, and CdSe films on SS substrate.

Sample	Cd	Se	CdSe
Deposition potential (V/SCE)	-0.79	-0.41	-0.78

It is observed that the deposition potential of CdSe lies among the reduction potentials of Cd and Se. The reddish-brown colored CdSe thin films were deposited at deposition potential -0.78 V/SCE.

6.2.3.2.4 Deposition of CdSe thin films

For CdSe deposition, solutions of 0.05 M $CdSO_4.8H_2O$ (pH = 5.2 ± 0.1) and 0.01 M SeO_2 (pH = 3.1 ± 0.1) were utilized as cationic and anionic precursors, respectively. The both solutions were mixed in 1:1 volumetric ratio in glass container and the pH of electrolytic bath maintained at 2.9 ± 0.1 by addition of dilute H_2SO_4. The potentiostatic deposition of CdSe thin films was carried out at constant potential -0.78 V/SCE for 40 min using three electrode system at room temperature. After film deposition, it was annealed at 400 K for 60 min in air atmosphere and stored in sealed container.

6.2.3.3 Deposition of rGO/CdSe composite thin films

6.2.3.3.1 Precursor solution preparation

For CdSe thin films preparation, 100 ml solution of cadmium sulfate octahydrate (0.05M $CdSO_4.8H_2O$) and 100 ml solution of selenium dioxide (0.01M SeO_2) were used as sources for cadmium (Cd) and selenium (Se) ions, respectively. Dilute H_2SO_4 was used to adjust pH of aqueous deposition bath. The rGO deposited SS substate is used as a substrate for rGO/CdSe composite thin film.

6.2.3.3.2 Estimation of the deposition potentials

In order to estimate deposition potential, the polarization curves were recorded for Cd, Se, and CdSe (on fixed rGO deposited SS substrate of surface area 1 X 1 cm^2) from their respective baths as 0.05 M $CdSO_4.8H_2O$ (pH = 5.2 ± 0.1), 0.01 M SeO_2 (pH = 3.1 ± 0.1), and 0.05 M $CdSO_4.8H_2O$ + 0.01 M SeO_2 (pH = 2.9 ± 0.1). The potential was scanned from 0 to -1 V/SCE with scan rate 20 mV/s. **Fig. 6.2** shows the polarization curves for Cd, Se, and CdSe thin films on rGO deposited SS substrate. An estimated deposition potentials are tabulated in **Table 6.2**.
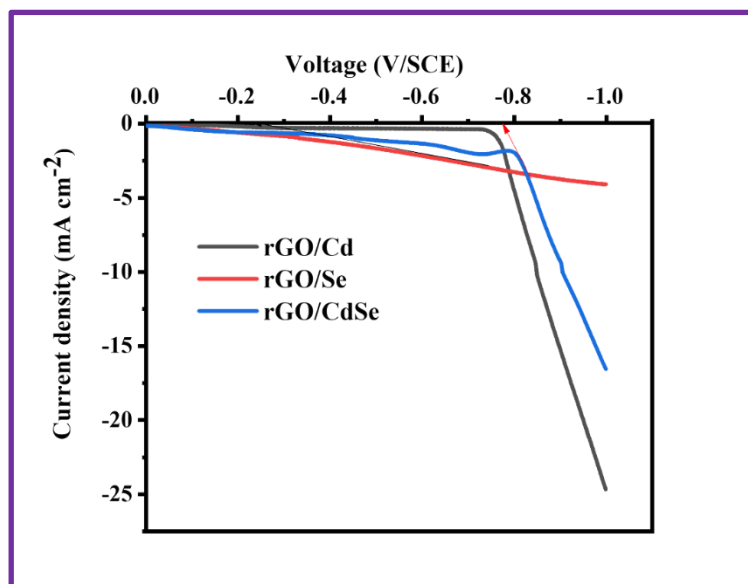
Fig. 6.2 Polarization curves of Cd, Se, and CdSe on rGO deposited SS substrate.

Table 6.2: Estimated deposition potentials for rGO/CdSe films on SS substrate.

Sample	rGO/Cd	rGO/Se	rGO/CdSe
Deposition potential (V/SCE)	-0.76	-0.24	-0.77

It is observed that the deposition potential of CdSe on rGO has reduction potentials of higher negative than individual Cd and Se. The CdSe thin film of reddish-brown color is deposited at deposition potential -0.77 V/SCE. From **Table 6.2**, slight difference is observed in deposition potentials of CdSe on SS and CdSe on rGO. The shift towards positive potential may because of the more active sites of rGO.

6.2.3.3.3 Deposition of rGO/CdSe composite thin films

The rGO thin films are deposited on SS substrate as explained in **section 6.2.3.1**. The rGO deposited SS substrate is used to deposit CdSe thin film by potentiostatic ED method. The potentiostatic deposition of rGO/CdSe thin films was carried out at constant potential - 0.77 V/SCE for 40 min using three electrode system. After film deposition, it was annealed at 400 K for 60 min in air atmosphere and stored in sealed container.

6.2.3.3.4 Thin film formation and reaction mechanism of rGO/CdSe composite

Formation of CdSe thin film on rGO deposited SS substrate surface takes place via following mechanism:

Cationic source cadmium sulfate dissociates in water to give metal cations that is Cd^{+2} ions,

$$3CdSO_4.8H_2O + H_2O \rightarrow Cd^{+2} + SO_4^{-2} + 9H_2O \qquad (6.1)$$
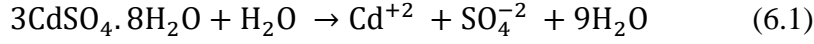
Anionic source SeO_2 after dissolution in water gives selenious acid (H_2SeO_3),

$$SeO_2 + H_2O \rightarrow H_2SeO_3 \qquad (6.2)$$

It further undergoes six electron transfer process, in which Se^{+4} ion after four electron transfer changes to Se^0, which again turns to Se^{-2} ions, upon two electron transfer (at potential = -0.77 V/SCE). This process takes place as an underpotential deposition (UPD) process.

$$H_2SeO_3 + 4H^+ + 4e^- \rightarrow Se + 3H_2O \qquad (6.3)$$

$$Se + 2e^- \rightarrow Se^{2-} \qquad (6.4)$$
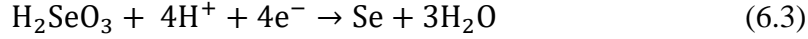
In short, co-deposoition process proceeds via overall equation [20],

$$H_2SeO_3 + Cd^{+2} + 4e^- + 4H^+ \rightarrow CdSe + 3H_2O \qquad (6.5)$$
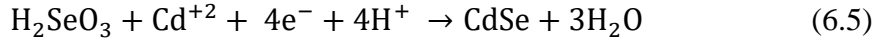
6.3 Thin film characterizations

The characterizations of CdSe and rGO/CdSe were carried out as mentioned in **chapter III section 3.3**.

6.4 Thickness measurement

The thickness of CdSe, and rGO/CdSe thin films were calculated using weight difference method by formula given in **chapter III** section **3.2.2.5**.

The thickness of CdSe film is found to be 590 nm. For rGO/CdSe film, thickness of rGO film measured first and it used as a substrate for further CdSe deposition. The calculated thicknesses for rGO, and rGO/CdSe were 90 and 730 nm, respectively. The increase in film thickness of rGO/CdSe thin film may be due to the availability of more nucleation sites of rGO surface for the deposition of CdSe over it [17].

6.5 Results and discussions

6.5.1 XRD analysis

X-ray diffraction (XRD) is a prime technique for structural findings. XRD patterns of CdSe, and rGO/CdSe thin films are shown in **Fig. 6.3**. The broad peak observed at $2\theta = 25.48$ ° in XRD patterns of CdSe and rGO/CdSe corresponds to (111) plane of the cubic crystal structure of CdSe which is good agreement with JCPDS card no 00-019-091 [21]. The broadening of peak in XRD evidences the nanocrystalline structure of CdSe thin films. The peaks marked by '*' are due to the

SS substrate. No separate rGO diffraction peak is observed in rGO/CdSe XRD pattern, this may because of low diffraction intensity and presence of relatively small amount of rGO in the composite. Scherrer's equation was used to estimate crystallite sizes. The XRD pattern reveals that, after composition of CdSe with rGO, the (111) plane peak becomes more intense, indicating an improvement in crystallinity of the electrodeposit. The increase in crystallinity may be related to availability of more nucleation cites and centers for growth of CdSe on rGO sheets [22-25].

CdSe and rGO/CdSe have the estimated crystallite sizes of 19 and 26 nms, respectively. The increment in the crystallite size may due to proper deposition potential, and time and mainly the nucleation sites provided by rGO.
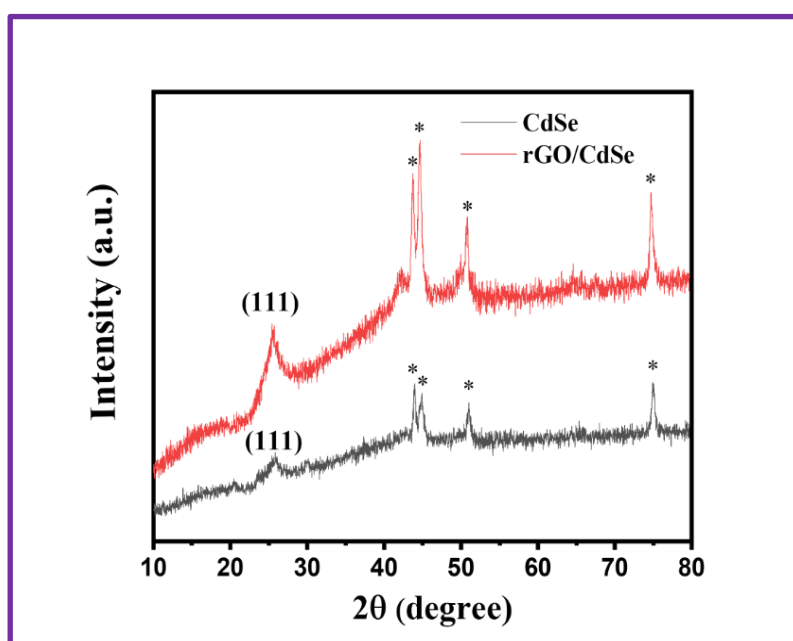
Fig. 6.3 The XRD patterns of CdSe, and rGO/CdSe thin films on SS substrate.

6.5.2 FE-SEM study

The morphology of CdSe, and modifications induced after rGO composition in CdSe thin films were studied using FE-SEM study. The FE-SEM images of CdSe, and rGO/CdSe at lower magnification (20 kX) and higher magnification (40 kX) are shown in **Fig. 6.4 (a-d)**. **Fig. 6.4 (a)** shows porous web of fiber-like morphology of CdSe thin film. As seeking towards higher magnification **Fig. 6.4 (b)**, the aggregations of particle like structures grown on fibrous web are observed. After composition with rGO, a compact and crowded web of interconnected nanofibers structures with marvelously bloomed buds formation is seen **Fig. 6.4 (c-d)**. The CdSe composite with rGO shows nanoparticles and the thread like structure becomes spongier and more porous which leads to better interaction between the electrolyte

and the electrode surface results in more wettability which is good sign for the better electrochemical properties of the photoelectrodes. Raut et al. **[21]** reported similar type of morphology for CdSe by electrodeposition method which results in the better capturing of photons and electrode electrolyte interface contact. Won-chun et al. **[26]** reported the uniform distribution of CdSe nanoparticles on rGO sheets by hydrothermal method. Shih et al. **[27]** reported the equal distribution of CdSe on rGO, effectively enhances the light absorbing capacity of photoelectrode and it reflects in efficiency of solar cells and photodetectors.
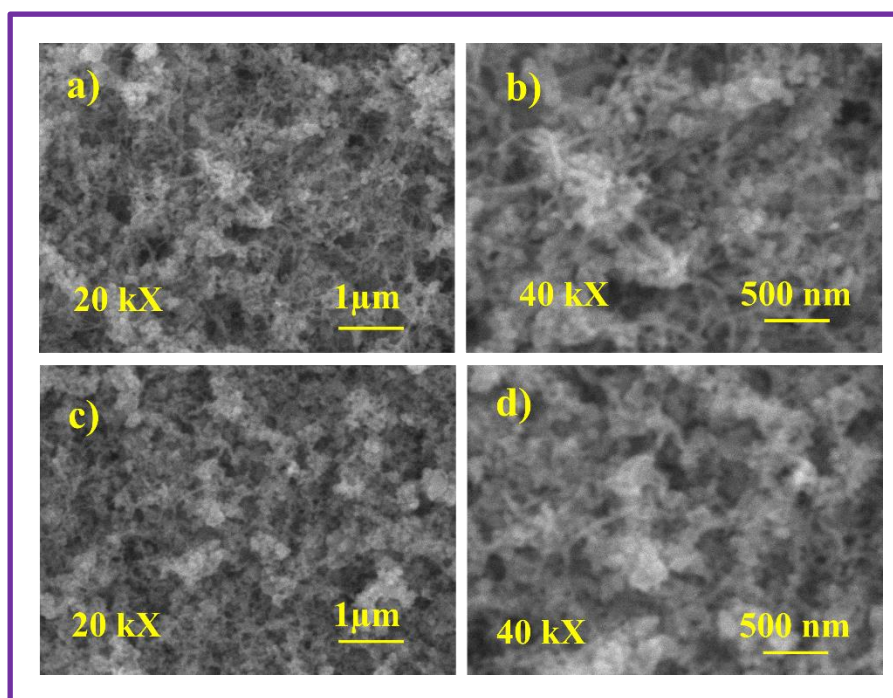
Fig. 6.4 FE-SEM images of (a-b) CdSe, (c-d) rGO/CdSe films at magnifications of 20 kX and 40 kX.

6.5.3 EDAX Study

The elemental composition of CdSe, and rGO/CdSe thin films are studied using EDAX study, as shown in **Fig. 6.5 (a, and b)**. **Fig. 6.5 a)** gives evidence of cadmium (Cd) and selenium (Se) species presence, the atomic percentage of cadmium to selenium is 44:56. **Fig. 6.5 (b)** shows that EDAX pattern of rGO/CdSe sample consists of Cd, Se, and carbon (C), species in the atomic percentage of 39:47:14. The EDAX of rGO/CdSe clearly shows successful composite formation of CdSe and rGO which supports to the XRD study. From the EDAX study it is seen that CdSe and rGO/CdSe samples are formed nearly in stoichiometric ratio. Besides, the C signals which come from rGO sheets were detected from the spectrum **[28]**.
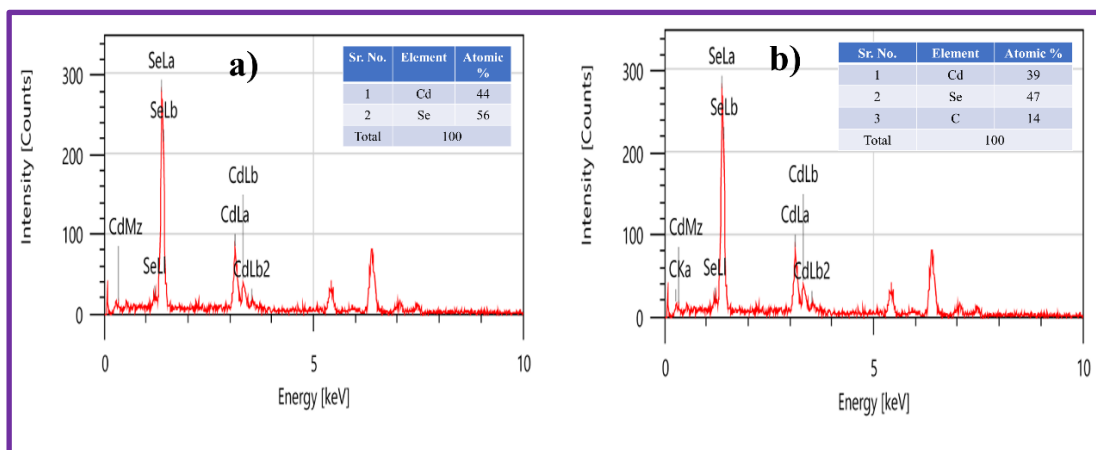
Fig. 6.5 EDAX patterns of a) CdSe, b) rGO/CdSe samples.

6.5.4 Surface wettability study

Wettability study discuss the interaction between CdSe, and rGO/CdSe electrodes surface with electrolyte which determined by the value of the contact angle. Higher wettability results in a smaller contact angle with the surface indicates a hydrophilic nature and vice versa. Water contact angle images of CdSe, and rGO/CdSe thin films are depicted in **Fig. 6.6 (a-b)**.
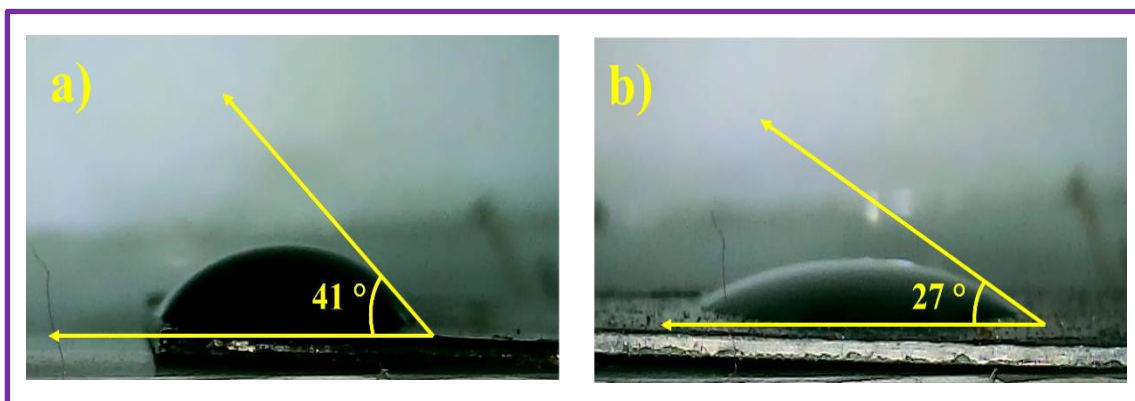
Fig. 6.6 Photographs of contact angles a) CdSe, and b) rGO/CdSe thin films.

The observed values of contact angles for CdSe, and rGO/CdSe thin films are 41, and 27 °, respectively show hydrophilicity. From the contact angle images CdSe composited with rGO showed the lower contact angle value than pristine CdSe. The reduction in contact angle value of rGO composited film may be due to the surface roughness and spongy nature of the electrode surface observed in FE-SEM study. The higher hydrophilicity leads the intimate contact between photoelectrode surface and redox electrolyte which results better electrochemical characteristics and makes it more suitable candidate for solar cell application than CdSe **[21]**.

6.5.5 BET study

The surface area of CdSe and rGO/CdSe composite were studied by BET study. **Fig. 6.7 (a, b)** shows the N_2 adsorption/desorption curves of CdSe and rGO/CdSe samples, respectively. Both samples exhibit type V isotherms, accompanied by H1 type hysteresis loop. The CdSe and rGO/CdSe show the specific surface areas of 14 and 23 m^2 g^{-1}, respectively. It is observed that, after CdSe composite with rGO, surface area is improved, which results in better electrochemical properties. The increase in surface area of rGO composited sample may be due to the higher surface area ability of rGO.
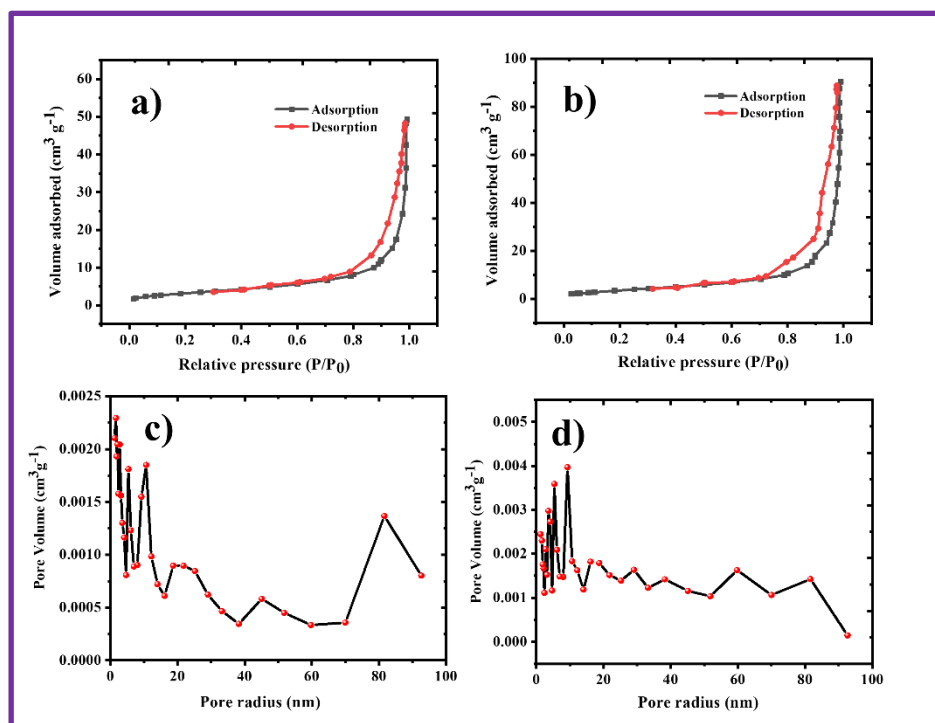
Fig. 6.7 The N_2 adsorption-desorption isotherms for a) CdSe, and b) rGO/CdSe samples and the BJH size distribution curves of c) CdSe, and d) rGO/CdSe samples.

The BJH graph is used to understand the pore size distribution of the material. **Fig. 6.7 (c, d)** depicts the plots of pore volume against pore radius for CdSe and rGO/CdSe samples, respectively. Both samples are mesoporous and macroporous in nature. Mesoporosity in CdSe and rGO/CdSe enhances PEC cell efficiency by increasing surface area for photon capture and facilitating charge transport. Interconnected pores enable swift movement of photoexcited charge carriers to electrode surfaces, minimizing recombination losses. Additionally, mesoporosity promotes intimate electrode-electrolyte contact and enhances surface reaction

kinetics. Efficient utilization of photo-generated charge carriers improves PEC device performance.

6.5.6 Optical absorption study

The optical absorption properties of CdSe and rGO/CdSe thin films were studied by diffuse reflectance spectra (DRS). The Tauc plots for CdSe and rGO/CdSe are displayed in **Fig. 6.8.** The absorbance of both electrodes in the 500-800 nm wavelength (visible region). The absorption band edges are found at 711 and 738 nm for CdSe, and rGO/CdSe, respectively (**Fig. 6.8 Inset**). The absorption edges showing red shift, which may be due to the composition with rGO increases the conductivity of the material and suppresses recombination of electron hole pairs **[29]**. The rGO/CdSe thin film shows more proficiency in utilizing visible light than that of CdSe **[17]**. Kubelka-Munk standard equation is used to calculate band gap *(E$_g$)* of the electrodes.
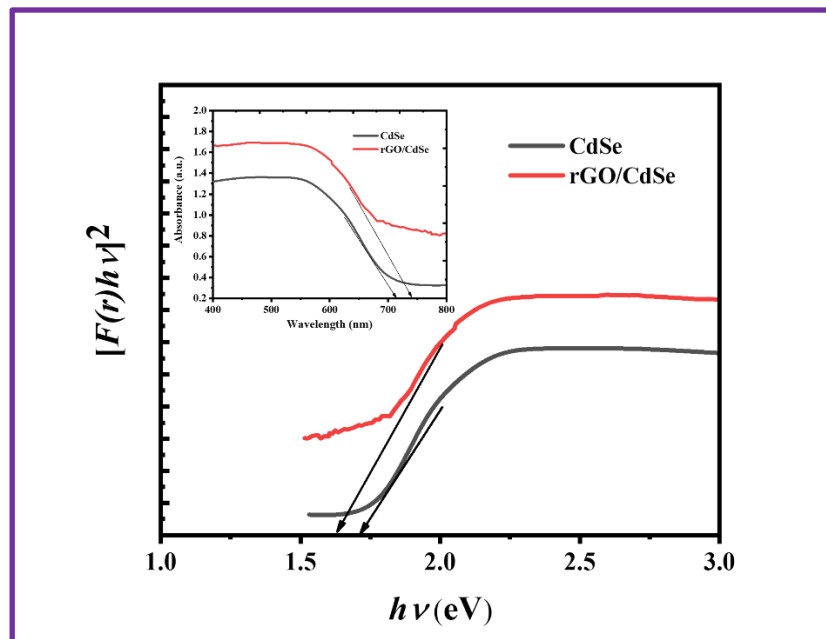
Fig. 6.8 Tauc plots of CdSe and rGO/CdSe thin film electrodes (Inset absorbance spectra of CdSe and rGO/CdSe thin film electrodes).

The band gap values are found to be 1.72, and 1.64 eV for CdSe and rGO/CdSe electrodes, respectively. Hence, composite with rGO exhibits shift in optical spectrum because of charge localizations in each nanocrystal. The reduced band gap value of rGO/CdSe electrode implies that a lower recombination rate of photogenerated electrons and holes under visible light irradiation. These further indicate that the electrons are excited from valence band (VB) to conduction band (CB) of CdSe and then captured by graphene nanosheets and the transferred to SS substrate which prevents the direct recombination of electron and holes. Also, the

band gap value narrower due to crystallite size-dependent modifications is observed in semiconductor properties **[14, 22**, **30]**. The improved absorbance in visible region due to composition with rGO reflects in the electrochemical properties of the electrodes **[15]**.

Section B

6.6 Electrochemical studies

Electrochemical investigations are crucial for PEC solar cell technology, assessing electrode-electrolyte junction quality, semiconductor material type, and charge carrier generation through I-V characteristics of CdSe and rGO/CdSe materials. Power output analysis of PEC cell devices helps to understand semiconductor photoelectrode parameters, identifying factors like charge recombination and electrode degradation for improvement strategies. The EIS elucidates charge transfer processes at electrode-electrolyte junctions for CdSe and rGO/CdSe electrodes.

6.6.1 I-V characteristics of CdSe and rGO/CdSe electrodes

The three-electrode PEC cell set up was made up with CdSe or rGO/CdSe as a working, saturated calomel electrode (SCE) as a reference, and graphite as a counter electrode in 1 M polysulfide electrolyte. The I-V curves of CdSe and rGO/CdSe electrodes in dark and under light are shown in **Fig. 6.9 (a-b)**.
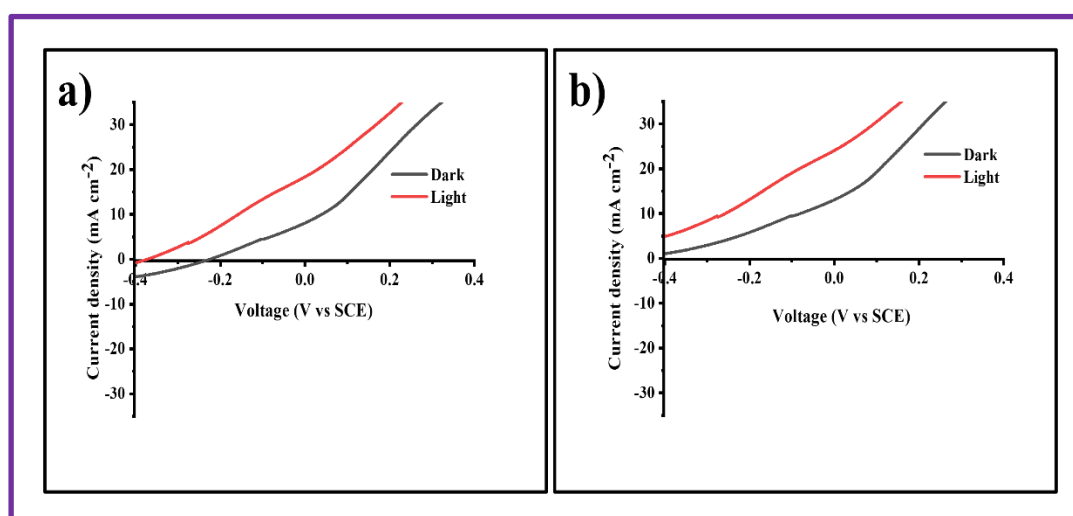
Fig. 6.9 I-V characteristics curves of a) CdSe, and b) rGO/CdSe electrodes in dark and under light conditions.

The I-V curve shows the nature of increase a current negatively depicts the n-type of the semiconductor material. The symmetry factor (β) was determined from the I-V curves in dark and under light conditions by employing the formulae as mentioned in **chapter I section 1.2.3**. The 'β' values for CdSe and rGO/CdSe are tabulated in **Table 6.3**.

Table 6.3: The 'β' values of CdSe and rGO/CdSe thin film electrodes in dark and under light conditions.

Sr. No.	Electrode	Condition	$\beta = \dfrac{2.303\, RT}{bF}$	$\beta = 1 - \dfrac{\left(\log \dfrac{I}{I_0}\right) RT}{qV}$
1	CdSe	Dark	0.94	0.96
		Light	0.95	0.97
2	rGO/CdSe	Dark	0.93	0.97
		Light	0.94	0.98

The higher 'β' value implies the quality of electrode electrolyte interface, where efficient transportation of the charge carriers through the interface without recombination losses. The reduction in the contact angle value after composition of CdSe with rGO proved by the greater 'β' value. The greater 'β' value replicates in the less losses leading better electrochemical and PEC properties.

6.6.2 Power output characteristics

The power output curves of CdSe or rGO/CdSe//polysulfide//graphite device is given in **Fig. 6.10 (a-b)** in dark, under light, and in chopping conditions. From cathodic behaviour of curve confirms the n-type electrical conductivity of both CdSe and rGO/CdSe. The PEC parameters like I_m, V_m, I_{sc}, and V_{oc} are estimated from power output curves in dark, and under light conditions using the respective formulae given in **chapter III section 3.5.6**.

The PEC parameters are tabulated in **Table 6.4**. The rGO/CdSe electrode showed a performance of $I_{SC} = 3.86$ mA cm^{-2}, $V_{oc} = 0.34$ mV, $FF = 0.35$, and $\eta = 1.8$ %. After composition of CdSe with rGO, a noticeable improvement is observed in an efficiency of the PEC cell. This may be due to good electrical, mechanical and surface structural properties of rGO support. Also, an improvement in the efficiency concerned to the surface roughness, good crystallinity, intimate contact between the electrolyte and the electrode surface resulting in better electrochemical properties along with more hydrophilicity.
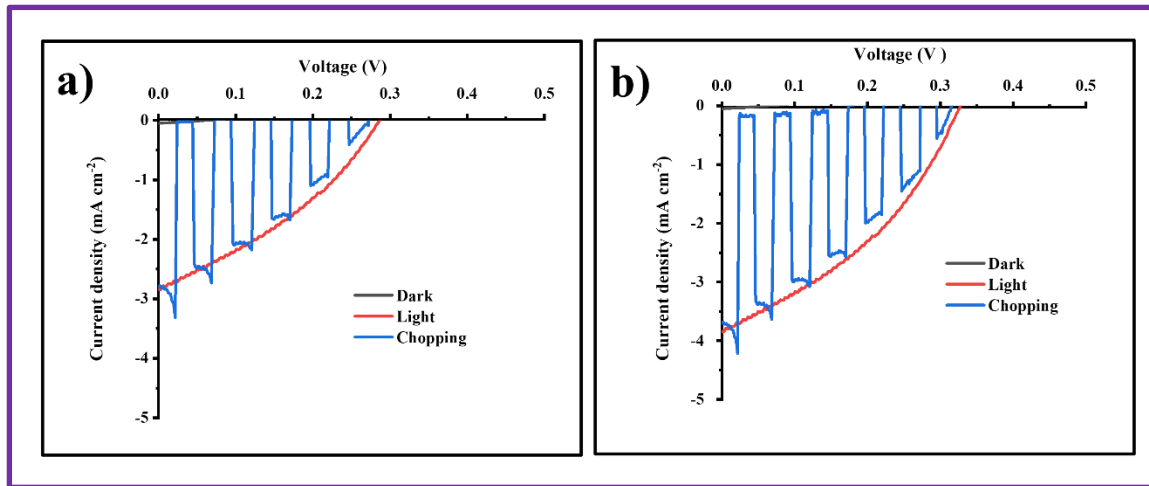
Fig. 6.10 Power output curves of a) CdSe, and b) rGO/CdSe electrodes in dark, under light, and in chopped conditions.

Table 6.4: The PEC parameters of CdSe and rGO/CdSe thin films in dark and under light conditions.

Sample	*Isc* (mA cm^{-2})	*V$_{OC}$* (V)	*I$_m$* (mA cm^{-2})	*V$_m$* (V)	*FF*	Efficiency 'η' (%)
CdSe	2.85	0.28	1.65	0.16	0.33	1.0
rGO/CdSe	3.86	0.34	3.20	0.15	0.35	1.8

6.6.3 EIS Study

The EIS study was conducted in dark and under light conditions within a frequency range of 1 kHz to 100 MHz to understand the charge transfer properties of CdSe, and rGO/CdSe electrodes as depicted in **Fig. 6.11**. The plot of real with imaginary impedance is called Nyquist plot. The Nyquist plot is generally divided into left, middle, and right portions, associated with higher, middle, and lower frequencies, respectively.

The resulting EIS parameters, including solution resistance (R_S), charge transfer resistance (R_{ct}), leakage capacitance (Q_1), and diffusion resistance (W) are summarized in **Table 6.5**.

Table 6.5 indicates that, under light exposure, there is slight change observed in R_s over in dark. The minimal value of R_{ct} indicates the predominant charge transfer kinetics in rGO/CdSe thin film under visible light compared to dark condition. This could be attributed to the increased density of generated electron-hole pairs in CdSe

and enhanced ability of rGO to capture, store, and transport electrons through its sp^2 aromatic network.
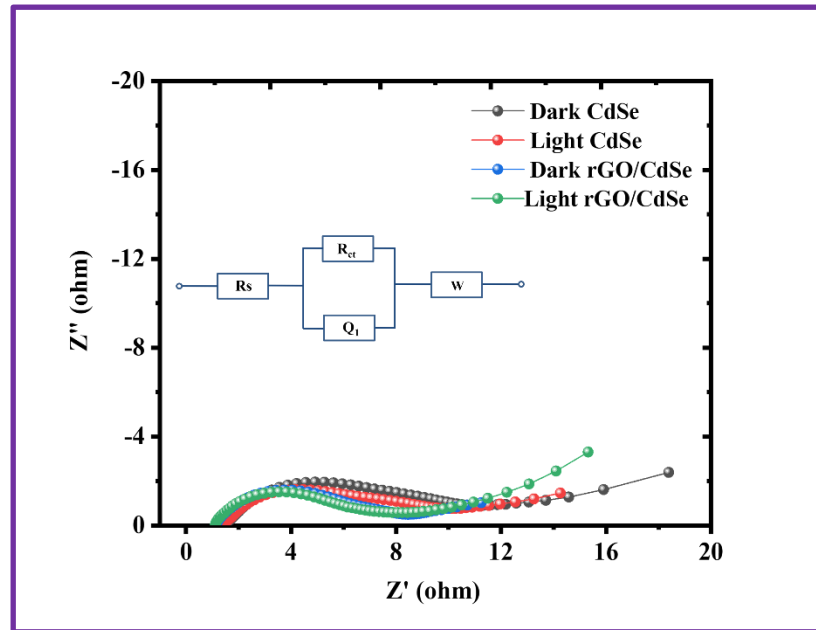
Fig. 6.11 Nyquist plots for CdSe, and rGO/CdSe thin films in dark and under light conditions with an equivalent circuit diagram.

Consequently, when combined with rGO, the likelihood of recombination of photoexcited electron-hole pairs from pure CdSe could be significantly reduced, resulting in higher PEC activity of rGO/CdSe nanocomposite compared to bare CdSe. Therefore, rGO serves a crucial role by facilitating electron transfer between CdSe and the SS substrate, consequently enhancing photocurrent [31].

Table 6.5: The EIS parameters of CdSe, and rGO/CdSe electrodes in dark and under light conditions.

Sample	Condition	Rs (Ω cm^{-2})	R_{ct} (Ω cm^{-2})	Q_1 (μF)	W (mΩ)
CdSe	Dark	1.6	11.3	41	81
	Light	1.5	10.2	53	73
rGO/CdSe	Dark	1.2	8.6	62	65
	Light	1.1	7.5	87	39

The EIS results closely align with the I-V characteristics of the photocurrent. Also, an enhancement in 'η' of the electrode containing rGO can be attributed to the reduced charge transfer resistance due to good conductivity of rGO.

6.7 Conclusions

Current chapter comprises the deposition of CdSe and rGO/CdSe thin films by electrodeposition method on SS substrate. The CdSe and rGO/CdSe showed fibrous web-like morphology with cubic crystal structure. The EDAX studies revealed the presence of Cd, Se, and C in stoichiometric amount in rGO/CdSe films. Wettability study of CdSe and rGO/CdSe revealed hydrophilic nature with contact angle value of 41 and 27 °, respectively. The rGO/CdSe thin film showed reduced energy band gap due to quantization in nanocrystalline semiconductor and rGO supports to increase generation of electron hole pairs with less recombination. The fill factor (*FF*) and photoconversion efficiency (*η*) were 0.35, and 1.8 %, respectively for rGO/CdSe thin film. The EIS studies showed that rGO composite lowers the charge transfer resistance which is valuable for superior charge transport process. Hence, it is concluded that composite of rGO with CdSe increases the 'η' nearly 1.8 times compared to CdSe.

6.8 References

1] R. Passalacqua, S. Perathoner, G. Centi, J. Energy Chem., 26 (2017) 219-240.

2] N. Shinde, D. Dubal, D. Dhawale, C. Lokhande, J. Kim, J. Moon, Mater. Res. Bull., 47 (2012) 302-307.

3] Y. Cao, C. Wang, B. Zhu, Y. Gu, Opt. Mater., 66 (2017) 59-64.

4] K. Chaudhari, N. Gosavi, N. Deshpande, S. Gosavi, J. Sci.: Adv. Mater. Devices, 1 (2016) 476-481.

5] P. Huo, J. Guan, M. Zhou, C. Ma, X. Liu, Y. Yan, S. Yuan, J. Ind. Eng. Chem., 50 (2017) 147-154.

6] S. Tilley, Adv. Energy Mater., 9 (2019) 1802877 (1-13).

7] K. Yu, G. Lu, S. Mao, K. Chen, H. Kim, Z. Wen, J. Chen, ACS Appl. Mater. Interfaces, 3 (2011) 2703-2709.

8] M. Molaei, Sol Energy., 196 (2020) 549-566.

9] H. An, X. Yan, H. Li, B. Yang, J. Wei, G. Yang, ACS Appl. Energy Mater., 2 (2019) 4195-4204.

10]   Q. Shen, X. Shi, M. Fan, L. Han, L. Wang, Q. Fan, J. Electroanal. Chem., 759 (2015) 61-66.

11]   A. Marlinda, N. Yusoff, S. Sagadevan, M. Johan, Int. J. Hydrog. Energy, 45 (2020) 11976-11994.

12]   D. Patidar, A. Yadav, D. Paul, A. Sharma, S. Nehra, Phys. E: Low-Dimens. Syst. Nanostructures, 114 (2019) 113560 (1-42).

13]   F. Kong, J. Wang, Z. Han, B. Qian, S. Tao, H. Luo, L. Gao, Chem. Comm., 55 (2019) 2996-2999.

14]   H. Li, X. Wang, L. Zhang, B. Hou, Corros. Sci., 94 (2015) 342-349.

15]   I. Lightcap, and P. Kamat, J. Am. Chem. Soc., 134 (2012) 7109-7116.

16]   Q. Shen, Y. Wang, J. Xue, G. Gao, X. Liu, H. Jia, Q. Li, B. Xu, Appl. Surf. Sci., 481 (2019) 1515-1523.

17]   P. Xie, S. Xue, Y. Wang, Z. Gao, H. Feng, L. Li, R. Zou, Ceram. Int., 42 (2016) 18264-18270.

18]   J. Feminus, and P. Deepa, Mater. Chem. Phys., 289 (2022) 126440 (1-12).

19]   O. Uguz, O. Budak, A. Koca, Int. J. Hydrog. Energy, 46 (2021) 35290-35301.

20]   S. Gangawane, S. Kamat, V. Malekar, V. Fulari, S. Patil, M. Dongare, J. Opt., 39 (2010) 167-174.

21]   V. Raut, C. Lokhande, V. Killedar, J. Electroanal. Chem., 788 (2017) 137-143.

22]   W. Ke, D. Zhao, A. Cimaroli, C. Grice, P. Qin, Q. Liu, L. Xiong, Y. Yan, G. Fang, Mater. Chem. A, 3 (2015) 24163-24168.

23]   M. Hassen, R. Riahi, F. Laatar, H. Ezzaouia, Surf. Interfaces, 18 (2020) 100408 (1-10).

24]   P. Li, B. Zhu, P. Li, Z. Zhang, L. Li, Y. Gu, Nanomater., 9 (2019) 957 (1-13).

25]   A. Abdel-Salam, M. Awad, T. Soliman, A. Khalid, J. Alloys Compd., 898 (2022) 162946 (1-9).

26]   O. Won-Chun, C. Mingliang, C. Kwangyoun, K. Cheolkyu, M. Zeda, Z. Lei, Chin. J. Catal., 32 (2011) 1577-1583.

27]   Y. Shih, Y. Chen, J. Tan, S. Chang, W. Uen, S. Chen, M. Lin, Y. Chen, W. Tu, IEEE Access, 8 (2020) 95855-95863.

28]   P. Xie, S. Xue, Y. Wang, Z. Gao, H. Feng, L. Li, R. Zou, Ceram. Int., 42 (2016) 18264-18270.

29]   A. Khalid, and A. Shawky, Ceram. Int., 46 (2020) 20769-20776.

30]   N. Ghobadi, P. Sohrabi, H. Hatami, Chem. Phys., 538 (2020) 110911 (1-17).

31]   N. Meng, Y. Zhou, W. Nie, P. Chen, J. Nanoparticle Res., 18 (2016) 1-13.

Chapter-VII

CdS/PANI and rGO/CdS/PANI films by successive ionic layer adsorption and reaction (SILAR) method: synthesis, characterization, and their gas sensing performance

CHAPTER- VII

CdS/PANI and rGO/CdS/PANI films by successive ionic layer adsorption and reaction (SILAR) method: synthesis, characterization, and their gas sensing performance

Section A

7.1 Introduction

The main cause of pollution is generally pollutants. Pollutants are mainly generated by natural activities such as hurricanes, volcanoes and forest fires, but man-made activities such as the burning of fossil fuels, waste products, industrial waste, transportation and household use are also largely responsible for pollutant generation. All kinds of pollution such as water pollution, air pollution, sound pollution, soil pollution and also light pollution have become a dangerous problem for mankind. Air pollution affects the living organisms, the most and is increasing day by day due to natural disasters, urbanization and industrialization [1, 2].

An increase in air pollution that poses a threat to the environment and public health. To protect the environment and living organisms, it is crucial to detect such harmful, dangerous and flammable gases [3]. While the human olfactory system is an excellent tool for identifying and detecting many odors, most hazardous gases and vapours can only be detected at extremely high concentrations or not at all. Toxic gases in the atmosphere, such as CO, H_2S, Cl_2, NO_2, SO_2, etc., must be detected below hazardous limits, and these can range from 1 part per million (ppm) to several hundred ppm, the sensors used for this purpose must be capable of detecting such concentrations.

The third type of gas monitoring includes igneous gases like C_2H_2, C_2H_4, C_3H_6, C_3H_8, LPG, and so forth. This means that in order to prevent the unintended development of fire or explosion, concentrations of explosive (flammable) gases below the lower explosive level (LEL), which for most gases is up to a few percent, must be monitored. In essence sensors that able to measure gases at low concentrations (in ppm) for dangerous and flammable gas monitoring applications must be required [4].

Gas sensors are fabricated utilizing a variety of materials, technologies, and phenomena due to the rising need of them for number of areas including national security, social security, food safety, and environmental monitoring. Metal oxides (MOs) chemoresistive principle based gas sensors are the most often used type of sensor in practical applications. Because of their excellent gas responsiveness, affordability, and ease of manufacture, oxides are a common component of chemoresistive type sensors. Nevertheless, problems with selectivity, stability, and high operating temperature limit their broad use [5].

In this context, materials with lower band gap energies, such as metal chalcogenides (MCs) from group II-VI, offer a high surface-to-volume ratio and potential adsorption sites like sulfur vacancies, edge sites, and defects, making them highly valuable in sensor technology. Additionally, MCs can address key challenges associated with MOs, including signal drift, oxygen vacancy diffusion, and high operating temperatures. Despite their potential, there has been limited research on the gas sensing capabilities of MCs. Specifically, studies on cadmium chalcogenide-based sensors are still in their early stages, indicating the need for further exploration in this area **[6]**.

The MCs with conducting polymers have many advantageous properties such as low-temperature synthesis, high flexibility, the possibility of large-scale synthesis, outstanding mechanical properties, and low cost. Also, the chemical and physical properties like enhanced surface area, controlled morphology, suitable diffusion kinetics, and an increase in number of interaction sites are important for sensing application **[7, 8]**.

Graphene is a two-dimensional (2D) monolayer comprising sp^2-bonded carbon atoms. Electron transport through graphene is highly sensitive to adsorbed molecules owing to the 2D structure of graphene that makes every carbon atom a surface atom. Graphene has been demonstrated as a promising gas-sensing properties due to higher electrical conductivity, higher surface area, and the honeycomb like structure supports more porous and conductive properties. The heterostructures of MCs with reduced graphene oxide (rGO) ascribes fast adsorption/desorption of gaseous can be leads to changes in the conductance of heterojunctions **[9, 10]**.

The various methods have been used to fabricate the heterojunctions of cadmium chalcogenides, conducting polymers, and rGO such as chemical oxidative polymerization, dip coating, In situ polymerization, electrodeposition, chemical co-dispersion, hydrothermal, chemical bath deposition (CBD), sputtering, vacuum evaporation, in-situ vulcanization **[5, 11-24]**. The SILAR is a most convenient method to fabricate layer-by-layer heterojunction films along with its merits like low temperature synthesis, easy controllable deposition parameters, low cost, and uniform deposition of the thin films.

In present work, the depositions of rGO, CdS, rGO/CdS, polyaniline (PANI), CdS/PANI, and rGO/CdS/PANI films were carried out via SILAR method on stainless steel (SS) substrates at room temperature (RT). The physicochemical properties of the heterojunction films were studied by different characterizations techniques. The gas sensing properties of CdS/PANI and rGO/CdS/PANI heterojunction devices were investigated at RT.

7.2 Experimental details

7.2.1 Substrate cleaning

The substrates were cleaned as procedure explained in **Chapter III section 3.2.1**.

7.2.2 Chemicals used

Graphite flakes, sodium nitrate ($NaNO_3$), cadmium chloride ($CdCl_2$), sulfuric acid (H_2SO_4), potassium permanganate ($KMnO_4$), hydrogen peroxide (H_2O_2), hydrazine hydrate (H_6N_2O), sodium sulfide (Na_2S), sulfur powder (S), sodium hydroxide (NaOH), aniline monomer, ammonium persulfate (APS) $(NH_4)_2S_2O_8$ were purchased from Thomas Baker and directly employed without purification. All solutions were prepared in double distilled water (DDW). Stainless steel (SS) strips measuring 1 cm x 5 cm were utilized as substrates for deposition.

7.2.3 Material synthesis

7.2.3.1 Synthesis of rGO thin films

The rGO thin films were synthesized as explained in **chapter III section 3.2.2.1 and 3.2.2.2**.

7.2.3.2 Synthesis of CdS and rGO/CdS thin films

The deposition of CdS, and rGO/CdS thin films by SILAR method on SS substrates were described in **chapter III in section 3.2.2.3**. The 80 SILAR cycles were performed to achieve desired thickness of films.

7.2.3.3 Synthesis of polyaniline (PANI) thin films

The PANI thin film was deposited on the SS surface by two beaker SILAR method. A 0.45 M aniline monomer dispersed into 0.5 M H_2SO_4, and 0.5 M APS is used as oxidizing agent. The pH of the acidic solution was between 3.1 ± 0.1. Firstly, SS substrate was immersed in cationic bath for 10 s and after that it was immersed in anionic solution APS for 5 s. Such 60 repeated cycles were performed to deposit green colour PANI thin film.

7.2.3.4 Synthesis of CdS/PANI thin films

The PANI thin film was deposited on CdS surface to fabricate heterojunction by two beaker SILAR method depicted in **Fig. 7.1**. The PANI film was deposited on CdS surface by SILAR method as explained in above section.
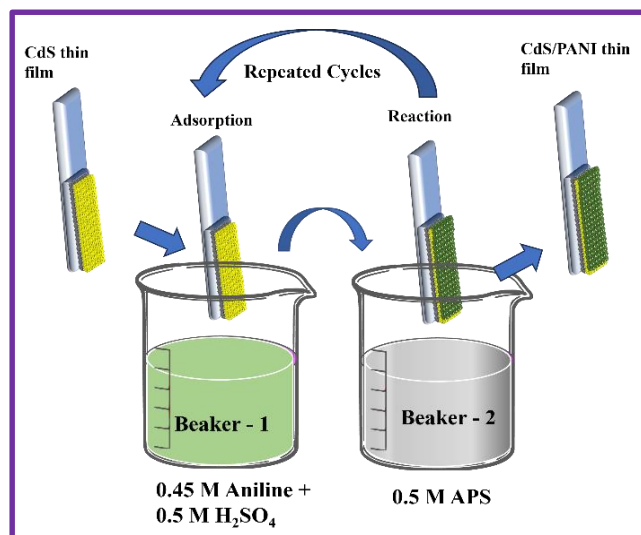
Fig. 7.1 Schematic of CdS/PANI heterojunction film deposition.

7.2.3.5 Deposition of rGO/CdS/PANI heterojunction thin films

The PANI thin film was deposited on rGO/CdS surface to form heterojunction by two beaker SILAR method as mentioned in above section.

7.3 Physicochemical and electrochemical characterization of heterojunction films

The all characterizations with FE-SEM cross section of heterojunction were carried out as mentioned in **chapter III section 3.3**.

7.4 Thickness measurement

The thickness of deposited films was estimated by using gravimetric weight difference method employing formula given in **chapter III section 3.2.2.5**. The discussion about thickness values of rGO, CdS, and rGO/CdS films is given in **chapter III section 3.2.2.5**. For PANI film the estimated thickness value is 1020 nm. For CdS/PANI heterojunction film an estimated thicknesses are 700, and 1460 nm for CdS and PANI, respectively. The total thickness of CdS/PANI heterojunction was 2160 nm which is the mathematical addition of CdS and PANI layer thicknesses. In case of rGO/CdS/PANI heterojuncton film, the estimated thickness values are 90, 1420, and 1460 nm for rGO, CdS, and PANI layers, respectively. The total thickness of rGO/CdS/PANI heterojunction was 2970 nm.

7.5 Results and discussions

7.5.1 XRD study

The XRD patterns of rGO, CdS, rGO/CdS, CdS/PANI, and rGO/CdS/PANI films on SS substrate are depicted in **Fig. 7.2**. The XRD patterns of rGO, CdS, and rGO/CdS are discussed in **Chapter III section 3.4.1.1 and 3.4.2.1**. The '*' peaks are observed in XRD patterns due to the SS substrate. From CdS/PANI XRD pattern, it is observed that, no peak was observed than the SS peaks, which proves the amorphous nature of outer layer of PANI film **[25]**.
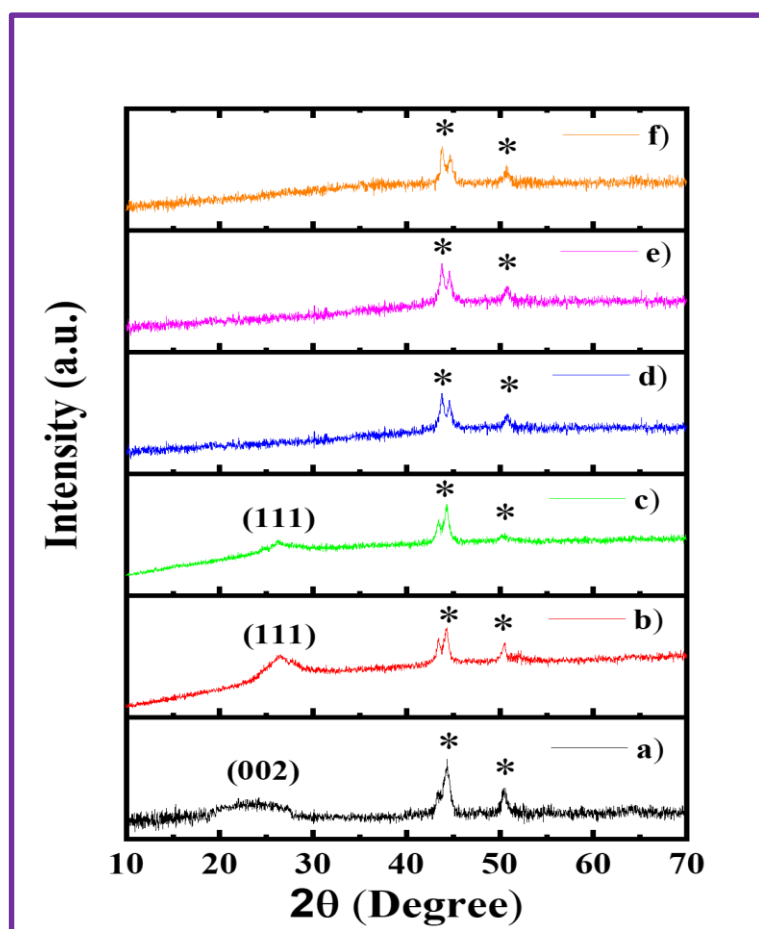
Fig. 7.2 XRD patterns of a) rGO, b) CdS, c) rGO/CdS, d) PANI, e) CdS/PANI, and f) rGO/CdS/PANI films on SS substrate.

The peaks for CdS are not observed may be due to the coating of PANI over CdS. Also, for rGO/CdS/PANI, no peaks of PANI, CdS, and rGO are observed due to the amorphous nature of PANI and the presence of CdS and rGO layers below PANI. The disappearance of CdS peaks in the both heterojunction films evidences the coating of PANI outer layer over CdS and rGO/CdS layers **[23, 26]**.

7.5.2 FE-SEM study

Surface morphology of films was studied using FE-SEM. **Fig. 7.3 a-f)** depicts the FE-SEM images of a) rGO, b) CdS, c) rGO/CdS, d) PANI, e) CdS/PANI, and f) rGO/CdS/PANI at 25 kX magnification. The morphologies of rGO, CdS, rGO/CdS **Fig. 7.3 a-c)** are given in **chapter III section 3.4.1.2 and 3.4.2.2**. **Fig. 7.3 d)** depicts that, the nanoparticles (coalesced nanograins with porous surface morphology) aggregated surface morphology of PANI film **[27]**.
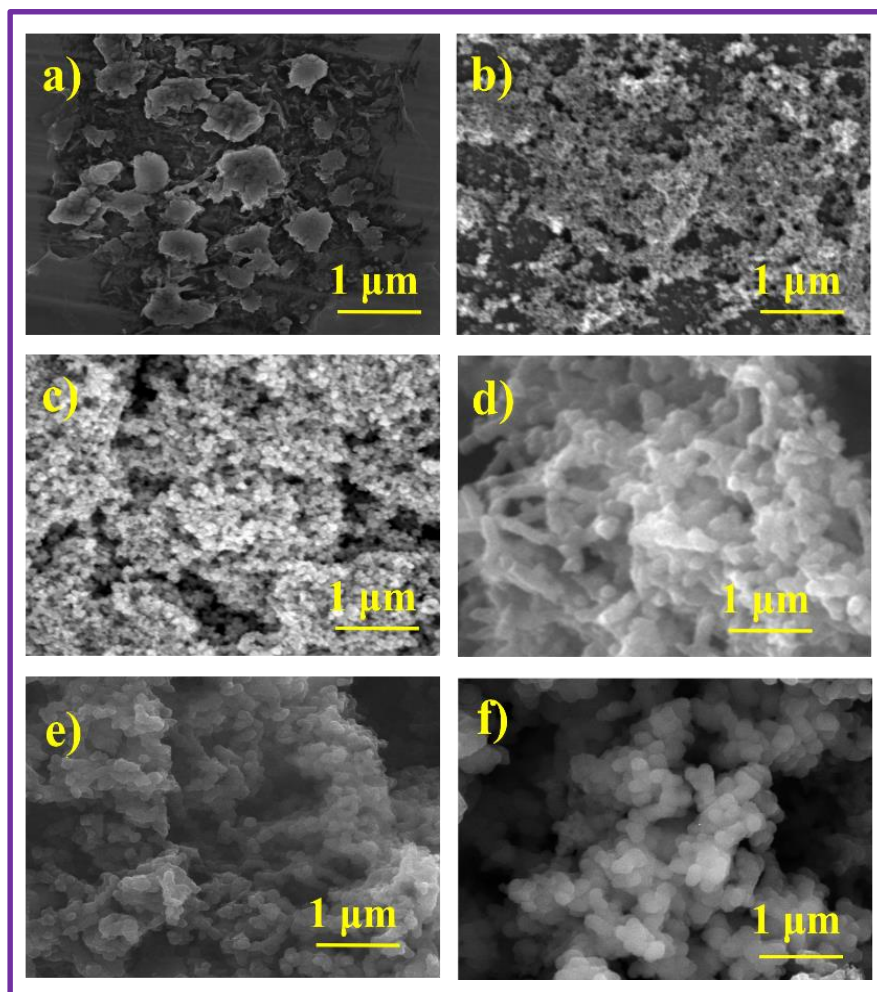
Fig. 7.3 FE-SEM images of a) rGO, b) CdS, c) rGO/CdS, d) PANI, e) CdS/PANI, and f) rGO/CdS/PANI films at magnifications of 25 kX.

The similar morphology of aggregated nanoparticles is seen in **Fig. 7.3 e)** for CdS/PANI heterojunction. **Fig. 7.3 f)** shows highly porous spongy nanoparticles like morphology for rGO/CdS/PANI heterojunction **[23]**. Pareek et al. **[19]** reported similar type of morphology for CdS/PANI heterojunctions. The porous morphology of electrode provides more easy access for enter the reactant gas molecules (species) towards p-n junction, resulting in improvement in the sensor performance. The porous

structure may result less response and recovery times which directly improves the sensor performance **[11-14]**.

In addition, the film thicknesses were also measured from FE-SEM cross-sectional images. FE-SEM cross-section images of CdS/PANI and rGO/CdS/PANI are given in **Fig. 7.4 (a-b)**. From **Fig. 7.4 a)** the observed thickness values for CdS and PANI layers are 710 and 1500 nm, respectively. From **Fig. 7.4 b)** the observed thickness values for rGO, CdS, and PANI layers are 109, 1375, and 1490 nm, respectively. The thickness values from FE-SEM cross-sectional images and gravimetric weight difference method, for CdS/PANI and rGO/CdS/PANI films are well matching with each other and clearly indicates the formation of semiconductor heterojunction structure. Semiconductor heterojunction structure can improve the diffusion as well as transport properties, which is helpful to improve the sensitivity of the gas sensors **[11-14, 28]**.
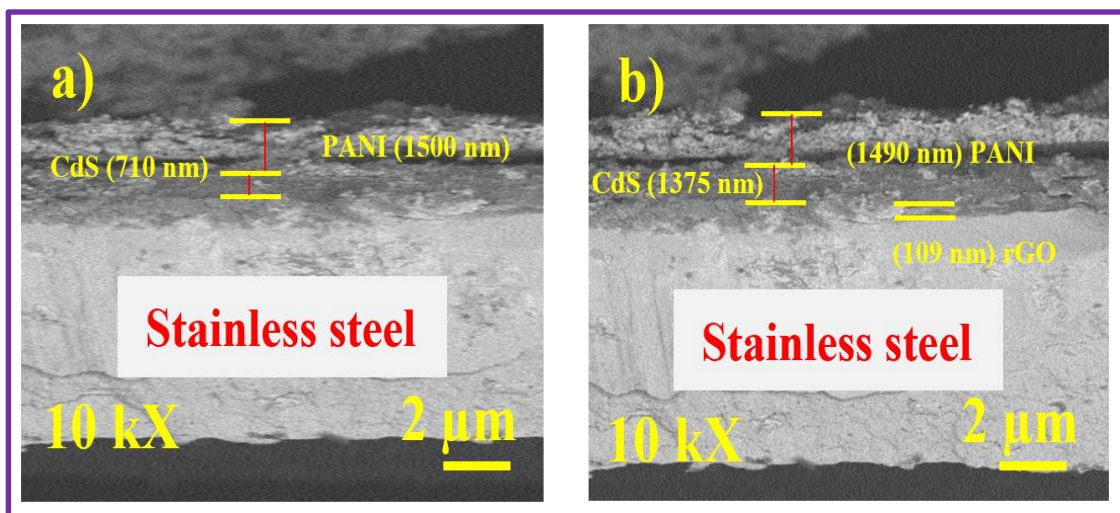
Fig. 7.4 FE-SEM cross-sectional images of a) CdS/PANI, and b) rGO/CdS/PANI thin films.

7.5.3 EDAX study

EDAX was utilized for elemental study of CdS/PANI and rGO/CdS/PANI thin films as shown in **Fig. 7.5 a), and b)**, respectively. **Fig. 7.5 a)** confirms the presence of carbon (C), nitrogen (N), oxygen (O), sulfur (S), and cadmium (Cd) in CdS/PANI sample. The rGO/CdS/PANI sample confirms the presence of C, N, O, S, and Cd species, as seen from **Fig. 7. 5 b)** which supports to XRD study.
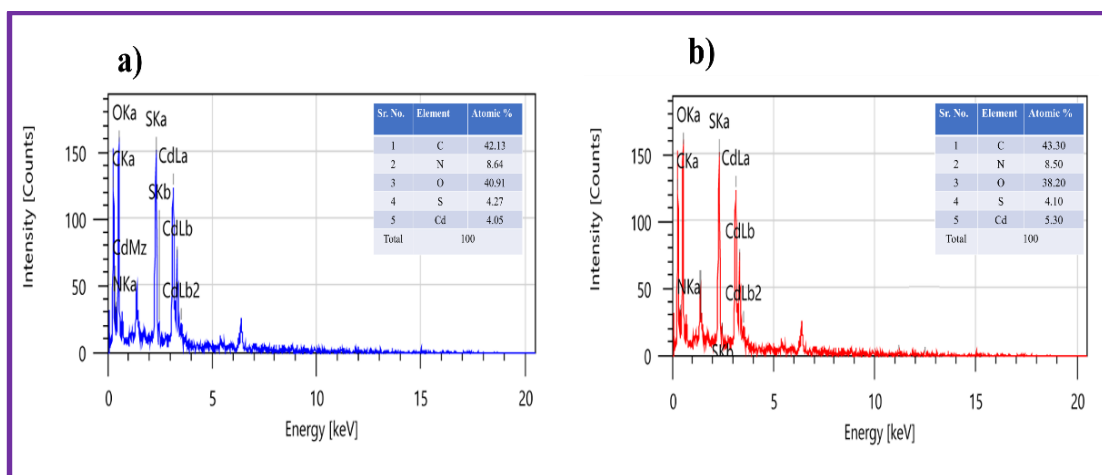
Fig. 7.5 EDAX patterns of CdS/PANI and rGO/CdS/PANI thin films.

7.5.4 Contact angle measurement

Contact angle plays a significant role in gas sensor studies due to surface interactions with target gas molecules. rGO showed hydrophobic property **Fig. 7.6 a)**.

The contact angle images of CdS, rGO/CdS, PANI, CdS/PANI, and rGO/CdS/PANI shown in **Fig. 7.6 b-f)** are hydrophilic. The discussion about contact angles of rGO, CdS, rGO/CdS is given in **chapter III section 3.4.1.4 and 3.4.2.4**. For CdS/PANI and rGO/CdS/PANI heterojunction films, the contact angle values of 28 and 21 ° are depicted in **Fig. 7.6 e and f)**.

The rGO/CdS/PANI heterojunction thin film shows more hydrophilicity of the material which leads more porous structure helpful for sensing properties **[29]**. The porosity of rGO/CdS/PANI heterojunction film may be due to the interconnected nanoparticles like surface morphology of PANI and the higher surface area of rGO.
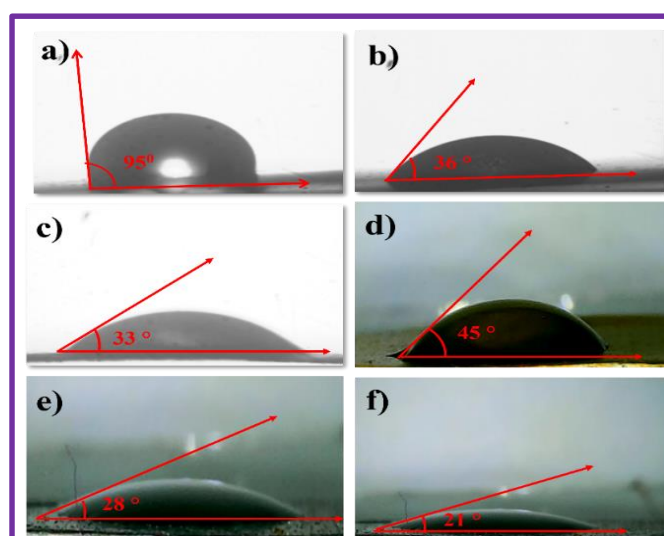
Fig. 7.6   Contact angle photographs of a) rGO, b) CdS, c) rGO/CdS, d) PANI, e) CdS/PANI, and f) rGO/CdS/PANI films.

7.5.5 BET study

The surface area and the pore sizes and its distribution plays an important role in sensor application. The higher surface area consists more active sites detect target gases at lower concentrations quickly (smaller values of response and the recovery times) with improved sensor performance.

The N_2 adsorption desorption curves of rGO, CdS, rGO/CdS, PANI, CdS/PANI, and rGO/CdS/PANI are shown in **Fig. 7.7 a-f).**
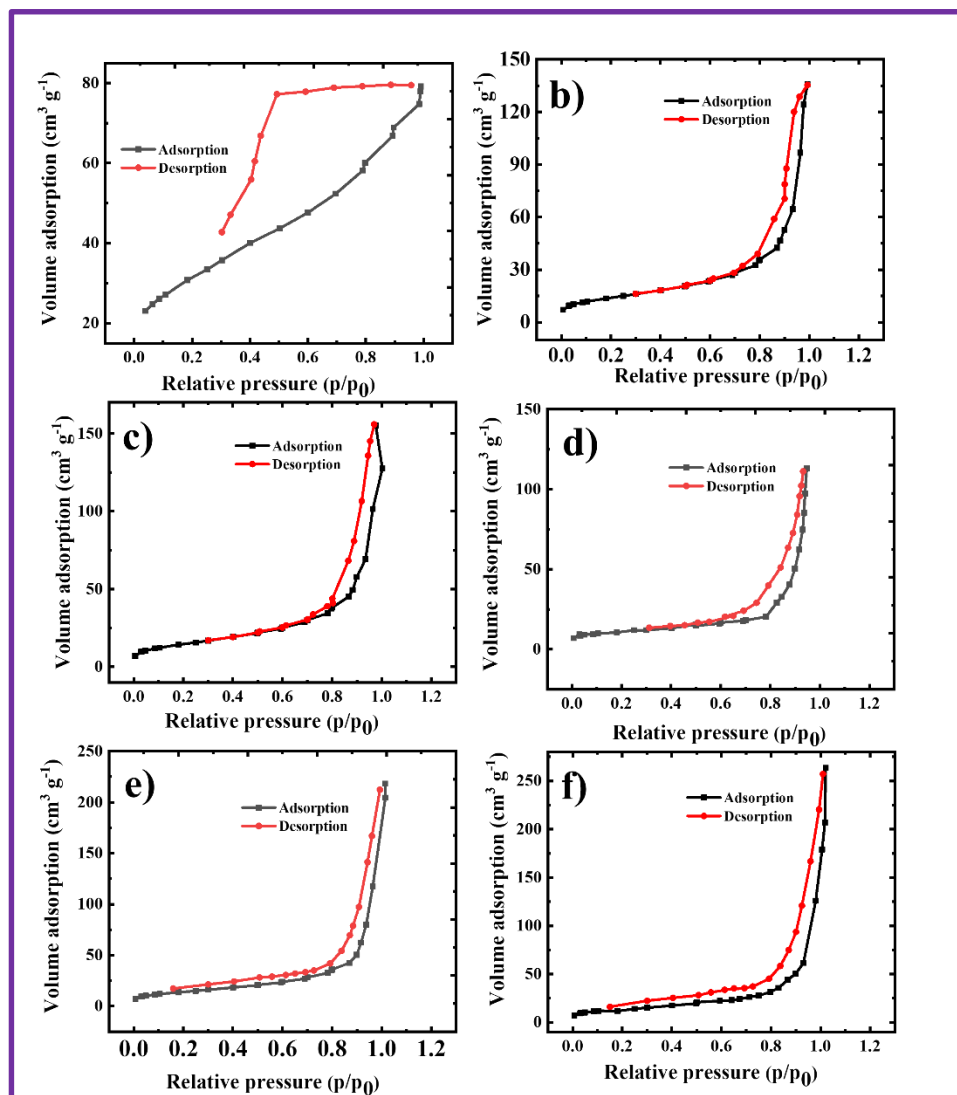
Fig. 7.7 N_2 adsorption desorption curves of a) rGO, b) CdS, c) rGO/CdS, d) PANI, e) CdS/PANI, and f) rGO/CdS/PANI samples.

The discussion of rGO, CdS, rGO/CdS is given in **chapter III section 3.4.1.5 and 3.4.2.5**. PANI, CdS/PANI, and rGO/CdS/PANI films exhibited surface areas of 60, 71 and 95 $m^2 g^{-1}$, respectively which is type IV of isotherm and amended by H1 type of BET hysteresis loop that specifies mesoporous nature and uniform pore size

distribution with more adsorption energy **[30]**. The rGO/CdS/PANI sample showed improved surface area than CdS/PANI, which may be due to higher surface area property of rGO material **[9]**.
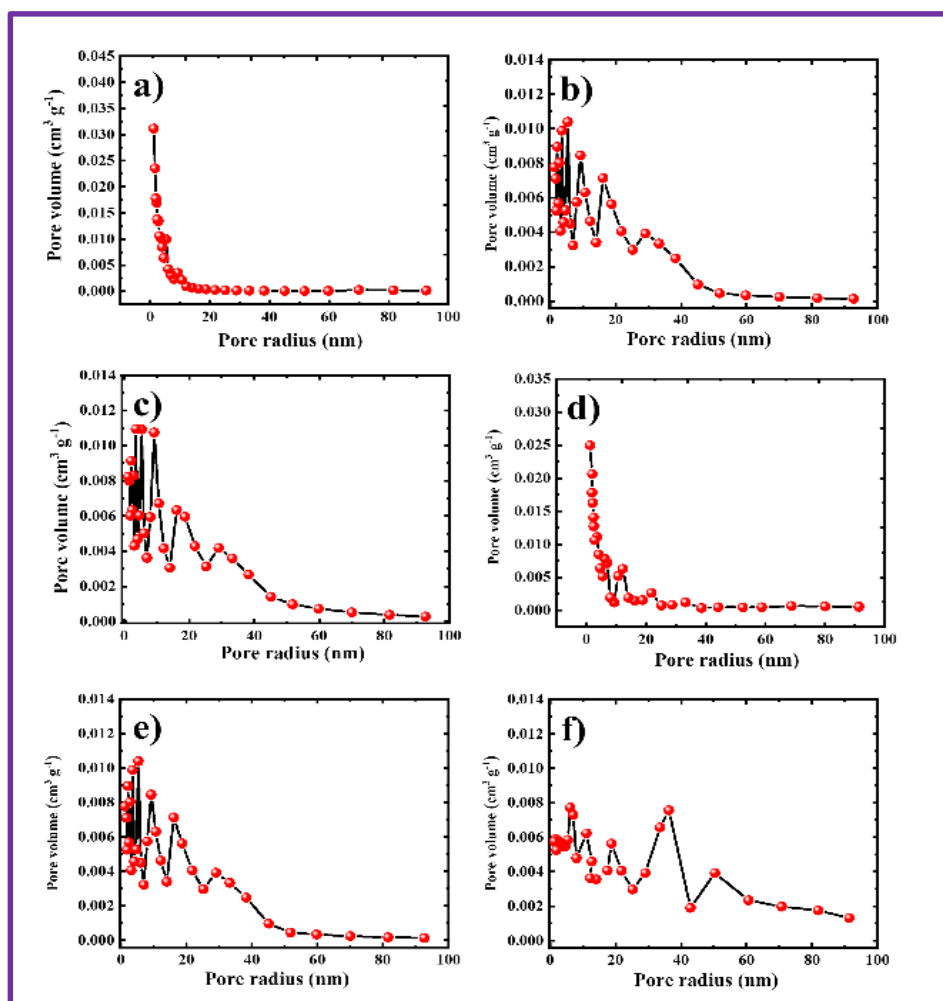
Fig. 7.8 BJH pore distrubution curves of a) rGO, b) CdS, c) rGO/CdS, d) PANI, e) CdS/PANI, and f) rGO/CdS/PANI samples.

BJH is illustrated to understand the pore size distribution of rGO, CdS, rGO/CdS, CdS/PANI, and rGO/CdS/PANI samples. As plotted in **Fig. 7.8 a-f),** all samples are mesoporous with an average diameter of 10-50 nm. The porosity of material surface influences how quickly the sensor can react and how easily gas can enter the material and increase its selectivity. Also, mesoporosity avails efficient gas exchange, which is crucial for the sensor to quickly reset and be ready for subsequent measurements. Mesoporosity helps greater interaction of gas molecules to heterojunction leads an improvement in sensitivity and detection limits.

7.5.6 UV-DRS of PANI

Fig. 7.9 shows DRS spectra for PANI with its absorption. PANI showed absorbance (534 nm) in visible region. The band gap of was 2.32 eV, estimated by formula and process as explained in **chapter III section 3.4.2.6**.
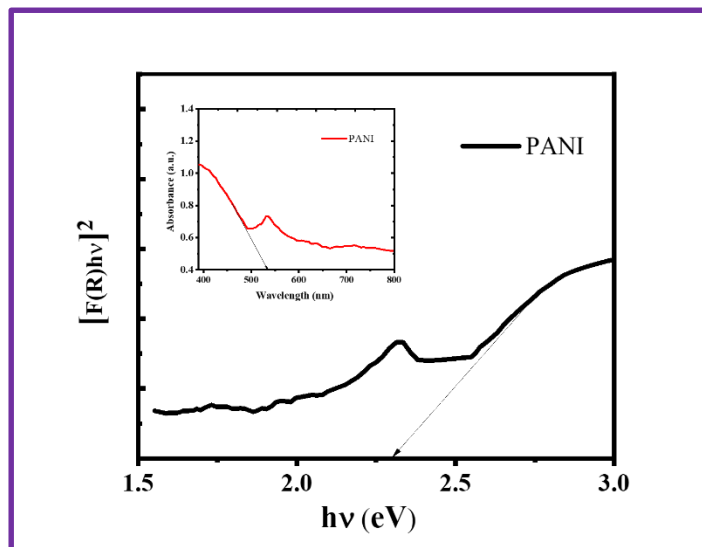
Fig. 7.9 DRS of PANI with absorbance spectra

Section B

7.6 I-V characteristics of rGO, CdS, rGO/CdS, PANI, CdS/PANI, and rGO/CdS/PANI films

For precise measurement of electrical parameters of semiconductor devices, it is an important to fabricate ohmic contacts. If the voltage drop is negligible across the contacts, the contacts are ohmic, and I-V characteristics of device are not to be affected. For good ohmic contacts, the metal should have a work function (ϕ) less than of the n-type semiconductor or greater than that of the p- type semiconductor. Metals like copper (Cu), silver (Ag), cobalt (Co), and nickel (Ni) of 1-2 cm^2 area were fabricated on PANI films by electrodeposition shows ohmic contacts **[11-14, 31].** Also, metal foil (Copper (Cu), Aluminum (Al)) press contacts are used for p-n heterojunctions in previous years. Dhawale et al. **[14, 32]** used Al press contacts for PANI films for n-CdS/p-PANI and p-PANI/n-TiO$_2$ heterojunctions for I-V, and gas sensing measurements.

In this work, the Al metal foil was used to fabricate press contact with rGO, CdS, rGO/CdS, PANI, CdS/PANI, and rGO/CdS/PANI films deposited on SS. To find nature of contact (ohmic or rectifying) between the films and metal contact, I-V measurements were carried out in the voltage range -2 V to +2 V at RT.

I-V characteristics of a) rGO, b) CdS, c) rGO/CdS, d) PANI, e) CdS/PANI, and f) rGO/CdS/PANI films on SS are given in **Fig. 7.10 (a-f)**.

From **Fig. 7.10 (a-f)**, it is observed that, a) rGO, b) CdS, c) rGO/CdS, and d) PANI films showed linear I-V curve which implies the fabrication of ohmic contacts. But, for e) CdS/PANI, and f) rGO/CdS/PANI films, the I-V curve is nonlinear (current gradual increasing in forward bias state), which indicates the junction formation between CdS and PANI in both films.
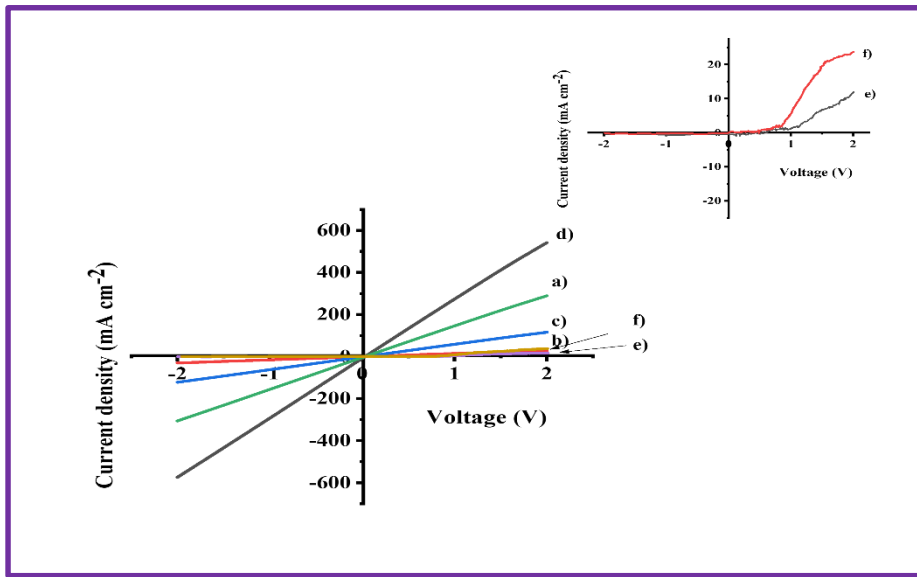
Fig. 7.10 I-V characteristics of a) rGO, b) CdS, c) rGO/CdS, d) PANI, e) CdS/PANI, and f) rGO/CdS/PANI films deposited on SS (Inset shows enlarge view of e) and f)).

7.7 Construction of energy band diagram

A heterojunction band profile is developed for better understanding of its rectification properties from a device perspective. Different semiconductor band gap energies (Eg_1 and Eg_2), their electron affinities (χ_1 and χ_2), and work functions (ϕ_1 and ϕ_2) are essential characteristics of heterojunction. While, band gap energy and electron affinity are material properties, but work function (ϕ) mainly varies with doping level, and fermi level position. When, two semiconductors brought in contact an interface is formed which shows fascinating properties due to changes in position of energy bands.

Many researchers have been used theoretical models for construction of n-p, p-n and n-n heterojunctions band diagrams. By referring data related to electron affinity (χ) and band gap energy (E_g) available from literature, one can draw band diagrams for materials. Sharma and Purohit **[31]** have reported the values of electron affinity and

bandgap of some semiconductors. The values of work function and band gap energy for PANI have been already reported **[14, 29, 30].**

The position of Fermi level for polyaniline and CdS was determined using measured electrode potentials with respect to saturated calomel electrode (SCE). CdS and PANI electrodes were dipped in 1 M KCl solution to determine their equilibrium chemical potentials.
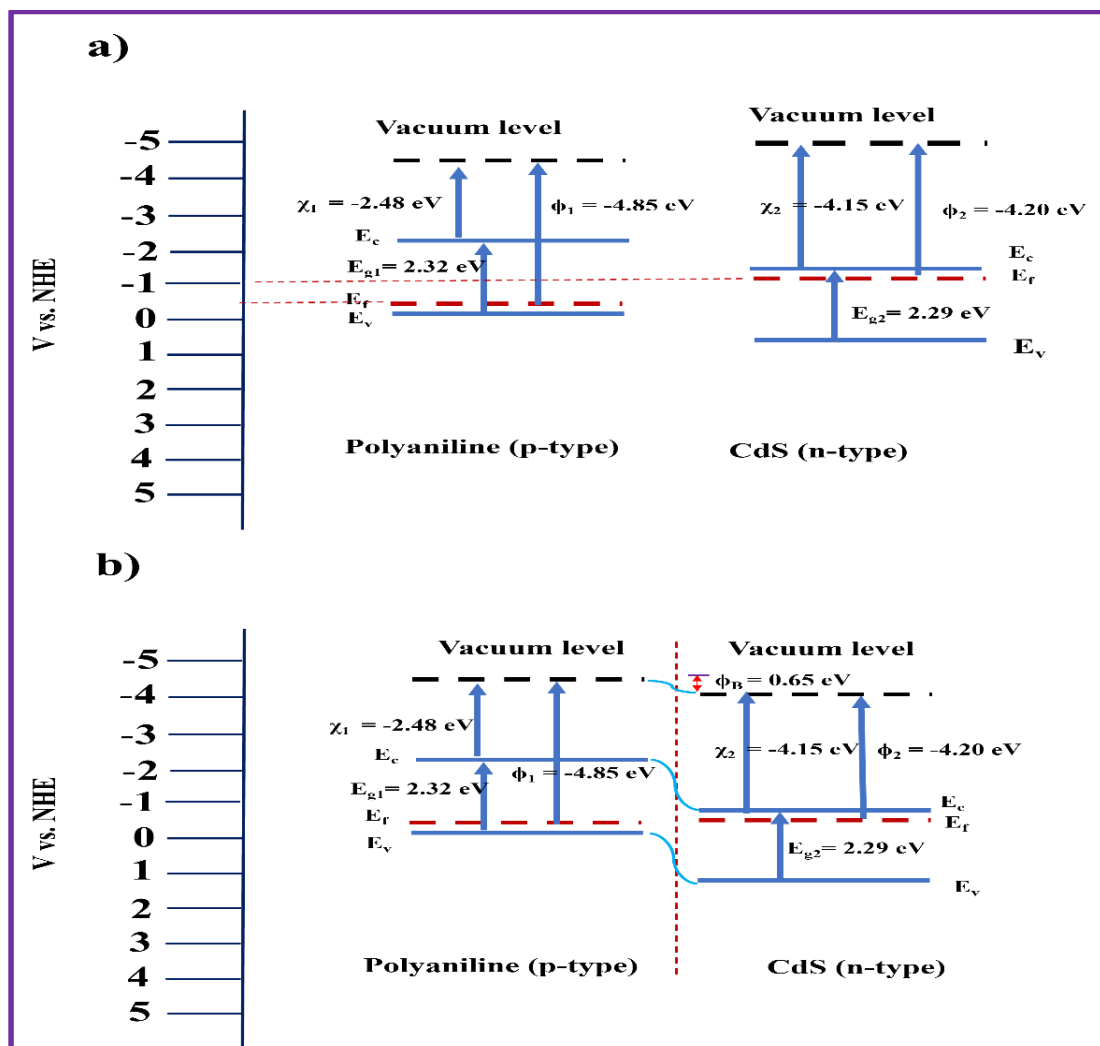
Fig. 7.11 Enery band diagrams of p-PANI and n-CdS junction a) before contact and b) after contact.

A SCE was employed as the reference electrode. The equilibrium potential between two electrodes was determined using a multimeter. The semiconductor (n-CdS or p-PANI) electrode was at the negative terminal with respect to SCE. The equilibrium chemical potentials for CdS and PANI were found to be +0.470 and +0.190 V/SCE, respectively. These readings were converted to chemical scale using the normal

hydrogen electrode (NHE). Band diagrams for p-PANI, and n-CdS before and after contact **(Fig. 7. 11 a-b)** are constructed by following manner;

Primarily, position of fermi levels of p-PANI, and n-CdS were fixed using measured equilibrium potentials. For our ease, for p- type PANI, valance band location is assumed at 0.05 eV below fermi level, and for n-type CdS, conduction band location is assumed at 0.05 eV above Fermi level.

By using band gap energies, the position of conduction and valence band levels were fixed for P-PANI and n-CdS, respectively. The work function for PANI (ϕ_1) is 4.85 eV, and for CdS (ϕ_2) is 4.20 eV. The present heterojunction having $Eg_1 > Eg_2$ as $\chi_1 < \chi_2$, and ($\phi_1 > \phi_2$). The equilibrium energy band profile after contact **Fig. 7.11 (b)** is similar with equilibrium energy band profile n-p anisotype heterojunction. In this case $\phi_1 - \phi_2 = 4.85-4.20 = 0.65$ eV. The flat band potential is 0.65 eV **[33].**

7.8 Gas sensing performance of CdS/PANI and rGO/CdS/PANI heterojunction films

To check fulfillment and eligibility of the fabricated gas sensor it is essential to test required standards through sensitivity, selectivity, and stability. The gas sensing study of PANI/CdS and rGO/CdS/PANI heterojunctions films were carried out by using lab made gas sensor unit combined with Zive MP1 Multichannel electrochemical workstation (Potentiostat). The selectivity, sensitivity, response and recovery times, and stability study of PANI/CdS and rGO/CdS/PANI heterojunction films were carried out at RT.

7.8.1 Fabrication of CdS/PANI or rGO/CdS/PANI heterojunction gas sensor device

CdS/PANI or rGO/CdS/PANI heterojunctions were fabricated by SILAR method, in which PANI film was deposited onto previously SILAR synthesized CdS and rGO/CdS film by two beaker SILAR method as mentioned in **section 7.2.3**. The schematic diagram of rGO/CdS/PANI heterojunction sensor device with its actual photograph is shown in **Fig. 7.12 a)**. To study the gas sensing properties, front aluminum (Al) foil press contacts and back SS contact are formed to heterojunction as shown in **Fig. 7. 12 b)**.
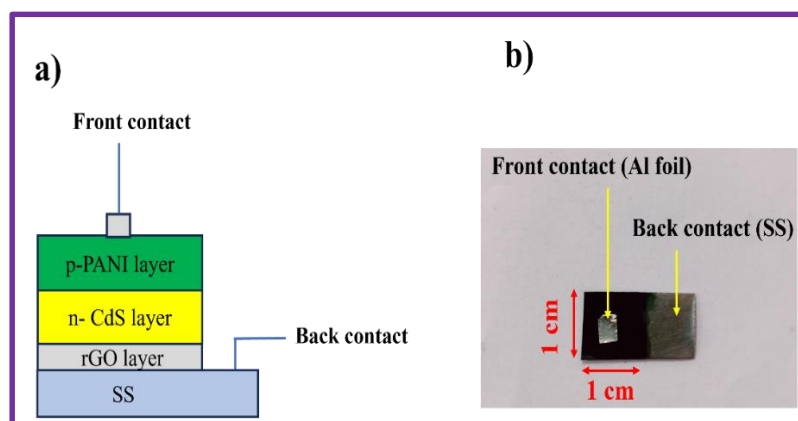
Fig. 7.12 a) Schematic representation, and b) actual photograph of rGO/CdS/PANI heterojunction sensor device.

7.8.2 Gas sensing measurement experimental setup

In order to test the gas sensing ability of heterojunction, a gas sensor unit was specially designed. The gas sensor unit consists of small dome shaped vacuum chamber (made up of SS) and sample holder with precise ohmic contacts was designed to mount the sample. After that, holder was placed into the dome and gas sensing study were recorded using potentiostat (Zive MP1 electrochemical workstation) by connecting sensor unit through the external connections. The actual experimental setup used for gas sensing study shown in **Fig. 7.13,** with photograph of gas sensor chamber (inset sensor device in sample holder).
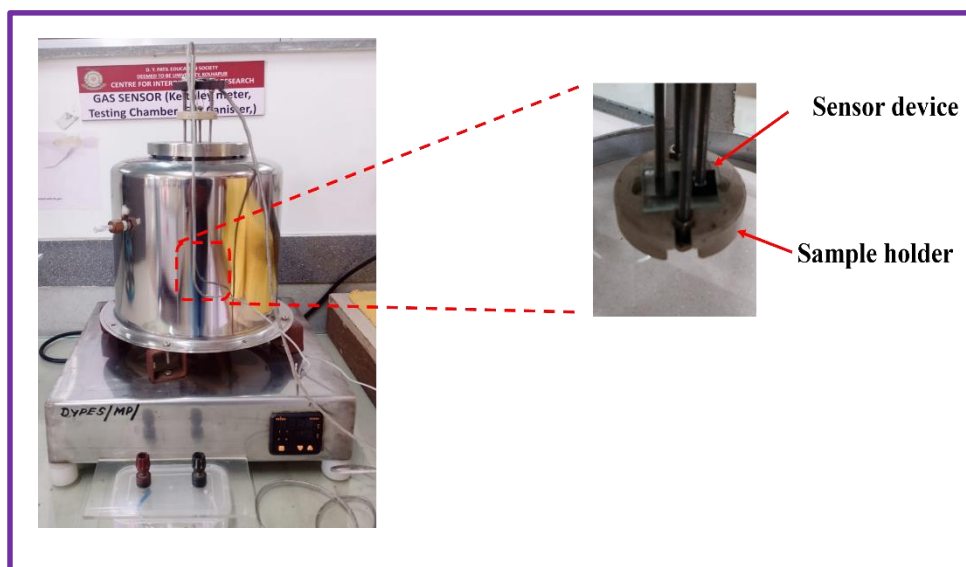
Fig. 7.13 Photograph of gas sensor (Inset shows sensor device fitted on sensor sample holder).

The forward biased I-V characteristics of the p-n junction before and after exposure of target gas were recorded by using the LSV curve test. The electrical

currents of heterojunction in air (I_a) and in the presence of gas (I_g) were measured and using following relation the gas response S (%) was calculated.

$$S\ (\%) = \frac{I_a - I_g}{I_a} \times 100 \qquad (7.1)$$

The response time (t_{res}) and recovery time (t_{rec}) of heterojunction sensor for selective gas were determined by holding a heterojunction to fixed potential and junction current change was recorded with time.

7.8.3 Selectivity

For selectivity of CdS/PANI and rGO/CdS/PANI heterojunction films, forward bias I-V study was carried out in voltage range 0 to +2.0 V at the scan rate of 20 mV s^{-1} at RT in the absence and presence of oxidizing (CO_2, Cl_2, NO_2, SO_2), reducing (LPG, NH_3) gasses. The **Fig. 7.14 A)** CdS/PANI and **B)** rGO/CdS/PANI heterojunction shows the typical forward biased I-V characteristics plots for 100 ppm concentration towards a) air, b) NH_3, c) CO_2, d) LPG, e) Cl_2, f) NO_2, and g) SO_2 gasses at RT.
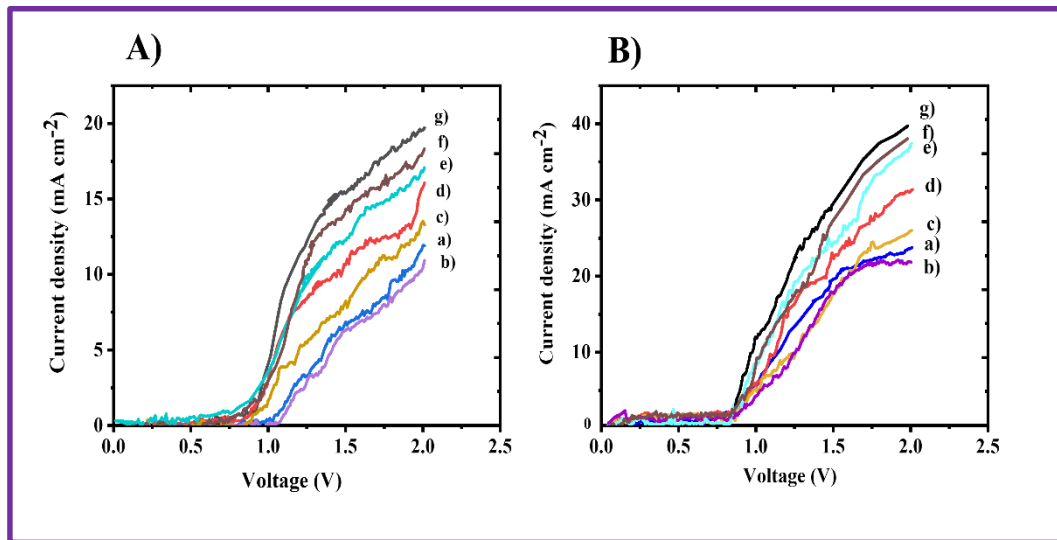
Fig. 7.14 Forward biased I-V characteristics of A) CdS/PANI and B) rGO/CdS/PANI heterojunction at a fixed voltage of +2.0 V and at a concentration of 100 ppm for various gases a) air, b) NH₃, c) CO₂ d) LPG, e) Cl₂, f) NO₂, and g) SO₂.

From heterojunction I-V characteristics for the maximum change in current was observed for SO_2 as compared to other exposed gases. The gas response of CdS/PANI and rGO/CdS/PANI to different gases is depicted in bar graph **Fig. 7.15**. The rGO/CdS/PANI heterojunction showed response towards SO_2 (65.21 %), NO_2 (60.10 %), Cl_2 (56.21 %), LPG (33.34 %), CO_2 (11.30 %), and NH_3 (6.8 %) as different gases have different energies.
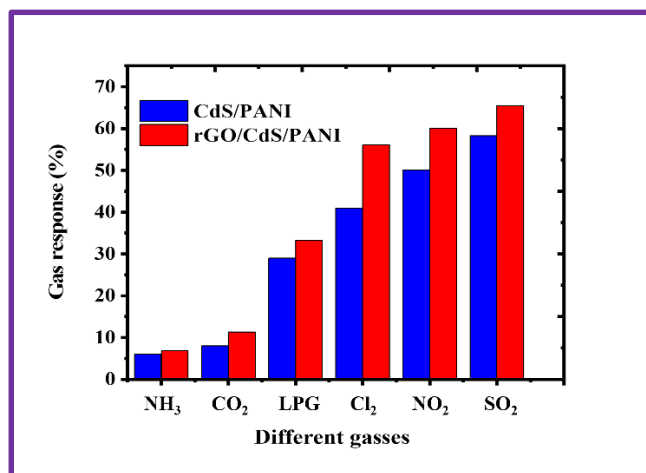
Fig. 7.15 Bar diagram of CdS/PANI and rGO/CdS/PANI heterojunctions response for six different exposed gases of fixed gas concentration of 100 ppm.

The CdS/PANI and rGO/CdS/PANI heterojunction films displayed more selectivity for SO_2 over other tested gases. It proves that CdS/PANI and rGO/CdS/PANI heterojunction films are most selective for SO_2 against other tested gases. Therefore, further SO_2 response was studied for its various concentrations.

7.8.4 Sensitivity

The forward-biased I-V characteristics were measured at room temperature (RT) in the presence and absence of different concentrations of SO_2 gas. Typical I-V characteristic plots for CdS/PANI and rGO/CdS/PANI heterojunction films are shown in **Fig. 7.16 A) and B)**, respectively to different concentrations of SO_2 ranging from 1, 10, 50, 100, and 120 ppm.
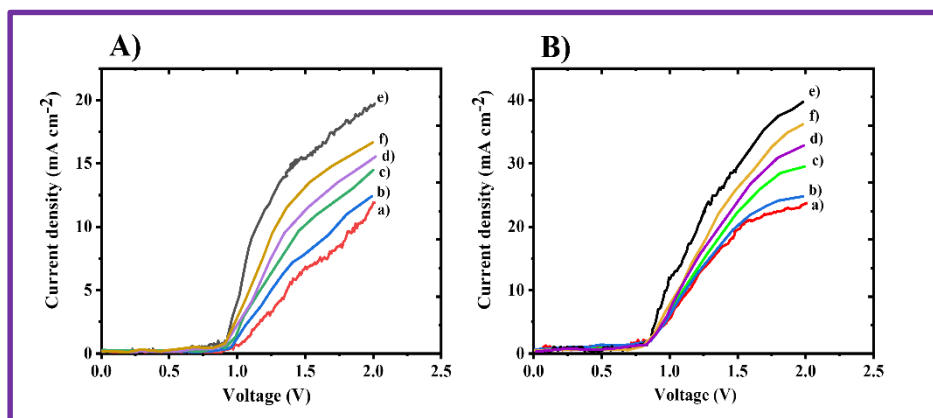
Fig. 7.16 Forward biased I-V characteristics of A) CdS/PANI and B) rGO/CdS/PANI heterojunction films at various concentrations of SO_2 in a) air, b) 1, c) 10, d) 50, e) 100, and f) 120 ppm.

As the junction was exposed to SO_2, forward biased current was increased. From I-V characteristics the maximum change in current was observed for 100 ppm

SO$_2$. The both CdS/PANI and rGO/CdS/PANI heterojunctions are sensitive upto 100 ppm SO$_2$. For further increase in SO$_2$ concentration to 120 ppm, current was decreased. Gas response of CdS/PANI and rGO/CdS/PANI heterojunction films for various concentration of SO$_2$ depicted in **Fig. 7.17**.
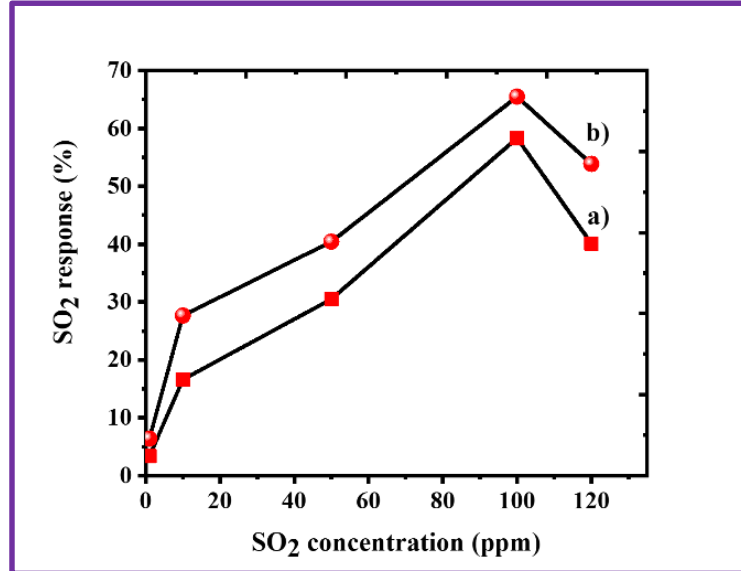
Fig. 7.17 The gas response (%) vs. SO$_2$ concentration (ppm) of a) CdS/PANI and b) rGO/CdS/PANI heterojunction films.

CdS/PANI heterojunction showed improvement in the gas response from 3.34 to 58.33% for 1 to 100 ppm SO$_2$ range and it decreased afterward for 120 ppm to 40.11 %. Also, for rGO/CdS/PANI gas response was increased continuously from 6.30 to 65.50 % with increasing the gas concentration in the range 1 to 100 ppm SO$_2$.

At 120 ppm SO$_2$, it was decreased to 53.87 %. This could be because the sensors active region is effective only up to 100 ppm, where the response rate increases more significantly. Below 100 ppm SO$_2$, the unimolecular layer of gas molecules would be expected to form on the interface, which would interact with the interface more actively giving larger response. There would be multilayers of gas molecules on the interface of junction above 100 ppm SO$_2$, resulting decrease in gas response **[14]**.

7.8.5 Gas sensing model for SO$_2$ sensing

Potential barrier-based model for operation of heterojunctions gas sensor is mostly used. **Fig. 7.18 (a and b)** shows the schematic representation of model for n-CdS/p-PANI heterojunction for SO$_2$ detection at RT with corresponding physical models **Fig. 7.18 (a' and b')** before and after exposure of SO$_2$, respectively.
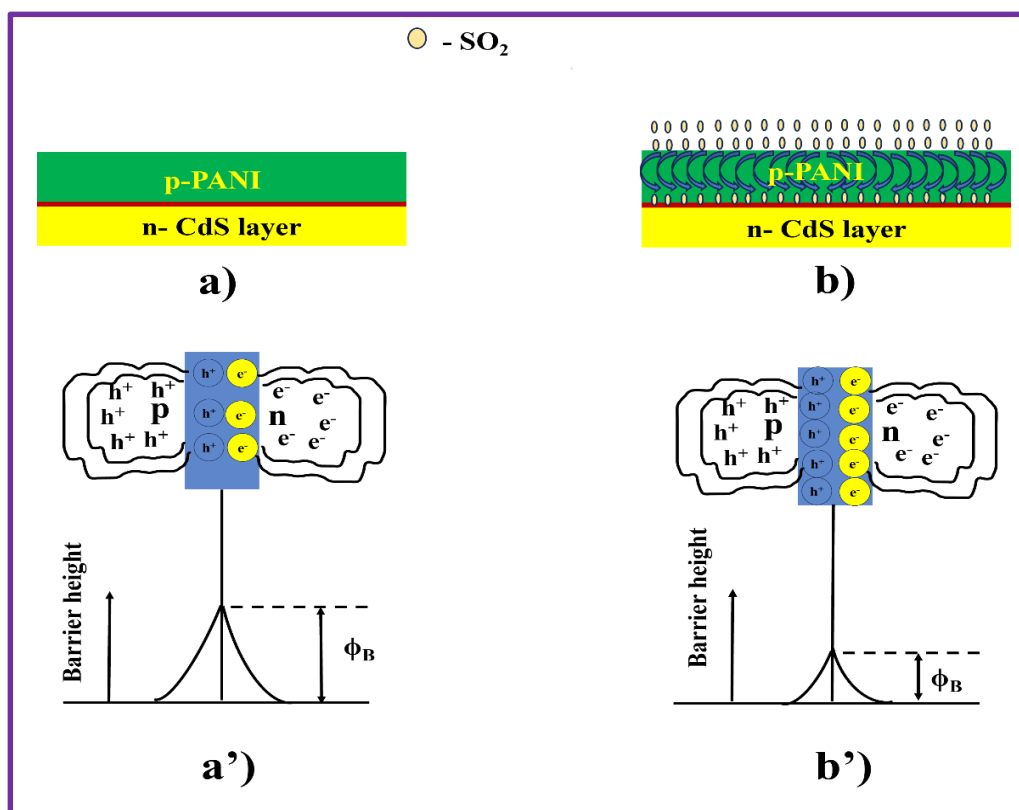
Fig. 7.18 a) and b) schematic representation of n-CdS/p-PANI heterojunction and a') and b') the physical models of heterojunction for SO₂ sensing.

A simple heterojunction diode device, can be utilized for detecting gas analytes. Present gas sensing model is based on principle of barrier height change mechanism of before and after exposure of SO_2 on n-CdS/p-PANI heterojunction. The effective barrier height 'ϕ_B' can be modulated by analyte, through changing doping level of polyaniline. The molecules of oxidizing gases (SO_2) are electron acceptors (hole rich species), which accepts charge carriers, that can change the concentration of charge carriers at the junction leads change in potential barrier height (ϕ_B) and consequently the current across the junction. From the **Fig. 7.18** it is seen that, when SO_2 molecules enter through the porous PANI and reaches at the interface of n-CdS/p-PANI heterojunction, the barrier height of heterojunction decreases as shown in **Fig. 7.18 (b')**.

The carrier concentration (positive charge) increases near the interface of n-CdS/p-PANI heterojunction upon exposure of SO_2. Also, this increase in carrier concentration gives lower potential barrier of n-CdS/p-PANI heterojunction. Patil et al. **[11]** have reported the sensing model for p-PANI/n-PbS for reducing gas (LPG), the barrier height of the junction increases with electron doner gas. Dhawale et al. **[14, 32]** discussed the sensing model for p-PANI/n-TiO₂ and p-PANI/n-CdS with both possibilities of barrier height increase or decrease for LPG gas. Lokhande et al. **[29]**

reported the sensing model of p-CTS/n-CdS for reducing gas (LPG), the barrier height of the junction increases with electron donating behavior of gas. In present work, on basis of change in electric current, it can be concluded that n-CdS/p-PANI heterojunction sensor is useful to detect the SO_2 at RT.

7.8.6 Response time (t_{res}) and recovery time (t_{rec})

The t_{res} and t_{rec} are also important parameters to study the activeness of the gas sensor. The CdS/PANI and rGO/CdS/PANI heterojunction device response versus time at a fixed forward bias of +2.0 V upon exposure 100 ppm SO_2 is shown in **Fig. 7.19**. After SO_2 is removed from the chamber and recovery time was measured till the current nearly dropped to 10 % of its original value.
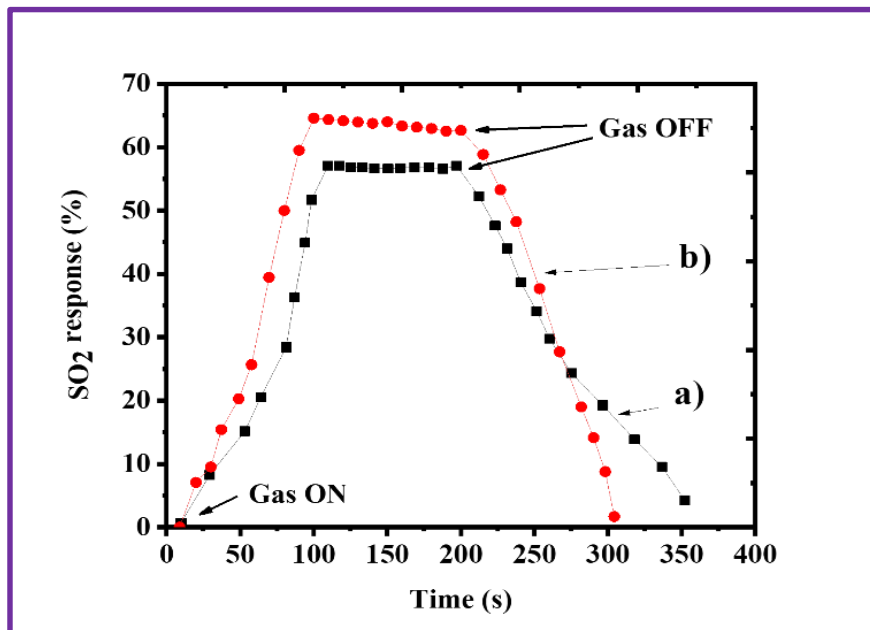
Fig. 7.19 Response and recovery times for a) CdS/PANI and b) rGO/CdS/PANI heterojunction films for 100 ppm SO_2.

The t_{res} and t_{rec} values for CdS/PANI are 108 s and 153 s. The t_{res} and t_{rec} values for rGO/CdS/PANI are 98 s and 105 s. From **Fig. 7.19**, it is observed that the values of t_{res} and t_{rec} for rGO/CdS/PANI are lesser than CdS/PANI heterojunction films. The reduction in t_{res} and t_{rec} times may be due to porous surface structure provides more access, plenty number of active cites and improved conductivity for sensing application. **Table 7.1** summarizes cadmium chalcogenide based heterostructures, composites and heterojunctions used for gas sensing application with present work.

7.8.7 Stability

To assess the stability of the CdS/PANI and rGO/CdS/PANI heterojunctions, forward-biased I-V characteristics were measured at room temperature after exposing

the sensors to 100 ppm SO_2 over a period of 45 days. Measurements were taken every 5 days following the initial reading, and the results showing the gas response over time are depicted in the **Fig. 7.20**.
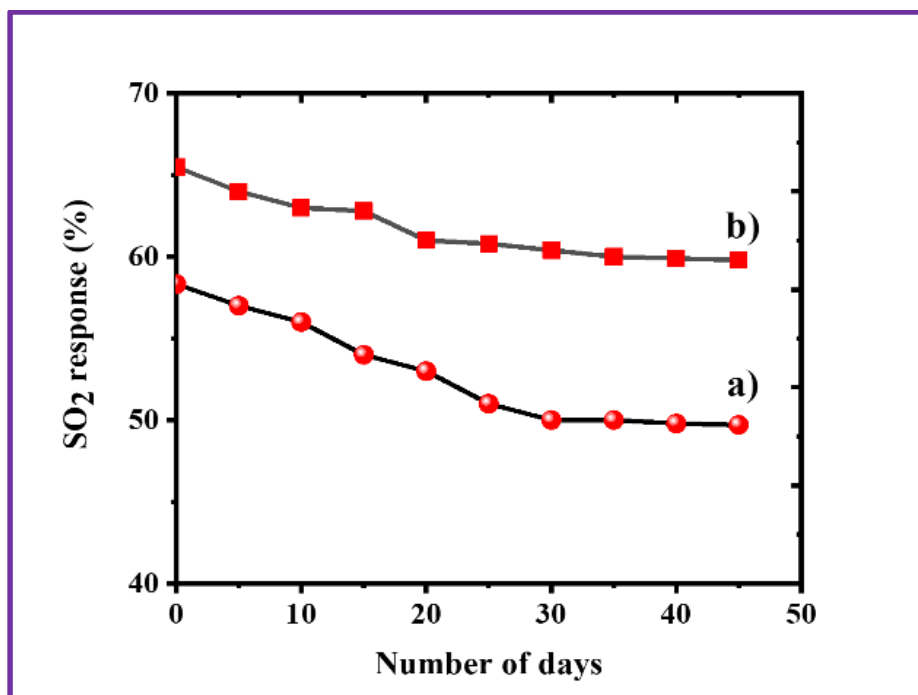
Fig. 7.20 Stability of a) CdS/PANI and b) rGO/CdS/PANI heterojunctions for 100 ppm SO_2 .

The CdS/PANI heterojunction gas sensor devices showed reduction in sensitivities of 58.33 to 50.10 % and rGO/CdS/PANI showed 65.50 to 60.21 %. The CdS/PANI and rGO/CdS/PANI heterojunctions showed nearly 86, and 92 % stability than initial values after 45 days. The rGO/CdS/PANI heterojunction shows more stability over CdS/PANI. This may be due to the stable surface structure of rGO/CdS/PANI.

The more decrement of sensitivity during first 15 day period may be due to some interface modifications occurred at initial stage heterojunction during operation. The higher selectivity, sensitivity and the lesser t_{res} and t_{rec} times of rGO/CdS/PANI heterojunction over CdS/PANI may due to presence of numerous active sites which are able to enhances the adsorption capacity of exposed gas and improves the affinity for gas molecules. Furthermore, the heterojunction formed between rGO/CdS/PANI provide conductive channel leads improvement in the performance of the sensor.

Table 7.1: Comparison of cadmium chalcogenide based heterostructures, composites, and heterojunctions used for gas sensing application with present work.

Sr. No.	Material	Type of sensor	Deposition method	Concentration of target gas	Gas response (%)	t_{res}	t_{rec}	Gas response equation	Ref.
1	PANI-CdS	Nanocomposite	Co-dispersion technique	NH_3 (100 ppm)	250	-	-	$S = \dfrac{R_g - R_a}{R_a} \times 100$	34
2	CdS-doped TiO_2	CdS-doped TiO_2 composite	Printing	Acetone (5000 ppm)	71	55	115	$S = \dfrac{R_a - R_g}{R_a} \times 100$	21
3	CdS QD/CO_3O_4 HMSs	Composite	Precipitation	H_2S (100 ppm)	0.6	0.7	12.7	$S = \dfrac{R_a}{R_g}$	35
4	RGO-MoS_2-CdS	Nanocomposite	Hydrothermal, solvothermal	NO_2 (0.2 ppm) at 75 °C	27.4	25	34	$S = \dfrac{R_g - R_a}{R_a} \times 100$	36
5	n-CdS/p-PANI	Heterojunction	ED	LPG (1040 ppm)	80	105	165	$S = \dfrac{I_a - I_g}{I_a} \times 100$	14
6	n-CdSe/p-PANI	Heterojunction	ED	LPG (0.08 vol %)	70	100	200	$S = \dfrac{\Delta I}{I_0} \times 100$	12
7	n-CdTe/p-PANI	Heterojunction	ED	LPG (0.14 vol %)	67.7	300	600	$S = \dfrac{\Delta I}{I_0} \times 100$	13

Sr. No.	Material	Type of sensor	Deposition method	Concentration of target gas	Gas response (%)	t_{res}	t_{rec}	Gas response equation	Ref.
8	p-PANI/ n-pbs	Heterojunction	CBD, ED	LPG (0.06 vol %)	70	125	200	$S = \dfrac{\Delta I}{I_0} \times 100$	33
9	p-Cu$_2$SnS$_3$/n-CdS	Heterojunction	Sputtering, ED	LPG (780 ppm)	56	31	56	$S = \dfrac{\Delta I}{I_a} \times 100$	29
10	PANI/Tio2	Heterojunction	CBD, ED	LPG (0.1 vol %)	63	140	180	$S = \dfrac{\Delta I}{I_a} \times 100$	32
11	n-Bi$_2$S$_3$-p-CuSCN	Heterojunction	Chemical rout (SILAR)	LPG (1370 ppm)	70	158	142	$S = \dfrac{\Delta I}{I_a} \times 100$	37
12	n- Ppy/n-TiO2	Heterojunction	CBD, ED	LPG (1040 ppm)	112	131	55	$S = \dfrac{\Delta I}{I_a} \times 100$	38
13	n-ZnO/ P-BaTiO$_3$/CuO/La$_2$O$_3$	Heterojunction	Chemical route	NO$_2$ (<1.5 ppm)	20	-	-	-	39
14	PANI/Cu$_2$ZnSnS$_4$	Heterojunction	ED, spray pyrolysis	LPG (780 ppm)	79	120	125	$S = \dfrac{I - I_0}{I_0} \times 100$	40
15	**n-rGO/CdS/p-PANI**	**Heterojunction**	**SILAR**	**SO$_2$ (100 ppm)**	**65.50**	**98**	**105**	$S = \dfrac{I_a - I_g}{I_a} \times 100$	**Present work**

7.9 Conclusions

Current research consists fabrication of CdS/PANI and rGO/CdS/PANI heterojunction films by SILAR method on SS substrates. CdS/PANI and rGO/CdS/PANI heterojunction films shows amorphous nature. rGO/CdS/PANI heterojunction film showed more porous and spongier surface than CdS/PANI. The EDAX studies revealed the presence of elements in both CdS/PANI and rGO/CdS/PANI samples. The formation of CdS/PANI and rGO/CdS/PANI heterojunctions is confirmed from the FE-SEM cross section images. Wettability study of PANI/CdS and rGO/CdS/PANI revealed hydrophilic nature with contact angle values of 28 and 21 °, respectively. rGO/CdS/PANI exhibited higher specific surface area of 95 $m^2 g^{-1}$ compared to 71 $m^2 g^{-1}$ of CdS/PANI. The both heterojunction films are selective to SO_2 gas as compared to other target gases. CdS/PANI and rGO/CdS/PANI exhibited maximum sensitivity of 58.33, and 65.50 %, respectively for 100 ppm SO_2 gas. Thus, the improvement in sensitivity and selectivity of rGO/CdS/PANI heterojunction films is may due to high surface area, and more porous structure. Hence, it is concluded that, rGO/CdS/PANI is more stable and sensitive for SO_2 compared to CdS/PANI.

7.10 References

1] S. Wasi, S. Tabrez, M. Ahmad, Environ. Monit. Assess., 185 (2013) 2585-2593.

2] P. Ukaogo, U. Ewuzie, C. Onwuka, Environmental pollution: causes, effects, and the remedies. In Microorganisms for sustainable environment and health, (Elsevier, 2020) pp. 419-429.

3] A. Dey, Mater. Sci. Eng. B, 229 (2018) 206-217.

4] M. Nikolic, V. Milovanovic, Z. Vasiljevic, Z. Stamenkovic, Sens., 20 (2020) 6694 (1-30).

5] A. Singh, S. Sikarwar, A. Verma, B. Yadav, Sens. Actuators A: Phys., 332 (2021) 113127 (1-22).

6] M. Alam, P. Pooja, M. Aamir, B. Souayeh, S. Mushtaq, M. Khan, M. Amin, K. Khan, S. Shajahan, Membr., 12 (2022) 555 (1-27).

7] V. Kumar, A. Mirzaei, M. Bonyani, K. Kim, H. Kim, S. Kim, Trends Anal. Chem., 129 (2020) 115938 (1-50).

8] M. Farea, H. Mohammed, S. Shirsat, P. Sayyad, N. Ingle, T. Al-Gahouari, M. Mahadik, G. Bodkhe, S. Shirsat, M. Shirsat, Appl. Phys. A, 127 (2021) 681 (1-12).

9] W. Tian, X. Liu, W. Yu, Appl. Sci., 8 (2018) 1118 (1-21).

10] G. Feng, M. Zhang, S. Wang, C. Song, J. Xiao, Appl. Surf. Sci., 453 (2018) 513-519.

11] S. Patil, P. Deshmukh, C. Lokhande, Sens. Actuators B: Chem., 156 (2011) 450-455.

12] S. Joshi, C. Lokhande, S. Han, Sens. Actuators B: Chem., 123 (2007) 240-245.

13] S. Joshi, T. Gujar, V. Shinde, C. Lokhande, Sens. Actuators B: Chem., 132, (2008) 349-355.

14] D. Dhawale, D. Dubal, V. Jamadade, R. Salunkhe, S. Joshi, C. Lokhande, Sens. Actuators B: Chem., 145 (2010) 205-210.

15] S. Al-Jawad, S. Rafic, M. Muhsen, Mod. Phys. Lett. B, 31 (2017) 1750234 (1-15).

16] R. Paulraj, P. Shankar, G. Mani, L. Nallathambi, J. Rayappan, J. Electron. Mater., 47 (2018) 6000-6006.

17] W. Nie, Z. Liu, M. Ruan, J. Zhou, Int. J. Hydrogen Energy, 52 (2024) 555-566.

18] P. More, C. Hiragond, A. Dey, P. Khanna, Sustain. Energy Fuels, 1 (2017) 1766-1773.

19] A. Pareek, P. Paik, J. Joardar, K. Murugan, P. Borse, Thin Solid Films, 661 (2018) 84-91.

20] Z. Zhang, M. Li, L. Zhai, J. Wu, L. Li, Anal. Methods, 15 (2023) 969-978.

21] A. Akbar, M. Das, D. Sarkar, Sens. Actuator A: Phys., 310 (2020) 112071 (1-11).

22] L. Zhang, X. Li, Z. Mu, J. Miao, K. Wang, R. Zhang, S. Chen, RSC Adv., 8 (2018) 30747-30754.

23] S. Sharma, D. Kumar, N. Khare, Polymer, 231 (2021) 124117 (1-16).

24] Q. Chen, M. Nie, Y. Guo, Sens. Actuators B: Chem., 254 (2018) 30-35.

25] P. Deshmukh, S. Patil, R. Bulakhe, S. Sartale, C. Lokhande, Mater. Today Commun., 8 (2016) 205-213.

26] D. Halge, V. Narwade, N. Kaawash, P. Khanzode, S. Shaikh, J. Dadge, P. Alegaonkar, R. Hyam, K. Bogle, Mater. Sci. Semicond. Process., 171 (2024) 108020 (1-17).

27] R. Singh, A. Shrivastava, A. Bajpai, Mater. Res. Express, 6 (2020) 1250a9 (1-14).

28] C. Cheng, H. Zhang, F. Li, S. Yu, Y. Chen, Mater. Chem. Phys., 273 (2021) 125098 (1-19).

29] A. Lokhande, A. Yadav, J. Lee, M. He, S. Patil, V. Lokhande, C. Lokhande, J. Kim, J. Alloys Compd., 709 (2017) 92-103.

30] J. B. Condon, Surface area and porosity determinations by physisorption measurements and theory, (Elsevier, Amsterdam; Boston, 2006) pp 1- 274.

31] B. Sharma, and R. Purohit, Theory of heterojunctions, Semiconductor heterojunctions, (Elsevier, 1974) pp. 1-23.

32] D. Dhawale, R. Salunkhe, U. Patil, K. Gurav, A. More, C. Lokhande, Sens. Actuators B: Chem., 134 (2008) 988-992.

33] S. Patil, P. Deshmukh, C. Lokhande, Sens. Actuators B: Chem., 156, (2011) 450-455.

34] A. Vishwakarma, A. Sharma, N. Yadav, L.Yadav, Vacuum, 191 (2021) 110363 (1-9).

35] M. Dun, J. Tan, W. Tan, M. Tang, X. Huang, Sens. Actuators B: Chem., 298 (2019) 126839 (1-10).

36] S. Shao, L. Che, Y. Chen, M. Lai, S. Huang, R. Koehn, J. Alloys Compd., 774 (2019) 1-10.

37] R. Ladhe, P. Baviskar, W. Tan, J. Zhang, C. Lokhande, B. Sankapal, J. Phys. D Appl. Phys., 43 (2010) 245302 (1-6).

38] R. Bulakhe, S. Patil, P. Deshmukh, N. Shinde, C. Lokhande, Sens. Actuators B: Chem., 181 (2013) 417-423.

39] Z. Ling, C. Leach, R. Freer, J. Eur. Ceram. Soc., 21 (2001) 1977-1980.

40] S. Patil, A. Lokhande, A. Yadav, C. Lokhande, J. Mater. Sci.: Mater. Electron., 27 (2016) 7505-7508.

Chapter-VIII

Summary and conclusions

8.1 Summary and conclusions

The energy demand of world is increasing day by day due to the over population. The current energy need of the world fulfilled by mainly fossil fuels. However, fossil fuels have the disadvantage that they are available in limited quantity, and release toxic pollutants when burned. To avoid these drawbacks, the best option is to use renewable green energy sources such as solar, tidal, wind, biomass, etc. Among them, solar energy is an abundant, environmentally friendly and economical source of energy for civilization in modern times. Solar energy has the potential to meet a sufficient portion of today's energy needs.

solid state solar cells need high-tech processes for the fabrication of junctions of completely crystalline materials which are costly and rarely available. Many efforts have been done for efficient and long-life solar cells of lower costs. At this situation, third generation photoelectrochemical (PEC) solar cell offers a technically strong and financially viable alternative idea. In the previous era, significant progress has been made in the investigation of reliable solid-liquid junction phototvoltaic (PV) solar cells for the PEC system. PEC cells and dye sensitized solar cells (DSSC) are a couple of modern gadgets. The PEC process is advantageous due to photoelectrolysis, allows direct translation of light energy into chemical energy of the PEC reaction products, and solves the storage problem along with suitable energy conversion.

The better physicochemical properties of metal chalcogenides (MCs) are more useful for electronic, optical, and optoelectronic devices. Cadmium chalcogenide (CdX, where X = S, Se, Te) electrodes of band gap energies (1.4 - 2.4 eV) are extensively used for photoelectrochemical (PEC) cells to alter solar energy into electricity. Due to lower band gap and sharp absorption edges CdX are prominently absorbers of the solar spectra. Additionally, tunable electrical, chemical, and physical properties of CdX makes them promising for gas sensing applications. But the photocorrosion in PEC, and operating temperature issues in gas sensing application needs composites with higher surface area and conducting materials like carbon-based materials, conducting polymers.

The main objective of present work is synthesis of cadmium chalcogenide (CdX, where, X = S, Se) and reduced graphene oxide/cadmium chalcogenide composite rGO/(CdX, where, X = S, Se) thin films with suitable optical and electrical properties using cost effective and simple SILAR and electrodeposition (ED) methods for efficient solar cell and gas sensor applications. The main approaches for material synthesis are

achieving uniform and adherent, controlled film composition, optimum thickness with stable phase formation and good reproducibility. The preparative parameters of each method have been optimized. The optimum thickness and carbon-based material composite approach described in chapter III and IV are based on SILAR deposition, whereas in chapter V and VI are based on ED method. Also, chapter VII describes heterojunction films fabrication of CdS and rGO/CdS with PANI via SILAR method. All mentioned approaches produced good quality thin films.

Further, the photo-activities of prepared cadmium chalcogenides and their composites with rGO were tested by fabricating the PEC solar cells. The heterojunctions of cadmium chalcogenides fabricated with polyaniline (PANI) was studied for gas sensing applications. Additionally, the PEC cell fabrication needs only a counter electrode, electrolyte and working electrode. So, PEC is useful to optimize the preparative parameters of cadmium chalcogenides and rGO/cadmium chalcogenide thin films and further to study the effectiveness of these approaches, the PEC cell and heterojunction gas sensor devices were fabricated and tested.

Chapter 1 gives the introduction about solar cells, its operation, types and the development of solar cells. The solar cell technology consists of generations of the solar cells. The generations of the solar cells are discussed in brief with its advantages and the disadvantages. Among them the PEC solar cell is the third generation thin film solar cell. The chapter deals with the construction and working of the PEC cell. Along with the junction properties and PEC parameters are discussed briefly. Chapter consists of the sensor introduction with its historical development. The types of sensors are discussed with their sensing parameters. Furthermore, the literature review of cadmium chalcogenides with rGO and conducting polymers and metal oxide composites and heterojunctions for PEC and gas sensor application is summarized. In the ending part of chapter, the objectives of the research work are mentioned.

Chapter 2 provides information about thin film deposition methods and comparison between them. Out of various chemical methods, the SILAR and ED methods are briefly explained with their deposition process parameters and preparative parameters. Furthermore, This chapter outlines different techniques and instruments used for characterization, providing a theoretical foundation for methods such as powder XRD, FE-SEM with EDAX, contact angle measurement, UV-DRS, and BET analysis. The subsequent sections of the chapter provide a brief overview of the theoretical

background of electrochemical techniques, including I-V measurements, LSV, and EIS, which are employed to assess the PEC performance of photoelectrodes and their sensing capabilities.

Chapter 3 deals with the synthesis, characterization, and PEC performance of rGO, CdS, and rGO/CdS thin films by SILAR method on stainless steel (SS) substrates. The effect of CdS and rGO/CdS film thicknesses on the physicochemical and PEC properties was studied. **Section A** of chapter comprises the synthesis of GO by modified Hummer's method and its chemical reduction to form rGO. The rGO thin film was deposited on SS substrate by employing 40 dip and dry cycles (immersion time- 10 s and drying time- 20 s) using rGO solution of 1 mg mL^{-1}. CdS thin films were deposited by four beaker SILAR method consisting 0.025 M cadmium chloride (0.025 M CdCl$_2$) as a cationic precursor and 0.025 M sodium sulfide (0.025 M Na$_2$S) as anionic precursor. The SS substrate was dipped in cationic and anionic precursors successively for 15 s and rinsed inbetween DDW for 10 s. Such 40, 60, 80, and 100 cycles were repeated to deposit films of various thicknesses. The rGO deposited SS substrate used as a substrate for deposition of CdS on rGO for rGO/CdS composite films. The thicknesses of rGO, CdS and rGO/CdS thin films were estimated by gravimetric weight difference method. rGO, CdS, and rGO/CdS composite thin films were characterized for various physicochemical properties via XRD, FE-SEM, EDAX, contact angle, BET, and UV-DRS. CdS and rGO/CdS showed cubic crystal structure with spherical nanoparticles nature. All CdS and rGO/CdS composite films showed hydrophilicity. The rGO composited CdS films showed improved specific surface area of 52.52 m^{2}g^{-1} reduction in energy band gap.

Section B deals with the electrochemical study of rGO, CdS and, rGO/CdS composite electrodes by I-V characteristics, power output measurements and EIS studies. The I-V characteristics of rGO, CdS, and rGO/CdS was carried out in dark and under light through three electrode system configuration with graphite plate as a counter, rGO or CdS or rGO/CdS film as a working, and SCE as a reference electrode in 1 M polysulfide electrolyte. The junction quality factor (β) was estimated from I-V characteristics of rGO, CdS and, rGO/CdS films. Power output characteristics of rGO, CdS, and rGO/CdS electrodes in dark, under light, and in chopping conditions were determined using two electrode PEC cell. rGO, CdS and, rGO/CdS used as a working and graphite used as a counter electrode in 1 M polysulfide electrolyte. The rGO/CdS

electrode deposited by 80 SILAR cycles showed maximum power conversion efficiency (η) of 0.31 % with fill factor (FF) 0.39. The EIS studies showed that rGO composite lowers the charge transfer resistance which is valuable for superior charge transport process. Hence, it is clear that, composite of rGO with CdS (0.31 %) lifts the η value nearly 3.5 times compared to pure CdS (0.09 %). So, CdS composite with rGO is an effective strategy for the PEC cell application over CdS.

Chapter 4 is associated with the synthesis, characterization, and PEC performance of CdSe and rGO/CdSe composite thin films by SILAR method. In **Section A**, CdSe and rGO/CdSe films were synthesized by using four beaker SILAR method. Cadmium sulfate ($CdSO_4$) and sodium selenosulfite (Na_2SeSO_3) are used as a cationic and anionic precursor, respectively. For CdSe film SS substrate was dipped alternately in cationic and anionic solutions for 40 s, and rinsed in DDW for 30 s. The optimized 400 cycles were repeated to achieve desired film thickness. For rGO/CdSe composite, CdSe film was deposited on rGO deposited SS substrate by the procedure used for CdSe deposition. CdSe and rGO/CdSe both shows cubic crystal structure confirmed by the XRD study. The rGO composition enhances the porosity of the composite surface, this may be due to reduced agglomeration of CdSe spherical nanoparticles. Stochiometric composition of CdSe and rGO/CdSe films was confirmed by EDAX. The rGO/CdSe composite showed mesoporosity with more specific surface area (13.86 m^2 g^{-1}) than CdSe (11.75 m^2 g^{-1}), this may be due to higher surface area of rGO. The rGO composition reduces the energy band gap of CdSe, this may be due to size dependent modifications occurred in semiconductor.

In **section B**, I-V characteristics, power output, and EIS studies of CdSe and rGO/CdSe electrodes were studied in 1 M polysulfide electrolyte. The CdSe and rGO/CdSe electrodes showed value of 'β' near to 1 which implies intimate contact between photoelectrodes and electrolyte. The rGO/CdSe electrode showed maximum *FF* and '*η*' of 0.37 and 2.18 % than 0.32 and 1.54 %of CdSe. The enhancement of '*η*' for rGO/CdSe electrode is due to the fast charge transfer and reduction in recombination. The EIS showed that, for rGO/CdSe electrode charge transfer resistance (R_{ct} = 5 Ω cm^{-2}) reduces which results in superior charge transport properties over CdSe (R_{ct} = 6 Ω cm^{-2}). Hence, rGO/ CdSe composite electrode is more PEC efficient over CdSe.

Chapter 5 comprises synthesis, characterization and PEC performance of CdS and rGO/CdS films by electrodeposition method. In **section A**, CdS and rGO/CdS thin

films deposited on SS substrates via potentiostatic electrodeposition (ED) method. CdS and rGO/CdS thin films showed cubic crystal system. The EDAX study shows successful composition of CdS and rGO/CdS. The less aggregation of CdS nanoparticles on rGO surface was observed from morphology study. The rGO/CdS electrodes showed more hydrophilicity, due to lower contact angle value of 41 ° compared to 58 ° of CdS. rGO/CdS and CdS revealed band gap values of 2.15, and 2.43 eV. rGO/CdS exhibited mesoporosity with higher specific surface area of 55 m^2 g^{-1} compared to 48 m^2 g^{-1} of CdS.

In **section B**, the electrode electrolyte junction and PEC properties of CdS and rGO/CdS were assessed using I-V, power output and EIS studies. CdS and rGO/CdS showed 'β' value nearer to 1, which shows proper junction formation between photoelectrode and electrolyte. The rGO/CdS electrodes showed an improved *FF*, and '*η*' of 0.38, and 0.22 % compared to 0.34 and 0.10 % respectively, over CdS. Under light illumination, R_{ct} values for CdS and rGO/CdS are 44.7 and 7.4 Ω cm^{-2}, which states superior charge transport properties of rGO/CdS. Hence, rGO/CdS have 2.2 times *η* compared over CdS, and rGO composite is a good option for PEC application.

Chapter 6 section A contains synthesis, characterization and PEC performance of CdSe and rGO/CdSe films by potentiostatic electrodeposition method. The modifications occurred in structural, morphological, compositional, and optical properties were studied through various physicochemical characterization techniques. The CdSe and rGO/CdSe showed cubic crystal structure and fibrous web like morphology studied by XRD, and FE-SEM, respectively. The EDAX studies evidence the stoichiometric formation of CdSe, and rGO/CdSe films. CdSe and rGO/CdSe both are hydrophilic with contact angle value of 41 and 27 °, respectively. The rGO/CdSe thin film showed less energy band gap value than CdSe due to composition with rGO.

In **section B**, CdSe and rGO/CdSe electrode and 1 M polysulfide (electrolyte) junction properties are studied by estimating the 'β' value which closer to 1. The rGO/CdSe electrode showed *FF* and '*η*' are 0.35, and 1.8 %, respectively. The rGO/CdSe showed lower charge transfer resistance than CdSe. Hence, it is concluded that composite of rGO with CdSe increases the 'η' nearly 1.4 times compared to CdSe.

Chapter 7 focuses on the synthesis of n-CdS/p-PANI, and rGO/n-CdS/p-PANI films by SILAR method and their physicochemical characterization with gas sensing

study. In **section A**, CdS/PANI and rGO/CdS/PANI heterojunction films are amorphous. The rGO/CdS/PANI showed more porous and spongier surface than CdS/PANI. The EDAX studies evidences the successful formation of CdS/PANI and rGO/CdS/PANI samples. CdS/PANI and rGO/CdS/PANI heterojunctions formation were confirmed by FE-SEM cross section images. The rGO/CdS/PANI shows more hydrophilicity (contact angle 21 °) compared to PANI/CdS (contact angle 28 °). The rGO/CdS/PANI heterojunction sample showed higher specific surface area 95 $m^2 g^{-1}$ which is greater than CdS/PANI sample 71 $m^2 g^{-1}$.

In **section B**, n-CdS/p-PANI and n-rGO/CdS/p-PANI films are selective to SO_2 gas at room temperature (RT) as compared to other target gases (NH_3, CO_2, LPG, Cl_2, NO_2). The rGO/CdS/PANI exhibited maximum sensitivity of 65.50 % compared to CdS/PANI 58.33% for 100 ppm SO_2 gas. The rGO/CdS/PANI film showed lower t_{res} and t_{rec} over CdS/PANI. The rGO/CdS/PANI showed more stability of 92 % more than CdS/PANI 86%, for 100 ppm SO_2 after 45 days. Thus, the improvement in sensitivity and selectivity, stability of rGO/CdS/PANI heterojunction may be due to presence of high surface area, more porous structure, and active cites. Finally, it is concluded that, rGO/CdS/PANI is more stable and sensitive for SO_2 compared to CdS/PANI.

In this research, thin films of CdX (where X = S, Se) and their composites with rGO) were synthesized using the SILAR and ED methods. The incorporation of rGO enhances the electrical conductivity, specific surface area, and overall electrochemical performance of the pure material. Future work will explore the use of other carbon allotropes, such as fullerenes, carbon nanotubes (CNTs), and carbon foam, in these composites. Physicochemical characterization analyses indicate that the porous morphology, increased surface area, mesoporosity, hydrophilicity, optimal band gap, and high electrical conductivity of cadmium chalcogenides and their rGO composites significantly contribute to improvements in PEC and gas sensing performance.

The obtained PEC results of respective synthesis methods are tabulated in **table 8.1**. In case of gas sensing application, the comparison of n-CdS/p-PANI and n-rGO/CdS/p-PANI is given in **table 8.2**.

Table 8.1: The obtained PEC results of rGO/CdX by SILAR and ED methods.

Sr. No.	Material	Deposition method	*FF*	η (%)
1	CdS	SILAR	0.38	0.09
	rGO/CdS		0.39	0.31
2	CdSe	SILAR	0.32	1.54
	rGO/CdSe		0.37	2.18
3	CdS	ED	0.34	0.10
	rGO/CdS		0.38	0.22
4	CdSe	ED	0.33	1.0
	rGO/CdSe		0.35	1.8

Table 8.2: Comparison of sensing results of n-CdS/p-PANI and n-rGO/CdS/p-PANI for SO$_2$ gas.

Sr. No.	Material	Method	S (%)	Stability after 45 days
1	n-CdS/p-PANI	SILAR	58.33	86 %
2	rGO/n-CdS/p-PANI		65.50	92%

From **table 8.1** and **8.2**, it is concluded that the both chemical methods yield uniform adherent deposits and showed good PEC and gas sensing properties**.** SILAR deposited rGO/CdSe composite films shows greater PEC performance.

Chapter-IX

80- Recommendations

80-Recommendations

9.1 Recommendations

In the present research work, thin films of cadmium chalcogenide (CdX, where, X = S and Se) and reduced graphene oxide/cadmium chalcogenide composite (rGO/CdX, where, X = S and Se) are deposited using SILAR and ED methods. The power conversion efficiency (η) and gas sensing properties of deposited electrodes were improved by means of enhancement in conductivity, and surface area which is due to composit formed with rGO.

Finally, it is recommended that, at 80 SILAR cycles, CdS thin film composited with 40 cycles rGO (thickness (t) = 90 nm) show maximum performance, and by ED it is obtained at 30 min. deposition time (deposition potential = -1.18 V/SCE). For CdSe, composition with rGO (t = 90 nm) of 400 SILAR cycles exhibited maximum PEC performance, while it observed by ED at 40 min. of deposition time (deposition potential = - 0.77 V/SCE). Also, rGO/CdS/PANI films fabricated by SILAR showed maximum SO_2 gas sensing performance at room temperature. The deposited films showed maximum PEC and gas sensing performance due to proper modifications occurred in physicochemical properties which is result of composite with rGO by both SILAR and ED methods. So, it is recommended that, rGO/CdX are the potential materials for solar energy conversion, and SO_2 sensing applications. Along with that, merits of both deposition methods like cost effectiveness, and simplicity could be easily adopted for large scale use with nominal adjustments.

9.2 Future scope

➢ In the present study, cadmium chalcogenide thin films and its composite with rGO were synthesized using SILAR and ED methods by optimizing preparative conditions and used for PEC, and gas sensing applications. Also, there is more scope to study other application like antimicrobial.

➢ The FF and η of cadmium chalcogenides composites with rGO electrodes require further enhancement for effective use in PEC applications.

➢ There is a scope for composite formation of cadmium chalcogenides with another carbon based materials like CNTs, MWCNTs for increase PEC performance.

➢ There is a scope for cadmium chalcogenides doped with indium, silver, zinc, and gold to improve the solar cell properties.

➢ There composite formation with another higher surface area materials is a one more aspect to improve physicochemical and electrochemical properties of cadmium chalcogenide materials.

➢ The used deposition methods are highly applicable for cost effective fabrication of the solar cells and sensors.

➢ The future work is proposed to prepare CdTe and rGO/CdTe composites electrodes using SILAR method and utilized in PEC and gas sensing applications.

➢ This research has made significant advancements in cadmium chalcogenides composites with rGO photoelectrodes, there are still challenges to overcome in order to enhance efficiency (η) and ensure a longer cycle life.

➢ There is a scope to deposit rGO/cadmium chalcogenide composite materials for improvement in 'η' and SO_2 sensitivity another chemical methods (CBD, spray pyrolysis etc.).

Publications

ORIGINAL ARTICLE

Chemical synthesis and photoelectrochemical study of CdS/rGO nanocomposite films

Ranjit P. Nikam[1] · Abhishekh C. Lokhande[2] · Sambhaji D. Khot[1] · Vikas J. Mane[1] · Chandrakant D. Lokhande[1]

Abstract

The cadmium sulfide/reduced graphene oxide (CdS/rGO) composite thin films were synthesized on stainless steel (SS) substrates using the successive ionic layer adsorption and reaction (SILAR) method. The physico-chemical properties of CdS/rGO films were studied. The X-ray diffraction (XRD) revealed the growth of nanocrystalline CdS/rGO films with a cubic crystal structure. The field-emission scanning electron microscopy (FE-SEM) images of CdS/rGO-80 composite thin films showed compact spherical nanoparticles and an optical band gap found to be 2.27 eV. The CdS/rGO-80 composite thin film displayed hydrophilic nature with a water contact angle of 33°. The photoelectrochemical (PEC) studies of CdS/rGO thin film in dark and under light exhibited n-type of electrical conductivity with an improved photoactivity over bare CdS in 1 M polysulfide ($NaOH + Na_2S + S$) electrolyte. It is observed that rGO composited CdS thin film enhances the conversion efficiency (η) from 0.09 to 0.31% than bare CdS films. The electrical transport properties were investigated by electrochemical impedance spectroscopy (EIS) study in dark and under illumination conditions and corresponding equivalent circuit of the impedance model is developed.

Graphical Abstract
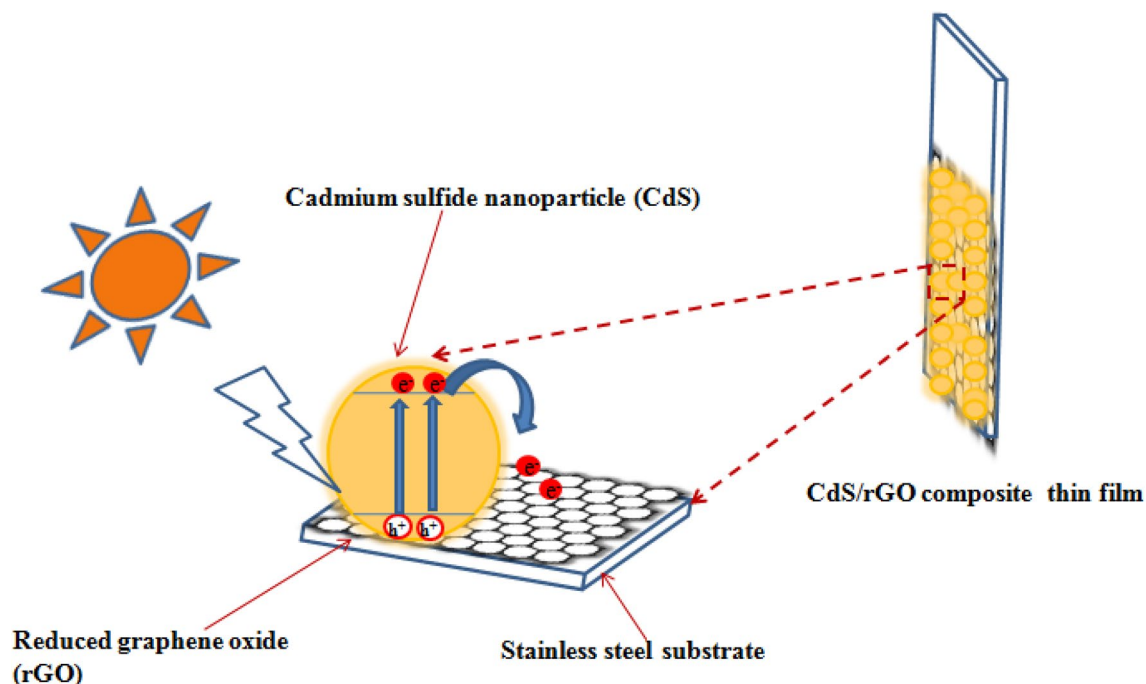
Effect of post annealing on chemisynthesized cadmium selenide (CdSe) thin films: physicochemical and photoelectrochemical properties

R. P. Nikam[1], V. C. Lokhande[2], S. D. Khot[1], P. P. Bagwade[1], J. L. Gunjakar[1], and C. D. Lokhande[1,*]

[1] *Centre for Interdisciplinary Research, D. Y. Patil Education Society (Deemed to be University), Kolhapur 416 006, India*
[2] *Department of Electrical, Electronic Communication and Computer Engineering, Chonnam National University, Yongbong-Dong, Puk-Gu, Gwangju 500 757, South Korea*

ABSTRACT

The utilization of solar energy is an essential aspect in order to sustain in the energy crisis situation. Semiconductor based photoelectrochemical (PEC) cells are used for it. Herein, a binder free approach was employed for the synthesis of CdSe thin films on stainless steel substrate and effect of post annealing (350–500 K) on physicochemical as well as photoelectrochemical properties were investigated. The characterization showed that CdSe thin films crystallized in cubic crystal structure with spherical granular morphology with optical band gap of 1.76 eV. The effect of post annealing on CdSe thin films is further tested by examining their PEC properties. Thin film CdSe electrode annealed at temperature 400 K showed highest fill factor (*FF*) and efficiency (*η*) of 0.32 and 1.54%, respectively. In addition, electrochemical impedance spectroscopy (EIS) study showed superior charge transfer properties.

1 Introduction

In recent days, the global energy need is rising day by day due to overpopulation and worldwide techno-economic growth. The progress of humans and nation is depending on the utilization of energy. In order to have rapid development, adequate energy is a key requisite. At present, mainly fossil fuels viz. petrol, diesel, coal, etc., are used to fulfill the energy requirement of the world. However, due to limited availability, environmental pollution, and overutilization of fossil fuels,

mankind is going through a drastic energy crisis situation. In order to resolve this energy crisis scientists are looking forward for pollution free, eco-friendly, affordable, secure, and sustainable sources of energy [1].

To reduce dependency on fossil fuels and quench energy requirement, researchers are gregariously paying interest in renewable energy sources (RES) including solar, nuclear, wind, tidal, geothermal, etc. Among them, solar energy is one of the best options. It is a clean and green energy source, as it does not generate any pollutants or byproducts hazardous

ELSEVIER

Check for updates

Performance of solid-state symmetric supercapacitors based on Dy_2S_3 electrodes

P.P. Bagwade [a], R.P. Nikam [a], R.P. Bhosale [b], S.D. Khot [a], C.D. Lokhande [a],[*]

[a] *Centre for Interdisciplinary Research, D. Y. Patil Education Society, Kolhapur 416 006, India*
[b] *Department of Physics, D. P. Bhosale College, Koregaon, Satara 415516, India*

ARTICLE INFO

ABSTRACT

Rare earth metal sulfides show good capacitance retention and better charge discharge performance. Dysprosium based materials could be a promising candidate for the utilization in supercapacitors due to it's multiple transition states. The dysprosium sulfide (Dy_2S_3) thin films were deposited on stainless steel (SS) substrate using facile successive ionic layer adsorption and reaction (SILAR) method. The films exhibits orthorhombic crystal structure and spherical nanoparticles morphology. The electrochemical supercapacitive performance of Dy_2S_3 film showed maximum specific capacitance (C_s) of 273 F g^{-1} at a scan rate of 5 mV s^{-1} with excellent (83 %) cycling performance over 2000 cycles in 1 M Na_2SO_4 electrolyte. The industrial application of SILAR deposited Dy_2S_3 thin film was examined by fabricating flexible solid-state symmetric supercapacitor (FSS-SSC) device with configuration Dy_2S_3/PVA-Na_2SO_4/Dy_2S_3. It exhibited C_s of 26 F g^{-1} with specific energy of 17 Wh kg^{-1} and specific power of 520 W kg^{-1}. A good cyclic stability was observed with capacitive retention of 79 % at the scan rate of 100 mV s^{-1} after 5000 cyclic voltammetry (CV) cycles. This study highlights the potential application of Dy_2S_3 for supercapacitor application.

Introduction

Large energy shortages and renewable energy sources have inspired the overall efforts for research to expand the use of energy saving devices that are beneficial and environmentally friendly. Hence, various energy storage devices are under investigation [1,2]. A battery-powered energy storage system has a shorter life cycle and requires more space for the system. Supercapacitors (SCs), on the other hand, have emerged as potential competitors for remarkable features, such as high charging-discharging rates, excellent life cycles and reversibility. The SCs are energy storage devices having capacitance greater than common capacitors [3,4]. SCs are categorized as electrical double layer capacitors (EDLCs) and pseudocapacitors based on the charge storage mechanism [5]. The EDLC (carbon-based substances) possesses greater surface area and extensive life span. The charge storage mechanism in pseudocapacitors are based on reversible faradic redox reactions. Metal sulfides, oxides, and polymers are some of the pseudocapacitive materials [6,7].

Recently, transition metal sulfides have emerged as potential pseudocapacitive materials [8]. Of these, compounds based on rare earth metals owing to their excellent electrical conductivity and abundance,

attracting significant research attention. Dysprosium is a promising rare earth metal which exhibits various oxidation states (Dy^{+3}, Dy^{+2}, Dy^{+1}) useful for pseudocapacitive performance. As of now, many researchers have employed rare earth compounds for the SC application [9]. Ghogare et al. [10] reported hydrothermal method for lanthanum sulfide (La_2S) thin film with specific capacitance (Cs) of 121.4 F g^{-1}. Pujari et al. [11] and Patil et al. [12] synthesized ytterbium sulfide (Yb_2S_3) and lanthanum telluride (La_2Te_3) and obtained C_s of 270 and 469 F g^{-1}, respectively. Arunachalam et al. [13] using chemical precipitation process produced neodymium hydroxide ($Nd(OH)_3$) thin films with C_s of 871 F g^{-1}.

Though various methods are useful for the deposition of thin films on different substrates, SILAR method comes out as an effective approach by providing direct deposition on any kind of substrate without having to use binder for the adhesion purpose. It gives access to control the film thickness by means of varying deposition cycles. In addition, one can have large area deposition using SILAR method which is applicable at industrial scale [6]. As a result, SILAR is being widely used for the deposition of many materials for various applications [10].

In continuation to our previous work [14], this report highlights a direct deposition of Dy_2S_3 thin film and evaluation of its supercapacitive

Porous NiCo$_2$O$_4$ electrodes for high-energy asymmetric supercapacitor: effect of annealing

J. P. Thorat[1] (ID), R. P. Nikam[1], V. C. Lokhande[2], and C. D. Lokhande[1,*]

[1] *Centre for Interdisciplinary Research, D. Y. Patil Education Society, (Deemed to Be University), Kolhapur, India 416006*
[2] *Department of Electronics and Computer Engineering, Chonnam National University, Gwangju 61186, South Korea*

ABSTRACT

Nickel–cobalt hydroxide thin films were synthesized using the chemical bath deposition method, and the effect of thermal annealing (373–673 K) on their physicochemical and electrochemical characteristics was explored. The X-ray diffraction study showed a cubic crystalline structure of NiCo$_2$O$_4$ electrode formed above annealing temperature of 573 K. Field emission scanning electron spectroscopy (FE-SEM) study revealed that after annealing, NiCo$_2$O$_4$ electrode showed urchin-like microspheres morphology with superhydrophilic nature. The electrode annealed at 573 K exhibited outstanding electrochemical performance with a specific capacitance of 470 F g^{-1} at 0.4 A g^{-1} current density. Over 2000 cycles, electrode demonstrated capacitive retention of 75.55%. Finally, NiCo$_2$O$_4$ and Fe$_2$O$_3$ thin films were used to construct the asymmetric supercapacitor (ASC) device. The ASC device manifested energy density of 40 Wh kg^{-1} at power density of 1.66 kW kg^{-1} and 82% retention after 2000 CV cycles.

 Springer

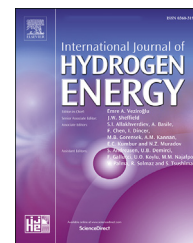# Nanocrystalline cobalt tungstate thin films prepared by SILAR method for electrocatalytic oxygen evolution reaction

P.P. Bagwade, D.B. Malavekar, V.V. Magdum, S.D. Khot, R.P. Nikam, D.J. Patil, U.M. Patil, C.D. Lokhande*

Centre for Interdisciplinary Research, D. Y. Patil Education Society, Kolhapur 416 006, India

HIGHLIGHTS

- $CoWO_4$ thin film electrocatalysts prepared by SILAR method was employed for oxygen evolution reaction.
- The $CoWO_4$ material exhibited porous morphology with specific surface area of 49.3 m^2 g^{-1}.
- $CoWO_4$ electrode exhibited excellent OER functioning with overpotential of 330 mV at a current density of 100 mA cm^{-2}.
- $CoWO_4$ thin film electrode exhibited remarkable stability (97%) after 24 h in 1 M KOH.

GRAPHICAL ABSTRACT

ARTICLE INFO

ABSTRACT

This study highlights on the application of nanocrystalline cobalt tungstate ($CoWO_4$) thin films as an electrocatalyst for oxygen evolution reaction (OER) prepared using successive ionic layer adsorption and reaction (SILAR) method. The X-ray diffraction, scanning electron microscopy, X-ray photoelectron spectroscopy, Fourier transform infrared spectroscopy etc. were employed for the characterization of $CoWO_4$ thin films, revealing the formation of crystalline $CoWO_4$ with spherical morphology. Furthermore, $CoWO_4$ showed excellent electrochemical performance with the overpotential of 330 mV and Tafel slope of 153 mV dec^{-1} with retaining 97% of electrochemical stability after 24 h of OER. The study confirmed the structural maintenance of $CoWO_4$ thin films after stability study.

© 2022 Hydrogen Energy Publications LLC. Published by Elsevier Ltd. All rights reserved.

MnS-La$_2$S$_3$/GO composite electrodes for high-performance flexible symmetric supercapacitor

Vikas J. Mane [a], Abhishek C. Lokhande [b], Ranjit P. Nikam [a], Navnath S. Padalkar [a], Vaibhav C. Lokhande [c], Dattatray S. Dhawale [d,*], Chandrakant D. Lokhande [a,*]

[a] *Centre for Interdisciplinary Research, D. Y. Patil Education Society (Deemed to be University), Kolhapur 416 006, India*
[b] *Department of Mechanical Engineering, Khalifa University of Science and Technology, P.O. Box 127788, Abu Dhabi, United Arab Emirates*
[c] *Department of Electrical, Electronic Communication and Computer Engineering, Chonnam National University, Yongbong-Dong, Puk-Gu, Gwangju 500 757, South Korea*
[d] *CSIRO Energy, Private Bag 10, Clayton South, Victoria 3169, Australia*

A B S T R A C T

We report on fabricating manganese-lanthanum sulfide/graphene oxide (MnS-La$_2$S$_3$/GO) composite electrodes by cost-effective economical successive ionic layer adsorption and reaction (SILAR) method for high-performance flexible symmetric supercapacitors. The prepared MnS-La$_2$S$_3$/GO composite electrode possesses a high specific surface area of 156 m^2 g^{-1} and a porous thin multilayer nanosheet structure, which helped to achieve improved supercapacitive performance. The assembled MnS-La$_2$S$_3$/GO flexible symmetric supercapacitor device exhibits excellent electrochemical performance with a cell voltage of up to 1.6 V, specific energy of 54.26 Wh kg^{-1} at a specific power of 1.3 kW kg^{-1} and demonstrates higher capacitance retention of 92.51% after 10,000 cycles.

1. Introduction

The continuous increase in the demand for flexible energy storage devices to power portable and wearable electronic devices has significantly expanded and created a massive impact on human life around the world [1]. Rechargeable energy storage devices, such as batteries and supercapacitors (SCs), are the leading electrical energy storage devices. Compared with lithium-ion batteries, SCs have attractive properties, such as short charging time, higher power density, variable operating temperature range, more safety, and extended cycling stability [2,3]. Much effort and resources have been devoted to research and development activity to improve the energy density of portable and flexible SCs to meet the demand for various electronic devices [4,5]. The flexible SCs are lightweight and thin, thus being capable of gratifying the safety needs of future energy storage device generation [6]. Rapid growth and demand for flexible and wearable electronic devices such as flexible touch screens, displays, generators, sensors, and actuators have recently increased [7]. Recently, transition metal sulfides (TMS) such as nickel, cobalt, molybdenum, copper, manganese, iron, and binary metal sulfides have paid more attention as alternative electrode materials for SCs

[8–14]. Among these, sulfides of manganese (MnS) and lanthanum (La$_2$S$_3$) are the best pseudocapacitive electrode materials owing to their ease of synthesis, inexpensiveness, and high specific capacitance (Cs) [15]. Moreover, the rich electrochemical redox sites of MnS and La$_2$S$_3$ electrode materials compared with their corresponding oxide counterparts could help increase the voltage window and the energy and power density of SCs [16]. However, the supercapacitive performance of the MnS and La$_2$S$_3$ electrode is still inferior to be considered at the commercial level, mainly due to their poor cyclic performance, low energy density, less electrical conductivity, significant volume changes, and sluggish kinetics during long-term stability [17,18]. Therefore, to overcome above mentioned limitations, making a composite of MnS and La$_2$S$_3$ with carbon-based conducting matrixes such as graphene oxide (GO) is an efficient way to enhance the voltage window, supercapacitance, mechanical strength, electrical conductivity, and cyclic stability [19,20].

The rare-earth metal chalcogenides have fascinated wide attention for storage device applications owing to their unique physical and chemical properties [21]. The supercapacitive performance of the single MnS or La$_2$S$_3$ electrode is not fulfilled, mainly due to its poor cyclic

Chemisynthesized tungsten oxide (WO$_3$) electrodes for high-performance asymmetric supercapacitor application: effect of deposition time

Sujata B. Patil[1] , Ranjit P. Nikam[1], Chandrakant D. Lokhande[1], and Raghunath S. Patil[1,*]

[1] *Centre for Interdisciplinary Research, D. Y. Patil Education Society (Deemed to be University), Kolhapur 416 006, India*

ABSTRACT

The tungsten oxide (WO$_3$) thin films were deposited on stainless steel substrates via low-cost chemical bath deposition method at different deposition time periods of 4, 8, 12, 16, and 20 h. The different deposition time periods affect the physico-chemical properties of electrodes. The electrode synthesized at 12 h time period showed maximum thickness of 2.27 µm and hexagonal crystal structure with nanobundle like surface morphology. The electrode synthesized at 12 h time period showed specific capacitance (C_s) of 1050 Fg^{-1} at 5 mV s^{-1} scan rate with 89% capacitive retention after 4000 CV cycles. The asymmetric supercapacitor device of configuration WO$_3$/PVA-H$_2$SO$_4$/PANI was fabricated using WO$_3$ as negative electrode and polyaniline (PANI) as the positive electrode. The fabricated WO$_3$/PVA-H$_2$SO$_4$/PANI device showed a specific capacitance of 484 Fg^{-1} with energy and power density of 113.7 Wh kg^{-1} and 1.1 kW kg^{-1}, respectively with 85% capacitive retention over 4000 CV cycles.

1 Introduction

In order to fulfill society's growing energy demand, it is necessary to transform and store energy from renewable resources. In current era energy storage devices are attracted more attention due to portable electronics and e-vehicles which are become lifeline for the present and future generations. To fabricate and develop prominent, energy storage devices many studies have been involved. Consequently, researchers are enthusiastically working on long lasting energy storage devices with higher energy and power capability, but are restricted by cost, dimensions and energy density as well as power density of the energy storage devices.

Supercapacitors (SCs) and batteries are two potential electrochemical energy storage technologies at the moment [1]. Due to peculiar power densities, rapid charge-discharge capabilities, and longer life cycles than batteries, SCs have gathered a lot of interest as promising and complementary energy storage devices [2, 3]. Electric double-layer capacitors (EDLC), pseudocapacitors, and battery-type supercapacitors are the three types of supercapacitors that are categorized according to the charge storage method [4]. EDLC: i.e., electrical double layer capacitors in which the electric double layer ions produce at the terminal of interface of electrolyte due to electrostatic mechanism. The carbon-based materials like carbon, carbon aerogels, and carbon nanotubes show EDLC type behavior

Address correspondence to E-mail: rsp17658@gmail.com

Chemically synthesized ZnFe$_2$O$_4$ electrodes for electrochemical oxygen evolution reaction and supercapacitor applications

S. D. Jituri[1], R. P. Nikam[2], V. J. Mane[2], S. B. Shaikh[2], C. D. Lokhande[2], and S. H. Mujawar[1,*]

[1] *Department of Physics, Yashavantrao Chavan Institute of Science Satara, (Autonomous), Karmaveer Bhaurao Patil, University, Satara 415001, India*

[2] *Centre for Interdisciplinary Research, D. Y. Patil Education Society (Deemed to Be University), Kolhapur 416 006, India*

ABSTRACT

The spinel ferrites are versatile group of metal oxides with good photoelectro-chemical and unique magnetic properties, as well as low cost, biocompatible and huge abundance. The magnetic as well as photoelectrochemical properties have been extensively examined. Herein, we have synthesized zinc ferrite (ZnFe$_2$O$_4$) thin films on nickel foam via spray pyrolysis method at substrate temperatures of 300, 400, and 500 °C. The physicochemical properties of ZnFe$_2$O$_4$ films were investigated using X-ray diffraction, scanning electron microscopy, energy dispersive X-ray analysis and fourier transform infrared spectroscopy (FT-IR) spectroscopy. Electrochemical properties oxygen evolution reaction and supercapacitive performance of ZnFe$_2$O$_4$ thin films were investigated through linear sweep voltammetry, cyclic voltammetry, galvanostatic charge-discharge, and electrochemical impedance spectroscopy. The ZnFe$_2$O$_4$ thin film synthesized at 400 °C exhibited an overpotential of 319 mV at a current density of 50 mA/cm^2 with a Tafel slope of 115 mV/dec. Furthermore, it also showed a specific capacitance of 335 F/g at 1 mA/cm^2 current density in 1 M KOH electrolyte.

1 Introduction

In recent decades, demand for highly efficient and low-cost energy generation and storage devices is increasing with the depletion of fossil fuels, global warming, upcoming portable electronics and electric vehicles [1, 2]. Recently, hydrogen has proved to be ideal fuel for the future, offering several advantages over traditional fuel like high energy density of approximately 140 MJ/kg, almost two times than that of carbon based

fuels and production of harmless water as by-product when it is burned [3]. Till today, hydrogen production heavily relied on the fossil fuel industry, which comes with significant limitations like high cost, low purity, and emission of SO$_2$ and CO$_2$ as a byproduct. Among various hydrogen generating technologies, water splitting is recognized as the most promising technology for producing hydrogen at low cost and with high purity [4]. Water splitting involves an anodic oxygen evolution reaction (OER) and cathodic hydrogen
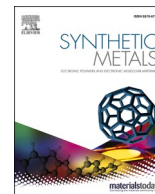
SILAR synthesized dysprosium selenide (Dy$_2$Se$_3$) thin films for hybrid electrochemical capacitors

S.D. Khot [a], D.B. Malavekar [a], R.P. Nikam [a], S.B. Ubale [a], P.P. Bagwade [a], D.J. Patil [a], V.C. Lokhande [b], C.D. Lokhande [a,*]

[a] Centre for Interdisciplinary Research, D.Y. Patil Education Society, Kolhapur 416006, India
[b] Department of Electronics and Computer Engineering, Chonnam National University, Gwangju 61186, South Korea

ABSTRACT

As the necessity of energy storage is continuously increasing, new materials have been investigated for electrochemical energy storage, especially for electrochemical capacitors. These storage devices are rapidly convertible as well as air pollution free. Therefore, a number of materials have been explored as electrode materials for supercapacitors to fulfill different requirements of electrochemical energy storage. Herewith, dysprosium selenide (Dy$_2$Se$_3$) films were prepared using the simple successive ionic layer adsorption and reaction (SILAR) method and characterized using different physico-chemical techniques. The specific capacitance (C_s) of 92 F g^{-1} was obtained at the current density of 2.85 A g^{-1} in 1 M LiClO$_4$ electrolyte with a retention of 85% over 5000 galvanostatic charge-discharge (GCD) cycles performed at a current density of 4 A g^{-1}. The flexible solid-state hybrid electrochemical capacitor of configuration Dy$_2$Se$_3$/LiClO$_4$-PVA/MnO$_2$ showed C_s of 83 F g^{-1} and specific energy of 18 Wh kg^{-1} at a specific power of 2.7 kW kg^{-1}. This hybrid device retained 92% of capacitance at a device bending angle of 160°. These results demonstrate the facile synthesis of Dy$_2$Se$_3$ and its possible use in electrochemical energy storage applications.

1. Introduction

In everyday life, advancing technology has made the most significant impact on the working nature of people. Therefore, it is essential to develop cheap and sophisticated technologies in the electronics, automobile industry, home appliances, biomedical field, etc., to uplift the quality of the human lifestyle. For this, a sustainable, green, and high-performance energy storage system is required which will play a vital role in our modern society [1]. There are different energy storage systems, but batteries, capacitors, and electrochemical capacitors (EC) are most promising. Among these, the charge accumulation mechanism is dissimilar for each of them. Currently, batteries have high energy density but possess disadvantages like low power density, finite cycle life, high cost of manufacturing, and several hours of charging time. The use of ECs can reduce those disadvantages due to their ability to deliver energy at a high rate, fast charging and discharging, efficient fabrication process, and long cycle life and hence gained significant attention in recent time [2,3].

The types of ECs materials mainly depend on the charge storage mechanism. They are broadly listed into three categories, i.e. electric double-layer capacitors (EDLC), pseudocapacitors and battery-type ECs. Charge accumulation in EDLCs is due to electrostatic mechanism across the electrode and electrolyte interface. The carbon derivatives and MXenes are of EDLCs type materials. In pseudocapacitors, redox reactions occurring on the surface and interior of the electrodes are responsible for charge accumulation. Metal oxides, chalcogenides as well as conducting polymers are the pseudocapacitive electrode materials. The battery-type ECs obey the faradic mechanism of charge storage [4,5]. Mostly nickel and iron oxides and phosphates are used as battery-type materials.

Due to their excellent redox activity, metal chalcogenides and conducting polymers show excellent pseudocapacitive behavior with high specific capacitance (C_s) than EDLCs [6]. The electrode material structure plays an important role by providing access to the electrolyte ions to electrode material for interaction. Many factors affect the electrode's charge storage, i.e., type of crystal structure, surface morphology, elemental composition, electrical resistivity, deposited mass of the electrode, and chemical composition [7]. The method of preparation

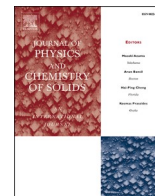# Synthesis of reduced graphene oxide (rGO)/dysprosium selenide (Dy$_2$Se$_3$) composite electrode for energy storage; flexible asymmetric supercapacitor

S.D. Khot [a], D.B. Malavekar [b], P.P. Bagwade [a], R.P. Nikam [a], C.D. Lokhande [a],[*]

[a] Centre for Interdisciplinary Research, D. Y. Patil Education Society, Kolhapur, 416 006, India
[b] School of Materials Science and Engineering, Chonnam National University, Gwangju, 500757, South Korea

ARTICLE INFO

ABSTRACT

In recent years, the requirement for flexible electrode materials has attracted scientific attention for developing flexible supercapacitors. The present work reports the porous reduced graphene oxide/dysprosium selenide (rGO/Dy$_2$Se$_3$) composite thin films preparation, employing successive ionic layer adsorption and reaction (SILAR) method. This work offers thorough information about the structure, morphology, and elemental analysis of prepared rGO/Dy$_2$Se$_3$ composite, as well as its electrochemical properties such as specific capacitance (C_s), charge transfer resistance, electrochemical stability, etc. The rGO/Dy$_2$Se$_3$ composite electrode achieved a C_s of 289 F g^{-1} at a 5 mV s^{-1} scan rate with 89% retention up to 5000 galvanostatic charge-discharge (GCD) cycles due to synergy between properties of Dy$_2$Se$_3$ and rGO. A flexible solid-state asymmetric supercapacitor (FSSAS) rGO-Dy$_2$Se$_3$/LiClO$_4$-PVA/MnO$_2$) device delivered C_s of 107 F g^{-1} at a 5 mV s^{-1} and a specific energy of 45 Wh kg^{-1} at a power of 9 kW kg^{-1}. The FSSAS device retained 91% of its capacitance at a 160° bending angle. These findings show that Dy$_2$Se$_3$ anchored on rGO using SILAR method is a promising candidate for supercapacitors.

1. Introduction

Technological advancement has accelerated energy consumption. As a result, different energy storage devices are required for various instruments in modern technology, such as healthcare, intelligent devices, micro-robotics, smartphones, flexible touchscreen displays, electronic skin, implantable medical devices, etc. Because of this, the need for flexible energy storage devices has increased and attracted tremendous research interest [1,2]. Together with secondary batteries, flexible supercapacitors have received a lot of attention due to their rapid charging, robust mechanical flexibility, long life, light weight, high operating voltage, superior safety, ability to provide required power density in a wide range of temperatures, and nearly constant performance even with mechanical deformation states [3–5]. Considering the above qualities of flexible supercapacitors, the implementation of flexible supercapacitors in wearable and flexible appliances has increased in the recent past. Therefore, the fabrication of flexible supercapacitors has been an attractive research topic in recent years.

One of the effective strategies to fabricate flexible SCs is to incorporate essential components like flexible and lightweight substrates, suitable electroactive materials, and electrolytes. The flexible substrates used so far are cellulose papers, textiles, paper, elastomeric polymers, cable-type matrices, stainless steel (SS), carbon sponge, and carbon-based papers (e.g., carbon cloth). However, the low conductivity, negative electrochemical activity, and low mechanical strength of some of these current collectors made obtaining desirable specific energy difficult. In this context, the SS substrate is the most favorable owing to its various benefits like low cost, high flexibility with mechanical strength, lightweight, ease of surface modification, and environment compatibility [6,7].

The electric double-layer capacitor (EDLC) and pseudocapacitive types of electrode materials are used in supercapacitors. The carbonaceous materials used in EDLCs have a low energy density [8]. Therefore, the present studies mainly focus on pseudocapacitive materials because of their high specific energy. Pseudocapacitive materials consist of transition metal oxides, chalcogenides, phosphates, nitrides, tungstate, and rare earth metal chalcogenides (REMC). The REMC possesses great potential as a pseudocapacitive material. The distinctive characteristics of REMC include 4f vacant orbital, high mechanical stability, rapid charge transfer, and high ionic conductivity at the electrode-electrolyte interaction [9,10]. Due to this, REMC materials are now widely utilized in a variety of applications like magnetic, catalysts, optical, and energy

---

Patents

क्रम सं/SL No :022131523

पेटेंट कार्यालय,भारत सरकार **The Patent Office, Government Of India**

पेटेंट प्रमाण पत्र | **Patent Certificate**

(पेटेंट नियमावली का नियम 74) | (Rule 74 of The Patents Rules)

पेटेंट सं. / Patent No.	:	473475
आवेदन सं. / Application No.	:	202121062097
फाइल करने की तारीख / Date of Filing	:	31/12/2021
पेटेंटी / Patentee	:	D.Y.PATIL EDUCATION SOCIETY(DEEMED TO BE UNIVERSITY),KASAB BAWADA,KOLHAPUR
आविष्कारकों का नाम /Name of Inventor(s)	:	1.PROF.CHANDRAKANT DYANDEV LOKHANDE 2.MR.RANJIT PANDURANG NIKAM 3.MR.SAMBHAJI DINKAR KHOT 4.MISS.PRITY PRAKASH BAGWADE 5.MR.DILIP JAGANNATH PATIL

प्रमाणित किया जाता है कि पेटेंटी को, उपरोक्त आवेदन में यथाप्रकटित *"CHEMICAL SYNTHESIS OF CADMIUM SELENIDE/REDUCED GRAPHENE OXIDE COMPOSITE THIN FILM AND PHOTOELECTROCHEMICAL CELL APPLICATION."* नामक आविष्कार के लिए, पेटेंट अधिनियम, 1970 के उपबंधों के अनुसार आज तारीख दिसम्बर 2021 के इक्तीसवें दिन से बीस वर्ष की अवधि के लिए पेटेंट अनुदत्त किया गया है।

It is hereby certified that a patent has been granted to the patentee for an invention entitled *"CHEMICAL SYNTHESIS OF CADMIUM SELENIDE/REDUCED GRAPHENE OXIDE COMPOSITE THIN FILM AND PHOTOELECTROCHEMICAL CELL APPLICATION."* as disclosed in the above mentioned application for the term of 20 years from the 31st day of December 2021 in accordance with the provisions of the Patents Act,1970.

अनुदान की तारीख :
Date of Grant : 28/11/2023

पेटेंट नियंत्रक
Controller of Patents

टिप्पणी – इस पेटेंट के नवीकरण के लिए फीस, यदि इसे बनाए रखा जाना है, दिसम्बर 2023 के इक्तीसवें दिन को और उसके पश्चात प्रत्येक वर्ष मे उसी दिन देय होगी।

Note. - The fees for renewal of this patent, if it is to be maintained, will fall / has fallen due on 31st day of December 2023 and on the same day in every year thereafter.

INTELLECTUAL PROPERTY INDIA
PATENTS | DESIGNS | TRADE MARKS
GEOGRAPHICAL INDICATIONS

क्रम सं/SL No :022124844

सत्यमेव जयते

पेटेंट कार्यालय,भारत सरकार
पेटेंट प्रमाण पत्र
(पेटेंट नियमावली का नियम 74)

The Patent Office, Government Of India
Patent Certificate
(Rule 74 of The Patents Rules)

पेटेंट सं. / Patent No.	:	434444
आवेदन सं. / Application No.	:	202221054562
फाइल करने की तारीख / Date of Filing	:	23/09/2022
पेटेंटी / Patentee	:	D.Y. PATIL EDUCATION SOCIETY (INSTITUTION DEEMED TO BE UNIVERSITY), KASABA BAWADA KOLHAPUR
आविष्कारकों का नाम /Name of Inventor(s)	:	1.PROF.CHANDRAKANT DNYANDEV LOKHANDE 2.MR.RANJIT PANDURANG NIKAM 3.MR.SOHEL BABULAL SHAIKH

प्रमाणित किया जाता है कि पेटेंटी को, उपरोक्त आवेदन में यथाप्रकटित *"ELECTRODEPOSITION OF LANTHANUM SELENIDE THIN FILMS AND THEIR APPLICATION IN OXYGEN EVOLUTION REACTION"* नामक आविष्कार के लिए, पेटेंट अधिनियम, 1970 के उपबंधों के अनुसार आज तारीख सितम्बर 2022 के तेइसवें दिन से बीस वर्ष की अवधि के लिए पेटेंट अनुदत्त किया गया है।

It is hereby certified that a patent has been granted to the patentee for an invention entitled *"ELECTRODEPOSITION OF LANTHANUM SELENIDE THIN FILMS AND THEIR APPLICATION IN OXYGEN EVOLUTION REACTION"* as disclosed in the above mentioned application for the term of 20 years from the 23rd day of September 2022 in accordance with the provisions of the Patents Act,1970.

अनुदान की तारीख :
Date of Grant : 13/06/2023

पेटेंट नियंत्रक
Controller of Patents

क्रम सं/SL No :022126821

पेटेंट कार्यालय,भारत सरकार **The Patent Office, Government Of India**

पेटेंट प्रमाण पत्र | **Patent Certificate**

(पेटेंट नियमावली का नियम 74) | (Rule 74 of The Patents Rules)

पेटेंट सं. / Patent No.	:	445967
आवेदन सं. / Application No.	:	202221029730
फाइल करने की तारीख / Date of Filing	:	24/05/2022
पेटेंटी / Patentee	:	D.Y.PATIL EDUCATION SOCIETY (DEEMED TO BE UNIVERSITY)
आविष्कारकों का नाम /Name of Inventor(s)	:	1.PROF.CHANDRAKANT DNYANDEV LOKHANDE 2.MS.PRITY PRAKASH BAGWADE 3.MR.DHANAJI BALASO MALAVEKAR 4.MR.SAMBHAJI DINKAR KHOT 5.MR.RANJIT PANDURANG NIKAM

प्रमाणित किया जाता है कि पेटेंटी को, उपरोक्त आवेदन में यथाप्रकटित *ELECTROCHEMICAL SUPERCAPACITOR DEVICE* नामक आविष्कार के लिए, पेटेंट अधिनियम, 1970 के उपबंधों के अनुसार आज तारीख मई 2022 के चौबीसवें दिन से बीस वर्ष की अवधि के लिए पेटेंट अनुदत्त किया गया है।

It is hereby certified that a patent has been granted to the patentee for an invention entitled *ELECTROCHEMICAL SUPERCAPACITOR DEVICE* as disclosed in the above mentioned application for the term of 20 years from the 24th day of May 2022 in accordance with the provisions of the Patents Act,1970.

अनुदान की तारीख : 21/08/2023
Date of Grant :

पेटेंट नियंत्रक
Controller of Patents

टिप्पणी – इस पेटेंट के नवीनरण के लिए फीस, यदि इसे बनाए रखा जाना है, मई 2024 के चौबीसवें दिन को और उसके पश्चात प्रत्येक वर्ष मे उसी दिन देय होगी।

Note. - The fees for renewal of this patent, if it is to be maintained, will fall / has fallen due on 24th day of May 2024 and on the same day in every year thereafter.

INTELLECTUAL PROPERTY INDIA
PATENTS | DESIGNS | TRADEMARKS
GEOGRAPHICAL INDICATIONS

पेटेंट कार्यालय,भारत सरकार
पेटेंट प्रमाण पत्र |
(पेटेंट नियमावली का नियम 74)

The Patent Office, Government Of India
Patent Certificate
(Rule 74 of The Patents Rules)

पेटेंट सं. / Patent No.	:	479403
आवेदन सं. / Application No.	:	202221039656
फाइल करने की तारीख / Date of Filing	:	11/07/2022
पेटेंटी / Patentee	:	D.Y.PATIL EDUCATION SOCIETY (DEEMED TO BE UNIVERSITY),KASABA BAWADA,KOLHAPUR
आविष्कारकों के नाम /Name of Inventor(s)	:	1.PROF.CHANDRAKANT DNYANDEV LOKHANDE 2.MR.DILIP JAGANNATH PATIL 3.DR.DHANAJI BALASO MALAVEKAR 4.MR.SAMBHAJI DINKAR KHOT 5.MR.RANJIT PANDURANG NIKAM

प्रमाणित किया जाता है कि पेटेंटी को, उपरोक्त आवेदन में यथाप्रकटित *A METHOD OF SYNTHESIZING COMPOSITE OF REDUCED GRAPHENE OXIDE AND NICKEL TUNGSTATE FOR ENERGY STORAGE* नामक आविष्कार के लिए, पेटेंट अधिनियम, 1970 के उपबंधों के अनुसार आज तारीख जुलाई 2022 के ग्यारहवें दिन से बीस वर्ष की अवधि के लिए पेटेंट अनुदत्त किया गया है।

It is hereby certified that a patent has been granted to the patentee for an invention entitled *A METHOD OF SYNTHESIZING COMPOSITE OF REDUCED GRAPHENE OXIDE AND NICKEL TUNGSTATE FOR ENERGY STORAGE* as disclosed in the above mentioned application for the term of 20 years from the 11th day of July 2022 in accordance with the provisions of the Patents Act,1970.

अनुदान की तारीख	
Date of Grant :	08/12/2023

पेट निबंधक
Controller of Patents

टिप्पणी - इस पेटेंट के नवीकरण के लिए फीस, यदि इसे बनाए रखा जाना है, जुलाई 2024 के ग्यारहवें दिन को और उनके पश्चात प्रत्येक वर्ष में उसी दिन देय होगी।

Note. - The fees for renewal of this patent, if it is to be maintained, will fall / has fallen due on 11th day of July 2024 and on the same day in every year thereafter.

INTELLECTUAL PROPERTY INDIA
PATENTS | DESIGNS | TRADE MARKS
GEOGRAPHICAL INDICATIONS

सत्यमेव जयते

भारत सरकार
GOVERNMENT OF INDIA
पेटेंट कार्यालय
THE PATENT OFFICE
पेटेंट प्रमाणपत्र
PATENT CERTIFICATE
(Rule 74 of The Patents Rules)

पेटेंट सं. / Patent No.	:	433033
आवेदन सं. / Application No.	:	202221021506
फाइल करने की तारीख / Date of Filing	:	11/04/2022
पेटेंटी / Patentee	:	D.Y.PATIL EDUCATION SOCIETY (DEEMED TO BE UNIVERSITY)
आविष्कारक (जहां लागू हो) / Inventor(s)	:	1.PROF.CHANDRAKANT DNYANDEV LOKHANDE 2.MR.SAMBHAJI DINKAR KHOT 3.MR.RANJIT PANDURANG NIKAM 4.MS.PRITY PRAKASH BAGWADE 5.MR.DHANAJI BALASO MALAVEKAR

प्रमाणित किया जाता है कि पेटेंटी को, उपरोक्त आवेदन में यथाप्रकटित CHEMICAL SYNTHESIS OF REDUCED GRAPHENE OXIDE - DYSPROSIUM SELENIDE COMPOSITE THIN FILMS FOR ENERGY STORAGE नामक आविष्कार के लिए, पेटेंट अधिनियम, 1970 के उपबंधों के अनुसार आज तारीख अप्रैल 2022 के ग्यारहवें दिन से बीस वर्ष की अवधि के लिए पेटेंट अनुदत्त किया गया है।

It is hereby certified that a patent has been granted to the patentee for an invention entitled CHEMICAL SYNTHESIS OF REDUCED GRAPHENE OXIDE - DYSPROSIUM SELENIDE COMPOSITE THIN FILMS FOR ENERGY STORAGE as disclosed in the above mentioned application for the term of 20 years from the 11th day of April 2022 in accordance with the provisions of the Patents Act,1970.

अनुदान की तारीख :
Date of Grant : 29/05/2023

पेटेंट नियंत्रक
Controller of Patent

टिप्पणी - इस पेटेंट के नवीकरण के लिए फीस, यदि इसे बनाए रखा जाना है, अप्रैल 2024 के ग्यारहवें दिन को और उसके पश्चात प्रत्येक वर्ष मे उसी दिन देय होगी।

Note. - The fees for renewal of this patent, if it is to be maintained will fall / has fallen due on 11th day of April 2024 and on the same day in every year thereafter.

Conferences

2nd Asian e-Conference on Engineered Science

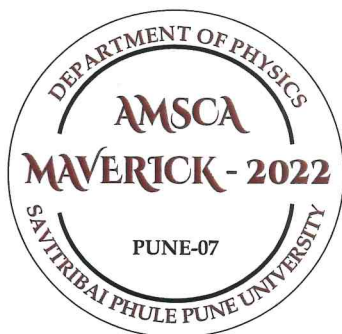## CERTIFICATE

Ranjit Nikam

This is to certify that Miss/Mr/Mrs/Dr

has Presented a Paper in 2nd Asian e-Conference on Engineered Science jointly

organized by Prof. C. D. Lokhande Endowment Charitable Trust and Engineered

Science Publisher, USA held during 5-6 December 2021.

Prin. Dr. J. D. Desai
President, Prof. CDLET, Pune

Prof. John Zhanhu Guo,
ES Publisher, USA

Certificate
of Appreciation

R. P. NIKAM

D. Y. Patil Education Society, Kolhapur

for her invaluable contribution to the **Best Oral / Poster** from **PP-05 Photovoltaic Materials**.Theme made in the International Conference on **Advanced Materials Synthesis, Characterization and Applications (AMSCA Maverick-2022)** With Special Topic: New Education Policy held at the Department of Physics, Savitribai Phule Pune University, Pune07, Maharashtra, India during **18th - 20th October, 2022.**

Convener
(AMSCA Maverick-2022)

Co-Convener
(AMSCA Maverick-2022)

Chairperson
(AMSCA Maverick-2022)

Three days International Conference on
Nano Composites for Aerospace Applications
Hybrid Mode

02nd to 04th February 2023

ICNCAS - 2023

Sponsored by

CERTIFICATE

This certificate is presented to

Mr. R.P. Nikam

Centre for Interdisciplinary Research, D.y. Patil Education Society, Kolhapur,

for presenting the Research Paper Entitled on

Chemisynthesized CDSE/RGO composite electrodes for Photochemical cell application.

in the 2023 Three days International Conference on Nano Composites for Aerospace Applications (ICNCAS - 2023) held at the Department of Basic Sciences and Electronics & Communication Engineering, Cambridge Institute of Technology, Bengaluru, India.

Dr. Ravi Shankar
Assoc. Professor, Dept. of Basic Sciences
Cambridge Institute of Technology
Bangalore

Dr. G. Indumathi
Principal
Cambridge Institute of Technology
Bangalore

Shri. Nithin Mohan
CEO
Cambridge Institute of Technology
Bangalore

Shri. D.K. Mohan
Chairman
Cambridge Institute of Technology
Bangalore

CAMBRIDGE
INSTITUTE OF TECHNOLOGY

Organized by
Department of Basic Sciences and Electronics & Communication Engineering

D. Y. PATIL EDUCATION SOCIETY

(Deemed to be University), KOLHAPUR

NAAC 'A+' Grade in 3rd Cycle

Certificate

This is to certify that **Mr. Ranjit Pandurang Nikam** of Department of Medical Physics, Centre for Interdisciplinary Research, D. Y. Patil Education Society (Deemed to be University), Kolhapur has ~~delivered invited talk/ chaired the session/ presented oral/ presented poster/ participated~~ in the **International Conference on Nanotechnology Addressing the Convergence of Materials Science, Biotechnology and Medical Science (IC-NACMBM-2024)** held at the Centre for Interdisciplinary Research, D. Y. Patil Education Society (Deemed to be University), Kolhapur, Maharashtra, India during 12th to 14th February 2024. His contribution to the conference is highly appreciated.

Dr. Jayavant L. Gunjakar

Convener

Prof. Meghnad G. Joshi

Convener

Prof. Chandrakant D. Lokhande

Chairman

SHIVAJI UNIVERSITY, KOLHAPUR

SOPHISTICATED ANALYTICAL INSTRUMENT FACILITY (SAIF) – COMMON FACILITY CENTRE (CFC)

WORKSHOP & HANDS-ON TRAINING ON XRD ORGANISED BY SAIF-CFC UNDER STRIDE PROGRAMME

Certificate of Participation

This is certify that Mr. *Nikam Ranjit Pandurang* has successfully participated in the workshop & hands-on training on XRD organised by SAIF (CFC), Shivaji University, Kolhapur held during 11-12 Nov, 2021 under the STRIDE (Scheme for Trans-disciplinary Research for India's Developing Economy) programme.

Prof. R. G. Sonkawade
Co-ordinator : SAIF, Head (i/c) : CFC
Shivaji University, Kolhapur.
Chairman

D. Y. PATIL EDUCATION SOCIETY

(Institution Deemed to be University), Kolhapur

Re-Accredited by NAAC with 'A' Grade

CERTIFICATE

Workshop on

GOOD LABORATORY PRACTICES

Successfully attended by *RANJIT PANDURANG NIKAM*

on Saturday 06 February 2021

Organized By

Department of Stem Cell and Regenerative Medicine and Department of Medical Physics, Centre for Interdisciplinary Research

Prof. Dr. C. D. Lokhande

Chairman

Prof. Dr. S. Mohan Karuppayil

Convener

Dr Shivaji Kashte

Organising Secretary